EXPERIMENTAL INVESTIGATIONS AND NUMERICAL SIMULATIONS OF THE MECHANICAL BEHAVIOUR OF POLYAMIDES

Thesis destined for obtaining
the academic degree of Doctor of Engineering
at
"Politehnica" University of Timişoara
in the field of MECHANICAL ENGINEERING
by

Eng. Dan-Andrei ŞERBAN

Scientific coordinator: Prof. Dr. Eng. Liviu MARŞAVINA
Scientific referees: Prof. Dr. Eng. Werner HUFENBACH
Dr. Eng. Daniel PRICE
Prof. Dr. Eng. Dan Mihai CONSTANTINESCU

Thesis defence date: 10.12.2012

Seriile Teze de doctorat ale UPT sunt:

1. Automatică
2. Chimie
3. Energetică
4. Ingineria Chimică
5. Inginerie Civilă
6. Inginerie Electrică
7. Inginerie Electronică şi Telecomunicaţii
8. Inginerie Industrială
9. Inginerie Mecanică
10. Ştiinţa Calculatoarelor
11. Ştiinţa şi Ingineria Materialelor

Universitatea „Politehnica" din Timişoara a iniţiat seriile de mai sus în scopul diseminării expertizei, cunoştinţelor şi rezultatelor cercetărilor întreprinse în cadrul şcolii doctorale a universităţii. Seriile conţin, potrivit H.B.Ex.S Nr. 14 / 14.07.2006, tezele de doctorat susţinute în universitate începând cu 1 octombrie 2006.

România, 300159 Timişoara, Bd. Republicii 9,
tel. 0256 403823, fax. 0256 403221
e-mail: editura@edipol.upt.ro

Preface

In recent years, polymer industry has recorded a growth due to advancements in the science and technology of plastics that harness their unique properties. Due to the fair mechanical properties at a low specific mass, polymers are gaining new ground as structural components (either as a part of fibre reinforced composites or as stand-alone polymer parts).

This research was initiated by adidas in order to gain insights about the mechanical behaviour of a material that is used in manufacturing a footwear component, as it is subjected to various types of loadings (static, cyclic, dynamic).

The present work consists of a joint effort of several institutes: adidas innovation team, ILK (TU Dresden), Loughborough University and "Politehnica" University of Timişoara. I would like to take this opportunity to thank Prof. Vadim V. Silberschmidt for enabling this research by establishing the collaboration between adidas, Loughborough University and "Politehnica" University of Timişoara as well as for his support during my stay at Loughborough University. I would also like to thank Dr. Erwin Christian Lovasz for creating the possibility for me to set up research stages at The Institute of Lightweight Engineering and Polymer Technology (ILK), Technische Universität Dresden.

I want to express sincere appreciations to my PhD supervisor, Prof. Liviu Marşavina for his guidance and advice throughout this whole period of time. I like to thank Dr. Dan Price from adidas for his thorough analysis of my work and for ensuring a high standard, characteristic of a world class company. I would like to thank Prof. Dr. Eng. habil. Prof. E.h. Dr. h.c. Werner Hufenbach and Dr. Niels Modler for their collaboration, their willingness to help and for their support during my stays in Dresden. I would also like to thank Dr. Andy Harland and the staff at Sports Technology Institute, Loughborough University for their aid and assistance during my stay in the UK.

I would like to thank my colleagues form the Department of Mechanics and Strength of Materials, especially Manu and Tudor for helping me with various tasks whenever I was in need. I want to thank Bogdan for being such a good friend and for all his advices. I would like to express my gratitude towards all the friends and acquaintances that encouraged me all this time and towards the ones that made my life easier when being far away from home.

Last but not least, I am forever grateful to my parents and family for all the support that they gave me throughout my studies and for guiding me towards this path.

Şerban, Dan-Andrei

Identificarea experimentală şi simularea numerică a comportării mecanice a poliamidelor

Teze de doctorat ale UPT, Seria 9, Nr. 126, Editura Politehnica, 2013, 184 pagini, 138 figuri, 33 tabele.

ISSN: 1842-4937

ISBN: 978-606-554-589-2

Cuvinte cheie: Thermoplastic polymer; Mechanical properties; Tensile loading; Three-point bending; Dynamic properties; DMA; Puncture impact; Numerical simulations; Hyperelastic model; Elasto-plastic model; Viscoelastic model.

Rezumat:

The PhD Thesis entitled *Experimental investigations and numerical simulations of the mechanical behaviour of polyamides* deals with the analysis of the behaviour of a PA-12 based polymer that has applications in sports footwear components. The mechanical properties of this material were investigated for various loading scenarios, results being used in designing virtual material models for finite element analysis simulations. The thesis is structured in 5 chapters. The first chapter consists of the thesis introduction, presenting the research background, the state of the art and the objectives. The second chapter presents the experimental procedures and the obtained results for tensile loadings (monotone tests, cyclic tests, low-cycle fatigue tests), three-point bending tests, dynamic tests (dynamic tension, DMA tests, puncture impact tests) and for compression tests performed on footwear components. In the third chapter several analytical models for describing constitutive relations were presented: linear elasticity, hyperelasticity, plasticity and viscoelasticity. The fourth chapter presents the results for simulations performed on three constitutive formulations: an elasto-plastic model, a hyperelastic model and a viscoelastic model. The constitutive models were evaluated for several test scenarios (monotone tension, cyclic tension and three-point bending) and validated on component simulations. The fifth chapter presents the conclusions and the personal contributions.

CONTENTS

Table of figures

1. INTRODUCTION

1.1. Background

Polymers represent a class of materials whose structures consist of long covalently bonded chains of atoms of very high molecular weights (macromolecules) [**1**]. They can be found in natural form – biopolymers (fibres, amber, latex) – or can be obtained through various industrial processes of polymerization – synthetic polymers (most polymers encountered in everyday life) [**2**]. Due to this particular type of structure, polymers come in a variety of forms: rubbers, plastics, adhesives, foams, resins. As a consequence, the mechanical characteristics vary in a wide range from one class of polymers to the other (the Young's modulus of a polymeric foams can be as low as 5 MPa while for a liquid crystal polymer, it could become as high as 350 GPa, 70,000 times higher) and even for the same polymer in different states [**2**].

Although natural polymers knew extensive use for the past 6000 years (cotton, starch, wool, various adhesives, resins etc) [**3**], the exploitation of synthetic polymers recorded an exponential growth during the last 70 years (for the past 20 years, the total production of polymers exceeded the combined metal production volume wise) [**3**]. Due to their characteristics, especially low production costs, high productivity, fairly good mechanical properties at a low specific mass or good insulation, polymers started to replace some conventional materials (metals, wood and textiles) in almost any industrial branch. Polymer science evolved along, trying to gain insight into polymer's structure and the relation it has to morphology, physical and mechanical behaviour [**1**].

Before the structure of polymers was determined, their unique response to mechanical loads was observed: sometimes, polymer behave as elastic solids, sometimes, they behave as viscous fluids but in all cases, the properties are time- and temperature-dependent [**1**,**2**,**3**,**4**,**5**,**6**]. The first mathematical models developed in order to try to explain this behaviour were developed by Scottish scientists James Clerk Maxwell and Sir William Thompson, Lord Kelvin in the 19th century [**3**], along with the work of Austrian physicist Ludwig Boltzmann (the first to coin the term *viscoelasticity*), which studied the hereditary nature of materials throughout his scientific career [**3**].

The accurate prediction of polymer behaviour under various loading conditions remains a challenging technological problem, especially for structural components. Following the Challenger Space Shuttle disaster (January 28th, 1986), the Presidential commission led by William P. Rogers, with the important contribution of Nobel Prize in Physics laureate Prof. Richard Feynman determined that due to low temperatures recorded during the space shuttle launch, the rubber O-rings sealing the aft field joint on the right solid rocket booster became less resilient and failed subsequently allowing pressurised hot gasses to make contact with the external tank thus causing structural failure [**7**]. This catastrophic event proves the importance of anticipating polymers' behaviour during in-service loadings especially when they have a structural role in assemblies.

Although only some types of polymeric products are used as parts of potentially life threatening assemblies (another example would be the automotive industry with rubber dampers on engine mounts or tires [**8**]), high-performance products in all fields require in-depth knowledge of material behaviour. Recording an exponential growth in recent years, the sports equipment industry represents one field that is attracting more resources for the development of better products. In order to produce competitive equipment, companies have resorted to multi-field design through the joint efforts of engineers, designers and bio-medical staff for designing high performance products without neglecting aesthetics, athletes' safety and product durability. As with other industries, advanced materials such as synthetic polymers and composites are slowly taking over conventional sports materials (leather, wood, cotton). As a relevant example for this study, adidas began using polyamide components on performance running footwear. One of such polyamides, a polyamide-12 based semi-crystalline thermoplastic polymer named will be the centrepiece of this research programme.

Due to the specific material behaviour of advanced materials, the integration of finite element analysis (FEA) methods of complex structures in the product design step has become essential in order to predict product behaviour under in-service conditions. FEA software implement several constitutive formulations for simulating material behaviour, based on principles of *continuum mechanics.*

In the last century, breakthroughs in Physics had allowed us gain insights deeper and deeper into the fabric of the matter surrounding us. If zooming to a certain level, the continuum macroscopic structure becomes a more or less ordered arrangement of molecules or atoms: metals and some ceramics show a repeated pattern of atoms (crystalline structure), some polymers exhibit chains of entangled macromolecules (amorphous structure) while others show ordered patters only on local scale (semi-crystalline structure).

However, in engineering, the discrete composition of material bodies is ignored in favour of a continuous concept of matter [**9**,**10**,**11**]. Thus, the given body's substance is considered to be distributed uniformly, filling all the space it occupies. No matter how small the quantity will be considered, it will still hold all the properties of the matter it is made of, so different scalar or vector values can be attributed to it, like density, velocity, inertial moment, etc. This simplified approach is used in engineering because the structural and functional parts used in all products have dimensions far larger than the atomic scale. Additionally, all information regarding the material properties and behaviour is collected from testes performed on large scale specimens.

Continuum mechanics deals with the analysis of the kinematic and mechanical behaviour of materials modelled after the continuum approach. In continuum mechanics two main topics are discussed: the derivation of the fundamental equations valid for all continuous matter and the development of the constitutive equations that govern ideal material models.

1.2. State of the art

As mentioned in the previous paragraph, first mathematical models designed for polymers were elaborated in the 19th century by Maxwell (the Maxwell fluid [**2**,**3**,**5**]) and Kelvin (the Kelvin solid [**2**,**3**,**5**]). These models were developed in order to account for stress relaxation (Maxwell model) or creep (Kelvin model [**2**,**3**,**5**]) observed in natural materials such as tar, bread dough or pitch [**3**]. These

constitutive models as well as more accurate models based on the Maxwell and Kelvin elements (the four-parameter fluid, the standard linear solid, the generalized Maxwell model or the Kelvin-Voigt model [**1**,**2**,**3**,**5**]) considered linear elasticity and linear viscosity as constitutive formulations.

Though simulations of brittle polymers yield accurate results by employing simple linear elastic models [**1**,**3**,**6**], other classes of polymer such as semi-crystalline thermoplastic polymers, thermoplastic elastomers and rubbers show a significant non-linear characteristics and the generalized Hooke's law is able to describe material's behaviour only for very small strains. The behaviour of such materials at large strains was dubbed *hyperelasticity* and a new approach was established which considers that the constitutive equations are only dependent on the initial state and on the final state of the deformation [**11**]. In consequence, the stress-strain response is derived from a stored elastic potential function called the *strain-energy density function* [**11**].

The first explicit functions considered isotropic hyperelasticity in the principal directions, had polynomial form and were developed by R.S. Rivlin in 1948 (the Mooney-Rivlin material [**12**,**13**]) based on his observations on the behaviour or rubber in uniaxial tension.

Yeoh proposed a simplification of the polynomial form by excluding the dependency on the second invariant [**14**], assuming that the model will predict more accurate results due to the difficulty in evaluating II_C, which would produce erroneous results if measured inaccurately. A particular form of the reduced polynomial formulation represents the Neo-Hooke material which relates the hyperelastic function to the Lamé moduli [**11**].

R.W. Ogden proposed a generalized hyperelastic function expressed in terms of the principal stretches based on the polynomial formulation: for certain values of the function order, the Ogden models transforms into the Mooney-Rivlin model or the Neo-Hookean model [**15**].

The Van der Waals model proposed by H.G. Killian has a hyperelastic function similar to the thermodynamic interpretation of the equations of state of a real gas as it introduces two material parameters that account for the interaction between the particles and a locking stretch (the equivalent of the excluded volume parameter in the real gas equation) [**16**].

The Arruda-Boyce formulation [**17**] is based on a volumetric element with eight springs attached from the centre to its edges (hence its nickname: the *eight-chain model*). This function only considers the first invariant as the basis of deformation.

The Marlow model does not assume any explicit form, as it is calculated by integrating the nominal uniaxial traction from numerical data gathered from experiments [**18**].

The time effects of viscoelasticity also play an important role in determining material behaviour when subjected to cyclic loadings: L. Mullins observed a hysteresis of energy when unloading from a certain state of deformation, the material's softening as it is loaded in cyclic patterns of the same amplitude as well as strain hardening, when stretching the material past the previous deformation point (the stress-strain response follows the path described by a virgin specimen) [**19**,**20**,**21**]. This specific behaviour that encompasses the three phenomena was named the *Mullins effect* [**22**]. Though first attributed solely to rubbers [**20**,**21**], Mullins effect was also observed in thermoplastic elastomers [**23**,**24**,**25**], semi-crystalline thermoplastics [**26**,**27**,**28**], as well as in biological tissues [**29**,**30**,**31**].

Constitutive formulations for Mullins effect were elaborated for various types of materials and loading conditions. For rubbers, Dorfmann and Ogden [**32**] proposed a constitutive model that accounts for stress softening and permanent set (the stable material response resulted after the effects of stress softening become negligible [**22**,**33**]) using the theory of pseudo-elasticity. Diani *et al*. proposed a constitutive model based on a strain-energy function along the principal directions coupled with the theory of network alteration [**34**]. Another approach was developed by Cantournet *et al.* considering a thermodynamic model of internal sliding and friction [**25**]. Bergstrom and Boyce designed a constitutive model composed of two networks: one corresponding to the long-time (stress relaxation) behaviour and the other corresponding to the rate-dependent behaviour [**35**].

Accurate modelling of thermoplastic polymers requires more advanced formulations that additionally account for the progressive damage (reversible and irreversible [**1**]) induced during deformation. In this scope, viscoplastic formulation were developed, the first models being proposed by Nagdi and Murch [**36**] and further developed by Crochet [**37**], by introducing a new plasticity theory with a yield function that depends on the stress tensor, the plastic strain tensor, strain hardening and a time dependent factor that accounts for viscoelastic effects. The first phenomenological formulations for viscoplasticity were developed by Reiner [**38**] by modifying the Bingham model (which introduced a friction element that accounts for yielding [**39**]).

Based on these theories, more advanced viscoplastic models were elaborated, most noticeable being the work of A.D. Drozdov and collaborators, by developing a finite viscoplasticity model [**40**] and adapting it to accurately reproduce simulations in cyclic loadings (including the Mullins effect) for various experimental programs [**33**,**41**,**42**].

1.3. Objectives

In recent years, the development of specialized numerical analysis software allowed the evaluation of complex structures with relative ease thus becoming an indispensible tool for product design. Monotone loading simulations are performed by Adidas on their running footwear in order to determine the product behaviour and help with dimensioning procedures. The current material model for PA-12 consists of linear elasticity, providing a tool to engineer relative changes in structural stiffness based on geometry in the limits of elasticity.

The objective of this thesis is to develop a material model that can capture all non-linear aspects regarding the viscoplastic nature of the material: strain rate sensitivity, temperature dependency, plasticity, strain-softening, hysteresis etc in order to generate a better understanding regarding the damage induced behaviour and to ensure that appropriate safety factors are used.

The first step of the research will consist of gathering information about PA-12's behaviour in various loading condition:

- Behaviour in static loadings;
- Behaviour in dynamic loadings;
- Behaviour in cyclic loadings and low-cycle fatigue.

Apart from specimen testing, component testing will give insight on the product behaviour in actual loading scenarios.

The gathered data will become the foundation for numerical material models. The developed materials will be evaluated through experimental replication and are to be validated on top plate simulations.

2. EXPERIMENTAL INVESTIGATIONS

2.1. Overview

According to the material supplier (see Annex I), the PA-12 compound is a heat stabilized and light resistant polyamide 12-based semi-crystalline thermoplastic polymer. It was first developed for extrusion and co-extrusion of ski upper and decorative films. The material provider summarizes PA-12's characteristics as "high transparency, good screen and sublimation printing, outstanding scratch resistance, and excellent impact strength at low temperatures." Other properties include good scratch resistance, low friction coefficient and good chemical resistance. Some mechanical and physical characteristics are also provided, namely Young's modulus (1100 MPa), tensile stress as yield (37 MPa), tensile strain at yield (5%) and strain at break (over 200%).

The provided material specification sheet gives little information about the material's non linear behaviour and the properties variation with test conditions. Consequently, starting from the thesis objectives, an experimental plan was developed in order to cover a wide range of mechanical properties.

The experimental programme can be classified under several criteria:

- Considering the effect of time, experimental procedures include: static tests, cyclic tests, dynamic tests and creep tests.
- Considering the mode of deformation, experimental procedures include: tensile tests, three-point bending tests, puncture tests and compression tests.
- Considering the loading type, experimental procedures include: monotone tests, cyclic tests and low-cycle fatigue tests.

For the designed experimental programme, special attention was directed towards the parameters that influence the mechanical behaviour of the material: temperature, strain-rate and condition. Temperature dependency tests were performed in an interval similar to the product's usability envelope. As mentioned above, strain rate dependency tests considered static, dynamic and long term effects.

2.2. Tensile tests

2.2.1. Monotone static tensile tests

When studying mechanical properties tensile tests represent the basic experimental method for characterising most materials for a number of reasons. Apart for the simple test setup (tension clamps are standard features for most universal testing equipment) and specimen preparation (any regular shape can be tested although dogbones are recommended), tensile tests represent the closest experimental procedures to a pure uniaxial loading. The main material characteristics that are deducted from tensile tests are [**43**]:

- Young's modulus E [MPa];

- Tensile stress at break σ_b [MPa];
- Tensile strain at break ε_b [MPa];
- Tensile stress at yield σ_y [MPa];
- Tensile strain at yield ε_y [MPa];
- Tensile strength σ_{max} $[MPa]$.

All tensile tests were performed on standard ISO 527 dogbone specimens [**43**] (Figure 2.1).

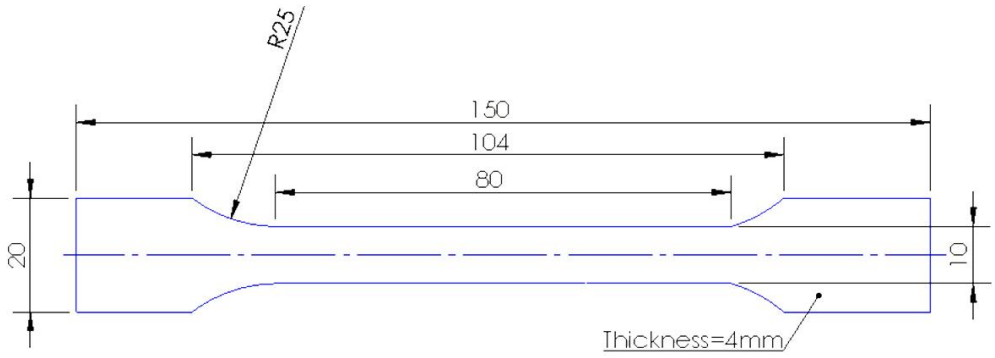

Figure 2.1 ISO 527 standard dogbone specimen

As stated in the previous chapter, PA-12 exhibits significant non-linear material behaviour as well as property variation with test parameters, mainly temperature and time (strain-rate). Thus the goal of these tests was the determination of the material's stress-strain variation with strain-rate and temperature.

The tensile tests performed on PA-12 can be divided in two main categories:

- Monotone tests;
- Cyclic tests.

In monotone tests, the specimen is loaded from a relaxed state until it reaches a degree of deformation that can produce relevant data such as the yield point or the break point.

Figure 2.2 Thermal chamber on Zwick Z250 machine

2.2.1.1. Temperature influence

Thermoplastic polymers' properties have a significant variation with temperature. Depending on temperature, a polymer is characterized by a glassy behaviour (materials are stiffer and sometimes become brittle) and a ductile behaviour (materials become more compliant and yielding before fracture can be observed). The transition region between the two states is call the *glass transition temperature* [**1**,**2**,**4**,**6**,**44**].

Regardless of what is the glass

transition temperature for PA-12, the temperature values chosen for the tests were picked in the temperature interval of the product's usability envelope: -25 °C to 50 °C. Thus, the test temperatures are:

- -25 °C;
- 0 °C;
- 23 °C;
- 50 °C;

Temperature influence tests were performed at Institut für Leichtbau und Kunststofftechnik, Technische Universität Dresden on an electronic Zwick Z250 machine equipped with a 10kN load cell, equipped with a thermal chamber was used (Figure 2.2).

The tests were performed at two crosshead travel speeds: 20 mm/min and 200 mm/min. As with the strain-rate influence tests, the strain was recorded with an incremental extensometer.

The results for the tests are presented in Figure 2.3.

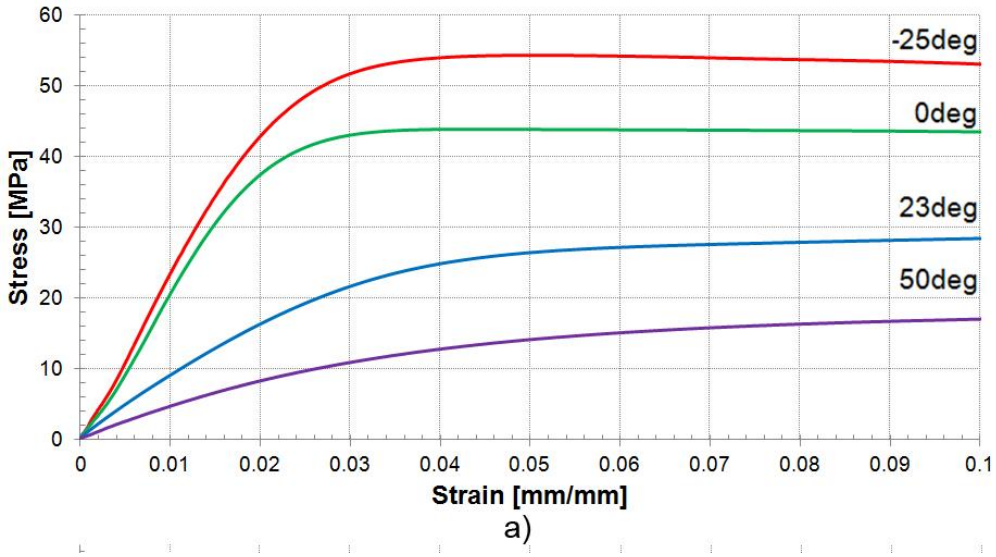

a)

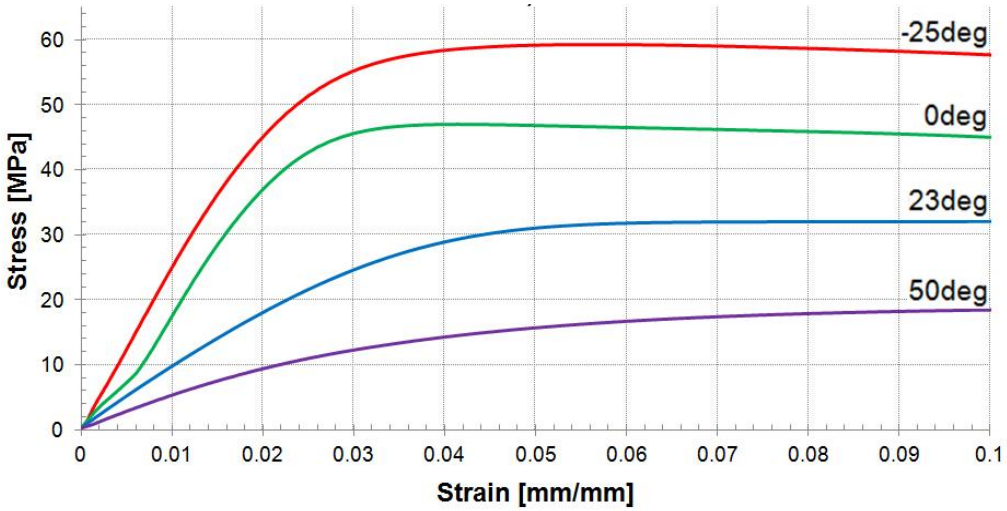

b)

Figure 2.3. Stress-strain curves for temperature dependency tests performed at a) 20 mm/min and b) 200mm/min

As is characteristic for ductile polymers, there is no singular point, at which the material starts to yield; instead, the yielding is associated with a finite region, [**1**,**2**,**3**]. As a result, the yield stress can be approximated with the tensile strength of a yielding region (subsequent hardening might determine higher tensile strength values in other regions beyond the first yielding).

The recorded values for the tensile strength and Young's modulus are presented in Table 2.1.

Table 2.1. Yield stress and Young modulus values for temperature dependency tests

	20 mm/min		200 mm/min	
Temp [°C]	Tensile strength σ_{max} [MPa]	Young's Modulus $E\ [MPa]$	Tensile strength σ_{max} [MPa]	Young's Modulus $E\ [MPa]$
-25	54	2100	57	2550
0	44	1400	47	1750
23	30	950	32	1000
50	19	480	20	500

At 20 mm/min crosshead travel speed, a drop in temperature from 50 °C to -25 °C resulted in a 337% increase in Young's modulus (from E = 480 MPa to E = 2100 MPa) and a 184% increase in tensile strength (from $\sigma = 19$ MPa to $\sigma = 54$ MPa).

At 20 mm/min crosshead travel speed, an increase in temperature -25 °C to 50 °C resulted in a 410% increase in Young's modulus (from E = 500 MPa to E = 2550 MPa) and a 185% increase in tensile strength (from $\sigma = 20$ MPa to $\sigma = 57$ MPa).

Regarding the yield strain, it decreases with temperature from around 6% at 50 °C down to around 3% at -25 °C.

2.2.1.2. Strain rate influence

The crosshead travel speeds used in the study of the strain-rate influence on tensile properties were chosen on logarithmic scale according to the values recommended in ISO 527 standard [**43**]:

- 2 mm/min;
- 20 mm/min;
- 200 mm/min;
- 2000 mm/min.

For studying strain-rate influence in monotone loadings, two types of machines were used:

For quasi-static tests, two machines were used: an electro-mechanical Zwick Z250 machine (central ball-lead screw drive) equipped with a 10 kN load cell for test speeds from 2 mm/min up to 200 mm/min and a servo-hydraulic Schenk PC63M equipped with a 40 kN load cell, for tests speeds of 2000 mm/min. The strain measurements were performed with incremental extensometers.

Figure 2.4 Zwick Z250 machine

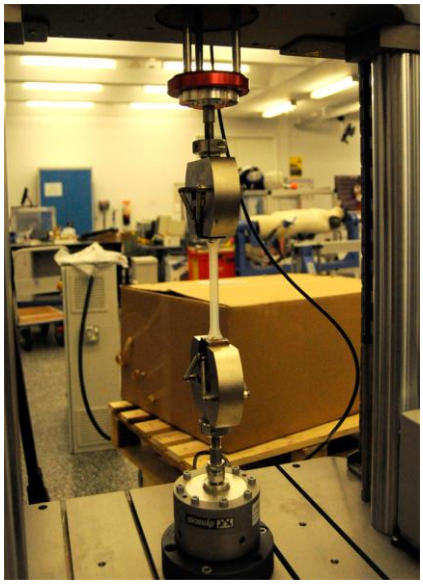

Figure 2.5 Schenk PC63M machine

The results for the low speed tests are presented in Figure 2.6 while the tensile strength and Young's modulus are presented in Table 2.2.

Table 2.2. Yield stress and Young's modulus from rate dependency tests

Test speed [mm/min]	Tensile strength σ_{max} [MPa]	Young's Modulus E [MPa]	Yield strain ε_y [mm/mm]
2	29.6	855	0.064
20	30.3	962	0.065
200	32.4	1012	0.063
2000	36.2	1106	0.064

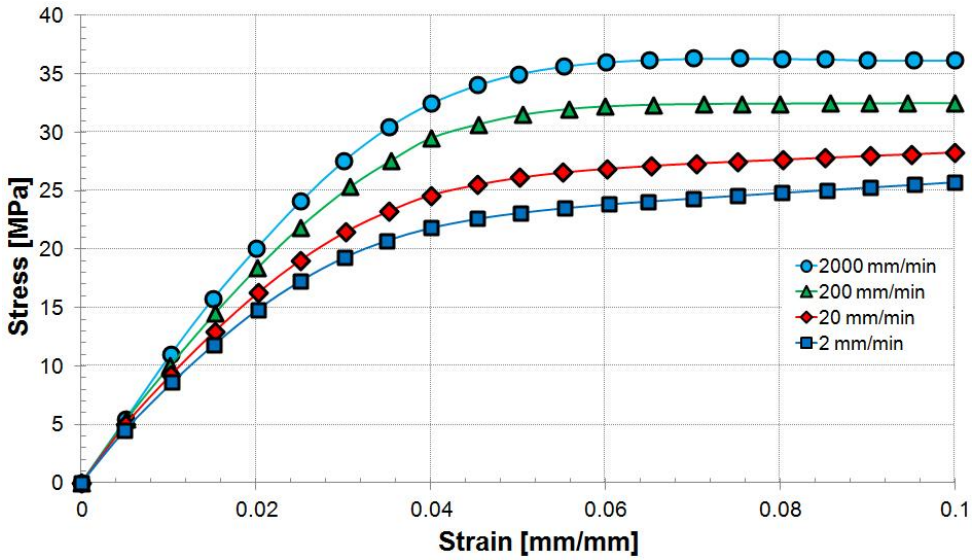

Figure 2.6. Stress-strain curves for quasi-static tests with various rates

For the tests performed at crosshead travel speeds between 2 mm/min and 2000 mm/min (100,000 % increase), there are variations of 29 % in the Young's modulus (from 850 MPa to 1100 MPa) and of 22 % in tensile strength (from σ_s=29.6 MPa to σ_s=36.2 MPa).

The variation of the instantaneous elastic modulus with strain is presented in Figure 2.1. In this case, the shapes of the instantaneous modulus curves are similar for all the test speeds, and no toe region is observed.

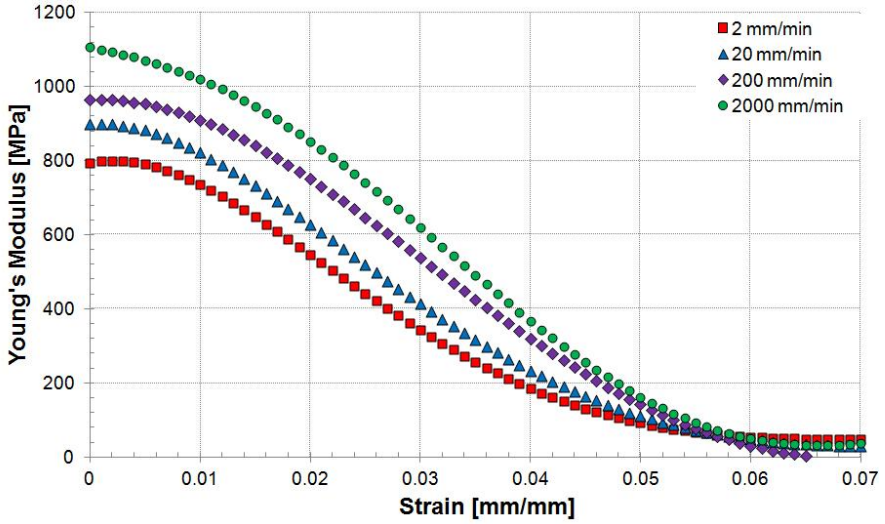

Figure 2.7. Elastic modulus variation with strain for quasi-static tests

For product design applications, the crosshead travel speed of the tests shows little relevance, and so it must be converted to the rate of deformation. As with the instantaneous elastic modulus, the strain rate was obtained by dividing the strain increment by the time increment. For the tests performed at low speeds, the correlation between the two parameters is presented in Figure 2.8.

For the tests performed at travel speeds of 2 and 20 mm/min, the strain-rate variation with time shows the influence of inertia linked to control of the rate of crosshead travel when the machine accelerates past the desired speed and slows down subsequently. For the tests at 200 mm/min, the electro-mechanical machine shows its limitation in terms of acceleration towards the desired speed. The servo-hydraulic machine provides a more stable response and is characterized by good acceleration. In all cases, the rate of deformation increases with strain, as the strain history does not have a linear progression, unlike the crosshead travel, as seen in Figure 2.9.

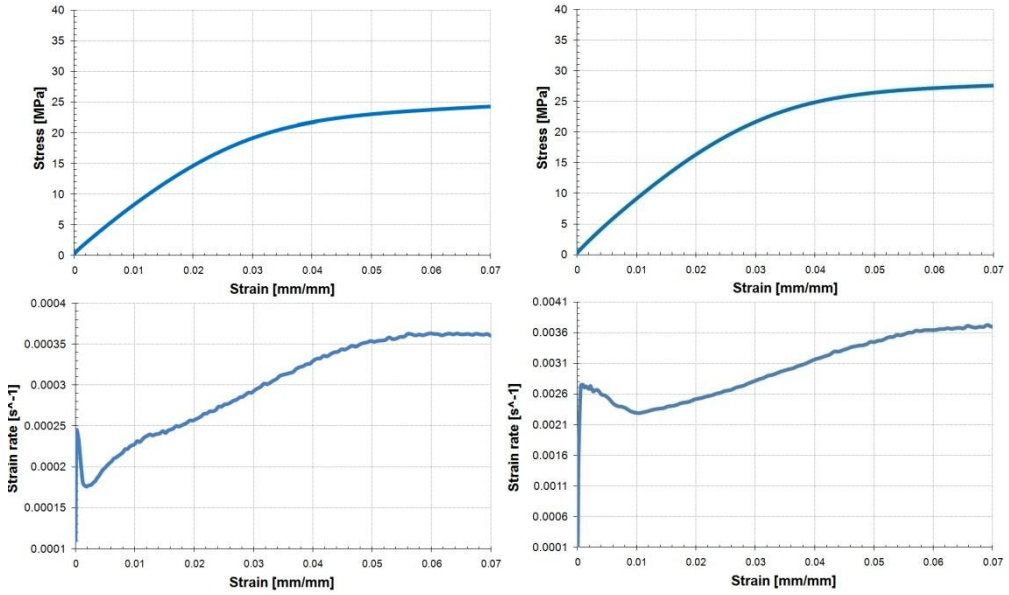

a) b)

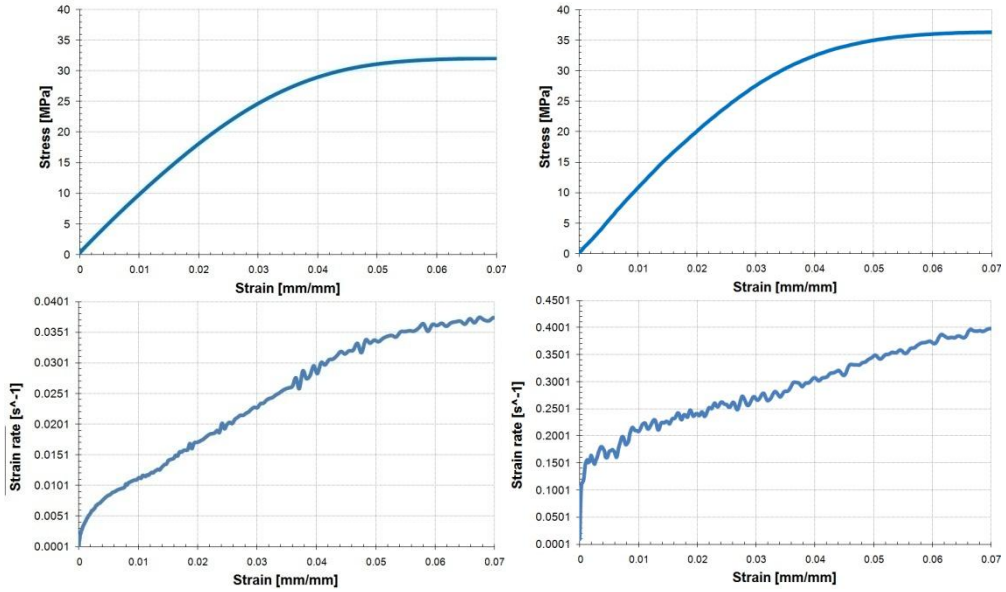

Figure 2.8. Strain rate variation with strain along with stress-strain curves for the speeds of 2 mm/min (a), 20 mm/min (b), 200 mm/min (c) and 2000 mm/min (d)

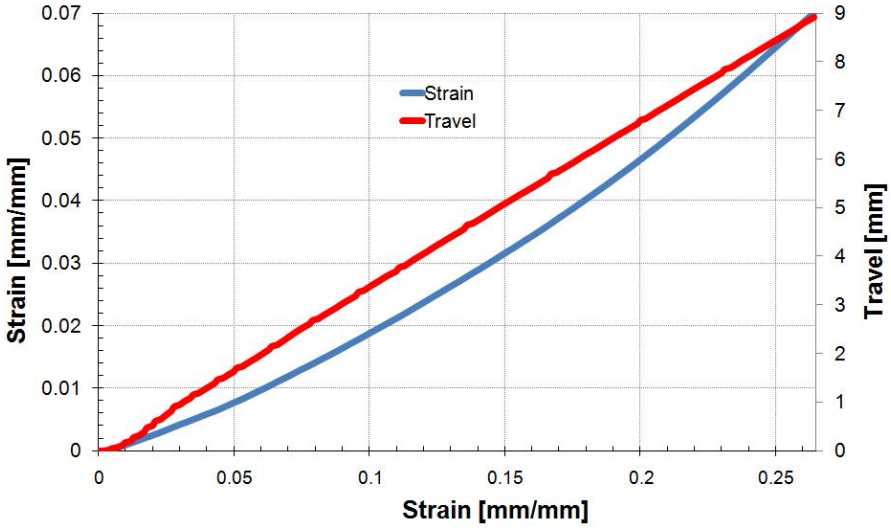

Figure 2.9. Strain and crosshead travel history for the tests performed at 2000 mm/min

2.2.2. Cyclic Tests

For studying the behaviour in cyclic loadings, three different experimental programs were chosen:

- 3 amplitudes, 10 cycles for each amplitude (Mullins effect test);
- 8 amplitudes chosen in equal stress increment, one cycle for each amplitude;

- 8 amplitudes chosen in equal strain increment, one cycle for each amplitude.

Apart for long-term time influence, cyclic tests can also be used for the determination of plasticity values. This aspect will be detailed in Section B of this work.

2.2.2.1. Mullins effect tests

Mullins effect tests were initially developed for rubber testing but were implemented for other types of polymers such as thermoplastic elastomers and semi-crystalline thermoplastic polymers [**25**,**33**,**45**]. There are three main material characteristics that are distinguishable for such tests:

- Hysteresis of energy;
- Strain softening;
- Strain hardening.

The graphic representation depicting the first loading/unloading cycle of each amplitude is called the *primary hyperelastic behaviour;* the material's loading path exhibits strain-hardening when loaded to stress values higher than the current cycle. If the material is subjected to several cycles with the same amplitude, it exhibits residual deformation because of the progressive damage induced by each cycle (strain-softening phenomenon). After a certain number of cycles of the same amplitude (depending on the material), the behaviour stabilizes to a stress-strain curve of the same magnitude, called the *permanent set* [**32**].

Mullins effect tests were performed at "Politehnica" University of Timişoara on a 10 kN Walter+Bai servo-hydraulic fatigue machine. The experimental programme consisted of three blocks of different amplitudes with 10 cycles being performed in each block (Figure 2.10). The machine was set in displacement control, with an equivalent crosshead travel of 25%, 50% and 75% of the approximated yield stress. The test speed was held constant at 2 mm/min.

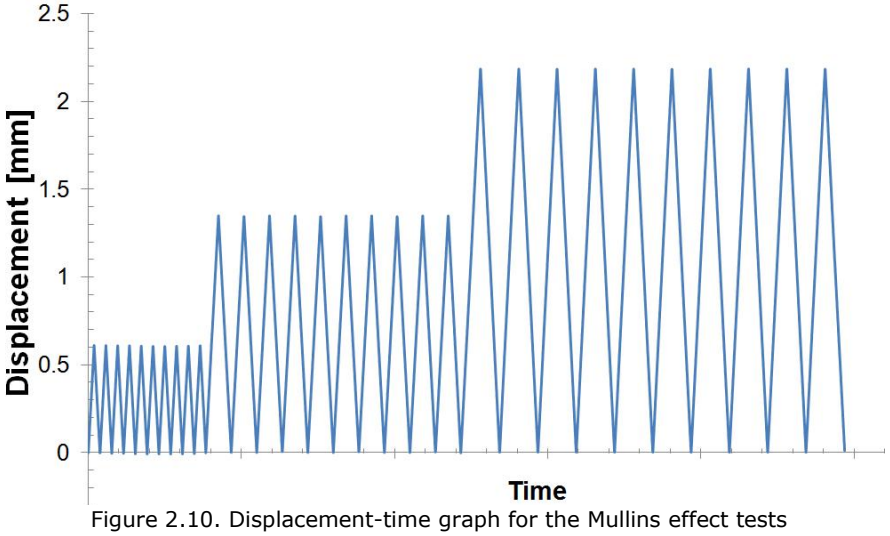

Figure 2.10. Displacement-time graph for the Mullins effect tests

The results for the Mullins effect tests are presented in Figure 2.11.

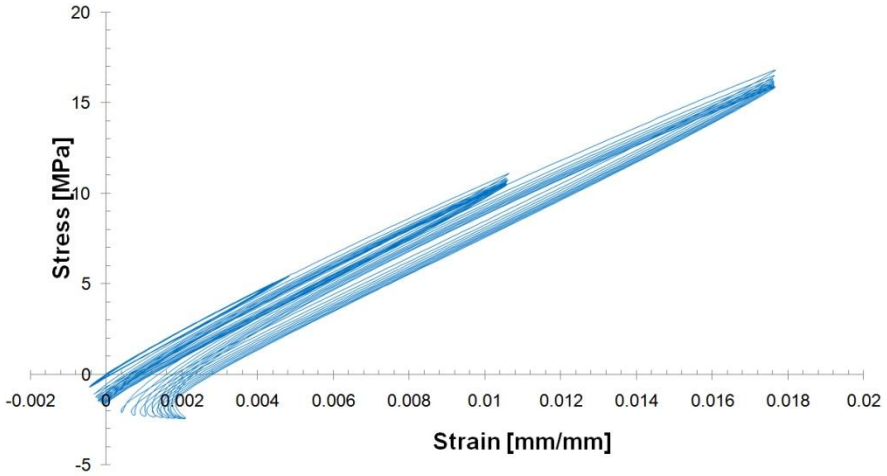

Figure 2.11. Results for the Mullins effect tests

PA-12 exhibits an energy dissipation determined by the area between the loading unloading paths. This effect is due to the heterogeneity of the polymers [**45**], caused by the crystalline lamellae [**33**].

Another aspect that can be noticed is the strain softening that occurs when the specimen is subjected to several cycles of the same amplitude. The material becomes more compliant because of both time-softening as well as accumulated plastic deformation. So, for small deformations, the permanent set is hardly distinguishable from the primary hyperelastic behaviour; all the cycles practically having the same shape. When further strained, the plastic deformation becomes evident and the difference between the unloading curves can be observed (Figure 2.12).

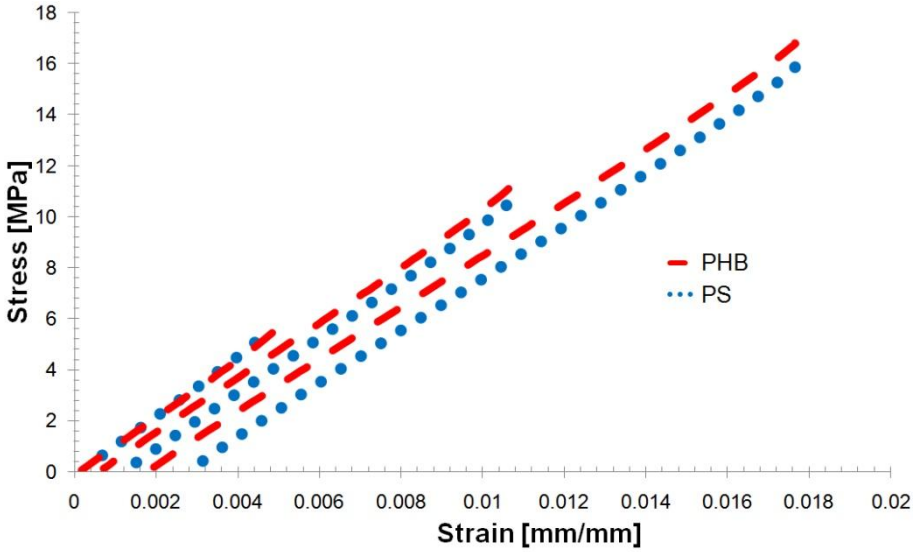

Figure 2.12. Unloading paths for primary hyperelastic behaviour (PHB) and permanent set (PS)

Mullins effect tests performed under the yield point determined hysteresis of energy and strain softening characteristics of PA-12. In order to gain insight about the strain hardening, cyclic tests that strain the material beyond the yield point must be performed.

2.2.2.2. Cyclic tests with equal stress increment

The cyclic tests with equal stress increment were performed in the Institut für Leichtbau und Kunststofftechnik, Technische Universität Dresden on a Zwick Z250 machine at ambient temperature (23 °C) with three crosshead travel speeds: 2 mm/min, 20 mm/min and 200 mm/min. The machine was programmed in stress control and the stress-time curve for the experimental program is presented in Figure 2.13.

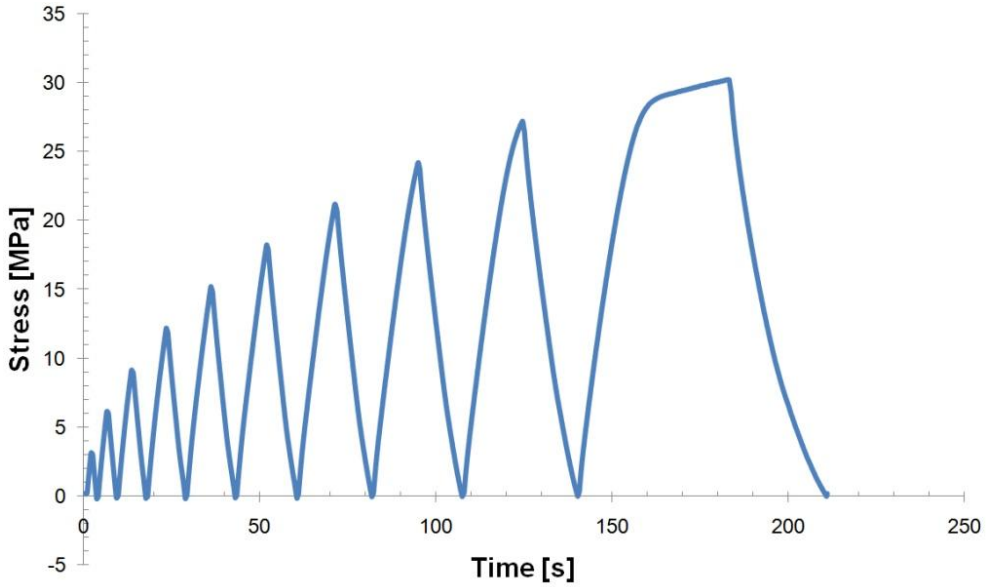

Figure 2.13. Stress-time diagram for the cyclic tests with equal stress increment

The results for the cyclic tests with equal stress increment are presented in Figures 2.15-17.

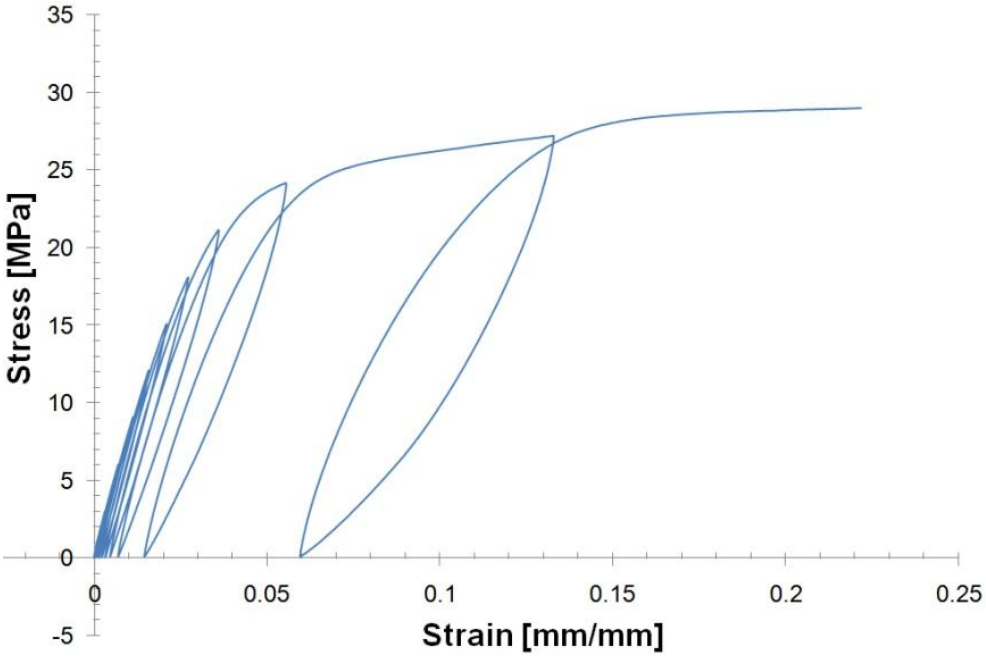

Figure 2.14. Cyclic test with equal stress increment at 2mm/min

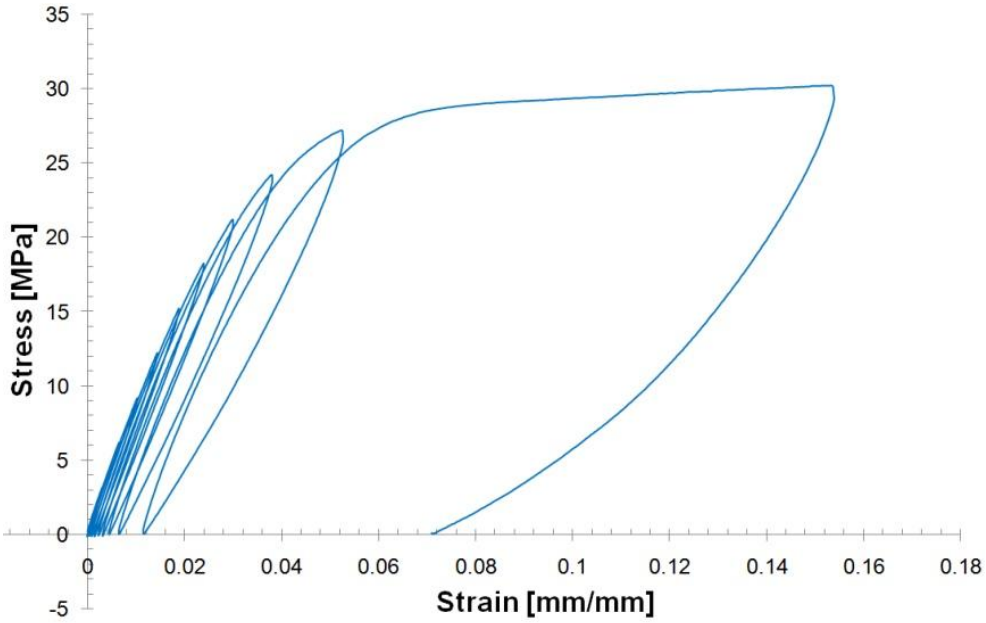

Figure 2.15. Cyclic test with equal stress increment at 20mm/min

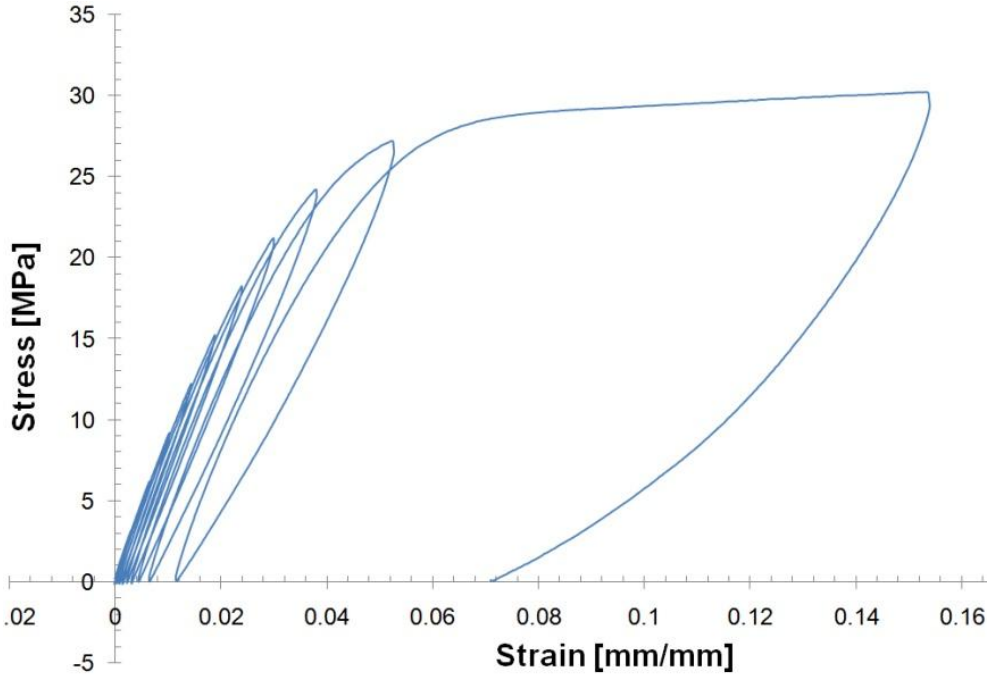

Figure 2.16. Cyclic test with equal stress increment at 200mm/min

2.2.2.3. Cyclic tests with equal strain increment

The cyclic tests with equal stress increment were performed on a Zwick Z250 machine at ambient temperature (23 °C) with three crosshead travel speeds: 2 mm/min, 20 mm/min and 200 mm/min. The machine was programmed in stress control and the stress-time curve for the experimental program is presented in Figure 2.17.

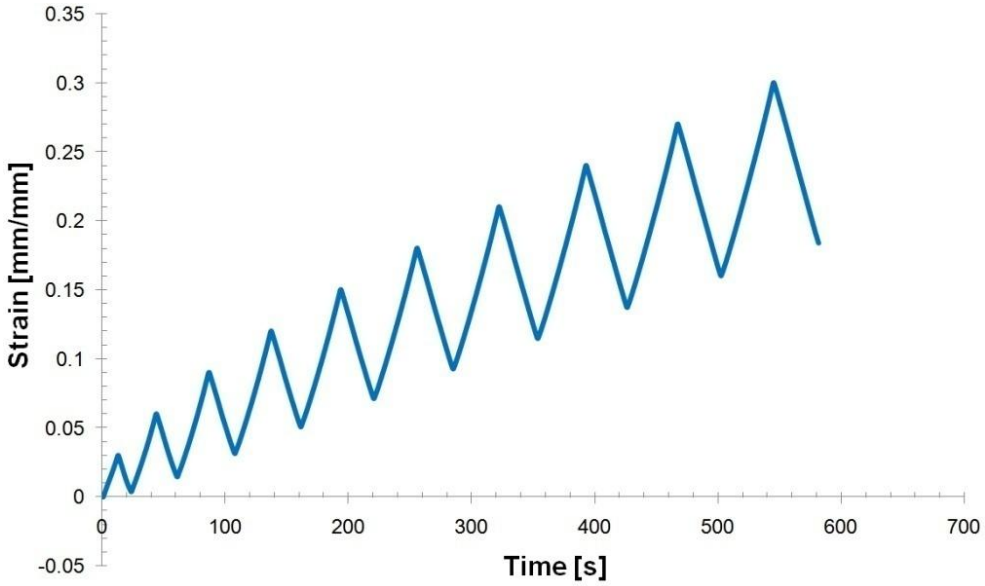

Figure 2.17. Stress-time diagram for the cyclic tests with equal strain increment

Results for the cyclic tests with equal stress increment are presented in Figures 2.2.18-2.2.20.

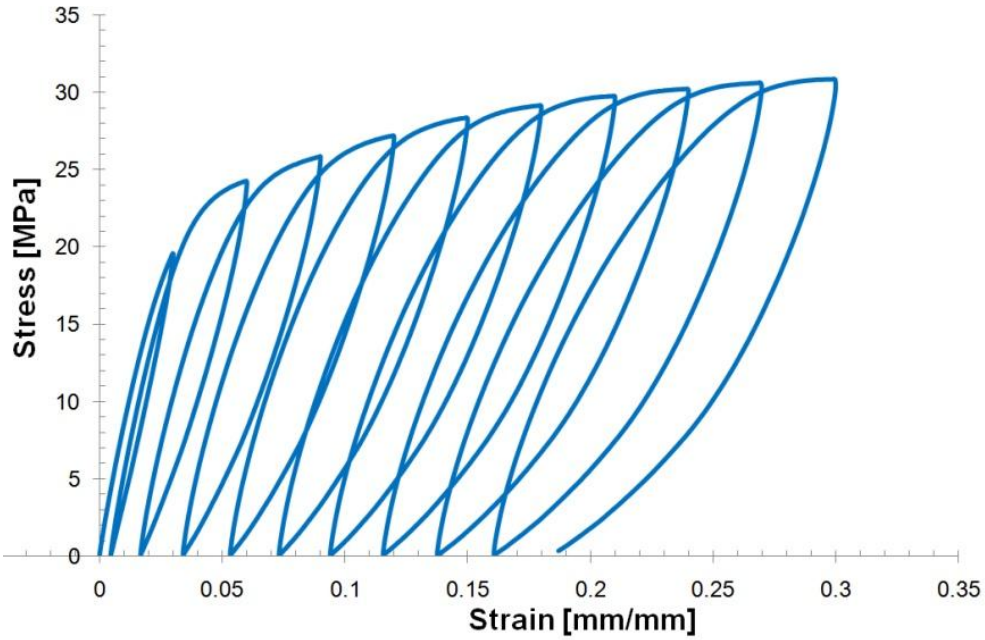

Figure 2.18. Cyclic test with equal stress increment at 2mm/min

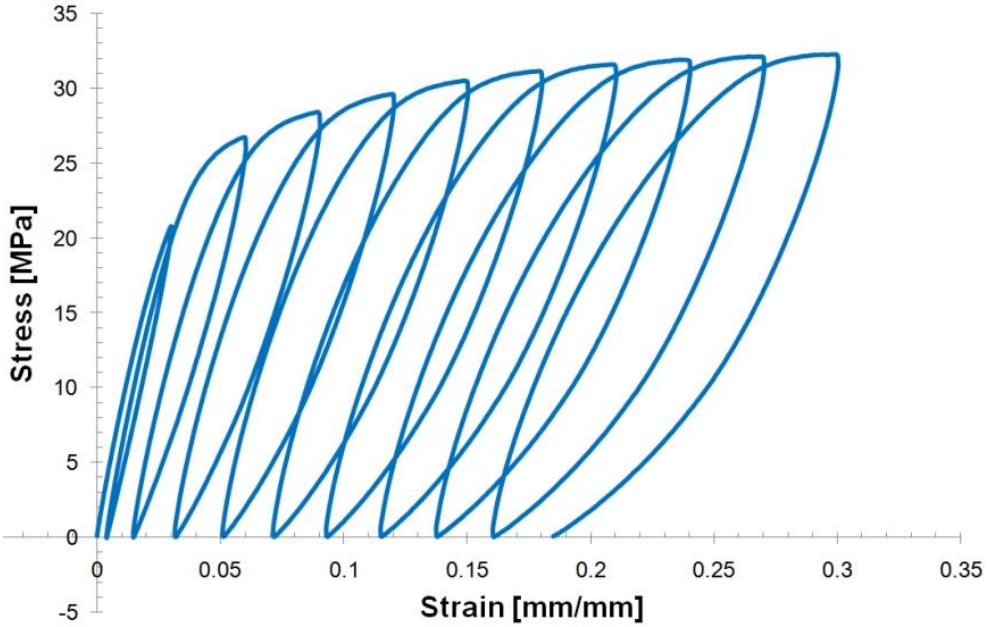

Figure 2.19. Cyclic test with equal stress increment at 20mm/min

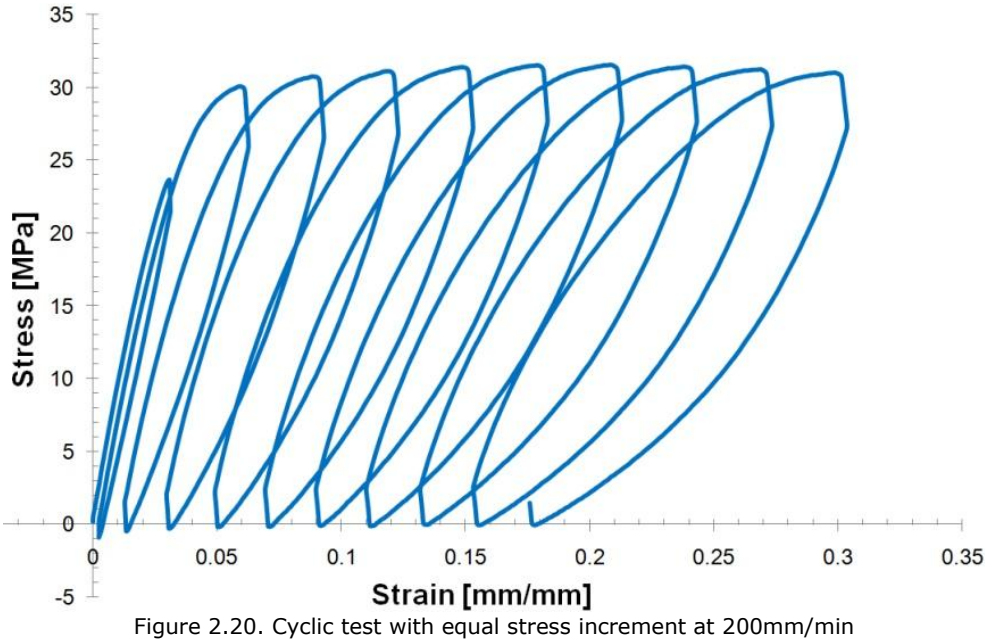

Figure 2.20. Cyclic test with equal stress increment at 200mm/min

The strain-hardening phenomenon can clearly be noticed in the case of cyclic loadings, as the peaks of the amplitudes tend to follow the original stress-strain curve (Figure 2.21) despite the damage induced with each cycle.

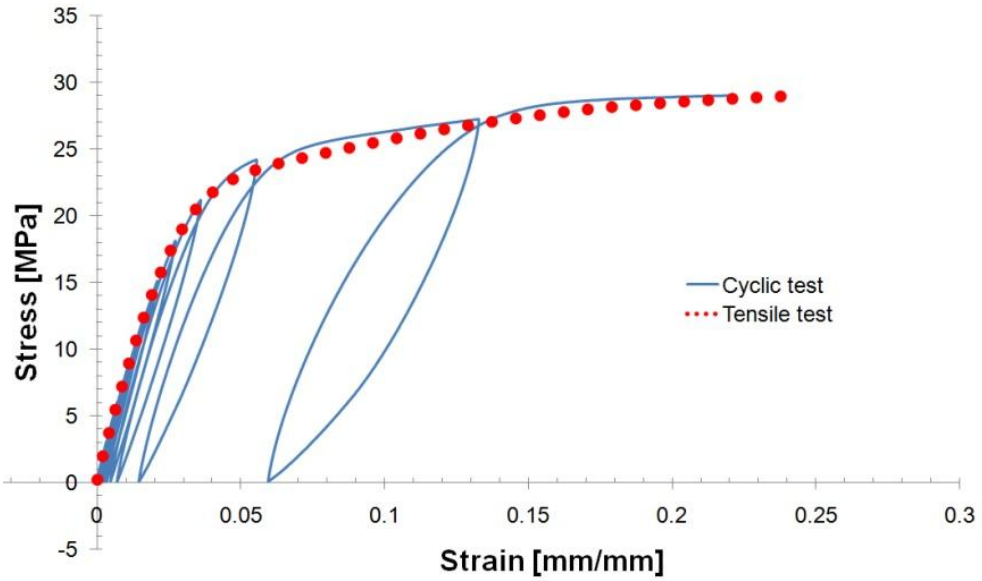

Figure 2.21. Strain hardening phenomenon observed in cyclic loadings

2.2.3. Low-cycle fatigue tests

Low-cycle fatigue tests were performed in the Institut für Leichtbau und Kunststofftechnik, Technische Universität Dresden on a servo-hydraulic Schenk PC63M equipped with a 40kN load cell. The deformation was recorded with a strain-gauge extensometer with a 50 mm opening, the machine being programmed in strain control. The machine was equipped with an environmental chamber set at 23 °C in order to correct any in service temperature variation caused by the heating of the servo-hydraulic actuator and of the circulating oil.

Several parameters were monitored in order to determine for which values the steady-state material behaviour is reached: number of cycles, frequency and strain level. In each test, two parameters would remain constant while the third would gain three different values. Tests were divided in 5 steps of equal number of cycles and the stress-strain response was recorded after each block. In order to determine the stress-strain response of the steady-state material, tensile tests were performed immediately after the low-cycle fatigue tests as well as after 24 hours, after the material recovered its reversible deformation.

2.2.3.1. Effect of number of cycles

In previous tests performed on this material in cyclic loading [**26**,**46**] a pronounced softening effect was observed (reduction in reaction forces for the same strain interval) in the first cycles then the softening would decay exponentially. The aim of this study was to determine the number of cycles after which induced delayed elasticity would become negligible. Thus, three test programs were designed, maintaining constant frequency (5 Hz) and strain interval: the reference strain was chosen 0.025 mm/mm with 0.0075 mm/mm amplitude, the specimen

being thus subjected to a deformation within a range between 0.0175 mm/mm and 0.0325 mm/mm. Three values for the number of cycles were chosen: 5,000 cycles (a), 10,000 cycles (b) and 50,000 cycles (c). Stress-strain curves were recorded after 1,000 cycles (a), 2,000 cycles (b) and 10,000 cycles (c), with the obtained results presented in Figure 2.22.

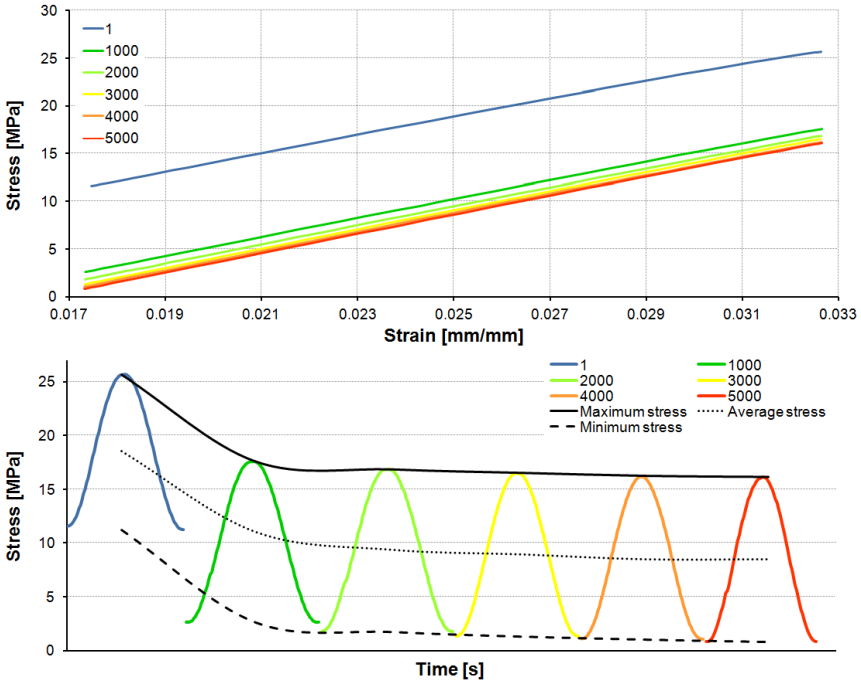

a)

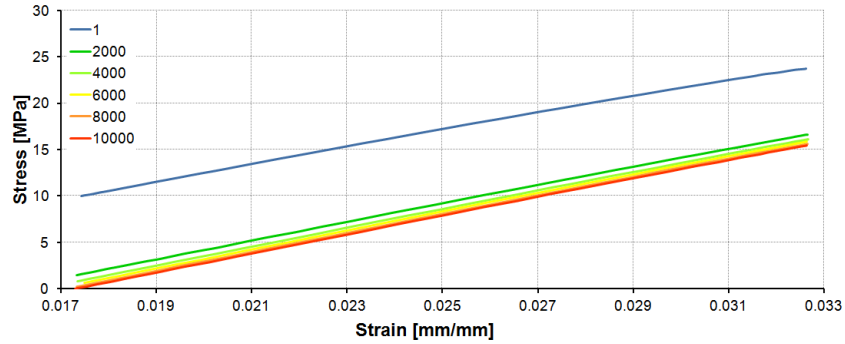

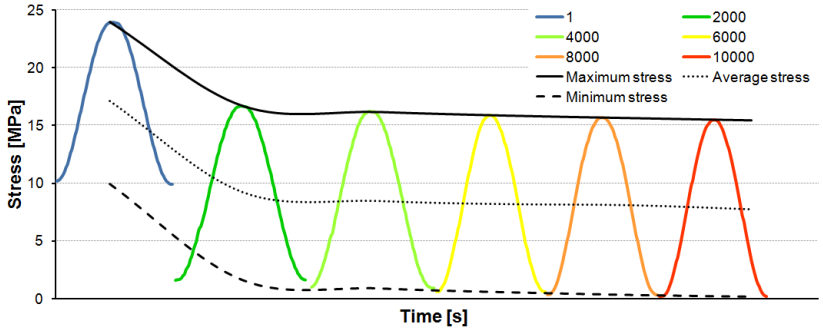

b)

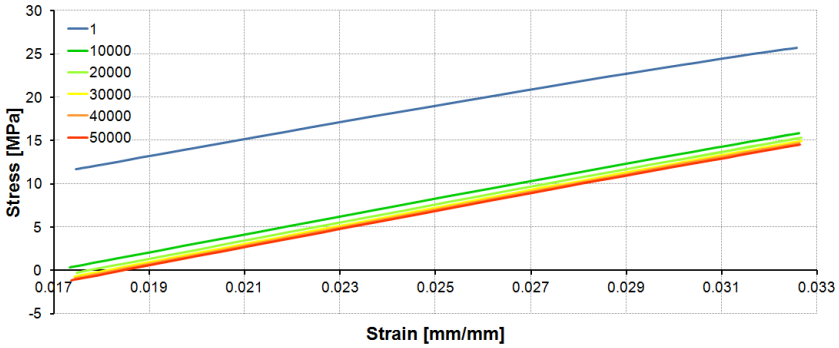

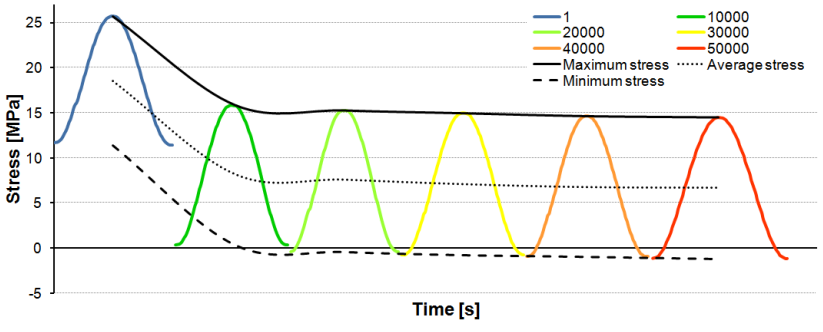

c)

Figure 2.22. Material softening for three test programs: (a) 5000 cycles, (b) 10,000 cycles and (c) 50,000 cycles

It can be observed that the polyamide's softening was considerable after the first 1,000 cycles: the tensile stress at 0.0325 mm/mm strain decreased with 32.4% (from 25.6 MPa to 17.3 MPa). For the next 4,000 cycles, a softening in tensile stress of only 6.9% was recorded (from 17.3 MPa to 16.1 MPa). After 50,000 cycles, the total softening resulted 43.9% (from 25.6 MPa to 14.4 MPa).

In order to analyze the PA's LCF-induced softening, tensile tests were performed on three types of specimens at various stages. Their results are presented in Figure 2.23 and demonstrate insignificant variations between the stress-strain responses of untested (virgin) specimens (denoted 'Initial' in the figure), a specimen tested immediately after the completion of the cyclic test ('Instant') and a one tested 24 hours after the LCF test ('Recovery').

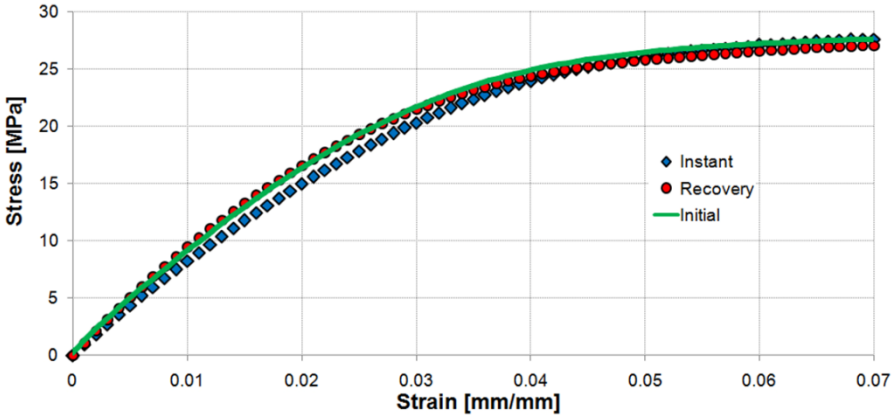

a)

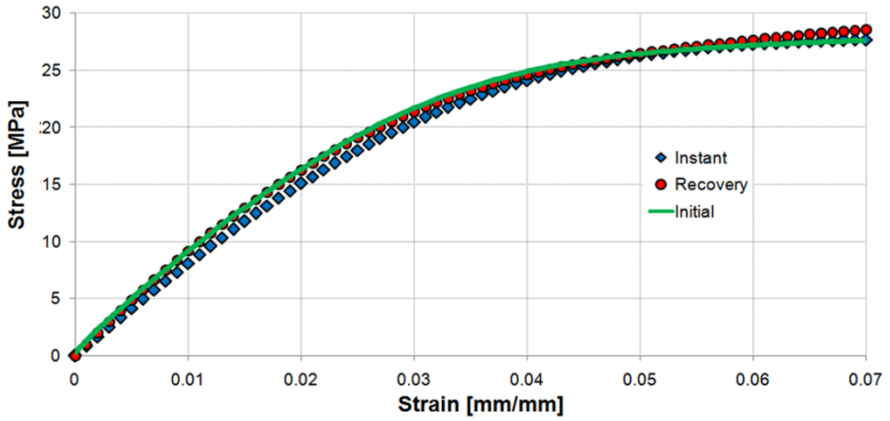

b)

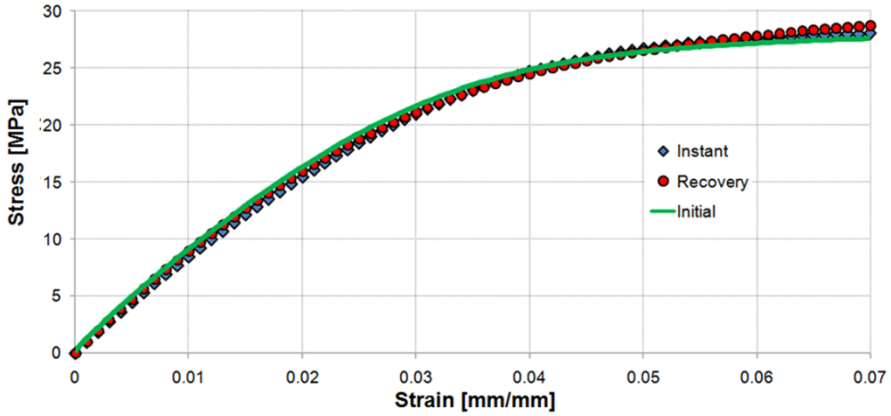

c)

Figure 2.23. Tensile test comparison for (a) 5000 cycles, (b) 10,000 cycles and (c) 50,000 cycles

Another parameter, which evolution during the LCF tests was monitored, is the variation of instantaneous elastic modulus with strain. The curves for this modulus (Figure 2.24) were obtained by dividing the stress increment by the respective strain increment. The results obtained in such a way demonstrate an increase in the elastic modulus with the number of cycles.

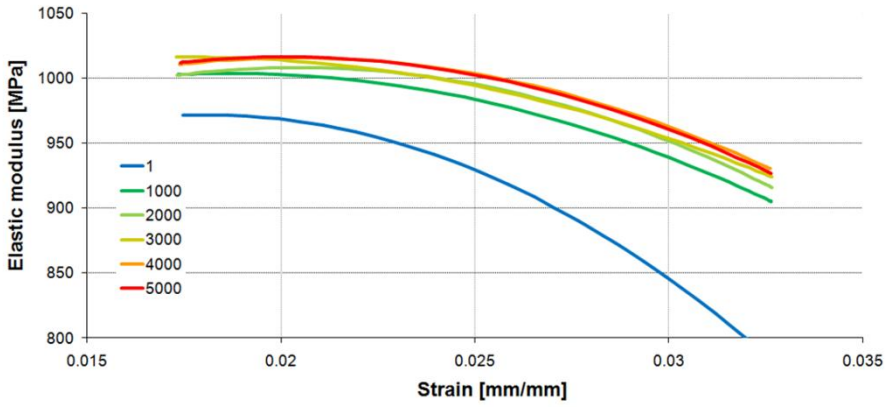

a)

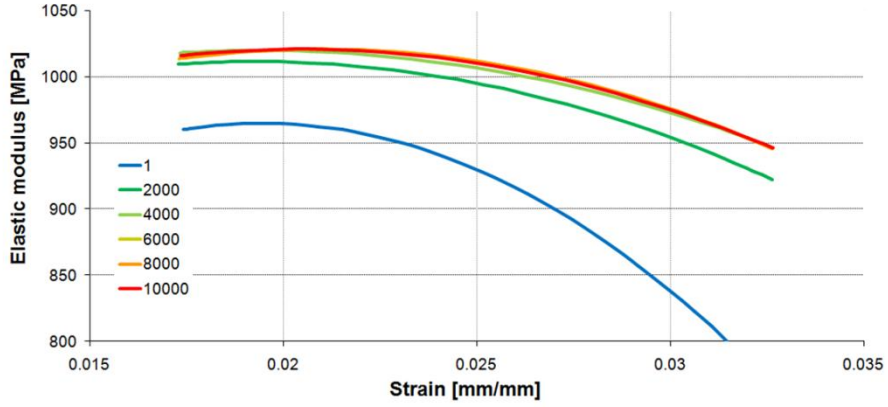

b)

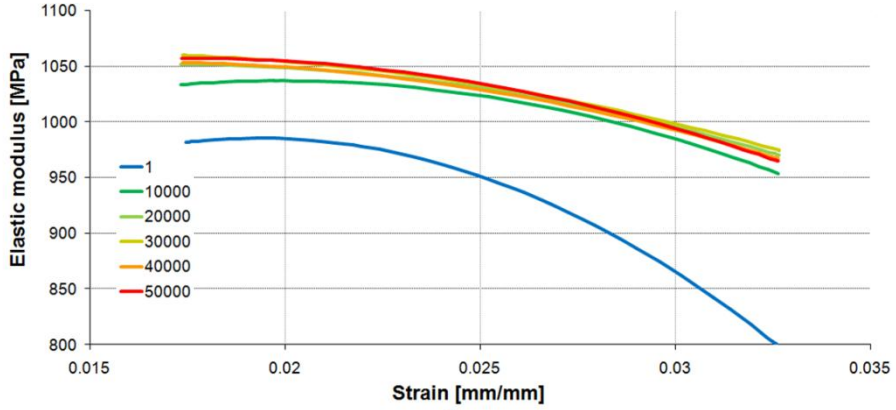

c)

Figure 2.24. Variation in elastic modulus with strain for three test programs: (a) 5000 cycles, (b) 10,000 cycles and (c) 50,000 cycles

2.2.3.2. Effect of frequency

Our previous experiments on the studied material revealed a noticeable influence of strain rate (in tensile tests) and frequency (in DMA tests) on its behaviour [**46**,**47**,**48**]. In order to quantify the effect of frequency on the cyclic loading behaviour, three different frequencies were used: 3 Hz, 5 Hz and 7 Hz. At this stage of testing, the strain level was maintained constant (0.025 mm/mm reference with 0.0075 mm/mm amplitude) and a number of 5,000 cycles was chosen. The results for 3 Hz and 7 Hz are presented in b) Figure 2.25 (results for 5000 cycles and 5 Hz can be taken from Figure 2.22 a).

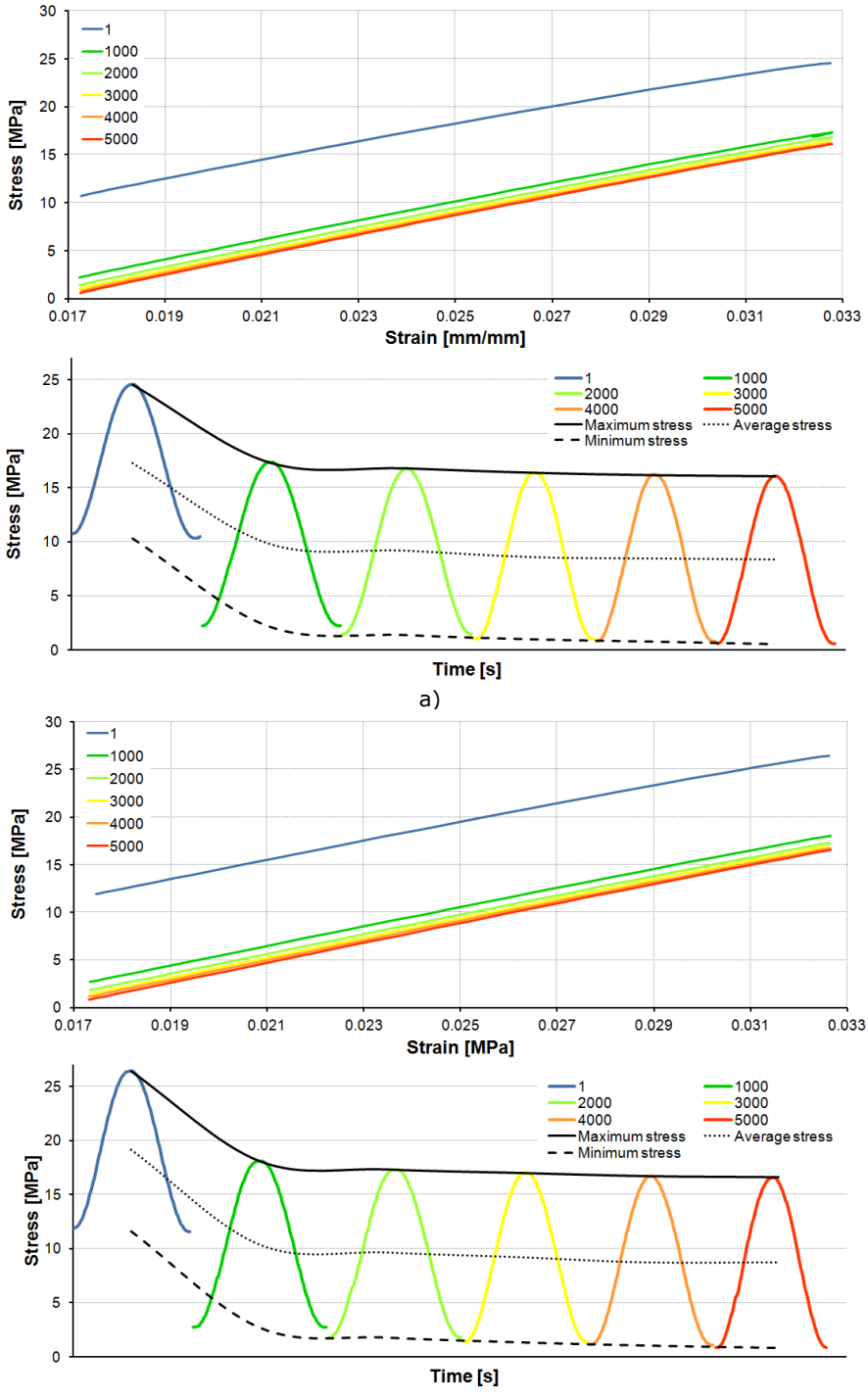

Figure 2.25 Effect of frequency on material softening: (a) 3 Hz and (b) 7 Hz (see Fig. 1 for 5 Hz)

Similar to other rate-dependent tests performed on this material, a higher frequency resulted in higher level of responses for the same strain (an increase of around 8% when changing from 3 Hz to 7 Hz). The results of tensile tests for previously untested specimens, specimens tested immediately after LCF tests and specimens tested 24 hours after LCF tests are presented in Figure 2.26, showing similar features as the results for the effect of number of cycles. The variation of instantaneous elastic modulus with strain is presented in Figure 2.27.

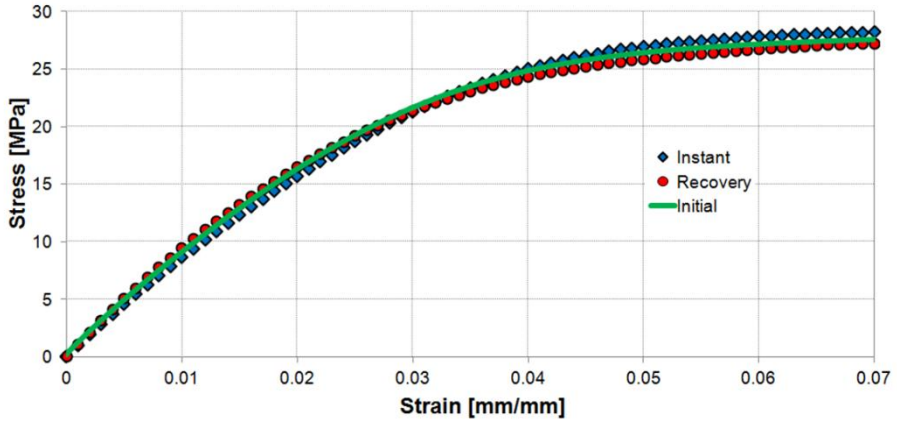

a)

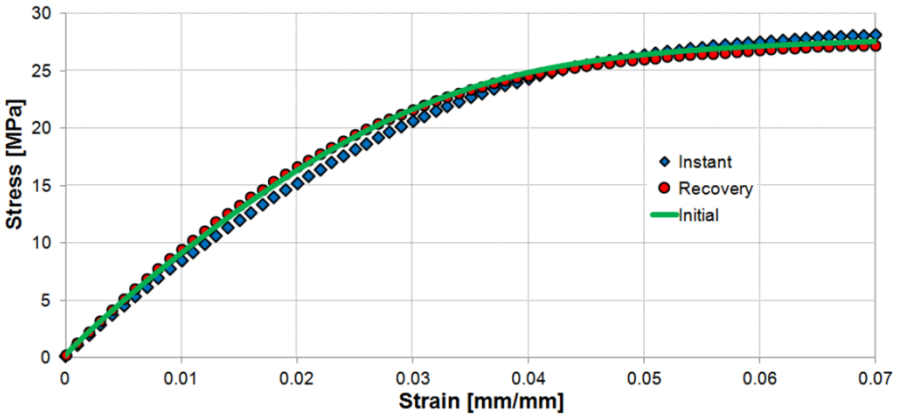

b)

Figure 2.26. Comparison of tensile tests for 3 Hz (a) and 7 Hz (b) (see Fig. 2 for 5 Hz)

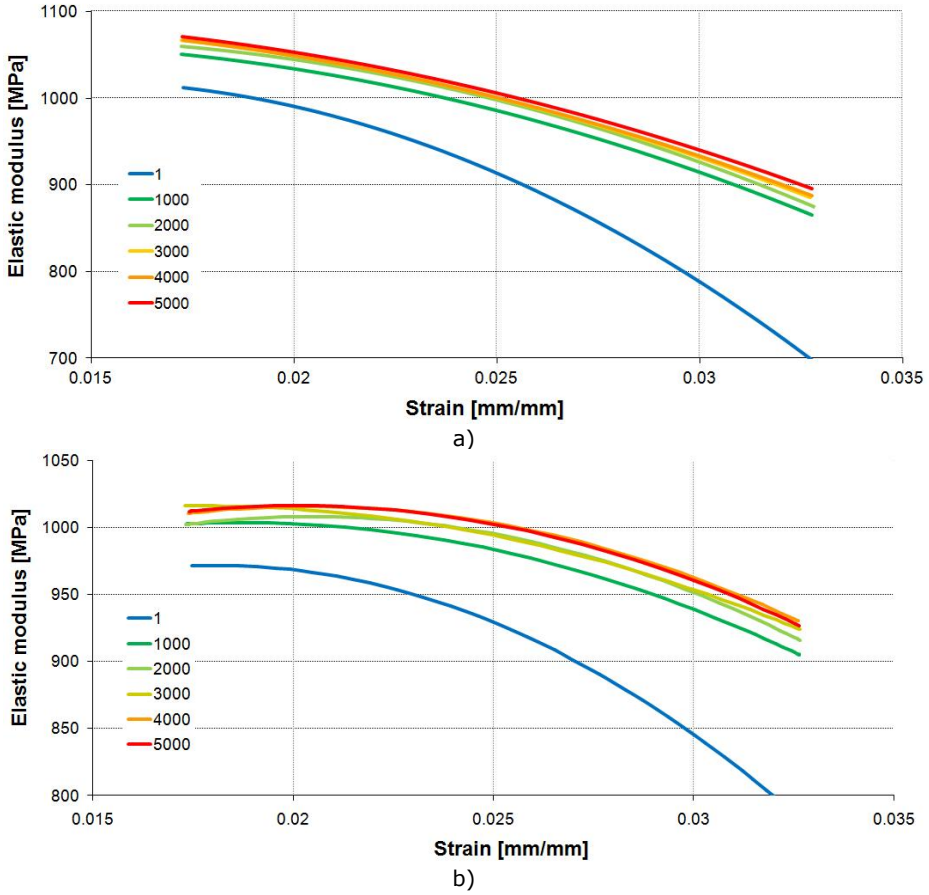

Figure 2.27. Effect of frequency: variation of elastic modulus with strain for 3 Hz (a) and 7 Hz (b) (see Fig. 2 for 5 Hz)

2.2.3.3. Effect of strain

Considering the non-linear stress-strain response of PA, its plastic deformation accumulates as strain increases, even before yielding. The effect of the magnitude of deformation in cyclic loadings on the steady-state material behaviour was studied by choosing a constant strain amplitude (0.0075 mm/mm) and three levels of reference strain: 0.025 mm/mm, 0.035 mm/mm and 0.045 mm/mm. All tests were performed for 5,000 cycles at 5 Hz. The results for 0.035 mm/mm and 0.045 mm/mm are presented in Figure 2.28 a and b (the results for 0.025 mm/mm are presented in Figure 2.22 a).

After 1,000 cycles a slight increase in softening with strain level can be observed: for the tests with reference strain of 0.025 mm/mm the peak tensile stress decreased by 29.6% (from 24.6 MPa to 17.3 MPa), for 0.035 mm/mm it showed a 32.5% decrease (from 28.9 MPa to 19.5 MPa) and for 0.045 mm/mm, the decrease was 34.5% (from 31 MPa to 20.3 MPa). The same trend was observed after 5,000 cycles, with softening in tensile stress of 37.1% being recorded for

reference strain of 0.025 mm/mm (from 25.6 MPa to 16.1 MPa), 38.7% for 0.035 mm/mm (from 28.9 MPa to 17.7 MPa) and 40% for 0.045 mm/mm (from 31 MPa to 18.6 MPa).

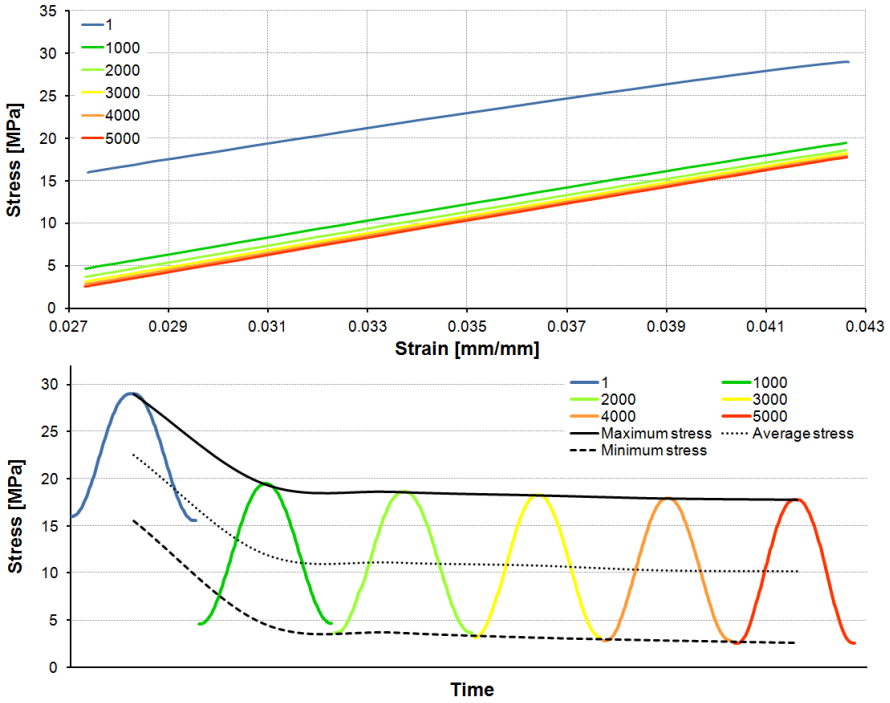

a)

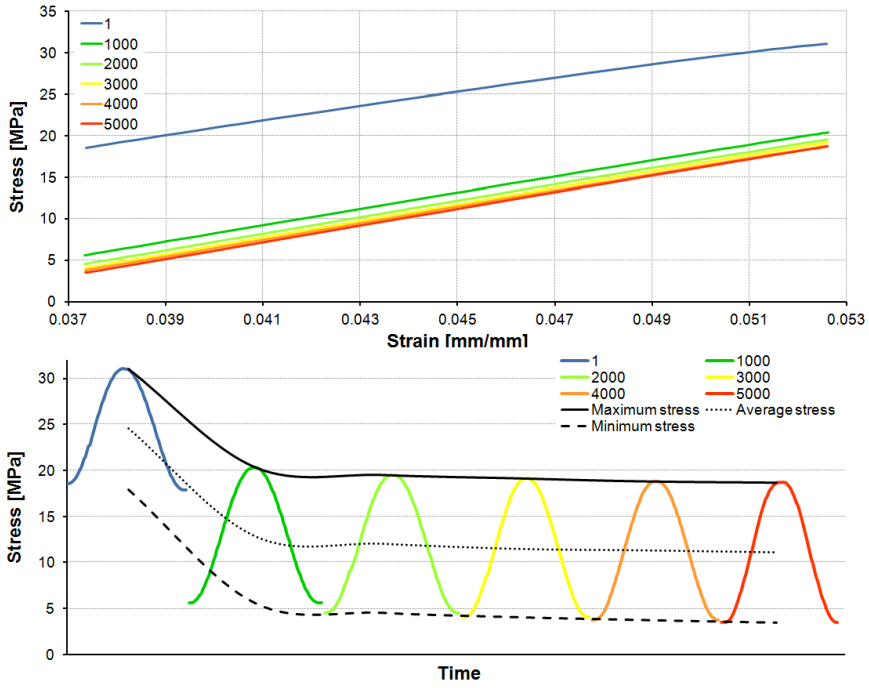

b)

Figure 2.28 Effect of strain on material softening: (a) 0.035 mm/mm and (b) 0.045 mm/mm (see Fig. 2.22 for 0.025 mm/mm)

The results obtained in tensile tests for previously untested specimens, specimens tested immediately after LCF tests and specimens tested 24 hours after LCF tests are presented in Figure 2.29 while the change in the instantaneous elastic modulus with strain is shown in Figure 2.30.

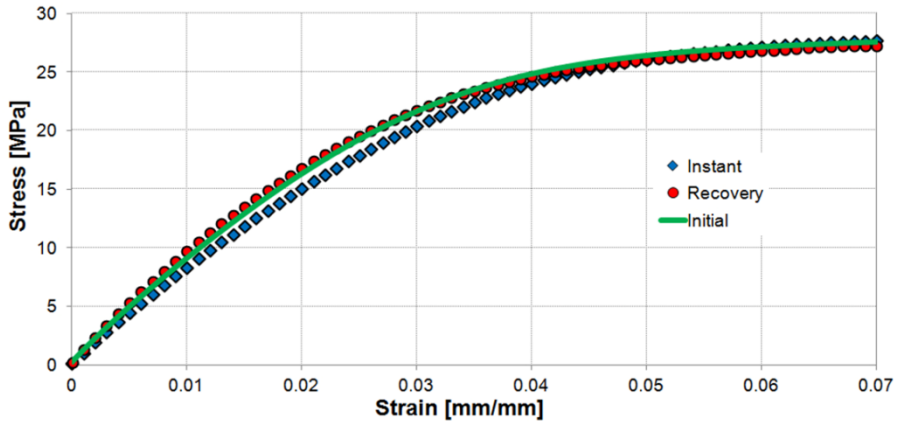

a)

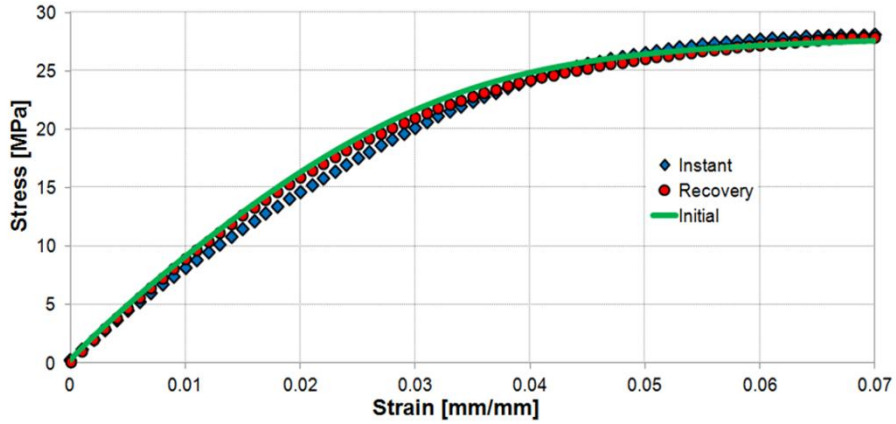

b)

Figure 2.29. Comparison of tensile tests for 0.035 mm/mm (a) and 0.045 mm/mm (b) (see Fig. 2 for 0.025 mm/mm)

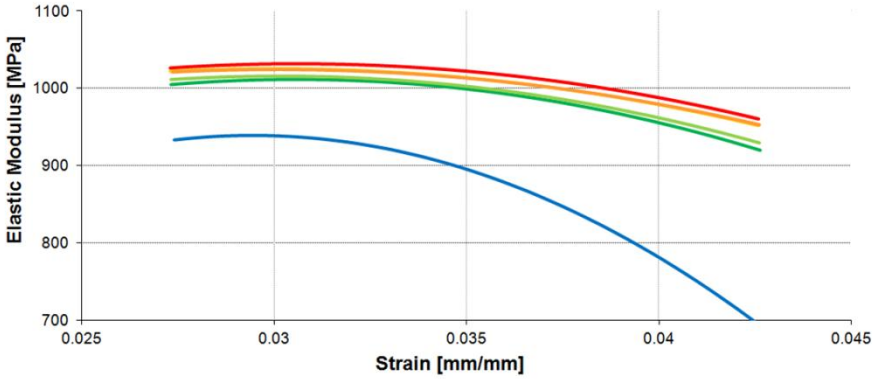

a)

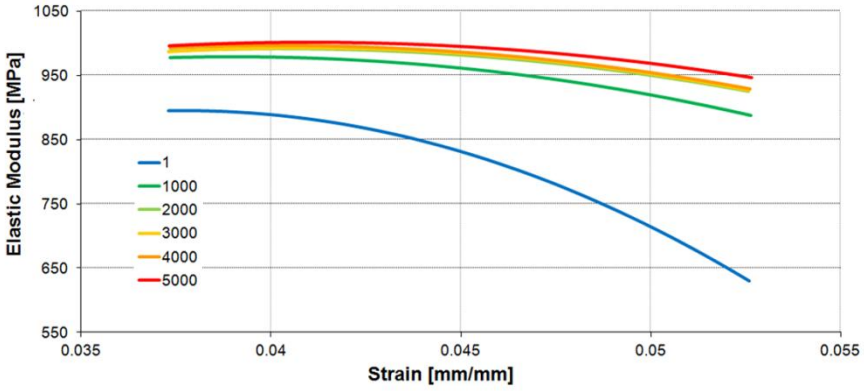

b)

Figure 2.30. Effect of reference strain: variation of elastic modulus with strain for 0.035 mm/mm (a) and 0.045 mm/mm (b) (see Fig. 3 for 0.025 mm/mm)

2.2.3.4. Discussion

In order to explain the softening behaviour of this polyamide one must present the various types of deformations polymers undergo due to their particular macromolecular structure. The generic term 'plastic strain' used in throughout this work refers to the irreversible deformation observed at the time of the experiment. Due to the viscous nature of polymers, a part of this remnant strain will be recovered in time through relaxation. As stated in the thesis introduction, the structure of the semi-crystalline polymers is composed of two phases: a crystalline phase (atoms arranged in ordered patterns) and an amorphous phase (entangled macromolecules) (Figure 2.31). The irreversible deformation that polymers undergo is manifested through the slippage of atomic planes (similar to metal plasticity [**49**]) or by macromolecular chain scission [**1**]. The elastic component of polymers' deformation can be decomposed into instantaneous elasticity and delayed elasticity. The instantaneous elastic component is the correspondent of a spring while the delayed component is the correspondent of a dashpot in the mathematical models for describing viscoelasticity, which will be covered later (Chapter 2, Paragraph 4). Delayed elasticity can manifest through a number of molecular phenomena such as viscous flow (the movement of macromolecules past one another), Thirion relaxation (a relaxation of the trapped entanglements in elastomeric networks) or molecular relaxation (stress relief caused by high temperatures) [**1**].

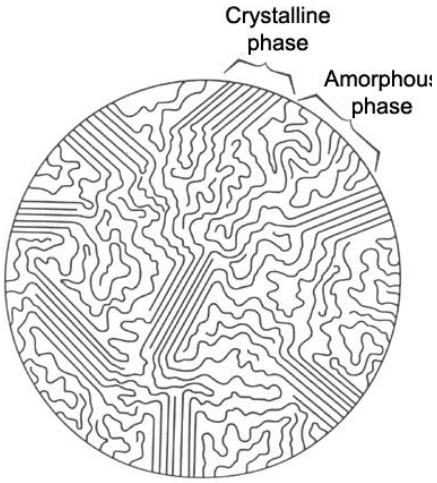

Figure 2.31. Polymer semi-crystalline structure [**78**]
[courtesy of Case Western Reserve University]

If the specimen undergoes deformations before the yield point the ratio of permanent strain to reversible strain is rather small. If stress is maintained for a longer period of time, the reversible deformation grows until it reaches saturation, while the instantaneous elastic strain and the permanent strain remain constant. If the specimen is further strained towards yielding, the permanent deformation steadily increases until it gains a linear increase with strain, as the reversible deformation reaches a plateau. This aspect will be detailed in Chapter 2, Paragraph 3 and in Chapter 3, Paragraph 3.

As a general conclusion derived from our programme of LCF tests, variations in test parameters have a low effect the apparent material softening. Considering the diagrams of stress-strain or stress-time variations for different cycles, a significant softening is observed (29.6%) after the first thousand cycles; an additional 16.7% of drop in tensile stress at 0.0325 mm/mm strain is recorded after 50,000 cycles.

In the case of different frequencies, the tensile stress at 0.0325 mm/mm demonstrates a small variation in a similar manner with regular tensile tests at different rates of deformation. A noticeable difference can be observed in the shape

of the unloading stress-strain curve: the lower the frequency, the larger the area inside the hysteresis (Figure 10). This phenomenon can be associated with a higher relaxation time at lower strain rates, which determines a softer material behaviour.

In case of the LCF tests at various strain levels, the magnitude of the reference deformation has a small effect on material softening: due to the non-linear nature of the stress-strain curve [**48**], the strain increase is accompanied by a growth of its component responsible for the remnant deformation observed at the end of the test (a combination of permanent and reversible strains, as discussed above) (Figure 2.32). So, at reference strain of 0.025 mm/mm (denoted with a vertical red line in Figure 2.33), plastic strain is around 0.007 mm/mm while at 0.045 mm/mm (a vertical blue line), it reaches values of 0.021 mm/mm. As a result, after 1,000 cycles, the tests performed at 0.045 mm/mm produce a 34.5% decrease in the tensile stress at peak strain (0.0525 mm/mm), those performed at 0.035 mm/mm cause a decrease of 32.5% at the peak strain (0.00425 mm/mm) while the tests performed at the reference strain of 0.025 mm/mm results in a 29.6% decrease (0.00325 mm/mm).

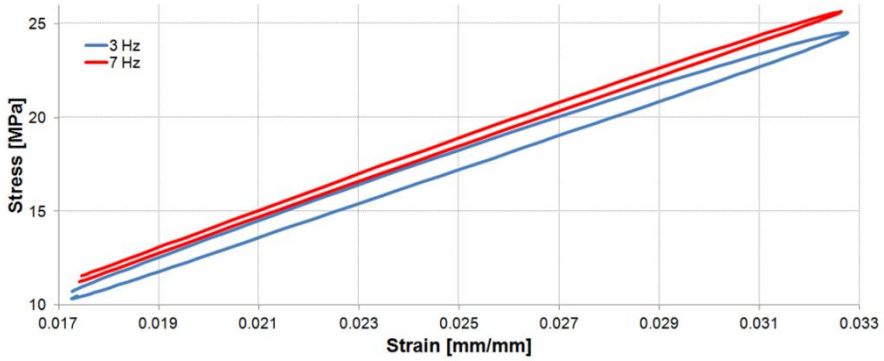

Figure 2.32. Comparison of first cycles for tests at 3 Hz and 7 Hz

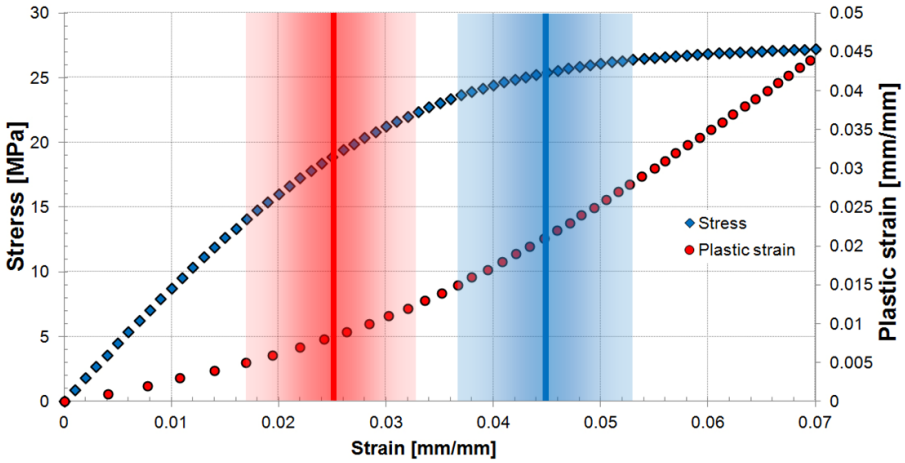

Figure 2.33. Stresses and plastic strains for reference strain values of 0.025 mm/mm (vertical red line) and 0.045 mm/mm (vertical blue line) and their correspondent amplitude range (areas with blue gradient and red gradient)

The low-cycle tensile fatigue tests performed on specimens provide an insight into the behaviour of fatigued specimens as well as mechanics of fatigue-induced damage. Regardless of the level of test parameters within the used envelope, PA12 has a similar behaviour in tension: in comparison with the stress-strain curve of a previously untested specimen, the stress-strain curve of the specimen tested immediately after the LCF test shows slightly lower stress values between 0.01 mm/mm and 0.04 mm/mm deformation but determines almost identical yield stresses and strains (27 MPa at around 0.07 mm/mm at a crosshead travel speed of 20 mm/min). The tensile stress-strain curves of specimens subjected to a 24 h recovery demonstrate insignificant differences when compared to the curves of previously untested specimens. Analyzing the acquired data from the tensile tests that followed immediately LCF tests, it was observed that when unloading to 0 N, a remnant deformation was recorded, ranging from 0.013 mm/mm to 0.02 mm/mm, depending on the test parameters. Considering that the tensile response of a fatigued specimen is almost identical with that of a previously untested specimen, it can be concluded that softening determined by fatigue at deformations below the yield point is responsible for inducing a temporary residual deformation without affecting material properties in a noticeable manner (delayed elasticity opposed to permanent deformations). This statement is supported by the graphs depicting the elastic modulus' variation with strain: for the same extensometer opening (tests being performed in strain control), the elastic modulus increases with the number of cycles as the mechanical response drops. This aspect is presented in (Figure 2.34 a). The same trend is observed for stress-strain curves of previously untested specimens. Figure 2.34 b presents the variation of stress and elastic modulus with strain as well as the interval of stress variation for the first cycle (blue gradient for the stress interval) and for the 5000th cycle (red gradient for the stress interval). It can be observed that the stress interval of the first cycle (17 – 30 MPa) determines lower values for the elastic modulus (900 – 600 MPa) in comparison with the values recorded for the stress interval of the 5000th cycle (modulus values of 1100 – 1000 MPa for a stress interval of 0 – 15 MPa).

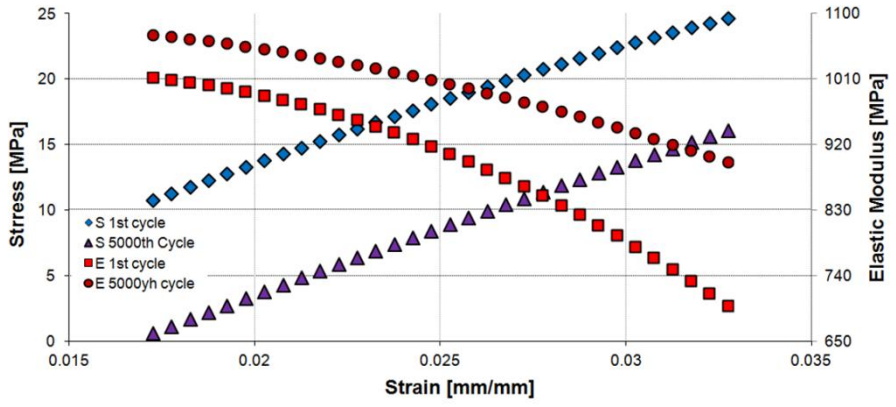

(a)

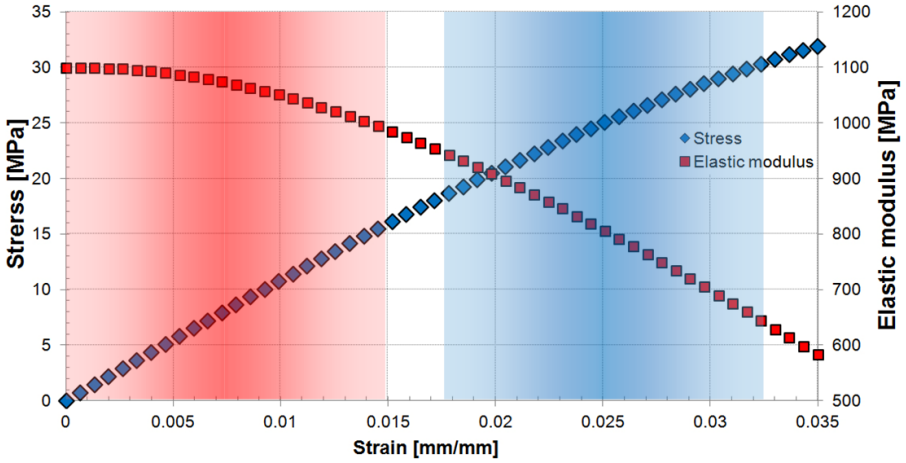

(b)

Figure 2.34. Variation of stress and elastic modulus with strain for LCF tests (a) (s – stress and E – instantaneous elastic modulus) and for previously untested specimen (b)

2.2.4. Creep tests

Creep tests determine the material compliance $D(t)$ as a function of time, expressed as the instantaneous strain $\varepsilon(t)$ divided by the constant stress $\sigma(0)$.

$$D(t) = \frac{\varepsilon(t)}{\sigma(0)} \quad [MPa^{-1}] \tag{1.1}$$

Another way of measuring creep is with the help of the adimensional normalized compliance:

$$d(t) = \frac{D(t)}{D(0)} = \frac{\varepsilon(t)}{\sigma(0)} \cdot \frac{\sigma(0)}{\varepsilon(0)} = \frac{\varepsilon(t)}{\varepsilon(0)} \quad [-] \tag{1.2}$$

The creep tests were performed on a Zwick/Roel Z005 machine and their aim was to determine the long-term viscoelastic properties of the material. In each tests, a constant load was maintained for a period of 24 hours. Based on the experimental data gathered from other tensile tests, three load levels were chosen, equivalent to 30%, 60% and 90% of the approximated yield stress for tests performed at ambient temperature and 2 mm/min crosshead travel speed. The loading time for the creep tests was chosen 24 hours.

2.2.4.1. Creep tests at 30% of yield stress

The variation of tensile compliance with time for the test performed at 30% of yield stress ($6.3MPa$) is presented in Figure 2.35 and Figure 2.36.

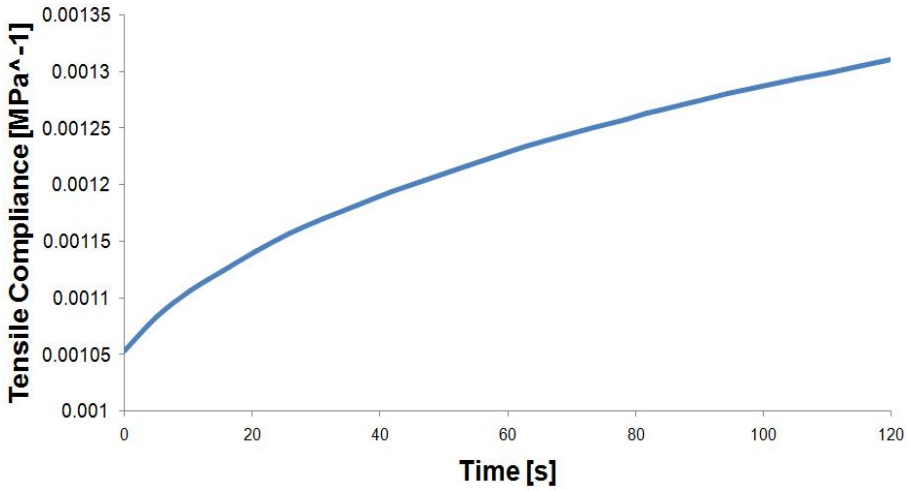

Figure 2.35. Compliance variation with time (2 minutes)

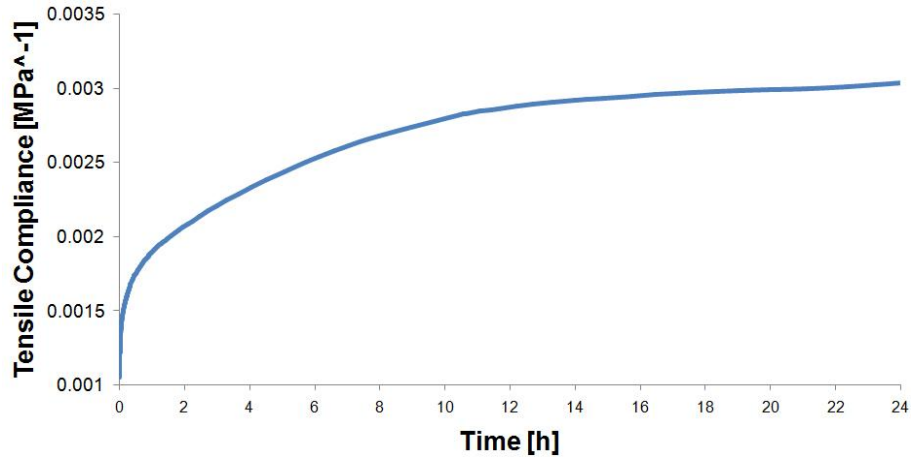

Figure 2.36. Compliance variation with time (24 hours)

2.2.4.2. Creep tests at 60% of yield stress

The variation of tensile compliance with time for the test performed at 60% of yield stress (11.4 MPa) is presented in Figure 2.37 and Figure 2.38.

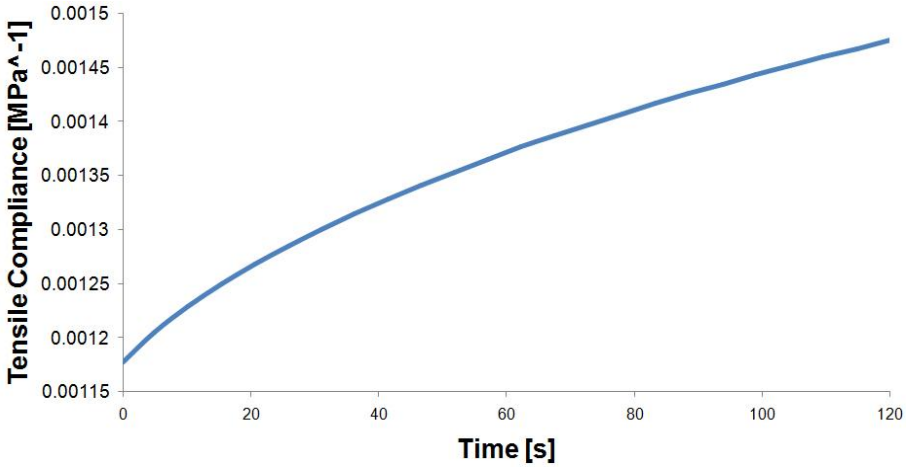

Figure 2.37. Compliance variation with time (2 minutes)

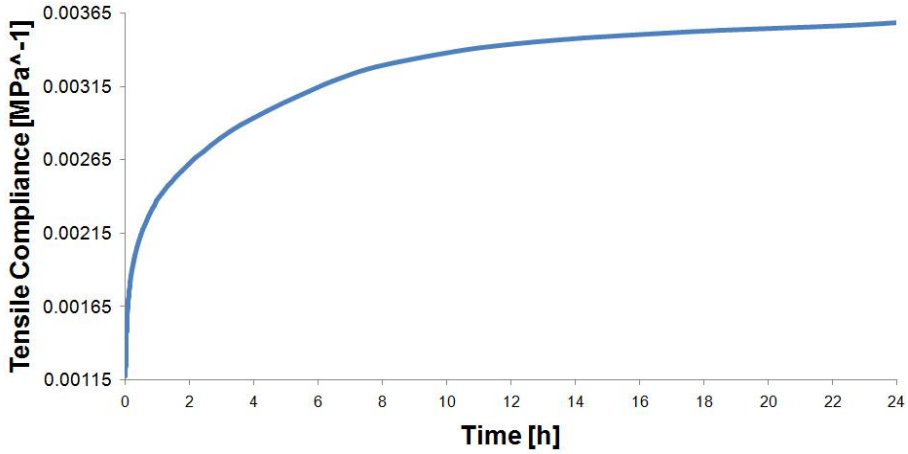

Figure 2.38. Compliance variation with time (24 hours)

2.2.4.3. Creep tests at 90% of yield stress

The variation of the tensile compliance with time for the test performed at 90% of yield stress (17.2 MPa) is presented in Figure 2.39 and Figure 2.40.

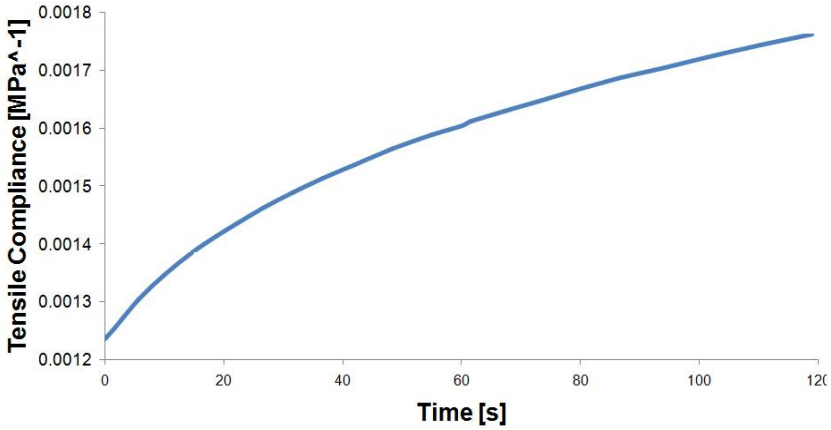

Figure 2.39. Compliance variation with time (2 minutes)

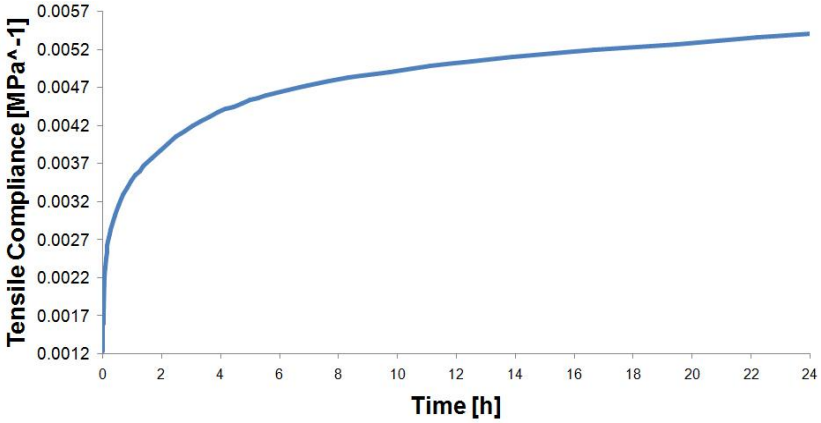

Figure 2.40. Compliance variation with time (24 hours)

2.2.4.4. Discussion

A drastic increase in tensile compliance can be observed in the first hour of each test. Afterwards, the increase in compliance becomes gradually smaller, ending with a near-plateau region after about 7 hours.

Given the non-linear behaviour of the material, the values for compliances differ for each level of loading. Higher loads will determine higher compliances (increase of 17% in compliance for a 300% increase in stress). This increase in compliance can be considered a measure of the material's strain softening.

Comparing variation of the normalized tensile compliance with time (Eq. 2.2, Figure 2.41) a significant difference can be observed between the tests performed at 90% of the yield stress level those at 60% and 30%. Though the compliance increases with the increase in stress, the maximum levels reached are nearly twice as high for the tests performed at high stress levels (the region where permanent damage becomes significant) in comparison with those performed at lower levels (the region where time-dependent reversible strains are prevalent): compliance after 24 h is 4.37 times higher than the initial compliance for the 90%-yield-stress

test; compliance at 60% of yield stress is 3.04 times higher than the initial one; for the 30%-yield-stress tests, compliance increases 2.88 times.

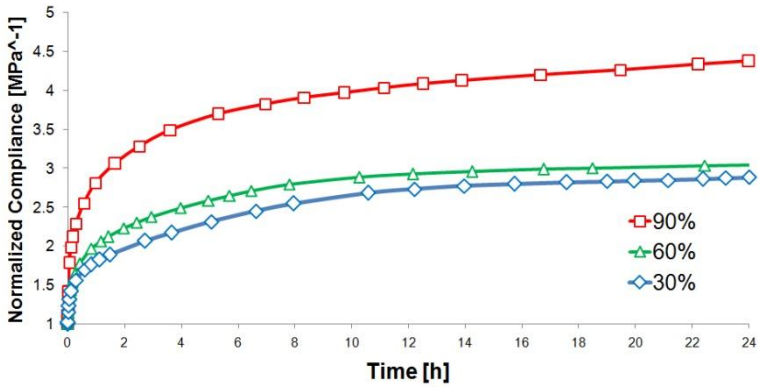

Figure 2.41. Variation of normalized compliance with time (24 hours) for three stress levels

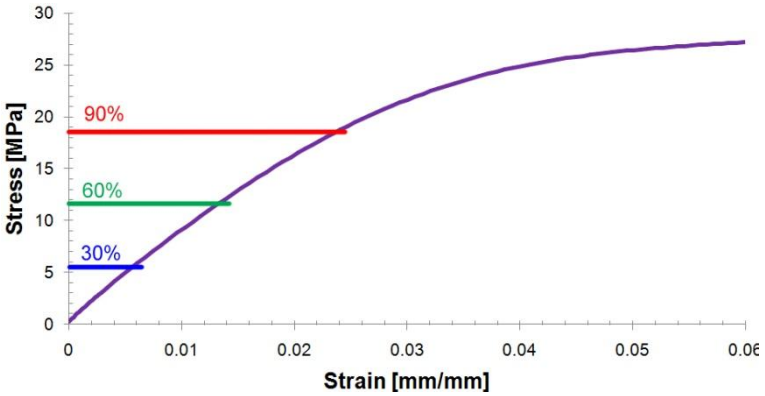

Figure 2.42. Tensile stress-strain curve and three stress levels

This phenomenon may be caused by strain-softening of the material. As the total strain grows towards the yield point (Figure 2.42), the elastic strain reaches a plateau, as the plastic strain remains the only component that increases [**6**]. This irreversible damage could likely propagate as stress is kept constant for a given amount of time. Thus, the material will become compliant at a higher rate at large-strain creep tests than at small-strain ones.

2.2.5. Tests on conditioned specimens

Literature studies have determined that the amount of moisture accumulated in the volume of a polymer affects its mechanical behaviour [**44**]. The conditioning procedure was designed in accordance with the standards ISO 1110 and ISO 62 [**50**,**51**]: the temperature of the environmental chamber was set to 70 °C and the relative humidity to 62%. Specimens were maintained in this environment for 6 days. Tests on conditioned specimens were performed in tension with the study of the influence of strain-rate and temperature.

The experimental program for determination of strain rate influence consisted of four test speeds: 2 mm/min, 20 mm/min, 200 mm/min and 2000 mm/min. The results are presented in Figure 2.43. Stress strain curves for conditioned specimens Figure 2.43.

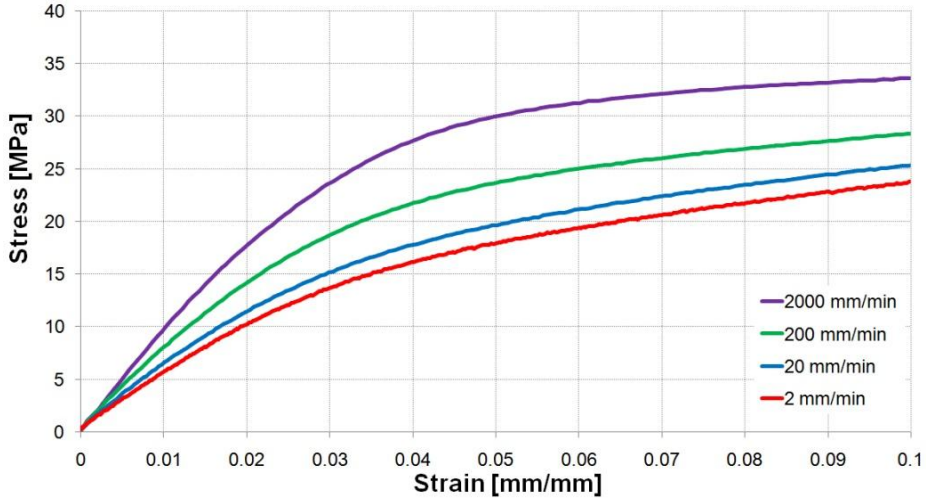

Figure 2.43. Stress strain curves for conditioned specimens

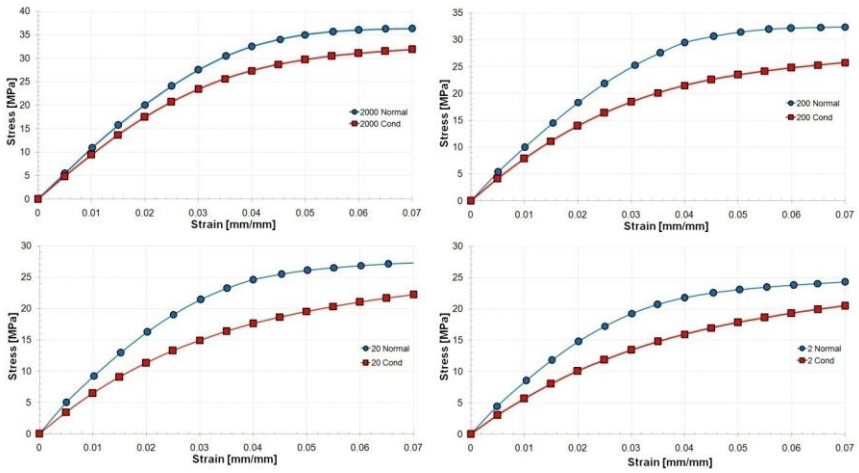

Figure 2.44. Comparison between stress-strain response of normal and conditioned specimens

In comparison with tests performed on unconditioned specimens, a softer stress-strain response was recorded (Figure 2.44). In terms of tensile strength at 7% deformation, for a test speed of 2 mm/mm, a 15.6% softening was recorded (from 24.29 MPa to 20.49 MPa), for a test speed of 20 mm/min, a 18.57% softening was recorded (from 27.3 MPa to 22.23 MPa), for a test speed of 200 mm/min, a 20.46% softening was recorded (from 32.39 MPa to 25.76 MPa) and for a test speed of 2000 mm/min, a 12.25% softening was recorded (from 36.3 MPa to 31.85 MPa).

Temperature dependency tests on conditioned specimens were performed at two crosshead travel speeds (20 mm/min and 200 mm/min) at three temperatures: 0 °C, 23 °C and 50 °C, results being presented in Figure 2.45

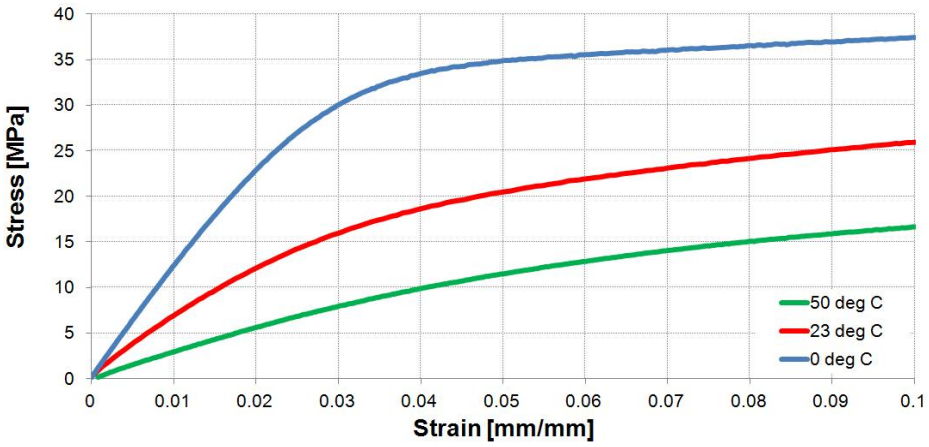

a)

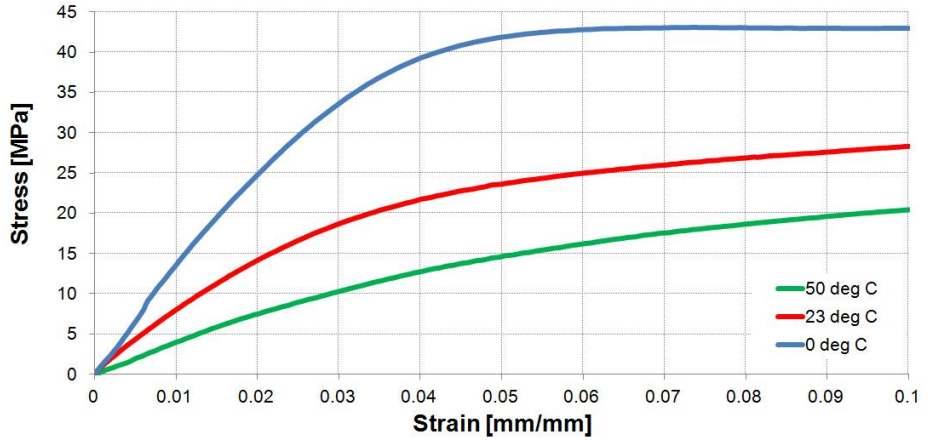

b)

Figure 2.45. Stress-strain curves for temperature dependent tests at a) 20 mm/min and b) 200 mm/min

As with strain-rate dependent tests on conditioned specimens temperature dependency tests also exhibit a softer stress-strain response compared to tests on unconditioned specimens (Figure 2.46 and Figure 2.47). In terms of tensile strength at 7% deformation, for a test speed of 20 mm/mm, a 21.3% softening was recorded at 0 °C (from 43.76 MPa to 36.06 MPa), a 18.37% softening was recorded at 23 °C (from 27.18 MPa to 22.98 MPa) and a 11.1% softening was recorded at 0 °C (from 15.59 MPa to 14.03 MPa). For tests performed at 200 mm/mm, a 7.4% softening was recorded at 0 °C (from 46.24 MPa to 43.03 MPa), a 23.4% softening was recorded at 23 °C (from 32.03 MPa to 25.96 MPa) while at 0 °C the tensile strength at 7% deformation remains the same, even though conditioned specimens exhibit softer response up until that point. Another observation can be noted, that, especially for lower temperatures, the yield point of conditioned specimens shifts to higher strain and the stress plateau is reached at higher strains as well (one of the reasons for the lower variations observed at 7% deformation).

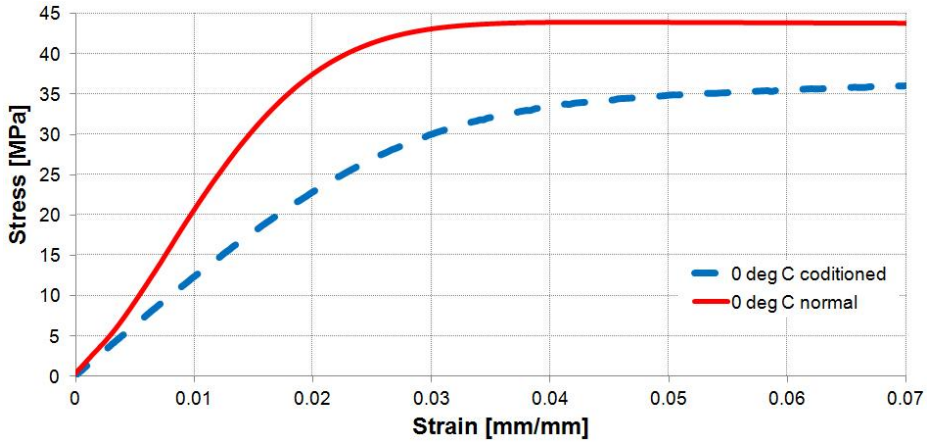

a)

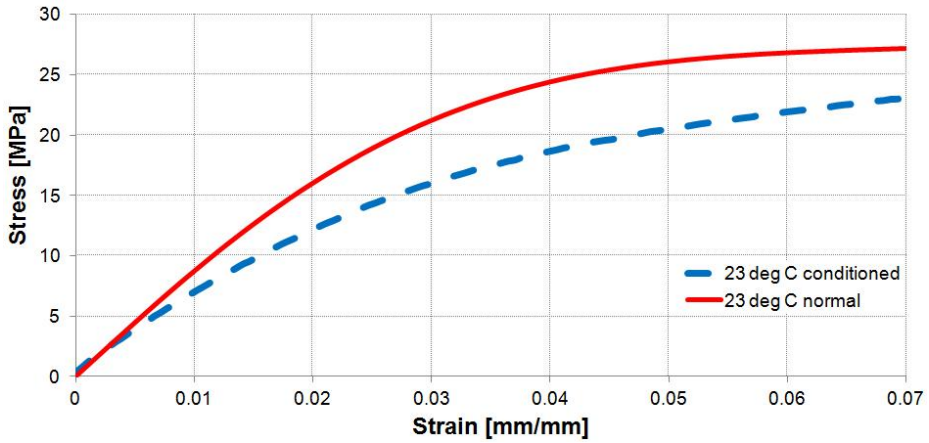

b)

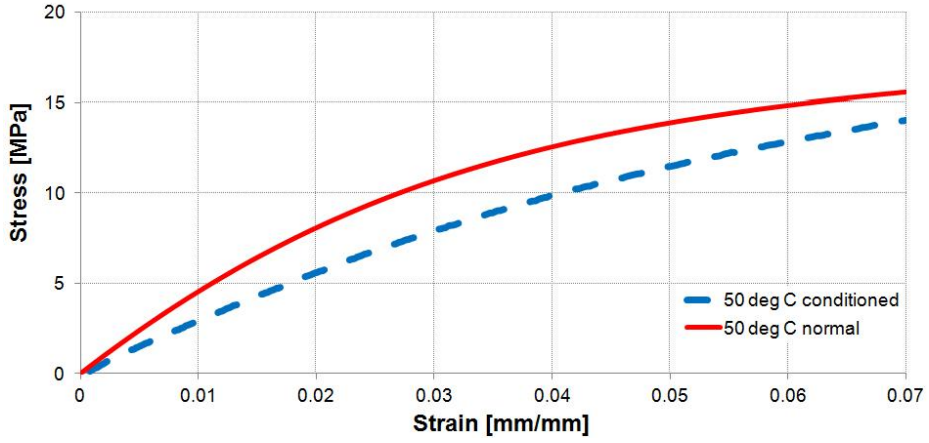

c)

Figure 2.46. Comparison between stress-strain response of normal and conditioned specimens for 20 mm/min tests

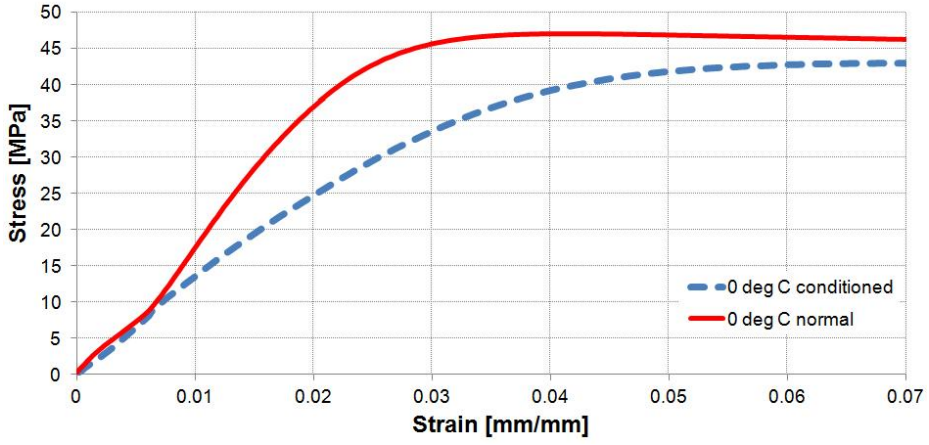

a)

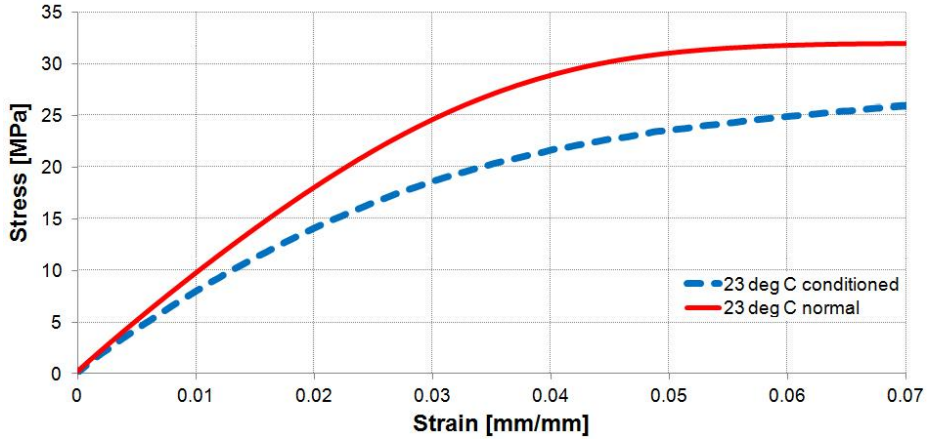

b)

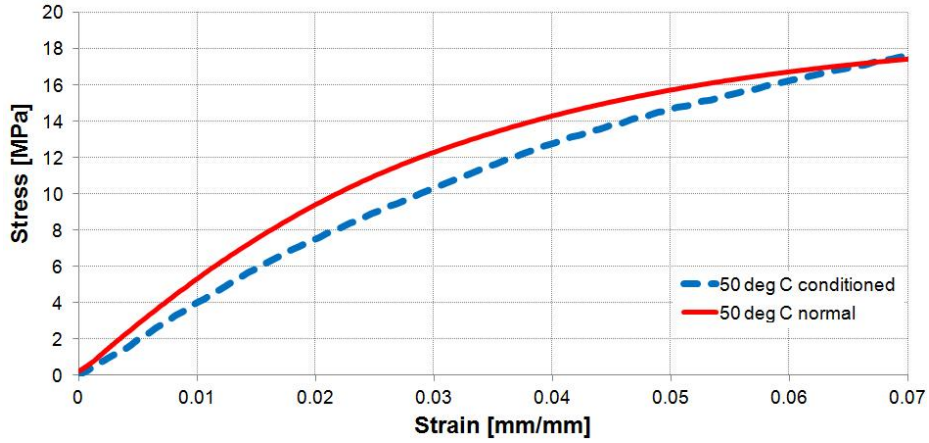

c)

Figure 2.47. Comparison between stress-strain response of normal and conditioned specimens for 200 mm/min tests

2.3. Three-point bending tests

Although the test poses some challenges, a three-point bending experimental plan was established because it is PA-12 component's main deformation mode during service. Apart from the parameters that influence the behaviour of the material (time and temperature, as shown in Paragraph 0) in the case of bending tests, the friction between the support and the specimen also plays an important role.

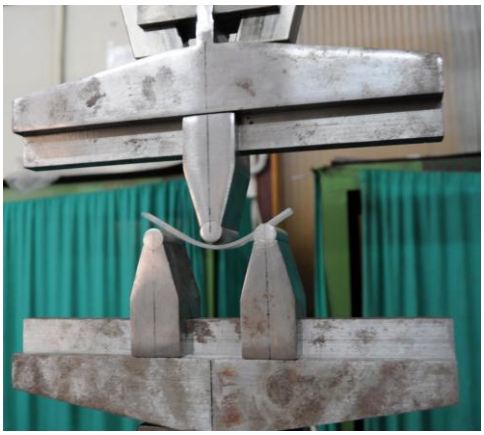

Figure 2.48Three point bending support wit PA-12 specimen

The main material characteristics deduced from three-point bending tests are given by the force-deflection graph [**52**]. Other values can be derived from the force-deflection data (force *F* and deflection *D*), clamping setup (support span *L*) and specimen dimensions (specimen depth *d* and width *b*) such as the flexural strength σ_{fM} (the peak value of the flexural stress σ_f), flexural strain (ε_f) or the chord modulus E_f [**52**].

$$\sigma_f = \frac{3 \cdot P \cdot L}{2 \cdot b \cdot d^2} \tag{2.1}$$

$$e_f = \frac{6 \cdot d \cdot D}{L^2} \tag{2.2}$$

$$E_f = \frac{\sigma_{f_2} - \sigma_{f_1}}{e_{f_2} - e_{f_1}} \tag{2.3}$$

The first set of tests were performed on prismatic specimens (95 x 10 x 2 mm) cut from injected sheets (200 x 200 mm). Due to the high dispersion in results caused by the sheet anisotropy, ISO 527 dogbone specimens were tested in later experiments.

The three-point bending experimental plan consisted only of monotone tests at different strain-rates (two sets of crosshead travel speeds were chosen, according to [**52**] and in accordance with the tensile tests respectively). A brief study of the influence of friction coefficients was also performed.

2.3.1. Specimen preparation and analysis

The first set of tests was performed on 95 x 10 x 2 mm prismatic specimens cut from injected sheets. The injection point was in the middle of the sheet and the flow direction was radial from that point. Consequently, the specimen distribution was chosen so that, from the same sheet, specimens should contain all flow directions (from parallel to perpendicular) as seen in Figure 2.49. The specimens

were cut with a guillotine. The number of specimens per sheet differed from test to test.

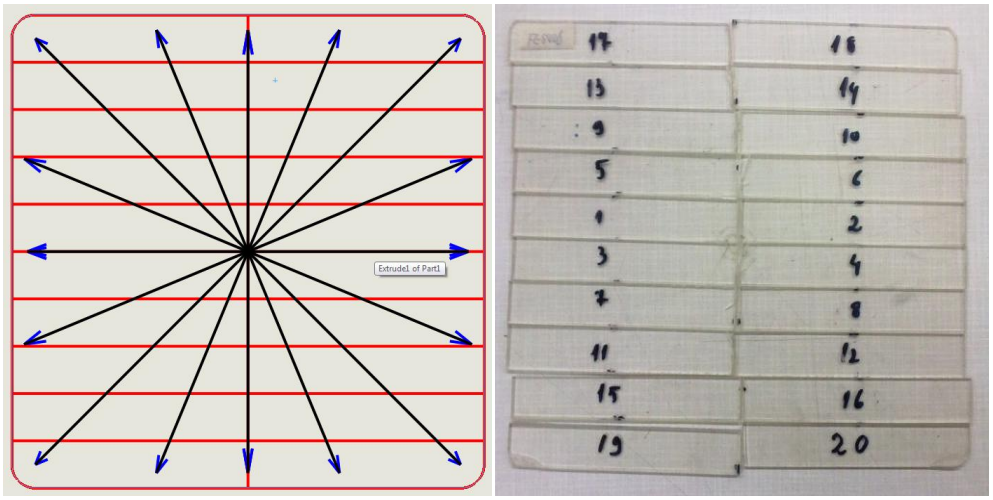

Figure 2.49. Flow directions (black arrows) and specimen grid (red lines) (left) and specimens numbering (right)

Considering that flow direction might influence mechanical properties, a residual stress analysis was performed with the help of a polariscope. After the specimens were cut, each of them was subjected to polarized light analysis and pictures were taken with the projection. The resulting pictures were cropped and a residual stress map was built for each sheet. Such a reconstructed map is presented in Figure 2.50.

The residual stress map indicates that there is a varying field of residual stress along the sheets. A quantitative evaluation cannot be established as calibration is required for PA-12 in order to connect the fringe variation with a numerical value for the stress.

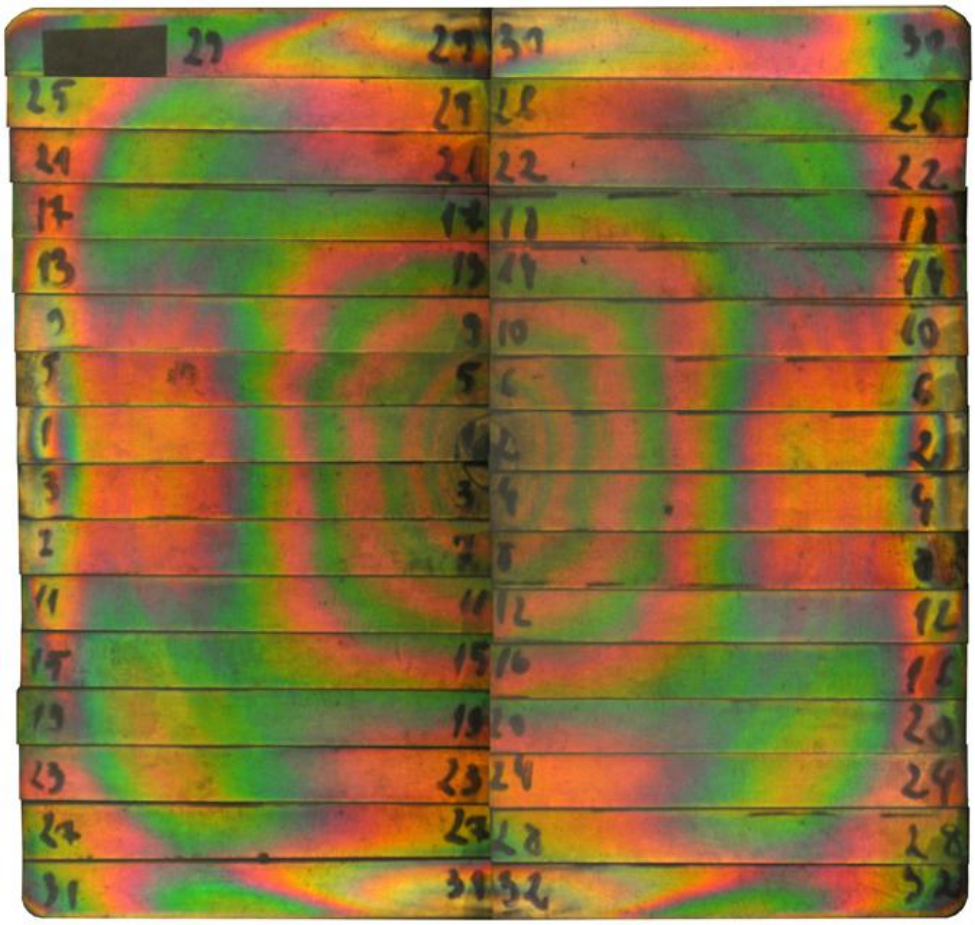

Figure 2.50. Residual stress map for PA-12 specimens

2.3.2. Experimental results for sheet specimens

The test parameters for the prismatic specimens cut from injected sheets were chosen according to the ASTM standard for determining the flexural properties of plastics [**52**]. Considering the depth of the beam, calculated value for the support span was 64 mm. The crosshead travel speed was calculated to be 3.41 mm/min, based on the values of the depth of the specimen, the support span and the rate of straining of the outer fibre [**52**,**53**]. Based on this value, two more values were chosen on a logarithmical scale: 34.1 mm/min and 341 mm/min. The strain being approximated with relation (2.2), there is a linear variation with deflection (and thus constant strain-rate):

- 0.00016 s^{-1} for 3.41 mm/min;
- 0.0016 s^{-1} for 34.1 mm/min;
- 0.016 s^{-1} for 341 mm/min.

The tests were performed on a 5kN Zwick/Roell machine.

In order to study the influence of friction, three types of interaction were used:

- The basic metal-plastic interaction (clear support);
- Plastic-Smooth Teflon (a smooth Teflon tape was stuck on the metal support), Figure 2.51;
- Plastic-Rough Teflon (a textured Teflon tape was stuck on the metal support, secured with the smooth Teflon tape), Figure 2.52.

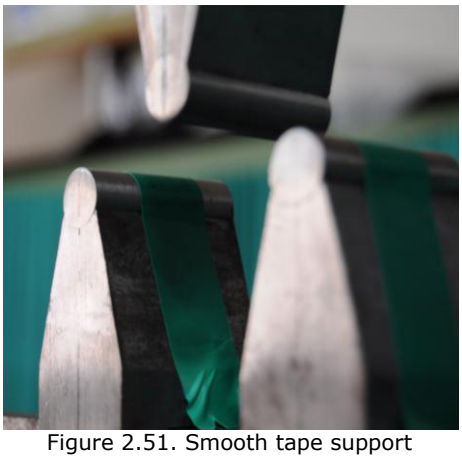

Figure 2.51. Smooth tape support

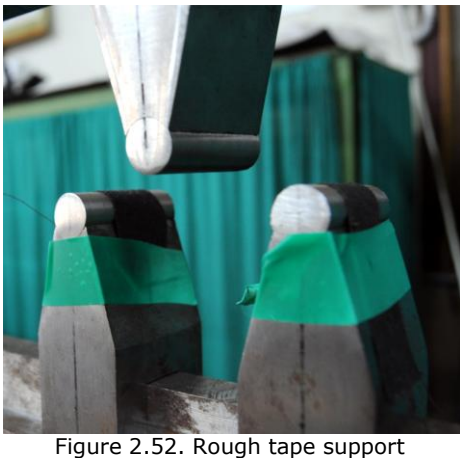

Figure 2.52. Rough tape support

The influence of strain-rate on material properties is exemplified for tests performed on clear supports (plastic-metal interaction), on specimens with 0° flow direction is presented in Figure 2.53.

The influence of specimen – support interaction on material properties is exemplified for tests performed at 341 mm/min, on specimens with 0° flow direction is presented in Figure 2.54.

The influence of flow direction on material properties is exemplified for tests performed at 341 mm/min, on clear support, is presented in Figure 2.55.

The results for the mean values of flexural strength (average values for all flow directions), their standard deviation and the variation for each interaction is presented in Table 2.3.

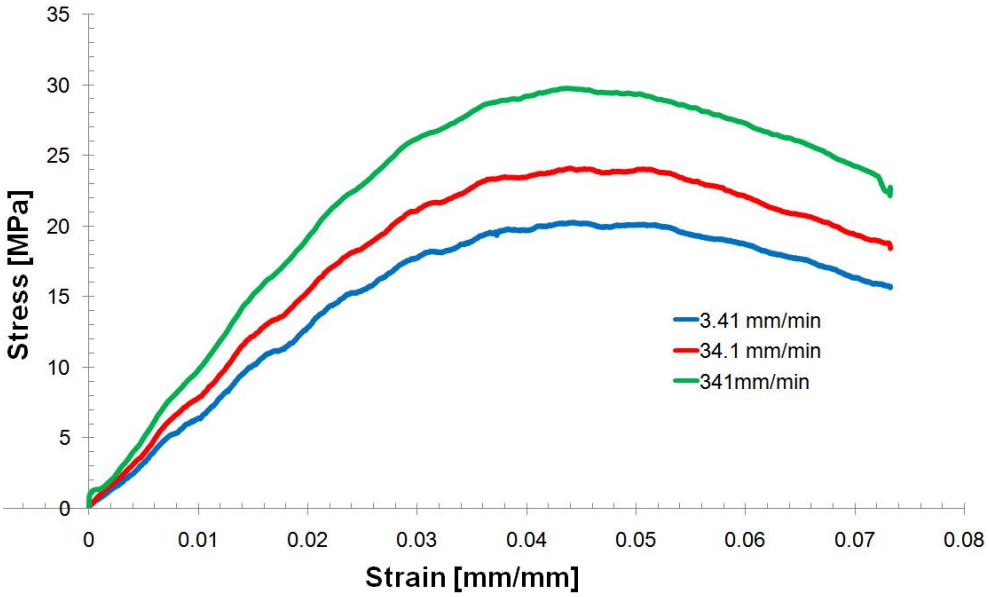

Figure 2.53. Strain-rate influence on flexural properties on sheet specimens PA-12

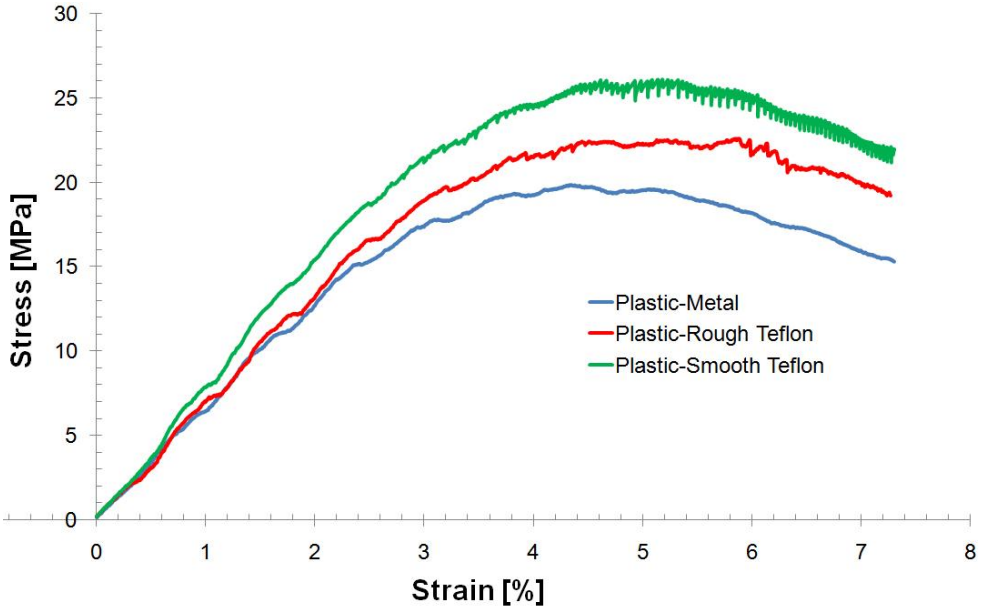

Figure 2.54. Specimen – support interaction on flexural properties on sheet specimens PA-12

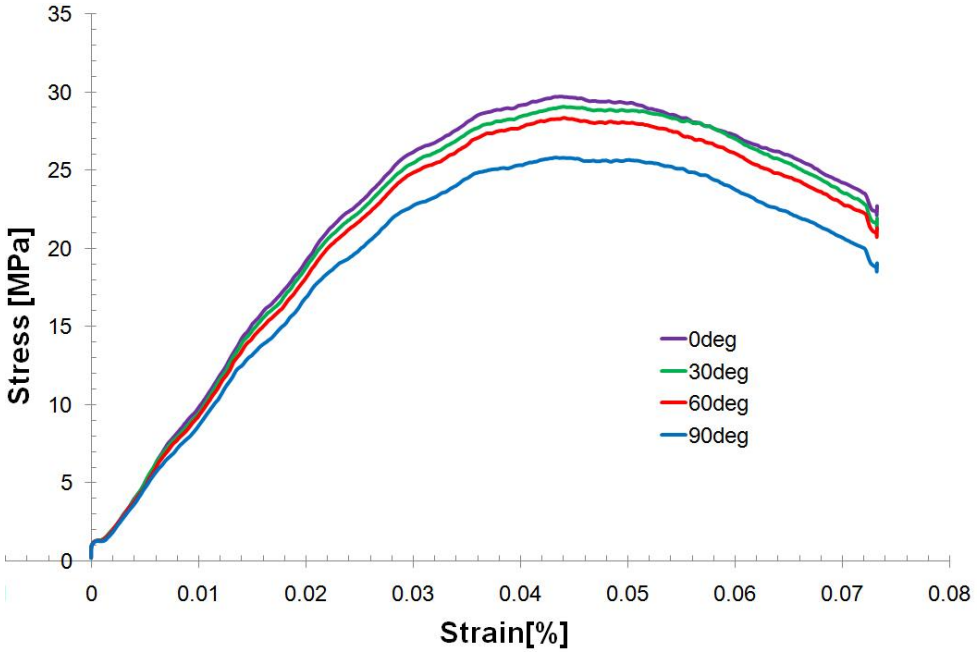

Figure 2.55. Flow direction influence on flexural properties on sheet specimens PA-12

Table 2.3. Variation of flexural properties with specimen-support interaction and crosshead travel speed

Interaction type	Test speed $[mm/min]$	Mean Flexural Strength $[MPa]$	Standard deviation [%]	Variation
Plastic – Metal	3.41	20.09	1.22	
	34.1	23.5	2.88	
	341	28.36	4.38	
				41.14%
Plastic – Rough Teflon	3.41	22.38	2.24	
	34.1	26.36	5.37	
	341	31.16	5.47	
				39.23%
Plastic – Smooth Teflon	3.41	25.69	3.2	
	34.1	29.03	3.66	
	341	31.2	3.57	
				21.44%

The variation of flexural strength with injection flow direction and crosshead travel speed is presented in Tables 2.3.2. – 2.3.4.

Surface graphs depicting the variation of flexural strength with injection flow direction and crosshead travel speed are presented in Figures 2.3.9 – 2.3.11.

Table 2.4. Flexural strength variation with injection flow direction and crosshead travel speed for clear support

Clear Support				
	0°	30°	60°	90°
$3.41mm/min$	20.27	20.22	20.17	19.60
$34.1mm/min$	24.09	23.96	23.16	22.3
$341mm/min$	29.7	29.07	28.36	28.03

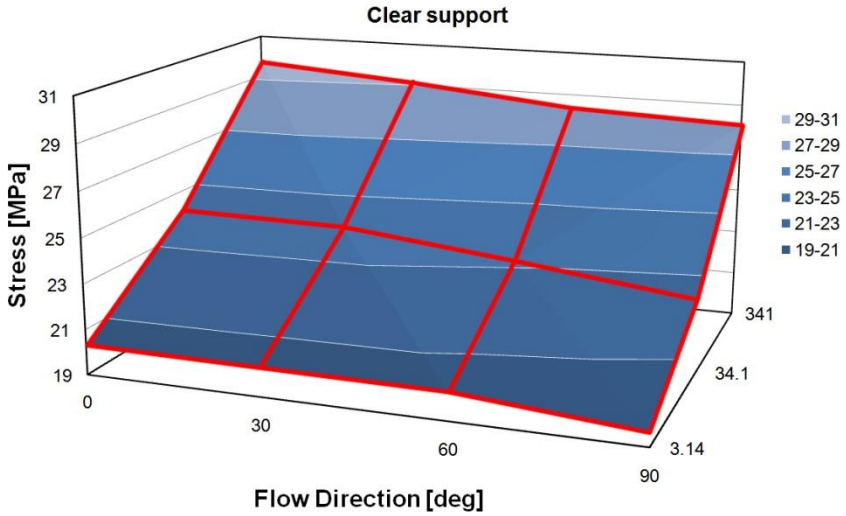

Figure 2.56. Flexural strength variation with injection flow direction and crosshead travel speed for clear support

Table 2.5. Flexural strength variation with injection flow direction and crosshead travel speed for rough Teflon

Rough Teflon				
	0°	30°	60°	90°
$3.41mm/min$	22.76	23.01	22.4	21.79
$34.1mm/min$	27.79	28.42	24.89	24.73
$341mm/min$	34.14	32.1	29.97	29.27

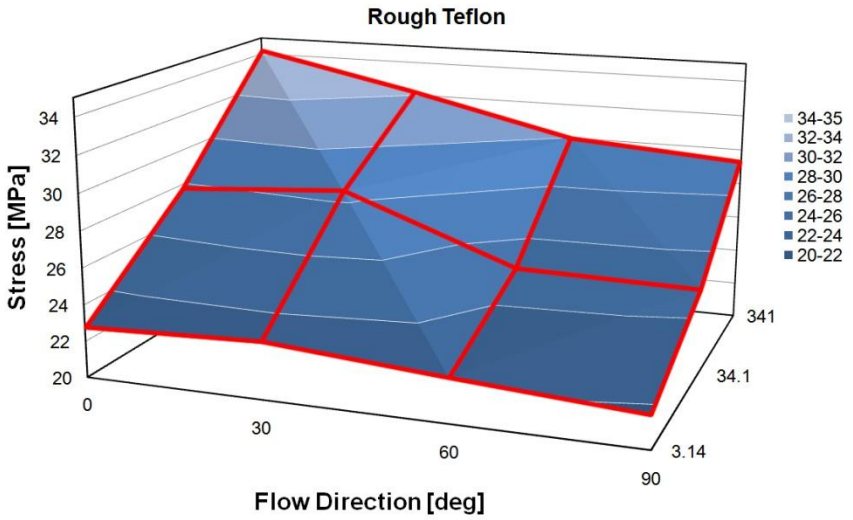

Figure 2.57. Flexural strength variation with injection flow direction and crosshead travel speed for rough Teflon

Table 2.6. Flexural strength variation with injection flow direction and crosshead travel speed for rough Teflon

Smooth Teflon				
	0°	30°	60°	90°
$3.41mm/min$	24.24	25.32	26.37	25.02
$34.1mm/min$	27.9	29.93	29.76	29.39
$341mm/min$	32.31	31.59	30.83	31.83

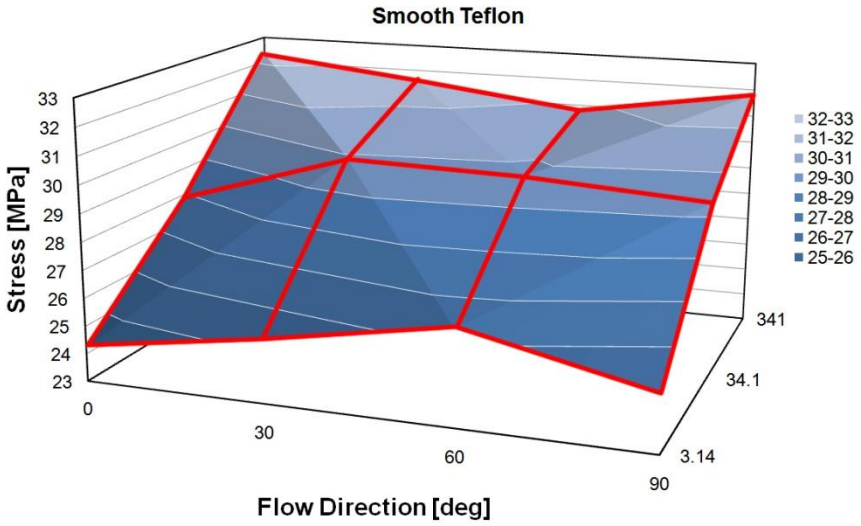

Figure 2.58. Flexural strength variation with injection flow direction and crosshead travel speed for Smooth Teflon

Strain-rate has the largest influence on the flexural properties of PA-12, determining an average variation of 40% with a 9900% increase in strain-rate. The behaviour in bending is similar to that in tension, where a 52% variation was recorded for a 9600% increase in strain-rate.

Friction also has a significant influence on flexural properties varying the flexural strength with as much as 30%. Though the smooth Teflon tape was used in order to reduce friction, the result was quite the opposite, test performed on the smooth tape support yielding the highest values for flexural strength. A possible cause for this is that the clear Teflon tape was more compliant than the textured one and the friction coefficient grew as it was getting compressed by the specimen.

Flow direction also determines a variation in flexural properties for as much as 16%. The variation for anisotropic specimens grows with strain-rate.

2.3.3. Experimental results for dogbone specimens

Noticing the small variation in tensile properties for dogbone specimens, a three-point bending experimental program was designed for such specimens in order to eliminate the sheet anisotropy aspect (dogbone specimens are moulded individually).

For these tests, the support span was kept at 64 mm while the crosshead travel speed was chosen in accordance with the tensile tests:

- 2 mm/min;
- 20 mm/min;
- 200 mm/min;
- 2,000 mm/min;
- 20,000 mm/min;
- 90,000 mm/min.

The strains were approximated with relation 2.2 and consequently there is a linear variation with deflection (and thus constant strain-rate for as long as the machine can keep a constant crosshead travel):

- 0.00002 s^{-1} for 2 mm/min;
- 0.0002 s^{-1} for 20 mm/min;
- 0.002 s^{-1} for 200 mm/min;
- 0.02 s^{-1} for 2,000 mm/min;
- 0.2 s^{-1} for 20,000 mm/min;
- 0.8 s^{-1} for 90,000 mm/min;

Similar to the experiments in tension, the tests at low speeds were performed on a 5kN Zwick/Roell machine while the tests at high speeds were performed on an Instron Electropuls machine.

The results for the tests performed at slow speeds are presented in Figure 2.59

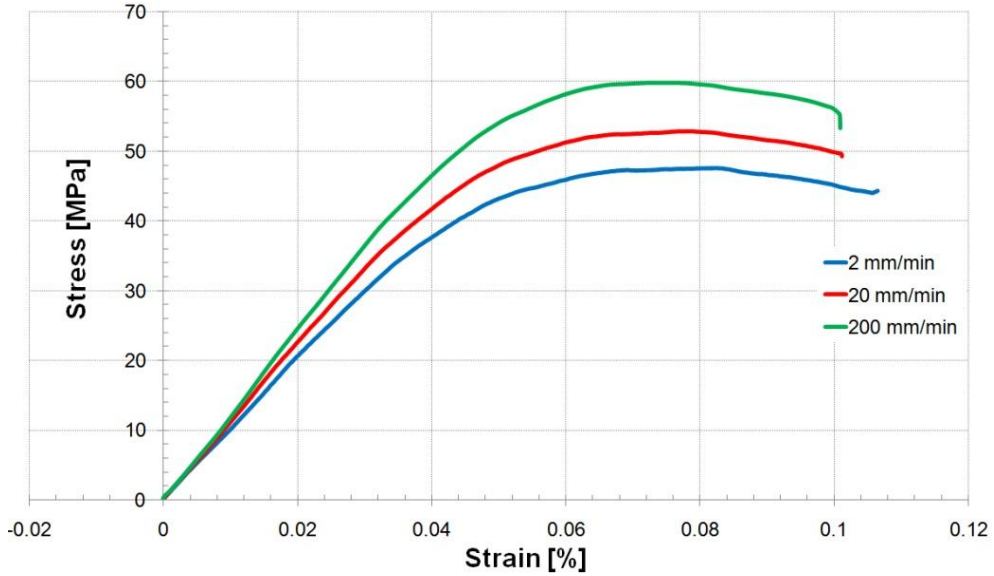

Figure 2.59. Stress-strain curves for low-speed three-point bending tests on dogbone specimens

The results for the tests performed at slow speeds are presented in Figure 2.60.

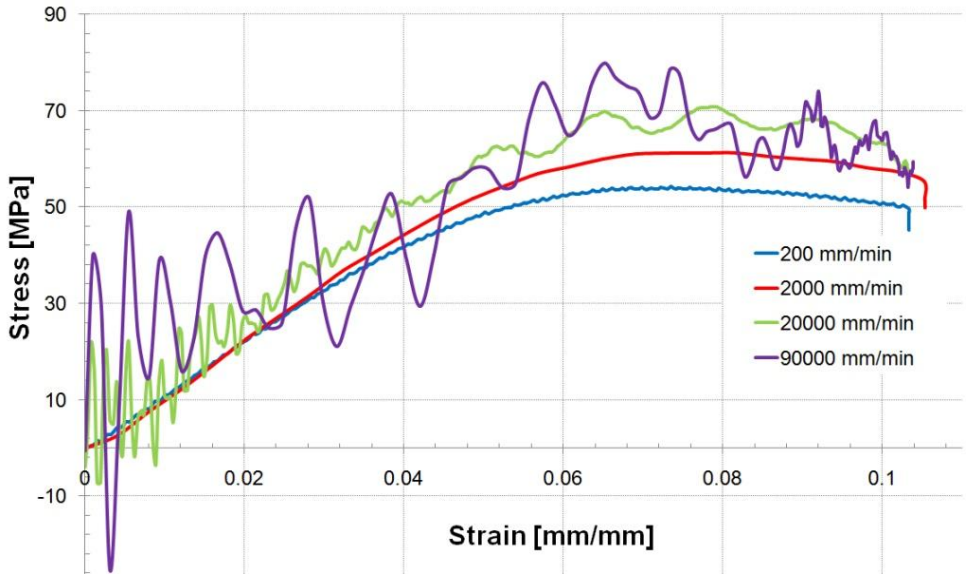

Figure 2.60. Stress-strain curves for high-speed three-point bending tests on dogbone specimens

Comparing the experimental data from tests performed on sheet specimens and from tests performed on dogbone specimens (Figure 2.53 and Figure 2.59), it is clear that the later tests determine a more stable response. One of the reasons for this effect is the low values of forces recorded for the tests performed on sheet specimens (around 20N) compared to the values of the forces recorded on dogbone specimens (around 100N), considering that both tests were performed on machines equipped with 5kN load cells. Dogbone specimens also determine a lower dispersion of results even when it comes to dynamic loadings (Figure 2.61).

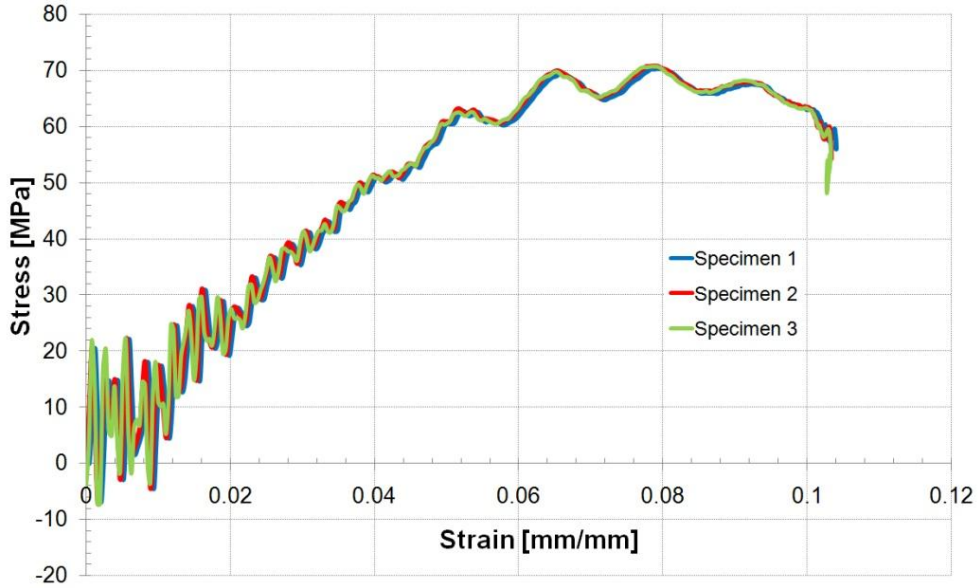

Figure 2.61. Results in three-point bending for three specimens tested at 20000 mm/min

For speeds faster than 20,000 mm/min, dynamic effects play an important role in determining the stress-strain response. When the indenter makes contact at high speed, due to inertia, the specimen contracts at first after which it begins to expand (because of its elasticity), expansion which is again followed by another contraction. This cyclic deformation is propagated through the material (with a certain degree of damping), and thus, stress waves are created [**54**,**55**]. The stress waves are consequently transmitted into the support (which is connected to the load cell), and due to the same inertial effects, errors appear in reading the reactions: when the vice is compressed, higher reaction forces are recorded and when the vice expands, it appears as if the vice is subjected to tensile loading (the negative values in reaction stress, Figure 2.60).

2.4. Dynamic tests

2.4.1. Dynamic tension

The tensile tests at high rate of deformation were performed in the Institut für Leichtbau und Kunststofftechnik, Technische Universität Dresden on a servo-hydraulic Instron VHS 160/20 machine, presented in Figure 2.62, which is capable of reaching crosshead travel speeds up to 10 m/s. The schematic of the machine's load train is presented in Figure 2.63. The specimen is secured to the bottom side of the vice by tightening the lower screws. The mobile part of the train, consisting of the clamp, the grip, the spacers (wedges) and the elastic element, is connected to the servo-hydraulic actuator. Pressure is applied on the spacers by tightening the side bolts. The machine is programmed to accelerate the assembly until it reaches the desired speed. At this point, an impact of the wedges with the cylindrical columns follows which determines the spacers to slide down thus closing the grips and starting to deform the specimen.

The reaction force is recorded with a Kistler 9017A 400 kN piezoelectric load washer mechanically preset at 200 kN. Strain evaluation was performed with digital image correlation technique, which proved to be an efficient strain recording method for thermoplastic polymers at high strains and speeds [**56**,**57**,**58**,**59**]. Images were recorded with a high speed camera of 600 x 800 pixels maximum resolution (reduced to 96 x 600 for these tests), 200 mm focal length and capable of recording 100,000 frames per second. The images were processed with the help of ARAMIS software by GOM using greyscale correlation (Figure 2.64).

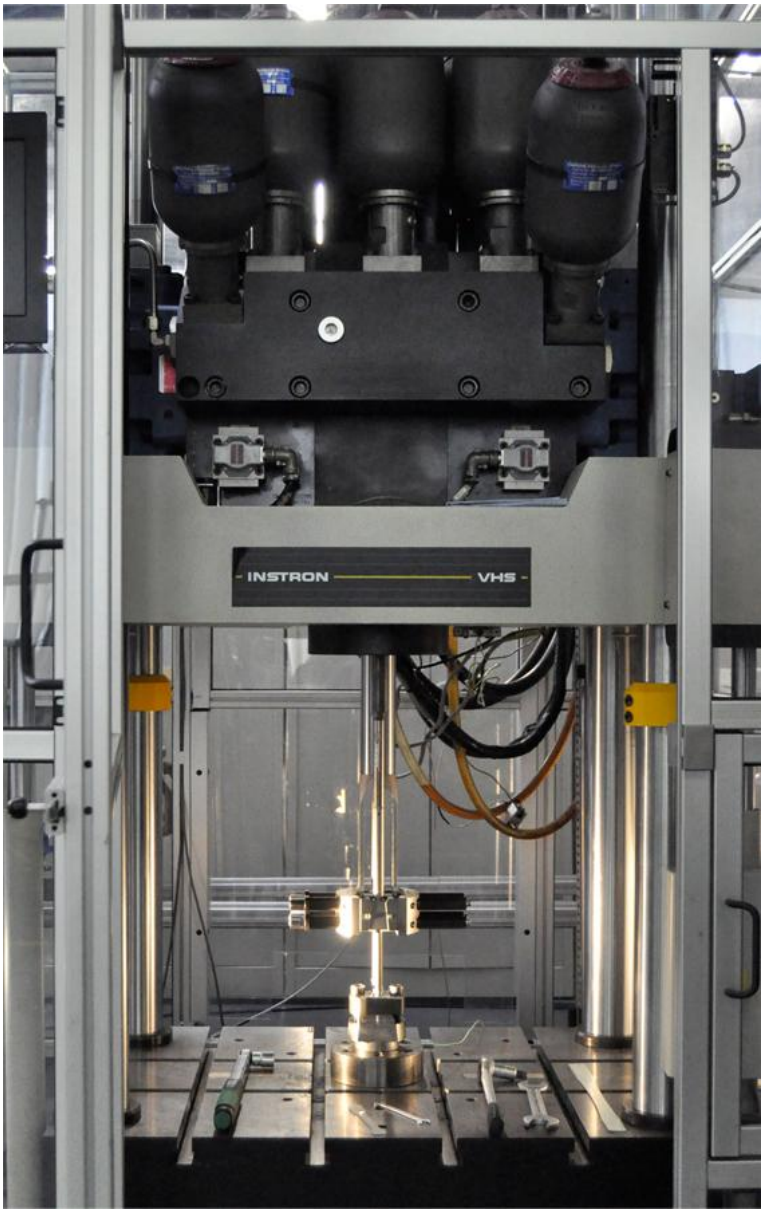

Figure 2.62. Instron VHS 160/20 high speed testing machine

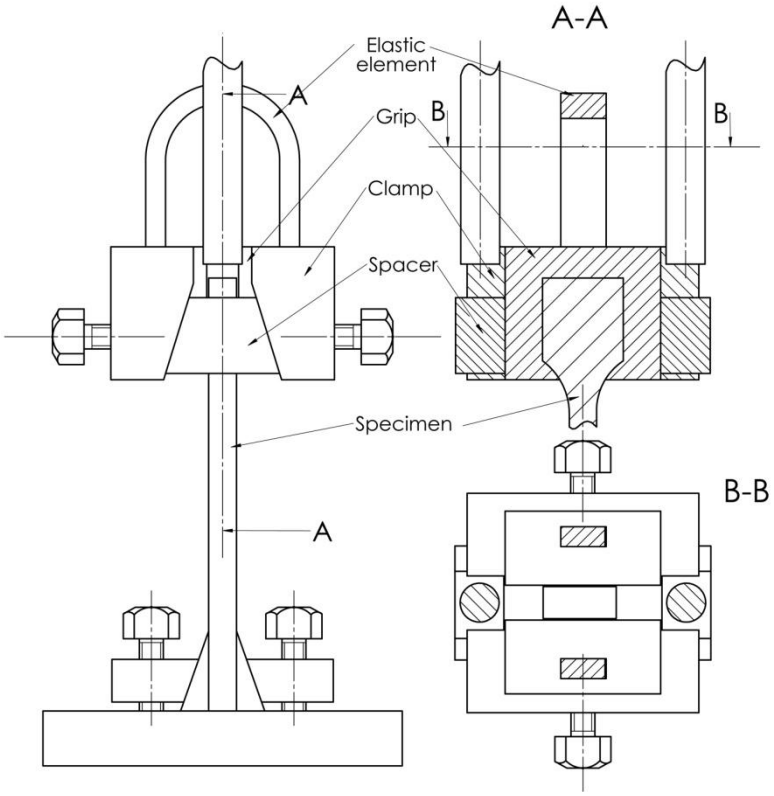

Figure 2.63. Schematic Instron VHS 160/20 load train

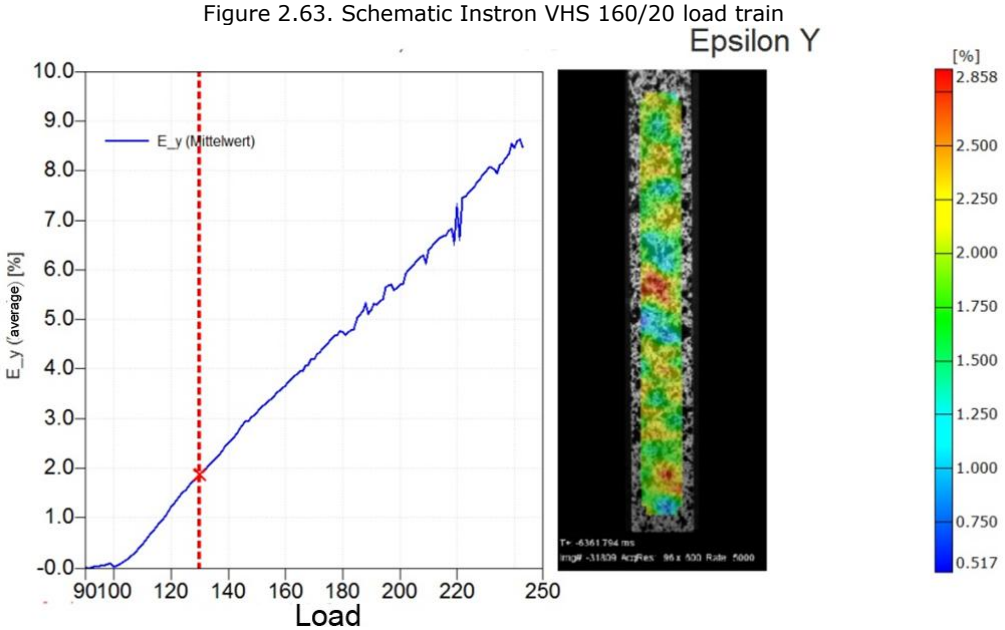

Figure 2.64. Strain evaluation with ARAMIS

Due to the fact that the 4 mm thick dog-bone specimens are semi-transparent, a white paint layer was airbrushed before the random speckle pattern (black paint) was applied (Figure 2.65), in order to eliminate possible erroneous reads during greyscale correlation.

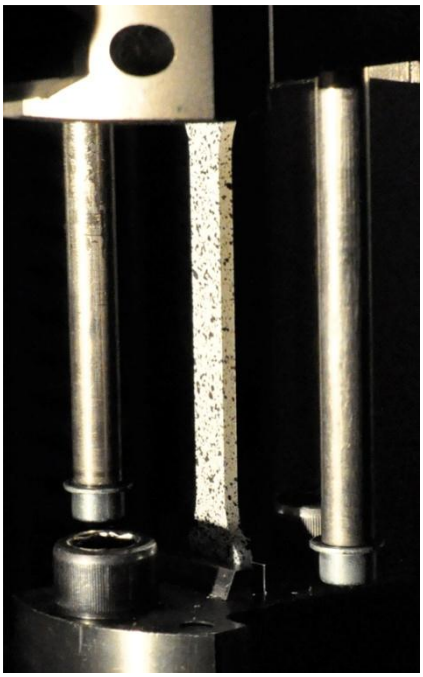

Figure 2.65. Prepared specimen clamped in machine grips

Various crosshead travel speeds were tested preliminary in order to determine the maximal value for which system ringing and stress waves influence is negligible [**60**]. As a result, three test speeds were chosen: 333 mm/s (equivalent of 20000 mm/min, next value on the logarithmical scale), 667 mm/s and 1000 mm/s (maximum speed which determines acceptable response). The results are presented in Figure 2.66, showing a similar behaviour (stress-strain curves tend to overlap determining a tensile strength of around 40 MPa) regardless of the test speed.

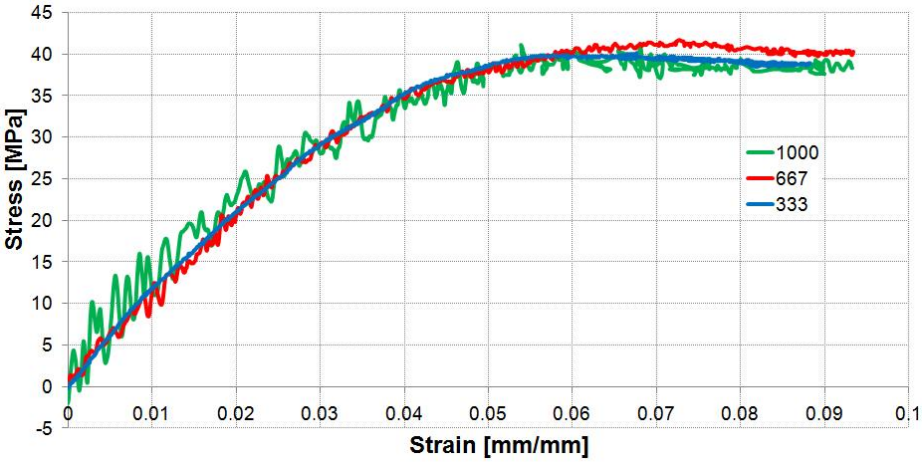

Figure 2.66. Stress-strain curves for high-speed rate dependent tests

A limitation of the optical method of strain recording was discovered during high-speed tests. As stated above, the semi-transparent material needed an opaque layer of paint to be applied before the speckle pattern. This layer proved to have a relatively low fracture strain (about 10%) compared to the base material. As deformation increased, the paint layer started to disintegrate (Figure 2.67) and the post-processing software could not keep track of the pixels, thus determining erroneous reads after a certain strain. In consequence, no fracture strain was recorded for the polyamide.

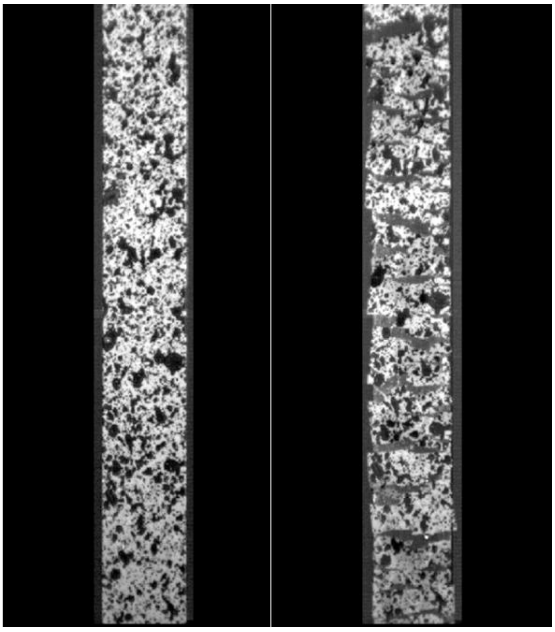

Figure 2.67. HS camera images from test initiations with intact paint layer (left) and test end with cracked paint layer (right)

Because of the induced noise at high test speeds, the elastic modulus determination required trend lines. For all test results, 6th order polynomial functions were fitted. Determination of Young's modulus values with ISO 527 [**43**] do not provide accurate material description as the results for a single specimen have a high margin of error due to the numerous possible ways of trend-line definition. The variation of the instantaneous elastic modulus with strain was obtained by trend line derivation, resulting in 5th order polynomial functions. The stress-strain trend lines and instantaneous moduli variation with strain for all test speeds is presented in Figure 2.68. Although the trend lines share a similar shape, the instantaneous modulus varies for each test speed, especially in the first 1% deformation (from 1100 MPa to 1600 MPa). As deduced from the stress-strain curves, the yield point (instantaneous modulus becomes null) is similar for all speeds, around 6%.

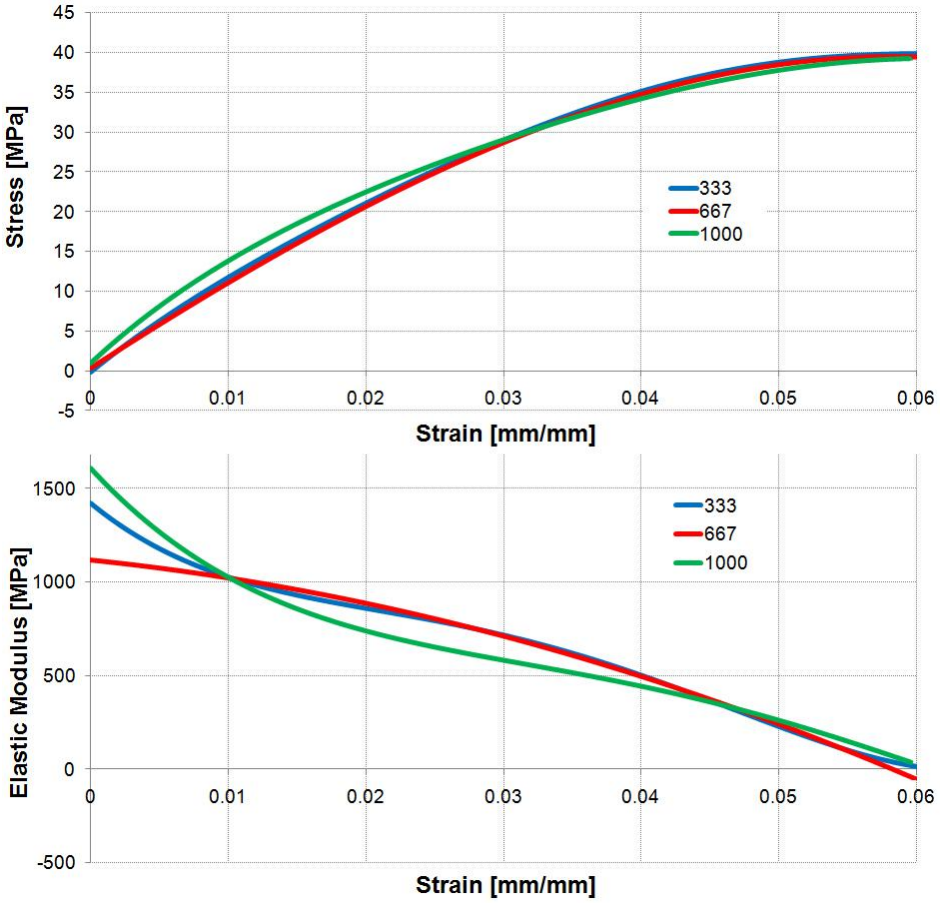

Figure 2.68. Stress-strain trend lines and instantaneous moduli variation with strain

2.4.2. DMA tests

2.4.2.1. Overview

The moduli of elasticity (E, G, K) used to describe the basic polymer properties refer to quasi-static measurements. When dealing with more complex loadings such as repetitive/cyclic loadings at high frequencies or dynamic loadings, the complex moduli must be introduced. By definition, a complex elastic modulus is expressed as[**44**]:

$$M^* = M' + iM'' \tag{2.4}$$

where M' is called the *storage modulus*, and it represents the stored elastic potential, M'' is called the *loss modulus* and it represents the measure of energy dissipated through heat.

The values for M' and M'' can be determined experimentally through *Dynamic Mechanical Analysis (DMA)*, by subjecting the specimen to sinusoidal strain [**5**]:

$$\varepsilon = \varepsilon_0 \cdot \sin \omega t \tag{2.5}$$

The stress will have a linear response, but due to the viscoelastic nature of the polymers, will be out of phase [**5**]:

$$\sigma = \sigma_0 \cdot \sin(\omega t + \delta) \tag{2.6}$$

or

$$\sigma = \sigma_0 \cdot \cos(\delta) \sin \omega t + \sigma_0 \cdot \sin(\delta) \cos(\omega t) \tag{2.7}$$

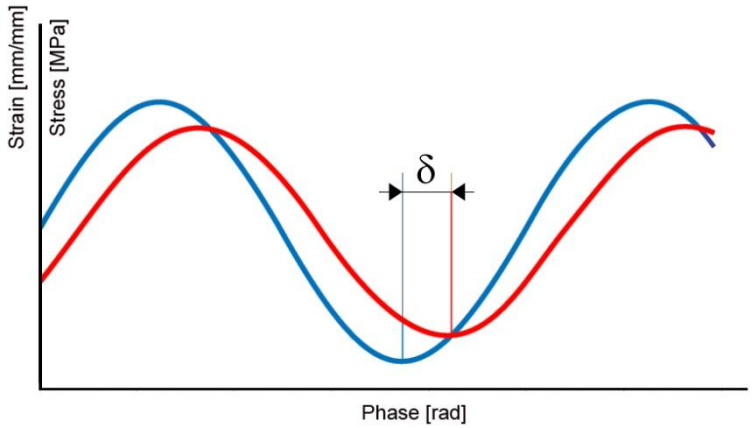

Figure 2.69. Phase difference between stress and strain

By definition

$$M' = \frac{\sigma_0}{\varepsilon_0} \cdot \cos(\delta) \quad and \quad M'' = \frac{\sigma_0}{\varepsilon_0} \cdot \sin(\delta) \tag{2.8}$$

The ratio of loss to storage modulus is called the *damping coefficient* and it can be considered an alternate measure of energy dissipation (3):

$$\tan(\delta) = \frac{M''}{M'} = \frac{\sin(\delta)}{\cos(\delta)} \tag{2.9}$$

2.4.2.2. DMA tests at low strains

The DMA tests at small strains were performed on specialized machines that export all calculated data (storage modulus, loss modulus and damping coefficient) in the output files. The first test was set up in shear at room temperature in Loughborough University on a Mettler Toledo DMA machine (Figure 2.70). Four frequencies were used: $0.1\,Hz$; $1\,Hz$; $10\,Hz$ and $100\,Hz$. The magnitudes of the shear strains γ were around $0.001\,\mathrm{mm/mm}$.

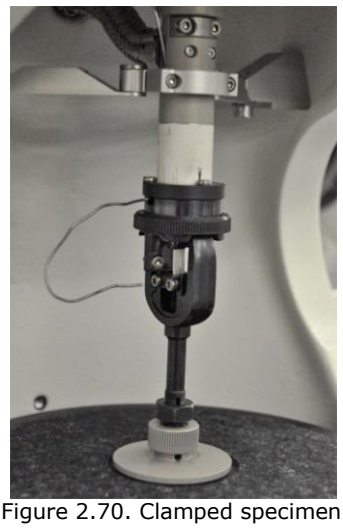

Figure 2.70. Clamped specimen in the Mettler Toledo

Another DMA test consisted of a temperature sweep from 0 °C to 60 °C at 2 frequencies (1 Hz and 10 Hz) was carried out at the company Gearing Scientific Ltd. in single cantilever clamping.

For the shear test, the obtained storage modulus, loss modulus and damping coefficient values are presented in Table 2.7.

The variation of the storage modulus, loss modulus and damping coefficient with frequency for the test in shear is presented in Figure 2.71. The variation of the storage modulus, loss modulus and damping coefficient with frequency and temperature for the test in single cantilever is presented in Figure 2.72 [**47**].

Table 2.7 Results for DMA test in shear

Frequency f [Hz]	Storage modulus G' [MPa]	Loss modulus G'' [MPa]	Damping coefficient $\tan\delta$ [−]
0.1	307	67	0.2175
1	320	65	0.2024
10	336	63	0.1885
100	350	55	0.158

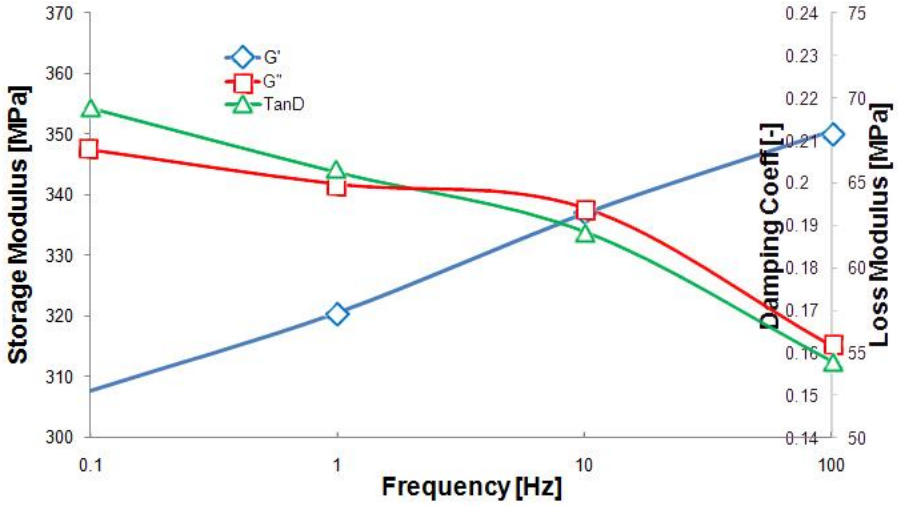

Figure 2.71. Moduli variation with frequency in DMA shear test

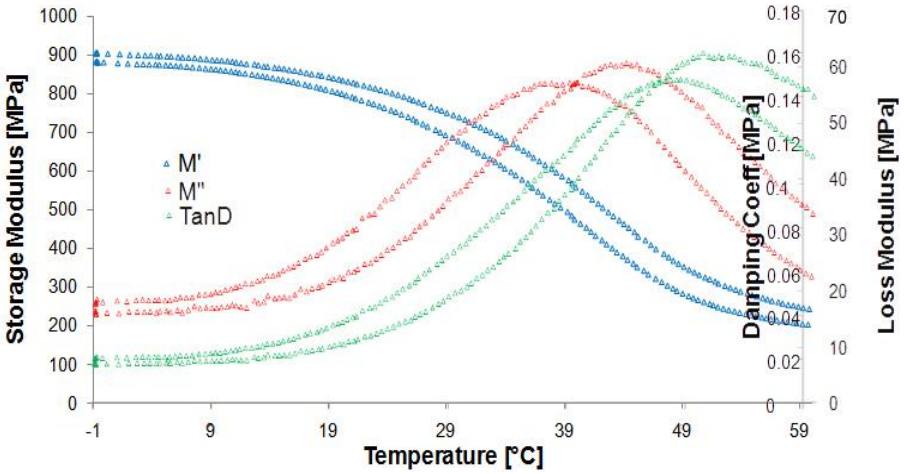

Figure 2.72. Moduli variation with temperature for the DMA single cantilever test

In accordance with the strain–rate- and temperature-dependency tests, the storage modulus (stored elastic potential) grows with the increase in strain rate (frequency) while both the loss modulus (dissipated energy through heat) and the damping coefficient decrease.

The temperature sweep DMA tests determined a glass transition temperature of around 37 °C at 1 Hz and 37 °C at 10 Hz. Below 10 °C, the behaviour of the material stabilizes (a plateau region for all parameters).

As seen in previous experiments, hyperelastic materials do not have a linear stress-strain response, and their moduli of elasticity vary with strain [**2**,**3**,**26**,**27**]. Thus, the DMA tests performed at small strains offer a limited perspective of the dynamical behaviour of such materials. In order to obtain material parameters for in-service conditions, a series of DMA tests at high strain were performed.

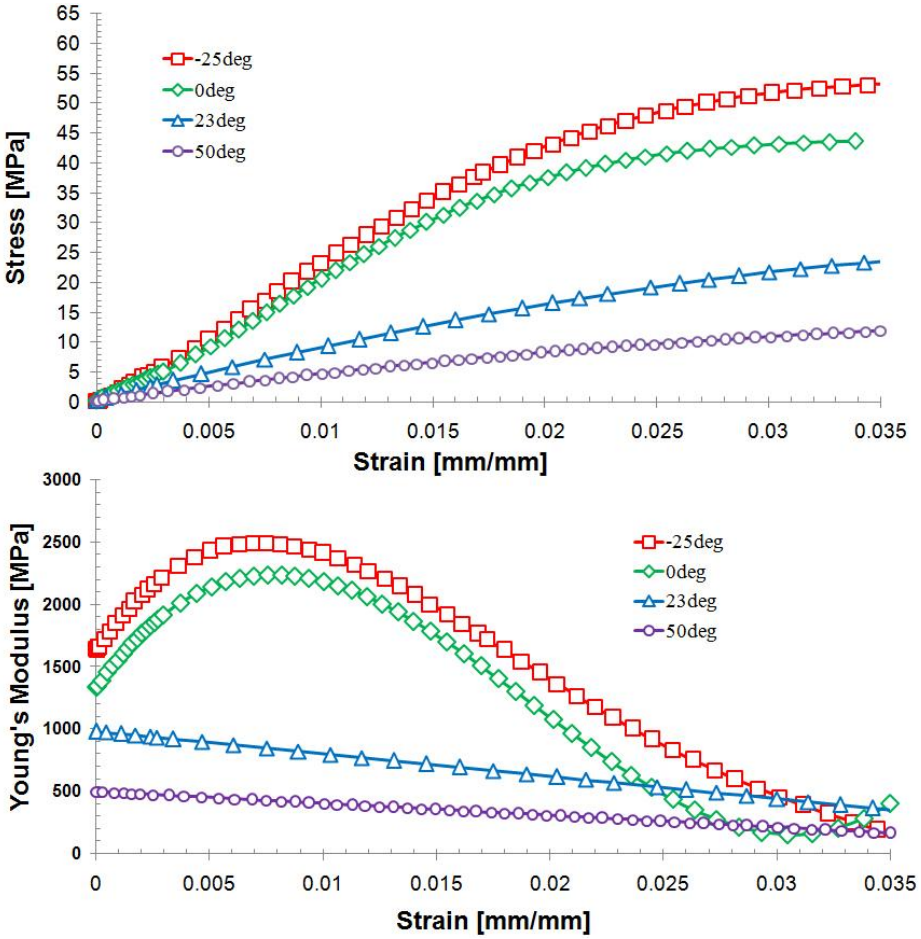

Figure 2.73. Variation of stress and Young's modulus with strain for different temperatures

2.4.2.3. DMA tests at high strains

The DMA tests at large strains were performed in tension in Loughborough University on ISO 527 standard dogbone specimens, on an Instron Electropuls machine. Several test programs were performed, all having a sinusoidal load pattern, with different pre-strains and strain amplitudes (ranging from 0.015 mm/mm to 0.043 mm/mm). For all programs, three frequencies were used: 0.1 Hz, 1 Hz and 10 Hz.

a) Pre-deformation 1mm; amplitude 0.75 mm (0.015 mm/mm total strain)

The results for the tests performed at pre-deformation of 1 mm and an amplitude of 0.75 mm are presented in Table 2.8.

Table 2.8 Results for the first DMA test in tension

Frequency f [Hz]	Storage modulus E' [MPa]	Loss modulus E'' [MPa]	Damping coefficient $\tan\delta$ [−]
0.1	709	107	0.1519
1	786	39	0.0503
10	734	55	0.075

b) Pre-deformation 1.65 mm; amplitude 1.15 mm (0.025 mm/mm total strain)

The results for the tests performed at pre-deformation of 1.65 mm and an amplitude of 1.15 mm are presented in Table 2.9.

Table 2.9 Results for the second DMA test in tension

Frequency f [Hz]	Storage modulus E' [MPa]	Loss modulus E'' [MPa]	Damping coefficient $\tan\delta$ [−]
0.1	682	86	0.1256
1	769	58	0.0755
10	837	45	0.0503

c) Pre-deformation 2 mm; amplitude 1.5 mm (0.031 mm/mm total strain)

The results for the tests performed at pre-deformation of 2 mm and an amplitude of 1.5 mm are presented in Table 2.10.

Table 2.10 Results for the third DMA test in tension

Frequency f [Hz]	Storage modulus E' [MPa]	Loss modulus E'' [MPa]	Damping coefficient $\tan\delta$ [−]
0.1	651	82	0.1263
1	751	75	0.1008
10	795	40	0.0503

d) Pre-deformation 4 mm; amplitude 0.75 mm (0.043 mm/mm total strain)

The results for the tests performed at pre-deformation of 4 mm and an amplitude of 0.75 mm are presented in Table 2.11.

Table 2.11 Results for the fourth DMA test in tension

Frequency f [Hz]	Storage modulus E' [MPa]	Loss modulus E'' [MPa]	Damping coefficient $\tan\delta$ [−]
0.1	580	103	0.1777
1	662	66	0.1005
10	781	36	0.0503

e) Pre-deformation 2.75 mm; amplitude 2 mm (0.043 mm/mm total strain)

The results for the tests performed at a pre-deformation of 2.75 mm and an amplitude of 2 mm are presented in Table 2.12.

Table 2.12 Results for the fifth DMA test in tension

Frequency f [Hz]	Storage modulus E' [MPa]	Loss modulus E'' [MPa]	Damping coefficient $\tan\delta$ [−]
0.1	625	95	0.1519
1	714	72	0.1008
10	778	58	0.075

For the results obtained from the tests performed at large strains, a similar behaviour to that at small-strain DMA tests was observed regarding the effect of frequency. Furthermore, the amplitude affects dynamic properties, as the elastic potential decreases with strain. Thus, a uniform variation of the storage modulus, the loss modulus and the damping coefficient with frequency and amplitude can be observed (Figure 2.74 and Figure 2.75): the storage modulus has a 22% increase in the chosen range of frequency and a 4% decrease with amplitude; the loss modulus has a 51% decrease with frequency and a 91% increase with amplitude; the damping coefficient has a 60% decrease with frequency and a 100% increase with amplitude.

For the same total strain (experiments d) and e)) a smaller amplitude determines lower values for the storage modulus (around 8%), and, consequently, increased values for the loss modulus and damping coefficient. Again, this is a consequence of strain-rate dependency; for the same frequency, smaller amplitude determines smaller strain rates.

Beyond the yield point, the viscoelastic and plastic components cannot be separated; a plateau of the loss modulus and damping coefficient is noticed, while the storage modulus decreases.

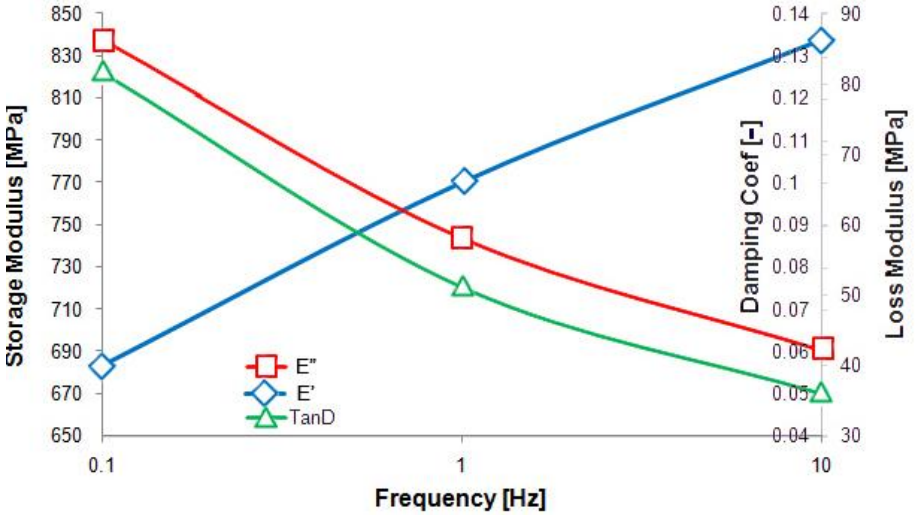

Figure 2.74. Moduli variation with frequency for DMA test in tension

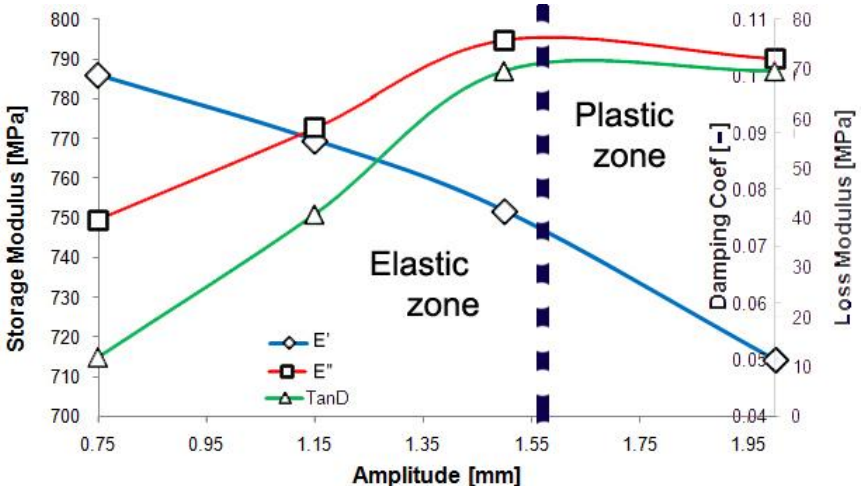

Figure 2.75. Moduli variation with amplitude for DMA test in tension

2.4.3. Puncture impact tests

2.4.3.1. Test overview

The puncture impact tests were performed in Loughborough University on an Instron Dynatup machine according to ISO 6630 [**61**]. The carrier mass of the striker had a value of around 20 kg. The striker diameter was ϕ 20 and it was lubricated with Vaseline before each test. Two different test speeds were used: 1 m/s and 4.4 m/s and two different temperatures: 23 °C and -10 °C.

Three types of PA-12 samples were used:

- Sample 1 – Injected by material supplier (70 x 70 mm) (codenamed **S1**)
- Sample 2 – Injected by injection manufacturer (70 x 70 mm) (codenamed **S2**)
- Sample 3 – Injected by injection manufacturer (100 x 100 mm) (codenamed **S3**)

S3 specimens have 4 textures with different roughness.

Figure 2.76 Instron Dynatup machine

2.4.3.2. Comparison of PA-12 samples

For this test, three samples from each category were used. The test temperature was 23 °C and the striker speed was 4.4 m/s. The results are presented in Figure 2.77

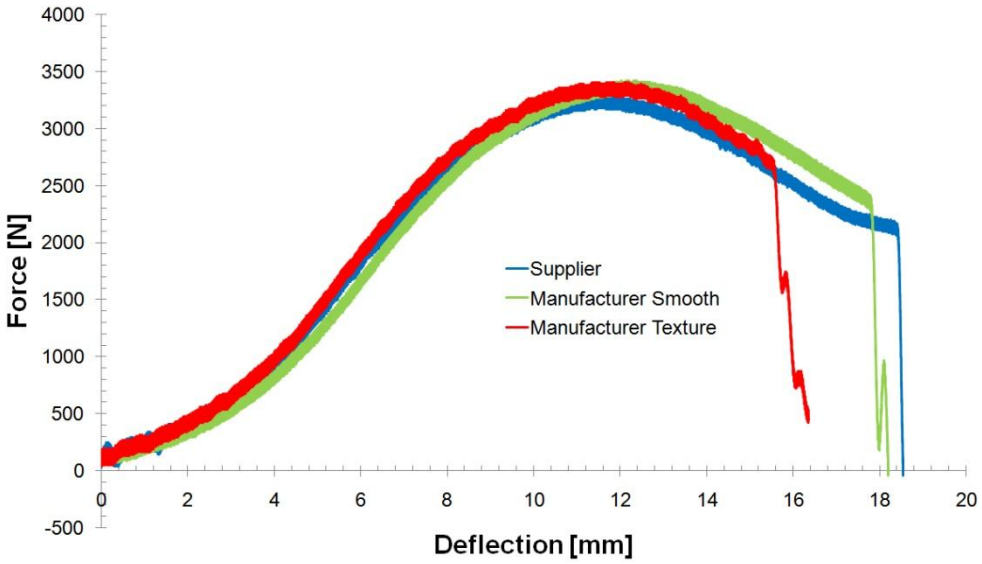

Figure 2.77. Force – deflection curves for different PA-12 samples

The resulting puncture energies in Joules are presented in Table 2.13.

Table 2.13 Puncture energies for different PA-12 samples

Specimen	Puncture energy [J]	Specimen	Puncture energy [J]	Specimen	Puncture energy [J]
S1-1	42.28024	S2-1	38.07019	S3-1	39.47512
S1-2	38.4927	S2-2	37.82643	S3-2	33.99899
S1-3	38.91812	S2-3	34.62048	S3-3	34.70669
Average	**39.89702**	***Average***	**36.83903**	***Average***	**36.06027**

All tested specimens were punctured, showing a ductile behaviour. The condition of the specimens after the test is presented in Figure 2.78.

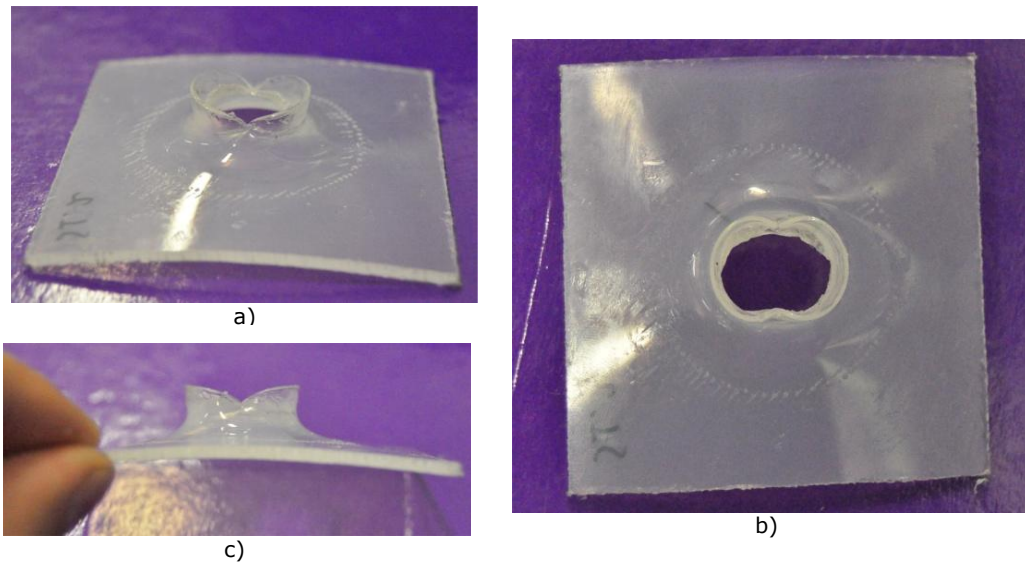

a) b) c)

Figure 2.78. Punctured PA-12 sample at ambient temperature; a) isometric view, b) top view, c) side view

2.4.3.3. PA-12 behaviour at low temperatures

For the puncture tests performed at cold temperatures, only textured samples were tested. The temperature was -10 °C while the test speed was 4.4 m/s.

The resulting force – deflection curves show a similar shape as with the tests performed at room temperature (Figure 2.78). All tested specimens got punctured, PA-12 showing ductile behaviour, the condition of the specimens after the test being presented in Figure 2.80.

PA-12's puncture energy remains constant (Table 2.13 and Table 2.14), but the peak force is higher and the deflection at break is lower at cold temperatures (Figure 2.79).

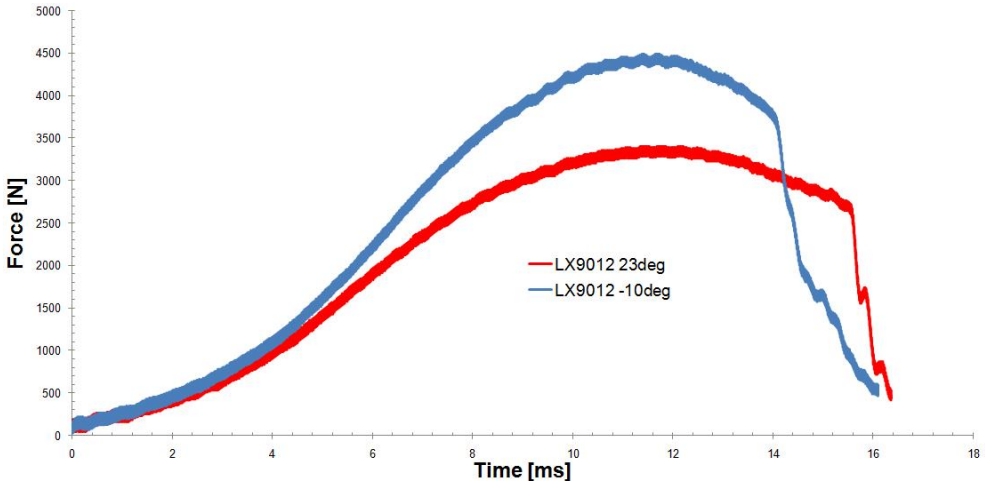

Figure 2.79. Force – deflection curves for tests at two temperatures

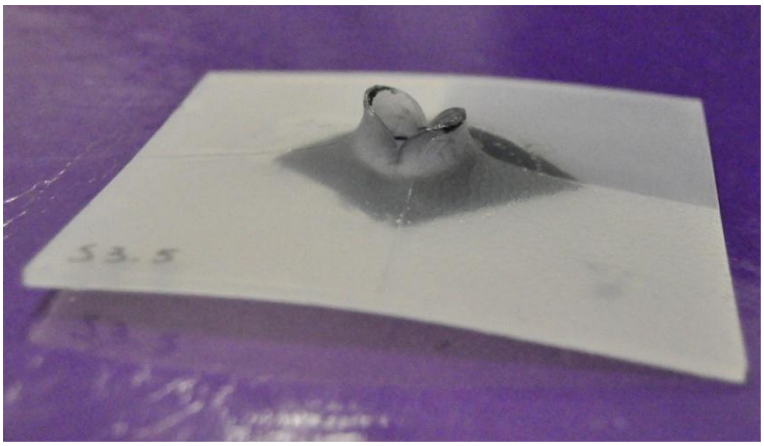

Figure 2.80. Punctured PA-12 sample during low temperature tests

Table 2.14 Puncture energies PA-12 samples tested at low speeds

Specimen	Puncture energy [J]
S3-4	34.76965
S3-5	37.41506
S3-6	37.22823
Average	36.47098

2.4.3.4. Behaviour of PA-12 at low stroke speeds

As with the test performed at low temperatures, for the puncture tests performed at low speeds, only textured samples were tested. The temperature was 23°C while the test speed was 1 m/s.

Due to misprogramming, the entire stroke was not recorded, and no energies could be obtained. The resulting force – deflection curves are pictured in Figure 2.81. None of the specimens were penetrated with these tests parameters.

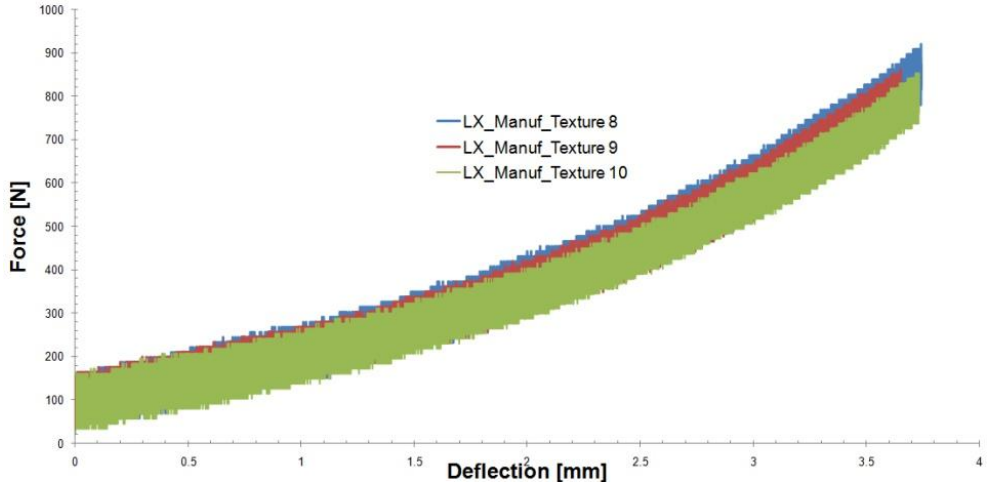

Figure 2.81. Force – deflection curves for tests at low speeds

The PA-12 specimens did not break, but showed a region of plastic deformation where the striker hit. The condition of the specimens after the test is presented in Figure 2.82.

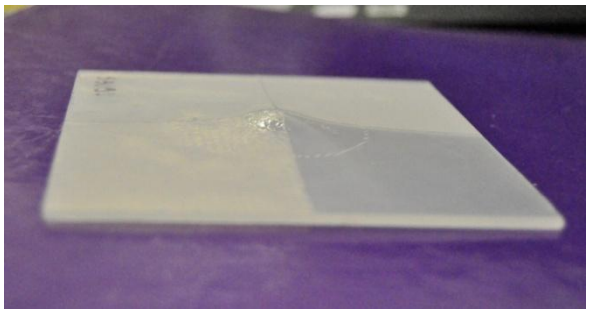

a)

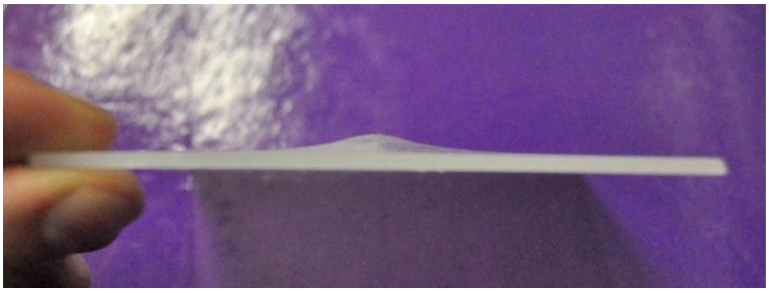

b)

Figure 2.82 Deformed PA-12 sample: a) isometric view; b) side view

2.5. Tests on components

The main application of the studied polyamide in sports footwear is in a component is called 'top plate', which is connected to the upper and houses the Bounce structures. The provided specimens are components of the adidas Titan™ running shoe (Figure 2.83). The aim of the tests was to replicate the deformation mode of the component and thus only the rear cushioning element was compressed (the element that first contacts the ground during a foot strike). The schematic of the testing device is presented in Figure 2.84.

Figure 2.83. adidas Titan™ running shoe

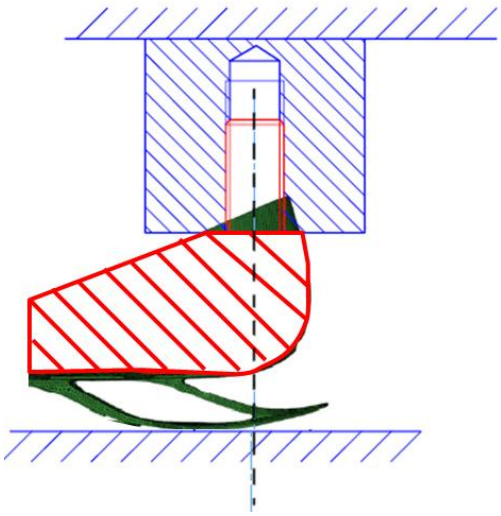

Figure 2.84. Schematic of device for component testing.

In order to aid the tests, an Uriol shoe last was provided which was assembled with the help of a stud screw and intermediary piece to the bottom part of the machine. The top plate was secured on the last with the help of Teflon tape (Figure 2.85).

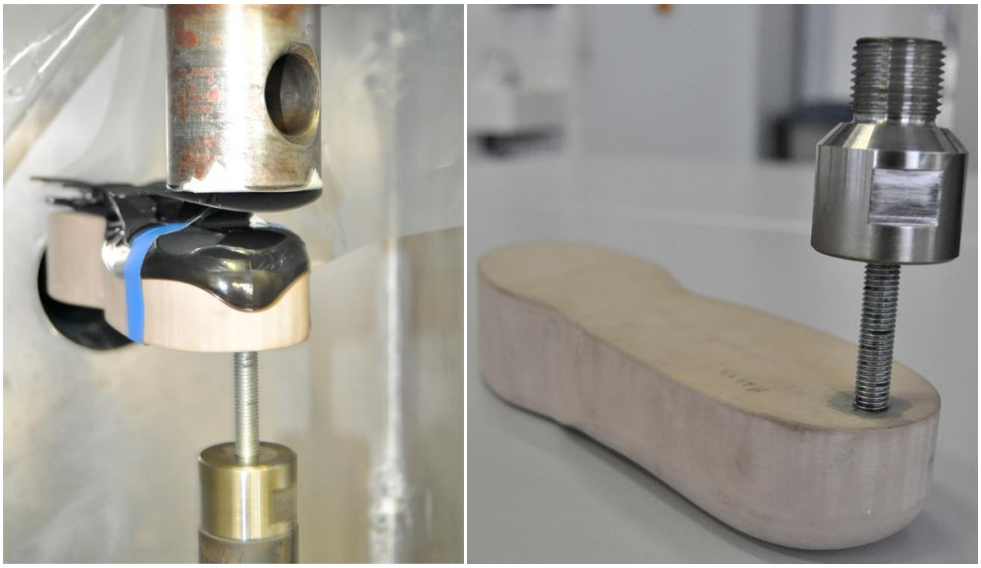

Figure 2.85. Shoe last with adaptation

2.5.1. Compression tests

Compression tests were performed in the Institut für Leichtbau und Kunststofftechnik, Technische Universität Dresden on normal components as well as on conditioned components. Tests on regular top plates were performed at four different crosshead travel speeds, chosen on logarithmical scale: 2 mm/min, 20 mm/min, 200 mm/min and 2000 mm/min (Figure 2.86). Tests on conditioned top plates were performed a two crosshead travel speeds: 2 mm/min and 2000 mm/min.

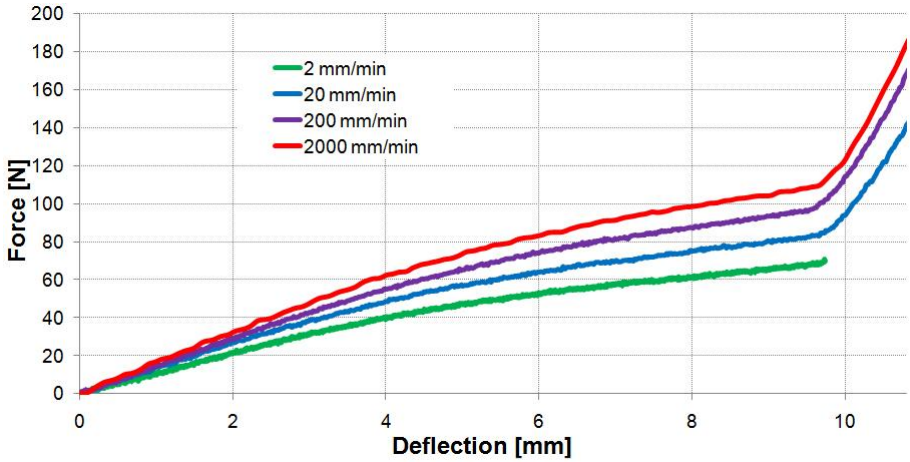

Figure 2.86. Force-deflection curves for compression tests performed on regular components

The force-deflection graphs show two regions: the first region, characterized by a steady increase in reaction is representative for the compression of the

cushioning element. The second region, characterized by an exponential increase in reaction is caused by the "flattening" of the top plate as the cushioning element touches the heel, and the component acts like a solid subjected to compression. An increase in deformation speed from 2 mm/min up to 2000 mm/min (100,000%) determines a 55% increase in reaction force (at the end of the first region), from 70.6 N up to 109.8 N.

The recovery from compression was also recorded (identical crosshead travel speeds). A remnant deformation of about 2 mm can be observed (difference in crosshead travel values for the 0 N point on the force-deflection graph), as seen in Figure 2.87.

In case of conditions components, moisture determines a variation between 21.7% (from 67.8 N down to 53.1 N at 2 mm/min) and 15.9% (from 108 N down to 90.8 N at 2000 mm/min), as seen in Figure 2.88. Also, conditioned specimens show more deformation for the same amount of compression, reaching the second region about 3 mm earlier and determining larger plastic deformation (about 3 mm) in loading-unloading cycles.

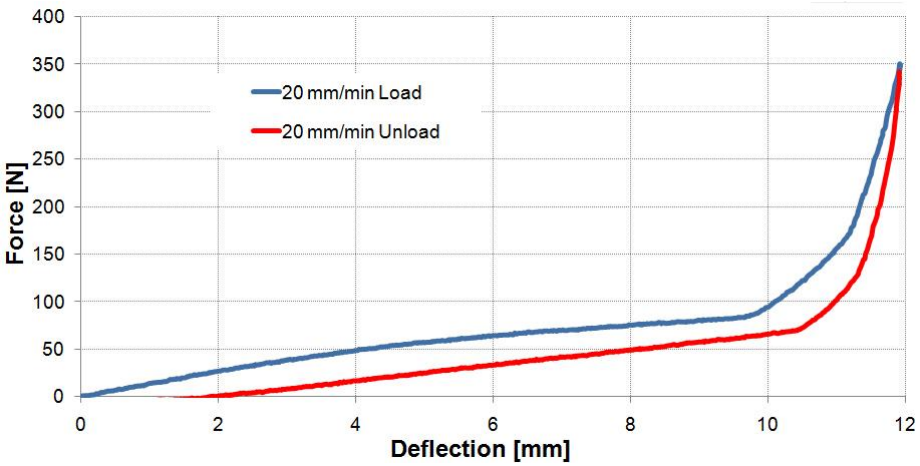

Figure 2.87. Loading-unloading curve for 20 mm/min test on normal components

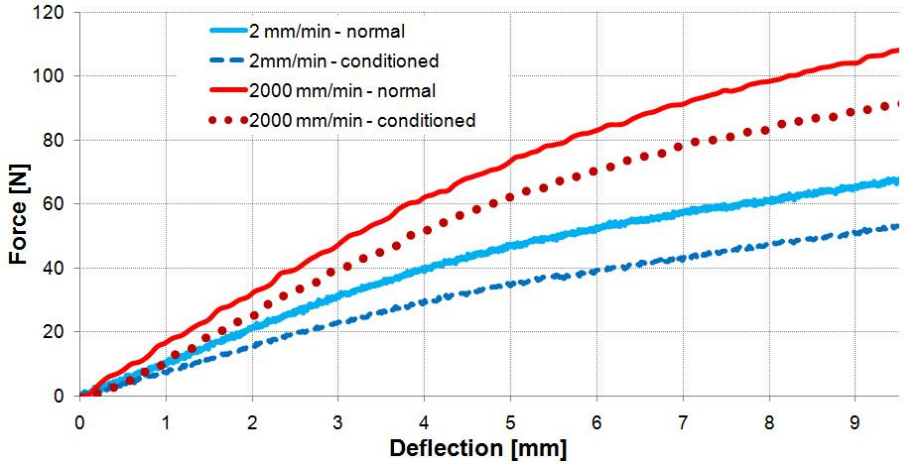

Figure 2.88. Softening effect of moisture on compression tests

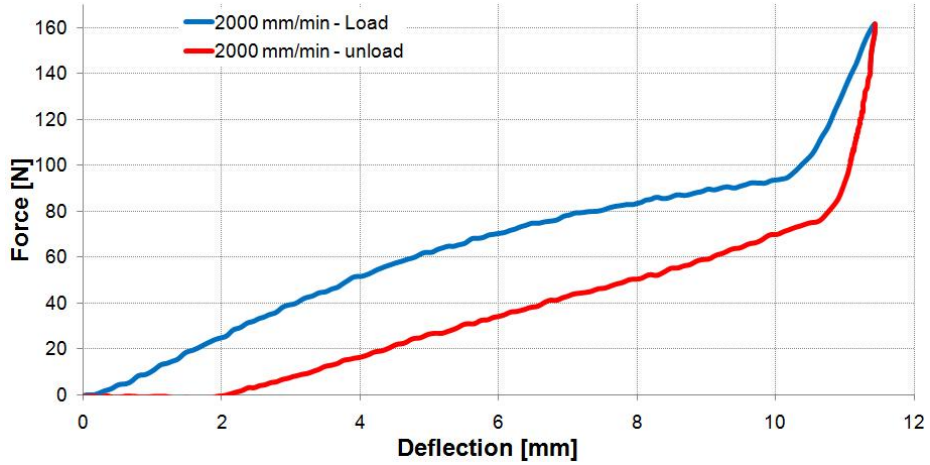

Figure 2.89. Loading-unloading curve for 20 mm/min test on conditioned components

2.5.2. Low-cycle fatigue tests

Low-cycle fatigue tests on normal components were performed with the parameters determined during the LCF tests on dogbone specimens in tension. Thus, the tests were performed at 5 Hz for 5000 cycles. Two levels of deformations were chosen, one situated in the cushioning element compression region, presented in Figure 2.90 (6 mm average deformation, 1.1 mm amplitude) and one situated in the material compression region, presented in Figure 2.91 (9 mm average deformation, 1.1 mm amplitude). After the fatigue tests, a compression test was performed at 20 mm/min. The results for each test, compared with the compression test of a virgin component are presented in Figure 2.92.

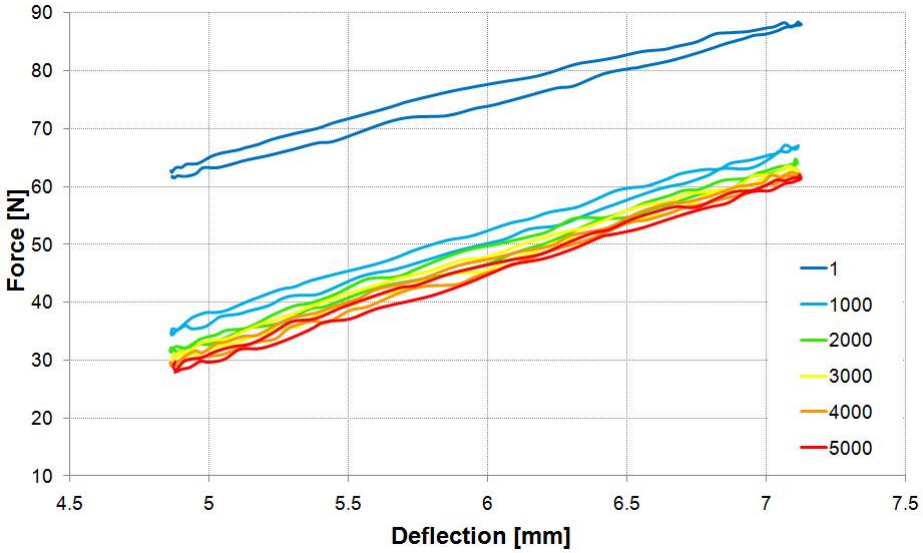

Figure 2.90. LCF tests for normal specimens at 6 mm average deformation

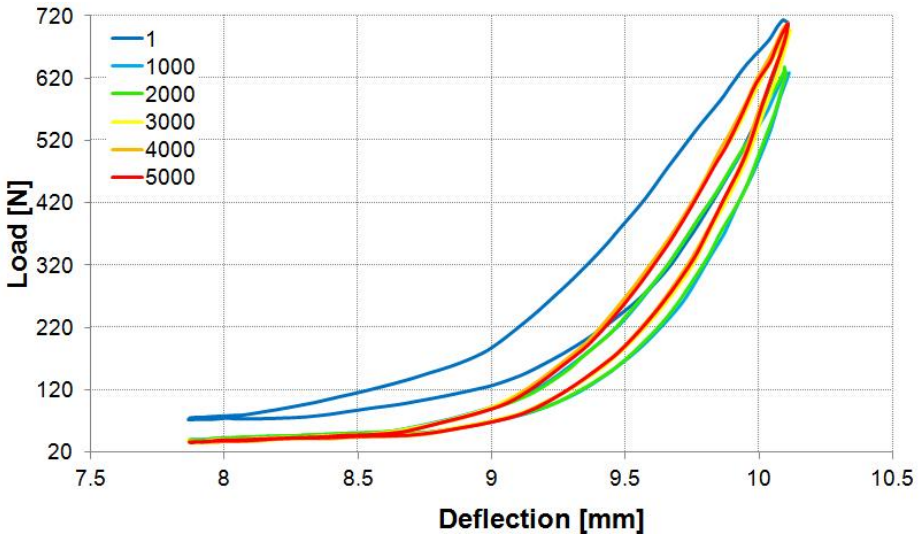

Figure 2.91. LCF tests for normal specimens at 9 mm average deformation

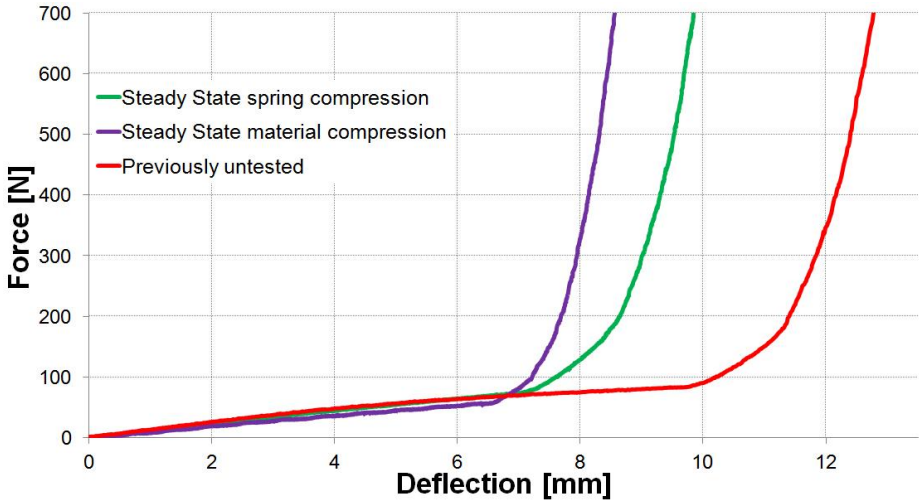

Figure 2.92. Force-deflection diagrams in compression for components in different condition

In the case of LCF tests with amplitudes situated in the cushioning element compression region, behaviour similar to LCF on dogbones was observed: the first cycles determine a significant softening and after the first 1000 cycles, a 23.9% decrease in reaction force is observed, from 90.7 N to 69 N. Between 1000 cycles and 5000 cycles the reaction decreases with only 6.3%, from 69 N down to 64.7 N.

For the tests performed in the cushioning element contact region (material compression), after 1000 cycles, a softening of 11.7% is observed for peak reactions, from 712.8 N to 629.3 N and a softening of 46.8% in the cushioning element compression region for this set of tests (around 8mm, Figure 2.91), from 74.2 N to 39.5 N. As the total number of cycles increases a difference in behaviour

is noticed. The peak force increases after 3000 cycles and is close to the values recorded for the initial tests, even though the reaction in the cushioning element compression region decreases in a decelerated rate (10% softening from 2000 to 5000 cycles, from 39.5 N to 35.2 N). This phenomenon can be explained by analyzing the compression curves in Figure 2.92: due to the accumulation of plastic deformation, the material compression region starts at a lower deflection; the larger the plastic deformation, the lower the deflection at which material compression occurs. So, even though the material is softer in the case of LCF at high deformation after 3000 cycles, it had also accumulated plastic deformation which might be considered the equivalent of shifting the deformation spectrum up the deflection axis.

Low-cycle fatigue tests were also performed on conditioned top plates for 5000 cycles at 5 Hz, 6 mm reference deformation, 1.1 mm amplitude. The results are presented in Figure 2.93. The results are similar and as with the rest of the tests on conditioned specimens, a softening can be observed, in this case, of around 16%. Also, the softening during loading is a bit larger, compared to the normal components: between the first and the 1000th cycle, a softening of 29.5% was observed (from 76.1 N to 53.6 N) and between the 1000th and the 5000th cycle, a softening of 10.7% was observed (from 53.6 N to 43.9 N).

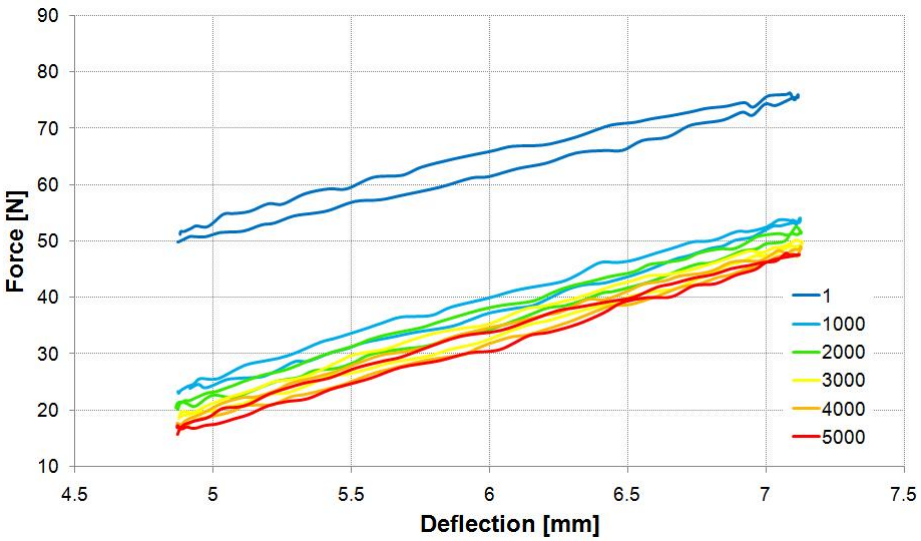

Figure 2.93. LCF tests for conditioned specimens at 6 mm average deformation

2.5.3. Discussion

In uniaxial compression, the top plates appear to be more strain-rate sensitive that dogbone specimens as a 100,000% variation in crosshead travel speed (from 2 mm/min up to 2000 mm/min) determines a 55% increase in reaction force, begin almost twice as large as the variations observed in tension (22% increase) and bending (29% increase).

The same pattern can be observed for tests on conditioned top plates, as they exhibit pronounced softening in comparison to conditioned dogbones tested in tension: for 2 mm/min tests, a decrease in compressive strength of 21% was

recorded, compared to 15% in tension and for 2000 mm/min, a decrease in compressive strength of 16% was recorded, compared to 12% in tension.

The behaviour of top plates subjected to low-cycle fatigue tests in the cushioning element compression region was anticipated in Paragraph 3.3.2 (LCF tests performed on dogbones): for specimens tested in compression immediately after LCF tests, the force – deflection curve is nearly identical with that of a previously untested specimen (there is a very small drop in reaction force) and, due to accumulated time-dependent reversible deformation, the second region associated with cushioning element contact occurs at lower deflections (at 7 mm deflection instead of 9.8 mm for a previously untested specimen, Figure 2.94).

For the low-cycle fatigue tests in the cushioning element contact region, the accumulated permanent deformation affects the behaviour of the component, determining lower reactions in monotone compression (17% decrease) as well as the earlier occurrence of the second region associated with the cushioning element contact (6.5 mm deflection instead of 9.8 mm for a previously untested specimen, Figure 2.94).

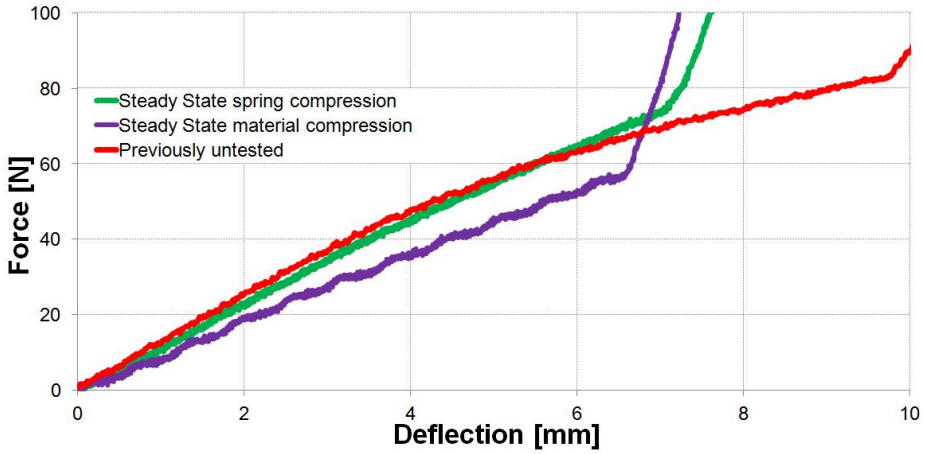

Figure 2.94. Compression force-deflection curves for top plates subjected to various testing conditions

2.6. Conclusions

In contrast to conventional materials such as metals, polymeric materials in general and this modified PA12 in particular exhibit a highly non-linear characteristic. In terms of the stress-strain response, the linear elastic domain is limited to a fraction of a percent in deformation (extending up to around 1% for low temperatures and being virtually nonexistent at high temperatures). Another particularity of polymers is the large strain they can be subjected to before yielding. Coupled with the non-linearity of their stress-strain response, this behaviour has been dubbed 'Hyperelasticity'.

Apart from their hyperelastic nature, several environmental parameters determine significant changes in the material's behaviour. This is due to the polymer's structure which consists of large macromolecules distributed in either an arranged state (crystalline phase) or an in a irregular state (amorphous phase). The

parameter that has the largest influence on mechanical properties is temperature. A change in temperature from 50 °C to -25 °C determines a 410 % increase in Young's modulus (500 MPa to 2550 MPa) and a 185 % increase in tensile strength (20 MPa to 57 MPa). Another parameter which determines significant variations in mechanical properties is time. The short-term effect of time (strain-rate dependency) determines a 64% increase in Youngs modulus (from from 850 MPa at a strain rate of 0.00028 s^{-1} to 1400 MPa at 9.4 s^{-1}) and an 33% increase in tensile strength (from 30 MPa at 0.00028 s^{-1} to 40 MPa at 9.4 s^{-1}). The long term effect of time was studied through cyclic loadings, low-cycle fatigue tests and creep tests. Low-cycle fatigue tests determined a stabilized material behaviour after around 5000 cycles for LCF tests (around 30% softening due to the accumulation of reversible viscous strain). Creep tests determined 4.5 times softer response after 24 hours of constant load. The percentage of humidity present in the material also influences its behaviour, determining around 20% softening.

3. ANALYTICAL MODELS FOR DESCRIBING MATERIAL BEHAVIOUR

3.1. Linear elasticity

In the Annexes, in Chapter II, preliminary notions of mathematics were presented while in Chapter III of the annexes, the equilibrium equations were written in terms of the stresses inside the body, which are the result of the deformations the body is subjected to. Several equations will be recalled in order to aid understating having roman numbering prefix corresponding for the given chapter (II. or III.)

In this paragraph, the stresses are expressed in terms of some measure of deformation, such as strains. These frame invariant (objective) relationships between the stresses inside a body and the deformations that caused them are called *constitutive equations*. They represent a material characteristic and can be influenced by various factors such as time or temperature.

Constitutive equations represent the basis of deformation analysis and are implemented in almost every commercial finite element analysis software [**11**,**62**,**63**].

Materials for which the constitutive behaviour is a function of the current state of deformation are called *elastic materials*. In other words, the stress inside an elastic material is a unique function of the deformation (strain).

3.1.1. Generalized Hooke's Law

The constitutive equations for a generic elastic anisotropic material are given by the so-called *Generalized Hooke's Law*, which establishes a relation between the engineering stress (the first Piola-Kirchhoff stress tensor $\boldsymbol{P}$ (III. 2.38)) and the engineering strain (the Green-Lagrange strain tensor for small deformations $\boldsymbol{e}_{\boldsymbol{G}}^{(l\cong L)}$ (III. 1.39b))

$$\boldsymbol{P} = J\boldsymbol{\sigma}\boldsymbol{F}^{-T} \tag{III. 2.38}$$

$$\boldsymbol{E}_{\boldsymbol{G}}^{(l\cong L)} = \sum_{\mathrm{i,j=1}}^{3} \left(\frac{l_{ij} - L_{ij}}{L_{ij}} \right) e_i \otimes e_j \tag{III. 1.39b}$$

$$\boldsymbol{E}_{\boldsymbol{G}}^{(l\cong L)} = \boldsymbol{a} : \boldsymbol{P} \tag{3.1a}$$

$$\boldsymbol{P} = \boldsymbol{A} : \boldsymbol{E}_{\boldsymbol{G}}^{(l\cong L)} \tag{3.1b}$$

where $\boldsymbol{a}$ is called the compliance tensor and $\boldsymbol{A}$ is called the stiffness tensor ($\boldsymbol{a} = \boldsymbol{A}^{-1}$), and are both fourth order symmetric tensors:

$$a_{abcd} = a_{bacd} = a_{abdc} = a_{cdab} \tag{3.2}$$

It should be noted that by "anisotropic" we refer to the difference in material properties regarding coordinate system *orientation*, while by "non-homogenous" we refer to the difference in material properties regarding coordinate system *location*.

In order to express anisotropy in a more elegant manner, the vector formulation for the stress and strain tensors will be adopted (consisting of a one-dimensional array composed of the non repetitive quantities of the symmetric Green-Cauchy strain tensor and first Piola-Kirchhoff stress tensor, (III. 1.37) and (III. 2.20)):

$$\boldsymbol{\varepsilon} = [e_{11} \quad e_{12} \quad e_{13} \quad e_{23} \quad e_{13} \quad e_{12}]^T \tag{3.3a}$$

$$\boldsymbol{\sigma} = [P_{11} \quad P_{12} \quad P_{13} \quad P_{23} \quad P_{13} \quad P_{12}]^T \tag{3.3b}$$

$$\boldsymbol{\varepsilon} = \boldsymbol{a} \cdot \boldsymbol{\sigma} \tag{3.4a}$$

$$\boldsymbol{\sigma} = \boldsymbol{A} \cdot \boldsymbol{\varepsilon} \tag{3.4b}$$

Following the above formulation, the compliance and elasticity tensors convert from fourth order tensors to 6 x 6 square symmetric matrices.

3.1.2. Types of elastic materials

3.1.2.1. General anisotropic materials

The most general type of anisotropic material is called the *triclinic material*. The compliance matrix has 21 distinct coefficients [**64**]:

$$\boldsymbol{a} = \begin{bmatrix} a_{11} & a_{12} & a_{13} & a_{14} & a_{15} & a_{16} \\ & a_{22} & a_{23} & a_{24} & a_{25} & a_{26} \\ & & a_{33} & a_{34} & a_{35} & a_{36} \\ & Symm & & a_{44} & a_{45} & a_{46} \\ & & & & a_{55} & a_{56} \\ & & & & & a_{66} \end{bmatrix} \tag{3.5}$$

The terms a_{ij} are called *elastic moduli* and represent the constitutive relations between the stress component over a given direction and its corresponding strain. General anisotropic materials exist only in theory, as all materials found in nature exhibit some symmetry regarding the material properties over different loading directions.

3.1.2.2. Monoclinic materials

Monoclinic materials contain one plane of symmetry and thus they have only 13 independent coefficients. A monoclinic material with symmetry over the $x0y$ plane is characterized by the following compliance matrix [**64**]:

$$\boldsymbol{a} = \begin{bmatrix} a_{11} & a_{12} & a_{13} & 0 & 0 & a_{16} \\ & a_{22} & a_{23} & 0 & 0 & a_{26} \\ & & a_{33} & 0 & 0 & a_{36} \\ & Symm & & a_{44} & a_{45} & 0 \\ & & & & a_{55} & 0 \\ & & & & & a_{66} \end{bmatrix} \tag{3.6}$$

3.1.2.3. Orthotropic materials

Orthotropic materials have three orthogonal planes of elastic symmetry and thus they are defined by 9 independent coefficients. The compliance matrix' coefficients can be expressed in terms of the engineering values: Young's Modulus E, shear modulus G and Poisson coefficient υ [**64**].

$$\boldsymbol{a} = \begin{bmatrix} \frac{1}{E_{11}} & -\frac{\upsilon_{21}}{E_{22}} & -\frac{\upsilon_{31}}{E_{33}} & 0 & 0 & 0 \\ -\frac{\upsilon_{12}}{E_{11}} & \frac{1}{E_{22}} & -\frac{\upsilon_{32}}{E_{33}} & 0 & 0 & 0 \\ -\frac{\upsilon_{13}}{E_{11}} & -\frac{\upsilon_{23}}{E_{22}} & \frac{1}{E_{33}} & 0 & 0 & 0 \\ 0 & 0 & 0 & \frac{1}{G_{23}} & 0 & 0 \\ 0 & 0 & 0 & 0 & \frac{1}{G_{13}} & 0 \\ 0 & 0 & 0 & 0 & 0 & \frac{1}{G_{12}} \end{bmatrix} \tag{3.7}$$

3.1.2.4. Tetragonal materials

Tetragonal materials are orthogonal materials which have a pair of coordinate directions for which the elastic properties are identical [**64**]:

$$\begin{gathered} E_{11} = E_{22} = E; \quad E_{33} = E' \\ G_{23} = G_{13} = G; \quad G_{12} = G' \\ \nu_{12} = \nu_{21} = \nu; \quad \nu_{13} = \nu_{23} = \nu' \frac{E}{E'}; \quad \nu_{12} = \nu_{21} = \nu' \end{gathered} \tag{3.8}$$

$$\boldsymbol{a} = \begin{bmatrix} \frac{1}{E} & -\frac{\upsilon}{E} & -\frac{\upsilon'}{E'} & 0 & 0 & 0 \\ & \frac{1}{E} & -\frac{\upsilon'}{E'} & 0 & 0 & 0 \\ & & \frac{1}{E'} & 0 & 0 & 0 \\ & & & \frac{1}{G} & 0 & 0 \\ & Symm & & 0 & \frac{1}{G} & 0 \\ & & & 0 & 0 & \frac{1}{G} \end{bmatrix} \tag{3.9}$$

3.1.2.5. Cubic materials

Cubic materials are a special case of tetragonal materials that have only three independent parameters

$$\begin{aligned} E_{11} &= E_{22} = E_{33} = E \\ G_{12} &= G_{23} = G_{13} = G \\ \nu_{12} &= \nu_{13} = \nu_{23} = \nu \end{aligned} \tag{3.10}$$

$$\begin{bmatrix} \frac{1}{E} & -\frac{\upsilon}{E} & -\frac{\upsilon}{E} & 0 & 0 & 0 \\ & \frac{1}{E} & -\frac{\upsilon}{E} & 0 & 0 & 0 \\ & & \frac{1}{E} & 0 & 0 & 0 \\ - & - & - & \frac{1}{G} & 0 & 0 \\ - & Symm & - & 0 & \frac{1}{G} & 0 \\ - & - & - & 0 & 0 & \frac{1}{G} \end{bmatrix} \tag{3.11}$$

3.1.2.6. Isotropic materials

Isotropic materials are the materials with the most particular characteristic. They are dependent on only 2 parameters, Young's modulus and the Poisson coefficient. Consequently, they obey the Poisson transformations [**64**]:

$$G = \frac{E}{2 \cdot (1 + \upsilon)} \tag{3.12a}$$

$$K = \frac{E}{3 \cdot (1 - 2\upsilon)} \tag{3.12b}$$

where G is the shear modulus and K is the bulk modulus. Note that for $= 1/2$, $K = \infty$, which is another particular case, the incompressible isotropic material.

The compliance matrix for the isotropic materials will be [**64**]:

$$\boldsymbol{a} = \frac{1}{E}\begin{bmatrix} 1 & -\upsilon & -\upsilon & 0 & 0 & 0 \\ & 1 & -\upsilon & 0 & 0 & 0 \\ & & 1 & 0 & 0 & 0 \\ & & & 2\cdot(1+\upsilon) & 0 & 0 \\ & Symm & & 0 & 2\cdot(1+\upsilon) & 0 \\ & & & 0 & 0 & 2\cdot(1+\upsilon) \end{bmatrix} \tag{3.13}$$

3.2. Hyperelasticity

In the previous paragraph elastic materials were defined as materials for which the constitutive equations are only a function of the current state of deformation. In contrast, for hyperelastic materials, the constitutive equations are only dependent on the initial state at a time $t = t_0$ and on the final state at time t. This implies that the constitutive behaviour is path independent. Equation (III. 2.37)

$$\delta W_\epsilon = \int_V (J\boldsymbol{\sigma}\boldsymbol{F}^{-T}) : \delta\frac{d\boldsymbol{F}}{dt}dV \qquad (\boldsymbol{P} = J\boldsymbol{\sigma}\boldsymbol{F}^{-T}) \tag{III. 2.37}$$

states that the first Piola-Kirchhoff strain tensor is work conjugate with the rate of deformation gradient. Considering the path independency property of the hyperelastic materials, a *strain-energy density function* also called *stored elastic potential* Ψ can be defined as a function of the deformation gradient and of the initial configuration $\boldsymbol{X}$ (to account for an eventual non-homogenous material) [**11**]:

$$\Psi(\boldsymbol{F}(\boldsymbol{X}),\boldsymbol{X}) = \int_{t_0}^{t} \boldsymbol{P}(\boldsymbol{F}(\boldsymbol{X}),\boldsymbol{X}) : \frac{d\boldsymbol{F}}{dt}dt, \qquad \frac{d\Psi}{dt} = \boldsymbol{P} : \frac{d\boldsymbol{F}}{dt} \tag{3.14}$$

If we use de inverse approach, to try to construct the strain-energy density function from experimental data, its rate of change will be [**11**]:

$$\frac{d\Psi}{dt} = \sum_{i,J=1}^{3} \frac{\partial\Psi}{\partial F_{iJ}} \cdot \frac{d\boldsymbol{F}}{dt} \tag{3.15}$$

Comparing equations (3.14) with (3.15), the components of the first Piola-Kirchhoff stress tensor $\boldsymbol{P}$ will be [**11**]:

$$P_{iJ} = \frac{\partial\Psi}{\partial F_{iJ}} \tag{3.16}$$

$$\boldsymbol{P}(\boldsymbol{F}(\boldsymbol{X}),\boldsymbol{X}) = \frac{\partial\Psi(\boldsymbol{F}(\boldsymbol{X}),\boldsymbol{X})}{\partial\boldsymbol{F}} \tag{3.17}$$

Equations (3.14) and (3.17) are the constitutive relations used to describe a hyperelastic material.

Considering the restrictions imposed by the objectivity conditions, other formulations of the strain-energy density functions can be obtained. Thus, Ψ must remain invariant under rigid body motion and it will be dependent on the distortional component $\boldsymbol{U}$ of the deformation gradient and independent on the rotational

component $\boldsymbol{R}$. Recalling the expression of the left Cauchy-Green strain tensor $\boldsymbol{C}$ (III. 1.15)**,** the strain energy density function can be expressed as [**11**]:

$$\boldsymbol{C} = \boldsymbol{F}^T\boldsymbol{F} \tag{III. 1.15}$$

$$\Psi(\boldsymbol{F}(\boldsymbol{X}), \boldsymbol{X}) = \Psi(\boldsymbol{C}(\boldsymbol{X}), \boldsymbol{X}) \tag{3.18}$$

Observing the relations between the derivative of the Green-Lagrange strain tensor $\boldsymbol{E_G}$ and the left Cauchy-Green strain tensor $\boldsymbol{C}$ (III. 1.72), a complete Lagrangian formulation (material description) can be written, considering that the second Piola-Kirchhoff stress tensor $\boldsymbol{S}$ is work conjugate with $\boldsymbol{E}$ (III. 2.48) [**11**]:

$$\frac{d\boldsymbol{E_G}}{dt} = \frac{1}{2}\frac{d\boldsymbol{C}}{dt} \tag{III. 1.73}$$

$$\delta W_\epsilon = \int_V \boldsymbol{S}\!:\!\frac{\partial \boldsymbol{E_G}}{\partial t} dV \tag{III. 2.48}$$

$$\frac{d\Psi}{dt} = \frac{\partial \Psi}{\partial \boldsymbol{C}}\!:\!\frac{d\boldsymbol{C}}{dt} = \frac{1}{2}\boldsymbol{S}\!:\!\frac{d\boldsymbol{C}}{dt} \tag{3.19a}$$

$$\boldsymbol{S}(\boldsymbol{C}(\boldsymbol{X}), \boldsymbol{X}) = 2\frac{\partial \Psi}{\partial \boldsymbol{C}} = \frac{\partial \Psi}{\partial \boldsymbol{E_G}} \tag{3.19b}$$

3.2.1. Elasticity tensors

3.2.1.1. The Lagrangian elasticity tensor

The nonlinear relation between the second Piola-Kirchhoff stress tensor $\boldsymbol{S}$ and the left Cauchy-Green tensor $\boldsymbol{C}$ or the Green-Lagrange strain tensor $\boldsymbol{E_G}$ must be linearized with respect to a increment $\boldsymbol{u}$ in the current configuration. A linear relationship between the directional derivative of the Piola-Kirchhoff stress tensor $\boldsymbol{S}$ and the linearized strain $D\boldsymbol{E}[\boldsymbol{u}]$ can be obtained using the chain rule [**11**]:

$$DS_{IJ}[\boldsymbol{u}] = \frac{d}{d\epsilon}\Big|_{\epsilon=0} S_{IJ}(E_{KL}[\phi + \epsilon\boldsymbol{u}]) = \sum_{K,L=1}^{3} \frac{\partial S_{IJ}}{\partial E_{KL}} DE_{KL}[\boldsymbol{u}] \tag{3.20}$$

Another way to express the relationship between the directional derivative of the second Piola-Kirchhoff stress tensor $\boldsymbol{S}$ and the directional derivative of the Green-Lagrange strain tensor $\boldsymbol{E_G}$ is through the help of a fourth order tensor called the Lagrangian or material elasticity tensor $\boldsymbol{\mathcal{C}}$ [**11**]:

$$D\boldsymbol{S}[\boldsymbol{u}] = \boldsymbol{\mathcal{C}} : D\boldsymbol{E_G}[\boldsymbol{u}] \tag{3.21}$$

where

$$\boldsymbol{\mathcal{C}} = \sum_{I,J,K,L=1}^{3} \mathcal{C}_{IJKL}\boldsymbol{E}_I \otimes \boldsymbol{E}_J \otimes \boldsymbol{E}_K \otimes \boldsymbol{E}_L \tag{3.22a}$$

$$\mathcal{C}_{IJKL} = \sum_{I,J,K,L=1}^{3} \frac{\partial S_{IJ}}{\partial E_{KL}} \boldsymbol{E}_I \otimes \boldsymbol{E}_J \otimes \boldsymbol{E}_K \otimes \boldsymbol{E}_L = \frac{4\partial^2 \Psi}{\partial C_{IJ} \partial C_{KL}} = \boldsymbol{\mathcal{C}}_{KLIJ} \tag{3.22b}$$

The Lagrangian elasticity tensor can also be expressed in a more abbreviated manner:

$$\boldsymbol{\mathcal{C}} = \frac{\partial \boldsymbol{S}}{\partial \boldsymbol{E}_G} = 2\frac{\partial \boldsymbol{S}}{\partial \boldsymbol{C}} = \frac{4\partial^2 \Psi}{\partial \boldsymbol{C} \partial \boldsymbol{C}} \tag{3.23}$$

3.2.1.2. The Eulerian elasticity tensor

A spatial description of the elasticity tensor must also be considered. This is achieved by linearizing the second Piola-Kirchhoff stress tensor $\boldsymbol{S}$ and the Green-Lagrange strain tensor $\boldsymbol{E_G}$ in the direction of the velocity $\boldsymbol{v}$ rather than in the direction of an arbitrary vector $\boldsymbol{u}$. It can be demonstrated that [**11**]:

$$D\boldsymbol{S}[\boldsymbol{v}] = \frac{d\boldsymbol{S}}{dt} \tag{3.24a}$$

$$D\boldsymbol{E_G}[\boldsymbol{v}] = \frac{d\boldsymbol{E_G}}{dt} \tag{3.24b}$$

Analogue to (3.21), the relationship between $D\boldsymbol{S}[\boldsymbol{v}]$ and $D\boldsymbol{E_G}[\boldsymbol{v}]$ will be :

$$\frac{d\boldsymbol{S}}{dt} = \boldsymbol{\mathcal{C}} : \frac{d\boldsymbol{E_G}}{dt} \tag{3.25}$$

Recalling equations (III. 1.58a) and (III. 2.58)

$$\boldsymbol{d} = \phi_* \left[\frac{d\boldsymbol{E}}{dt}\right] \tag{III. 1.76a}$$

$$\boldsymbol{\sigma}^{\circ} = J^{-1}\phi_* \left[\frac{d\boldsymbol{S}}{dt}\right] \tag{III. 2.58}$$

and consequently pushing forward equation (3.25) will yield:

$$\boldsymbol{\sigma}^{\circ} = \boldsymbol{c} : \boldsymbol{d} \tag{3.26}$$

where $\boldsymbol{c}$ represents the Eulerian or spatial elasticity tensor, defined as the push forward of the Lagrangian elasticity tensor $\boldsymbol{\mathcal{C}}$ [**11**]:

$$\boldsymbol{c} = J^{-1}\phi_*[\boldsymbol{\mathcal{C}}] \tag{3.27}$$

After some algebra, the coefficients of the Eulerian elasticity tensor $\boldsymbol{c}$ will be [**11**]:

$$\boldsymbol{c} = \sum_{\substack{I,J,K,L=1 \\ i,j,k,l=1}}^{3} J^{-1} F_{iI} F_{jJ} F_{kK} F_{lL} C_{IJKL} \boldsymbol{e}_i \otimes \boldsymbol{e}_j \otimes \boldsymbol{e}_k \otimes \boldsymbol{e}_l \tag{3.28}$$

Equation (3.27) is considered to be the fundamental constitutive equation for hyperelastic material behaviour. However, the use of such an approach will not guarantee hyperelastic behaviour as stresses cannot be obtained directly from the elastic potential, case in which the rate equation must be integrated with respect to time (yielding significant difficulties in finite element analysis).

3.2.2. Isotropic Hyperelasticity

The constitutive equations described in the previous paragraph are unrestricted in their application. A particular case (and the most commonly used) of hyperelastic materials is the isotropic hyperelastic material. This implies that the strain-energy density function is only dependent on the three invariants of the left Cauchy-Green tensor $\boldsymbol{C}$ [**11**]:

$$\Psi(\boldsymbol{C}(\boldsymbol{X}),\boldsymbol{X}) = \Psi(I_{\boldsymbol{C}}, II_{\boldsymbol{C}}, III_{\boldsymbol{C}}, \boldsymbol{X}) \tag{3.29}$$

where

$$I_{\boldsymbol{C}} = \mathrm{tr}\boldsymbol{C} = \boldsymbol{C}:\boldsymbol{I} \tag{3.30a}$$
$$II_{\boldsymbol{C}} = \mathrm{tr}\boldsymbol{C}\boldsymbol{C} = \boldsymbol{C}:\boldsymbol{C} \tag{3.30b}$$
$$III_{\boldsymbol{C}} = \det\boldsymbol{C} = J^2 \tag{3.30c}$$

In consequence, equation (III. 3.19b) can be rewritten as [**11**]:

$$\boldsymbol{S}(\boldsymbol{C}(\boldsymbol{X}),\boldsymbol{X}) = 2\frac{\partial\Psi}{\partial\boldsymbol{C}} = 2\frac{\partial\Psi}{\partial I_{\boldsymbol{C}}}\cdot\frac{\partial I_{\boldsymbol{C}}}{\partial\boldsymbol{C}} + 2\frac{\partial\Psi}{\partial II_{\boldsymbol{C}}}\cdot\frac{\partial II_{\boldsymbol{C}}}{\partial\boldsymbol{C}} + 2\frac{\partial\Psi}{\partial III_{\boldsymbol{C}}}\cdot\frac{\partial III_{\boldsymbol{C}}}{\partial\boldsymbol{C}} \tag{3.31}$$

The derivatives of the invariants with respect to the left Cauchy-Green tensor $\boldsymbol{C}$ can be evaluated in component form [**11**]:

$$\frac{\partial}{\partial C_{IJ}}\sum_{K=1}^{3} C_{KK} = \delta_{IJ}; \qquad \frac{\partial I_{\boldsymbol{C}}}{\partial\boldsymbol{C}} = \boldsymbol{I} \tag{3.32a}$$

$$\frac{\partial}{\partial C_{IJ}}\sum_{K,L=1}^{3} C_{KL}C_{KL} = 2C_{IJ}; \qquad \frac{\partial II_{\boldsymbol{C}}}{\partial\boldsymbol{C}} = 2\boldsymbol{C} \tag{3.32b}$$

The derivative of the third invariant is most commonly evaluated using the directional derivative of the determinant of a tensor.

Consider an arbitrary increment tensor $\Delta\boldsymbol{C}$ of the left Cauchy-Green strain tensor $\boldsymbol{C}$ as:

$$\det(\boldsymbol{C}+\Delta\boldsymbol{C}) = \det\boldsymbol{C} + D\det(\boldsymbol{C})\,[\Delta\boldsymbol{C}] \tag{3.33}$$

Considering equation (3.14) the eigenvalues $\lambda_1^{\boldsymbol{C}^{-1}\Delta\boldsymbol{C}}, \lambda_2^{\boldsymbol{C}^{-1}\Delta\boldsymbol{C}}, \lambda_3^{\boldsymbol{C}^{-1}\Delta\boldsymbol{C}}$ of the product $\boldsymbol{C}^{-1}\Delta\boldsymbol{C}$ and recalling the definition and properties of the trace of a tensor (II. 2.30) and (II. 2.31), the directional derivative of $\boldsymbol{C}$ can be expressed as [**11**]:

$$I_{\boldsymbol{S}} = \mathrm{tr}(\boldsymbol{S}) = \sum_{i=1}^{3} S_{ii} = S_{11} + S_{22} + S_{33} \tag{II. 2.30}$$

$$\mathrm{tr}(v \otimes w) = v \cdot w \qquad (\mathrm{II}.2.31a)$$
$$\mathrm{tr}(\boldsymbol{S})^T = \mathrm{tr}(\boldsymbol{S}) \qquad (\mathrm{II}.2.31b)$$
$$\mathrm{tr}(\boldsymbol{S}_1\boldsymbol{S}_2) = \mathrm{tr}(\boldsymbol{S}_2\boldsymbol{S}_1) \qquad (\mathrm{II}.2.31c)$$

$$\left.\frac{d}{d\epsilon}\right|_{\epsilon=0} \boldsymbol{\mathcal{F}}(\mathbf{x}_0 + \epsilon\mathbf{u}) = D\boldsymbol{\mathcal{F}}(\mathbf{x}_0)[\mathbf{u}] \qquad (\mathrm{II}.3.14)$$

$$DIII_C[\Delta\boldsymbol{C}] = \det\boldsymbol{C}\,(\boldsymbol{C}^{-1}\!:\Delta\boldsymbol{C}) \qquad (3.34)$$

Note that the directional derivative with respect to an arbitrary increment tensor $\Delta\boldsymbol{C}$ is related to the partial derivatives via

$$DIII_C[\Delta\boldsymbol{C}] = \sum_{I,J=1}^{3} \frac{\partial III_{\boldsymbol{C}}}{\partial C_{IJ}}\Delta C_{IJ} = \frac{\partial III_{\boldsymbol{C}}}{\partial \boldsymbol{C}} : \Delta\boldsymbol{C} \qquad (3.35)$$

For any arbitrary increment $\Delta\boldsymbol{C}$ from equations (3.34) and (3.55) it results that [**11**]:

$$\frac{\partial III_{\boldsymbol{C}}}{\partial \boldsymbol{C}} = J^2\boldsymbol{C}^{-1} \qquad (3.36)$$

Introducing equations $(3.29a)$, $(3.29b)$ and (3.33) in equation (3.28), the second Piola-Kirchhoff stress tensor can be expressed as [**11**]:

$$\boldsymbol{S} = 2\Psi_I\boldsymbol{I} + 4\Psi_{II}\boldsymbol{C} + 2J^2\Psi_{III}\boldsymbol{C}^{-1} \qquad (3.37)$$

where $\Psi_I = \frac{\partial\Psi}{\partial I_C}$, $\Psi_{II} = \frac{\partial\Psi}{\partial II_C}$, $\Psi_{III} = \frac{\partial\Psi}{\partial III_C}$.

In engineering design applications the spatial description is required in order to obtain the true (Cauchy) stress $\boldsymbol{\sigma}$, which can be derived from the second Piola-Kirchhoff (III. 3.34) stress tensor by recalling equations for the right Cauchy-Green deformation tensor $(\mathrm{III}.1.19b)$ and for the Cauchy stress $(\mathrm{III}.2.50b)$ [**11**]:

$$\boldsymbol{B} = \boldsymbol{F}\boldsymbol{F}^T \qquad (\mathrm{III}.1.19b)$$
$$\boldsymbol{\sigma} = J^{-1}\boldsymbol{F}\boldsymbol{S}\boldsymbol{F}^T \qquad (\mathrm{III}.2.50b)$$
$$\boldsymbol{\sigma} = 2J^{-1}\Psi_I\boldsymbol{B} + 4J^{-1}\Psi_{II}\boldsymbol{B}^2 + 2J\Psi_{III}\boldsymbol{I} \qquad (3.38)$$

In the above relation Ψ_I, Ψ_{II} and Ψ_{III} involve partial derivatives with respect to the components of the left Cauchy-Green deformation tensor $\boldsymbol{C}$. However, by recalling the properties of the trace of a tensor, it can be demonstrated the components of $\boldsymbol{C}$ are identical with the components of the right Cauchy-Green deformation tensor $\boldsymbol{B}$.

3.2.3. Isotropic elasticity in principal direction

3.2.3.1. Spatial description

In the case of experimental determination material parameters, the constitutive equations of the material must be presented in terms of the stretches $\lambda_1, \lambda_2, \lambda_3$ along the principal directions $\boldsymbol{N}_1, \boldsymbol{N}_2, \boldsymbol{N}_3$, i.e. the stored elastic function Ψ should be a function of λ_α instead of the left Cauchy-Green tensor $\boldsymbol{C}$.

There are three components of the second Piola-Kirchhoff stress tensor (equation 3.37) that need to be expressed in terms of the stretches λ_α: the identity tensor $\boldsymbol{I}$, the left Cauchy-Green strain tensor $\boldsymbol{C}$ and its inverse $\boldsymbol{C}^{-1}$. $\boldsymbol{I}$ can be expressed as a dyadic product of the element vectors while $\boldsymbol{C}$ and $\boldsymbol{C}^{-1}$ can be formulated with the help of equation (III. 1.43) [**11**].

$$\boldsymbol{I} = \sum_{\alpha=1}^{3} N_\alpha \otimes N_\alpha \tag{3.39a}$$

$$\boldsymbol{C} = \sum_{\alpha=1}^{3} \lambda_\alpha^2 N_\alpha \otimes N_\alpha \tag{3.39b}$$

$$\boldsymbol{C}^{-1} = \sum_{\alpha=1}^{3} \lambda_\alpha^{-2} N_\alpha \otimes N_\alpha \tag{3.39c}$$

Substituting equations (3.39) in equation (3.37) yields:

$$\boldsymbol{S} = \sum_{\alpha=1}^{3} (2\Psi_I + 4\Psi_I I \lambda_\alpha^2 + 2J^2 \Psi_{III} \lambda_\alpha^{-2}) N_\alpha \otimes N_\alpha \tag{3.40}$$

Given the fact that in the above equation, the term in the brackets is a scalar, it results that for isotropic hyperelastic materials, the principal directions for the stress and the strain coincide. Recalling that Ψ_I, Ψ_{II} and Ψ_{III} are the derivatives of the stored elastic potential Ψ with respect to the invariants of the left Cauchy-Green strain tensor $I_{\boldsymbol{C}}, II_{\boldsymbol{C}}, III_{\boldsymbol{C}}$ (equation (3.37)).

Noting that the square of the stretches λ_α^2 are eigenvalues for the left Cauchy-Green strain tensor $\boldsymbol{C}$, equations $(\text{II. } 2.47 - 49)$ can be introduced to define the invariants of $\boldsymbol{C}$ with respect to the stretches λ_α [**11**]:

$$I_{\boldsymbol{C}} = \lambda_1^2 + \lambda_2^2 + \lambda_3^2 \tag{3.41a}$$

$$II_{\boldsymbol{C}} = \lambda_1^4 + \lambda_2^4 + \lambda_3^4 \tag{3.41b}$$

$$III_{\boldsymbol{C}} = \lambda_1^2 \lambda_2^2 \lambda_3^2 \tag{3.41c}$$

Differentiating equations (3.41) with respect to λ_α^2 yields:

$$\frac{\partial I_{\boldsymbol{C}}}{\partial \lambda_\alpha^2} = 1 \tag{3.42a}$$

$$\frac{\partial II_{\boldsymbol{C}}}{\partial \lambda_\alpha^2} = 2\lambda_\alpha^2 \tag{3.42b}$$

$$\frac{\partial III_{\boldsymbol{C}}}{\partial \lambda_\alpha^2} = \frac{III_{\boldsymbol{C}}}{\lambda_\alpha^2} \tag{3.42c}$$

Introducing equations (III. 3.41) in equation (III. 3.40) and using the chain rule gives [**11**]:

$$\boldsymbol{S} = \sum_{\alpha=1}^{3} 2\frac{\partial \Psi}{\lambda_\alpha^2} N_\alpha \otimes N_\alpha \tag{3.43}$$

3.2.3.2. Material description

In order to obtain an equation analogous to the above expression, equation (3.43) is introduced in equation (III. 2.50b), resulting [**11**]:

$$\boldsymbol{\sigma} = J^{-1}\boldsymbol{F}\boldsymbol{S}\boldsymbol{F}^T = \boldsymbol{S} = \sum_{\alpha=1}^{3} \frac{2}{J}\frac{\partial \Psi}{\lambda_\alpha^2}(\boldsymbol{F}N_\alpha)\otimes(\boldsymbol{F}N_\alpha) \tag{3.44}$$

Considering that the polar decomposition of the deformation gradient yields that $\boldsymbol{F}N_\alpha = \lambda_\alpha n_\alpha$, equation (3.44) becomes [**11**]:

$$\boldsymbol{\sigma} = \sum_{\alpha=1}^{3} \sigma_{\alpha\alpha} \cdot n_\alpha \otimes n_\alpha, \qquad \sigma_{\alpha\alpha} = \frac{\lambda_\alpha}{J}\frac{\partial \Psi}{\lambda_\alpha^2} = \frac{2}{J}\frac{\partial \Psi}{\partial \ln \lambda_\alpha} \tag{3.45}$$

3.2.4. Hyperelastic functions

3.2.4.1. Polynomial model, n=1 (Mooney-Rivlin material)

Considering isotropic hyperelasticity in the principal directions, the strain-energy density function can be expressed as [**62**]:

$$\Psi = \sum_{i+j=1}^{n} (I_{\boldsymbol{C}} - 3)^i (II_{\boldsymbol{C}} - 2)^j + \sum_{i=0}^{m} \frac{1}{D_i}(J_{el} - 1)^{2i} \tag{3.46}$$

where the second term accounts for compressibility. If $D_1 = 0$ then the material is considered incompressible. J_{el} represents the elastic volume strain [**62**].

For $n = 1$, the Mooney-Riving material is obtained [**13**]:

$$\Psi = \sum_{i+j=1}^{2} C_{ij}(I_{\boldsymbol{C}} - 3)^i (II_{\boldsymbol{C}} - 3)^j + \sum_{i=1}^{1} \frac{1}{D_i}(J_{el} - 1)^{2i} \tag{3.47}$$

$$\Psi = C_{10}(I_{\boldsymbol{C}} - 3) + C_{01}(II_{\boldsymbol{C}} - 3) + \frac{1}{D_1}(J_{el} - 1)^2 \tag{3.48}$$

3.2.4.2. Reduced polynomial model, n=1 (Neo-Hookean material)

The reduced polynomial model is neglects the dependency on the second invariant II_C of the polynomial mode [**62**]:

$$\Psi = \sum_{i=1}^{n} C_{ij}(I_{\boldsymbol{C}} - 3)^i + \sum_{i=1}^{m} \frac{1}{D_i}(J_{el} - 1)^{2i} \tag{3.49}$$

The neo-Hook function is a reduced polynomial with $n = 1$

$$\Psi = C_1(\boldsymbol{I}_C - 3) + \frac{1}{D_1}(J_{el} - 1)^2 \tag{3.50}$$

The neo-Hookean function is a particularly simple case of isotropic hyperelastic material which exhibits characteristics that can be associated with familiar material parameters found in elastic analysis. The elastic potential can also be described as [**11**]:

$$\Psi = \frac{\mu}{2}(I_C - 3) - \mu \ln J + \frac{\lambda}{2}(\ln J)^2 \tag{3.51}$$

where μ and λ are material coefficients and $J^2 = III_{\boldsymbol{C}}$.

Due to its simple form, it is worthwhile to describe the constitutive relations for the neo-Hookean model. Thus, the second Piola-Kirchhoff stress tensor (3.34) will be:

$$\boldsymbol{S} = \mu(\boldsymbol{I} - \boldsymbol{C}^{-1}) + \lambda(\ln J)\boldsymbol{C}^{-1} \tag{3.52}$$

The Cauchy stress will be:

$$\boldsymbol{\sigma} = \frac{\mu}{J}(\boldsymbol{B} - \boldsymbol{I}) + \frac{\lambda}{J}(\ln J)\boldsymbol{I} \tag{3.53}$$

By differentiating equation (3.53) with respect to the components of the left Cauchy-Green tensor $\boldsymbol{C}$, the Lagrangian elasticity tensor will be obtained:

$$\boldsymbol{\mathcal{C}} = \lambda \boldsymbol{C}^{-1} \otimes \boldsymbol{C}^{-1} + 2(\mu - \lambda \ln J)\boldsymbol{\mathcal{I}} \tag{3.54}$$

where

$$\boldsymbol{C}^{-1} \otimes \boldsymbol{C}^{-1} = \sum_{I,J,K,L=1}^{3} (C^{-1})_{IJ} \cdot (C^{-1})_{KL} \cdot \boldsymbol{E}_I \otimes \boldsymbol{E}_J \otimes \boldsymbol{E}_K \otimes \boldsymbol{E}_L \tag{3.55}$$

and

$$\boldsymbol{\mathcal{I}} = -\frac{\partial \boldsymbol{C}^{-1}}{\partial \boldsymbol{C}}; \qquad \mathcal{I}_{IJKL} = -\sum_{I,J,K,L=1}^{3} \frac{\partial (C^{-1})_{IJ}}{\partial C_{KL}} \tag{3.56}$$

In order to obtain the components of the fourth order tensor $\boldsymbol{\mathcal{I}}$, we must consider the directional derivative of the inverse of a tensor as well the formulation of the directional derivative in terms of partial derivatives. After some algebra, the components of the tensor will be defined as:

$$\mathcal{I}_{IJKL} = \sum_{I,J,K,L=1}^{3} (C^{-1})_{IK} \cdot (C^{-1})_{JL} \cdot \boldsymbol{E}_I \otimes \boldsymbol{E}_J \otimes \boldsymbol{E}_K \otimes \boldsymbol{E}_L \tag{3.57}$$

After some algebra, the Eulerian elasticity tensor can be obtained by pushing forward the Lagrangian elasticity tensor (3.54) with the help of equations (3.27) and (3.28):

$$\boldsymbol{c} = \frac{\lambda}{J}\boldsymbol{I}\otimes\boldsymbol{I} + \frac{2}{J}(\mu - \lambda \ln J)\imath \tag{3.58}$$

where

$$\imath = \phi_*[\mathcal{I}] \tag{3.59a}$$

$$\imath = \sum_{I,J,K,L=1}^{3} F_{iI}F_{jJ}F_{kK}F_{lL}\mathcal{I}_{IJKL}\boldsymbol{E}_I\otimes\boldsymbol{E}_J\otimes\boldsymbol{E}_K\otimes\boldsymbol{E}_L = \delta_{ik}\delta_{jl} \tag{3.59b}$$

In terms of the effective Lamé moduli λ' and μ', equation the components of the Eulerian elasticity tensor can be expressed as:

$$c_{ijkl} = \sum_{I,J,K,L=1}^{3}\left(\lambda'\delta_{ik}\delta_{jl} + 2\mu'\delta_{ik}\delta_{jl}\right)\boldsymbol{e}_i\otimes\boldsymbol{e}_j\otimes\boldsymbol{e}_k\otimes\boldsymbol{e}_l \tag{3.60}$$

where the effective coefficients are:

$$\lambda' = \frac{\lambda}{J}; \qquad \mu' = \frac{\mu - \lambda\ln J}{J} \tag{3.61}$$

In case of incompressible hyperelasticity, equation (3.19a) should be rearranged so that:

$$\left(\frac{1}{2}\boldsymbol{S} - \frac{\partial\Psi}{\partial\boldsymbol{C}}\right):\frac{d\boldsymbol{C}}{dt} = 0 \tag{3.62}$$

The Jacobian J will be equal to 1 throughout the deformation and consequently, $dJ/dt = 0$. Thus, considering the constraint for the left Cauchy-Green strain tensor, the general constitutive equation for the incompressible hyperelastic material can be obtained:

$$\boldsymbol{S} = 2\frac{\partial\Psi(\boldsymbol{C})}{\partial\boldsymbol{C}} + \gamma J\boldsymbol{C}^{-1} \tag{3.63}$$

Introducing equations (III. 2.54b) and (III. 2.56b) in equation (3.63) yields:

$$\boldsymbol{S} = \boldsymbol{S}' + pJ\boldsymbol{C}^{-1}; \qquad \boldsymbol{S}' = J\boldsymbol{F}^{-1}\boldsymbol{\sigma}'^{\boldsymbol{F}^{-T}} \tag{III. 2.54b}$$

$$p = \frac{1}{3}J^{-1}\boldsymbol{S}:\boldsymbol{C} \tag{III. 2.56b}$$

$$p = \gamma + \frac{2}{3}J^{-1}\frac{\partial\Psi(\boldsymbol{C})}{\partial\boldsymbol{C}}:\boldsymbol{C} \tag{3.64}$$

For incompressible materials $III_C = \det\boldsymbol{C} = J^2 = 1$ (equation (3.30c)) which implies that the function $\Psi(\boldsymbol{C})$ is homogenous of order 0 for any arbitrary constant α:

$$\frac{\partial\Psi(\boldsymbol{C})}{\partial\boldsymbol{C}}:\boldsymbol{C} = 0 \tag{3.65}$$

Recalling the equation for the distortional component of a tensor (III. 1.54) , a modified energy function $\widehat{\Psi}(\boldsymbol{C})$ of the distortional component of the left Cauchy-Green strain tensor $\widehat{\boldsymbol{C}}$ can be defined:

$$\widehat{\boldsymbol{F}} = J^{-\frac{1}{3}}\boldsymbol{F} \tag{III. 1.54}$$

$$\widehat{\boldsymbol{C}} = J^{-\frac{1}{3}}\boldsymbol{C} \tag{3.66}$$

$$\widehat{\Psi}(\boldsymbol{C}) = \Psi(\widehat{\boldsymbol{C}}) \tag{3.67}$$

So, for incompressible hyperelastic materials the constitutive equation will be:

$$\boldsymbol{S} = 2\frac{\partial\widehat{\Psi}(\boldsymbol{C})}{\partial\boldsymbol{C}} + pJ\boldsymbol{C}^{-1} \tag{3.68}$$

3.2.4.3. Reduced polynomial model, n=3 (Yeoh material)

Another reduced polynomial model that considers $n = 3$ represents the Yeoh material defined by the function [**65**]:

$$\Psi = C_{10}(I_1 - 3) + C_{20}(I_1 - 3)^2 + C_{30}(I_1 - 3)^3 + \frac{1}{D_1}(J_{el} - 1)^2 \tag{3.69}$$

3.2.4.4. Ogden material

The Ogden model is a strain-energy density function is expressed in terms of principal stretches λ_i [**15**]:

$$\Psi = \sum_{n=1}^{\infty}\frac{\mu_n}{\alpha_n}\{\lambda_1^{\alpha_n} + \lambda_2^{\alpha_n} + (\lambda_1\lambda_2)^{-\alpha_n} - 3\} + \sum_{i=0}^{2}\frac{1}{D_i}(J_{el} - 1)^{2i} \tag{3.70}$$

3.2.4.5. Arruda-Boyce material

The Arruda-Boyce model was developed from an element with 8 springs that connect the centre of the cube to its corners [**17**]:

$$\Psi = \mu\sum_{n=1}^{5}\frac{C_i}{\lambda_m^{2i-2}}\left(I_1^i - 3^i\right) + \frac{1}{D}\left(\frac{J_{el} - 1}{2} - \ln J_{el}\right)^{2i} \tag{3.71}$$

where

$$C_1 = \frac{1}{2}; \quad C_1 = \frac{1}{20}; \quad C_1 = \frac{11}{1050}; \quad C_1 = \frac{19}{7000}; \quad C_1 = \frac{519}{673750};$$

and

$$\mu = \frac{\mu_0}{1 + \frac{3}{\lambda_m^2} + \frac{99}{175\lambda_m^4} + \frac{513}{875\lambda_m^6} + \frac{42039}{67375\lambda_m^8}}$$

3.2.4.6. Van der Waals material

The Van der Waals model also known as the Kilian model, derives its name from its analogous form with state equations of a real gas [**16**]:

$$\Psi = \mu\left\{-(\lambda_m^2 - 3)[\ln(1-\eta) + \eta] - \frac{2}{3}\alpha\left(\frac{\tilde{I}-3}{2}\right)^{\frac{2}{3}}\right\} \tag{3.72}$$

where

$$\tilde{I} = (1-\beta)I_1 + \beta I_2 \tag{3.73a}$$

$$\eta = \sqrt{(\tilde{I}-3)/(\lambda_m^2 - 3)} \tag{3.73b}$$

$$\alpha = \frac{2C_{01}}{3G} + \frac{\lambda_m^2}{\lambda_m^3 - 1} \tag{3.73c}$$

$$\beta = \beta(I_1, I_2); \quad 0 < \beta < 1 \tag{3.73d}$$

3.2.4.7. Marlow material

The Marlow model, which does not assume any explicit form, as it is calculated from numerical data from the experiment [**18**]:

$$\Psi = \int_0^{\varepsilon_I} T(\varepsilon)\, d\varepsilon \tag{3.74}$$

where ε_I represent the first invariant dependent strain ($\varepsilon_I = \lambda_T(I) - 1$) and $T(\varepsilon)$ represents the nominal uniaxial traction.

3.3. Plasticity

Plasticity represents materials' property to undergo non-reversible deformation when being strained [**67**]. In pure uniaxial tension, idealized material behaviour states that plastic deformation commences at a yield stress σ_y, which is defined as the level of stress for which an increase in strain will not determine an increase in stress (Figure 3.1) [**43**].

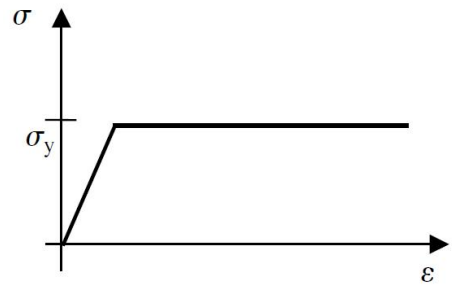

Figure 3.1. Stress-strain curve for perfect plasticity

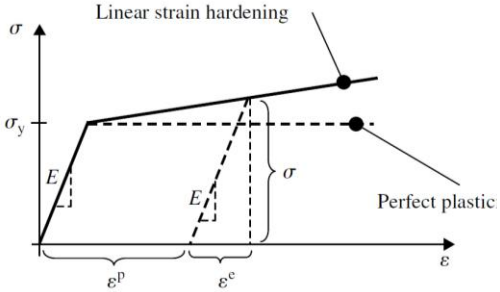

Figure 3.2. Linear hardening with strain decomposition

In practical applications, few materials exhibit a behaviour that can be approximated with perfect plasticity. Instead, they are characterized by the hardening phenomenon: the stress-strain response increases after the yield point, relative to perfect plasticity (Figure 3.2) [**67**].

In order to determine the plastic strain values of a certain deformation, the principle of strain decomposition must be applied, which states that the total strain ε is given by the sum of the elastic component ε^e and the plastic component ε^p [**67**].

$$\varepsilon = \varepsilon^e + \varepsilon^p \tag{3.75}$$

In the case of metals, if the material straining beyond the yield point (up to ε strain) is to be reversed until the stress is 0, the unloading will take place along a line parallel with Young's modulus. The remaining deformation represents the plastic strain ε^p. The elastic strain ε^e can be obtained by subtracting the plastic strain ε^p from the total strain ε [**67**].

In the case of polymers, due to their non-linear behaviour, plasticity is recommended to be extracted from step-cycle tests [**6**]. In such experiments, the tensile test is interrupted by unloading-loading cycles at various strains. The cycle amplitude will determine the total strain ε while the strain value recorded at 0 stress represents the plastic strain ε^p.

In the case of multiaxial stress stats, several yield criterions exist for calculating the equivalent stress σ_e for which the material yields. There are two main types of yield criteria: independent and dependent on the hydrostatic pressure component of the stress tensor (III. 2.53b). Criteria that are independent on hydrostatic pressure assume a symmetric behaviour in tension and compression (and are widely used in modelling metals and polymers), the most common of which being von Mises yield criterion, the Tresca yield criterion and the Drucker yield criterion [**67**,**68**].

Yield criteria accounting for the effect of hydrostatic pressure (different behaviour in tension and compression) were developed for modelling the yielding of soils [**68**]. These yield criteria can be divided in four categories depending on the profile of the yield surface (straight line, ellipse or parabola), the most commonly used being the Drucker-Prager criterion [**69**], the GAZT criterion [**70**], the Deshpande criterion [**71**] or the Raghava criterion [**72**].

For modelling of advanced materials (anisotropic inelastic materials) yield criteria were adapted. The Generalized Drucker-Prager criterion, proposed by Liu et al. [**73**], introduces Hill's anisotropic criterion [**74**,**75**] in the D-P yield criterion. Another model was proposed by Cazacu and Barlat as a generalization of the invariants of the stress deviator in Drucker's yield criterion [**76**].

In engineering applications, the most widely used criterion is the von Mises criterion which assumes that yielding occurs when the equivalent stress σ_e reaches a specific value σ_y [**67**]:

$$\sigma_e = \left[\frac{3}{2}(\sigma_{11}^2 + \sigma_{22}^2 + \sigma_{33}^2 + 2\sigma_{12}^2 + 2\sigma_{23}^2 + 2\sigma_{31}^2)\right]^{\frac{1}{2}} \tag{3.76}$$

According to Mohr's circle the relation between the shear stress σ_{ij} and the normal stress σ_{ii} is [**67**]:

$$\sigma_{ij} = \frac{(\sigma_{ii} - \sigma_{jj})}{2} \tag{3.77}$$

In consequence, the von Mises equivalent stress can be expressed as [**67**]:

$$\sigma_e = \frac{1}{\sqrt{2}}[(\sigma_1 - \sigma_2)^2 + (\sigma_2 - \sigma_3)^2 + (\sigma_3 - \sigma_1)^2]^{\frac{1}{2}} \tag{3.78}$$

Analogous to the above equation the rate of plastic deformation can be expressed as [**67**]:

$$\dot{p} = \frac{\sqrt{2}}{3}\left[\left(\dot{\varepsilon}_1^p - \dot{\varepsilon}_2^p\right)^2 + \left(\dot{\varepsilon}_2^p - \dot{\varepsilon}_3^p\right)^2 + \left(\dot{\varepsilon}_3^p - \dot{\varepsilon}_1^p\right)^2\right]^{\frac{1}{2}} \tag{3.79}$$

In terms of tensor formulation, the equivalent stress and the plastic strain rate can be expressed as [**67**]:

$$\sigma_e = \left(\frac{3}{2}\boldsymbol{\sigma}' : \boldsymbol{\sigma}'\right)^{\frac{1}{2}} \tag{3.80}$$

$$\dot{\boldsymbol{p}} = \left(\frac{2}{3}\dot{\varepsilon}^p : \dot{\varepsilon}^p\right)^{\frac{1}{2}} \tag{3.81}$$

where $\boldsymbol{\sigma}'$ is the deviatoric stress defined in equation (III. 2.53a).

3.3.1. The von Mises yield criterion

Consider a yield function f so that the material starts to yield when $f = 0$. The von Mises yield criterion is valid only considering three hypotheses [**67**]:

- The yield function is independent of the hydrostatic stress (so $f = f(\boldsymbol{\sigma}')$).
- Yielding is considered isotropic (so f must be a symmetric function).
- Yield in compression must equal the yield in tension.

Consequently, the von Mises yield criterion is defined as:

$$f = \sigma_e - \sigma_y = \left(\frac{3}{2}\boldsymbol{\sigma}' : \boldsymbol{\sigma}'\right)^{\frac{1}{2}} - \sigma_y \tag{3.82}$$

In the vector space formed by the three normal components of the stress tensor $(\sigma_{11}, \sigma_{22}, \sigma_{33})$ this yield function corresponds to a cylinder with the axis along the main diagonal of the orthogonal system $\sigma_1 = \sigma_2 = \sigma_3$.

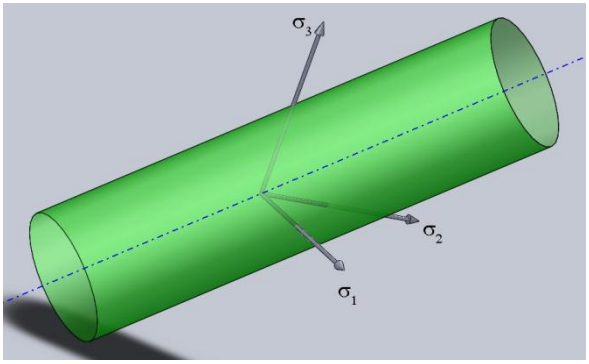

Figure 3.3. von Mises yield surface

3.3.2. Isotropic hardening

As stated above, only a small number of materials exhibit behaviour close to perfect plasticity. The majority present a hardening effect: in order to plastically deform the body, an increase in stress is required. In general, the increment in stress required to further strain the body is a function of the accumulated plastic deformation [**67**]:

$$p = \int \dot{p}\, dt \tag{3.83}$$

A typical isotropic hardening model with non-linear hardening is presented in Figure III.3.3. If the subsequent yield surfaces expand uniformly along all directions, the hardening is considered isotropic.

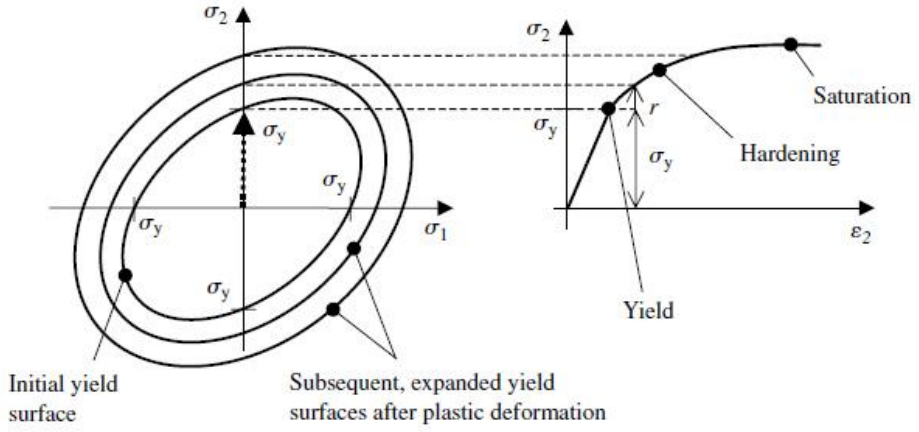

Figure 3.4. Non-linear isotropic hardening
[reprint from [**67**]]

In this example, when loading along the YY direction, the material starts to yield when $\sigma_{22} = \sigma_y$. As hardening occurs, the yield surface expands as σ_{22} increases, expansion which is expressed as a function of the accumulated plastic strain [**67**]:

$$f(\sigma, p) = \sigma_e - \sigma_y(p) \tag{3.84}$$

where the yield stress $\sigma_y(p)$ is expressed as:

$$\sigma_y(p) = \sigma_{y0} + r(p) \tag{3.85}$$

σ_{y0} represents the initial yield stress and $r(p)$ represents the isotropic hardening function. A typical form of the isotropic hardening function, which determines an exponential variation is given by the relation:

$$\mathrm{d}r(p) = b(Q - r)\mathrm{d}p \tag{3.86}$$

where b and Q are material constants.

Upon integration and considering the initial condition $r(0) = 0$, equation (3.85) becomes:

$$r(p) = Q(1 - e^{-bp}) \tag{3.87}$$

3.3.3. Kinematic hardening

For most cases of monotone loading scenarios, the isotropic hardening model is considered sufficient in describing material behaviour [**67**]. As depicted in Figure 3.5, if a material is deformed with a strain ε_i corresponding to the load point (1) and then the loading is reversed until the material compresses to the load point (2), the uniformly expanded yield surface would account for a very large elastic region. Experimental results for most materials contradict this behaviour [**67**], showing a much smaller elastic region (the Bauschinger effect). This behaviour was named kinematic hardening, which states that at deformations in the plastic region, the yield surface is translated rather than expanded (Figure 3.6).

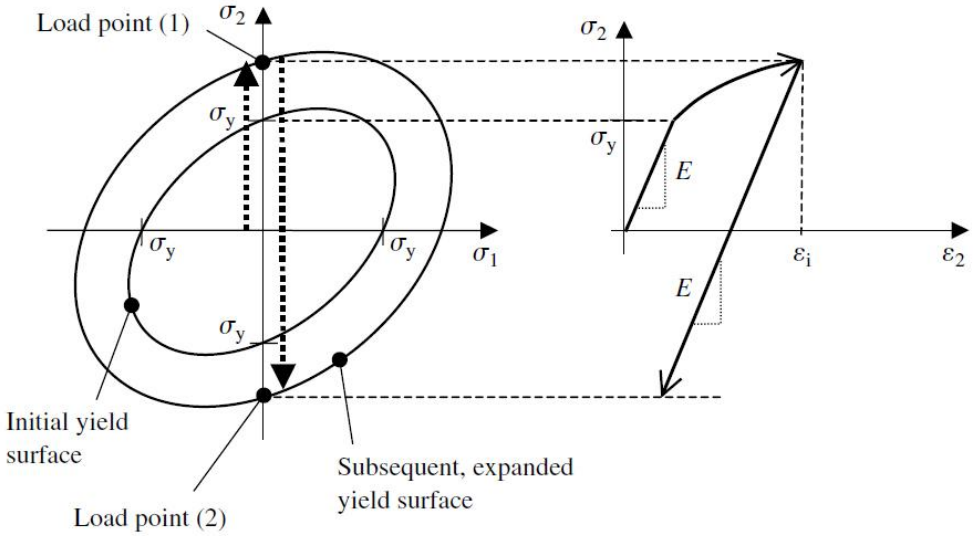

Figure 3.5. Isotropic hardening in compression
[reprint from [**67**]]

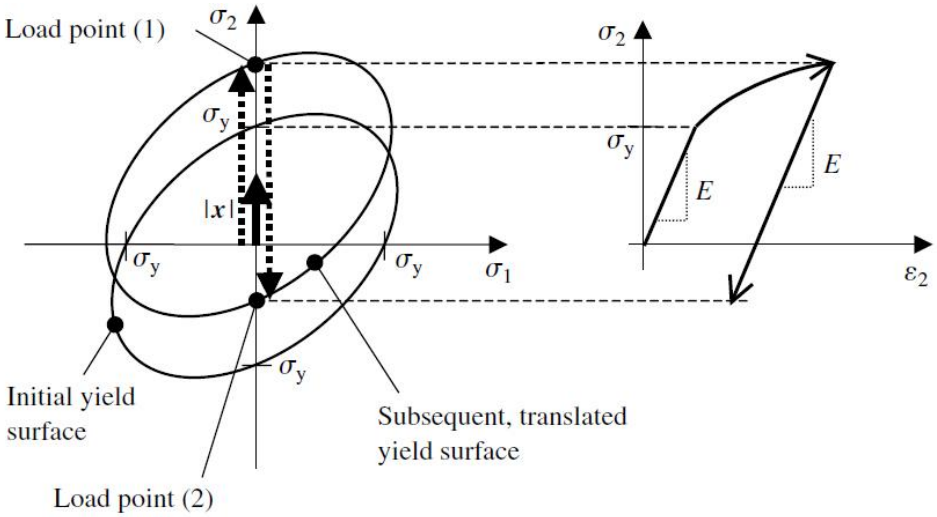

Figure 3.6. Kinematic hardening model
[reprint from [**67**]]

In order to determine the yield function for kinematic hardening, the translation of the yield surface must be taken into account. In Figure 3.6 the translation of the centre of the yield region was considered $|\boldsymbol{x}|$. The stress relative to the new yield region can be obtained by introducing this translation in the yield function (3.82)

$$f = \sigma_e - \sigma_y = \left(\frac{3}{2}(\boldsymbol{\sigma}' - \boldsymbol{x}'):(\boldsymbol{\sigma}' - \boldsymbol{x}')\right)^{\frac{1}{2}} - \sigma_y \tag{3.88}$$

where $\boldsymbol{x}$ represents a kinematic hardening variable (also known as the *back stress*), having the same components as the stress tensor $\boldsymbol{\sigma}$.

3.4. Viscoelasticity

In many practical applications materials of various components and structures are considered to be sufficiently characterized by simple laws (elasticity, plasticity, viscosity, etc.) in order to reduce computational complexity of their simulations. In reality, no solid exhibits perfect elasticity and no fluid exhibits pure Newtonian viscosity: deformation of every type of material has an elastic part and a flow part [**1**]. This behaviour is more evident in the case of polymers (due to the fact that their microstructure is composed on long molecular chains [**1**]), where, apart from the elastic/hyperelastic stress-strain response, a viscous-flow behaviour can be observed in the form of stress relaxation/creep as well as temperature- and strain-rate-dependent properties [**1**,**2**,**44**]. In many cases, it is impossible to separate permanent damage induced to the microstructure from the reversible damage. The molecular basis for stress relaxation and creep accounts for several

types of mechanisms that are responsible for softening of the material: chain scission, viscous flow, bond interchange, molecular relaxation, etc [1].

3.4.1. The Maxwell fluid

A way to incorporate this type of time-dependency into material models is by integrating viscoelasticity through mathematical models that deal with creep and stress relaxation. Over the years, several models were developed, the first being introduced by J.C. Maxwell (Figure 3.7) who approximated viscoelastic behaviour by connecting a spring (Hookean elasticity) with a dashpot (Newtonian viscosity) in series.

Figure 3.7. Mathematical model of the Maxell fluid

As stated in the previous paragraph, hookean elasticity can be described with the relation:

$$\varepsilon_s(t) = \frac{\sigma_s(t)}{E} \tag{3.89}$$

This simple constitutive behaviour (above written for uniaxial loadings) cannot incorporate dynamic aspects such as oscillations, time dependencies or inertial effect.

It is worth mentioning that the spring analogy should be taken into account as a mathematical model rather than a physical model. One could not shear the physical spring, but a linear elastic solid can be subjected to simple shear.

Newtonian viscosity defines the shear stress τ as:

$$\tau_{ij} = \eta\left(\frac{dv_i}{dx_j} + \frac{dv_j}{dx_i}\right) \tag{3.90}$$

where η represents the shear viscosity, v represents velocity and x displacement.

In simple shear, Equation (3.90) can be written as:

$$\sigma_{21} = \tau_{21} = \eta\frac{dv_2}{dx_1} = \eta\frac{d\gamma}{dt} \tag{3.91}$$

where $\frac{d\gamma}{dt}$ represents the shear rate.

In case of extension, the stress can be written as:

$$\sigma_{11} - \sigma_{22} = \sigma_E = 3\eta\frac{dv_1}{dx_1} \tag{3.92}$$

where $\mu = 3\eta$ represents the extensional viscosity (analogous to $E = 3G$)

In consequence, the analogous mathematical model for the dashpot, obtained by integrating Equation (3.92) is:

$$\varepsilon_d(t) = \frac{\sigma_d}{\mu} t \tag{3.93}$$

For the Maxwell model, both elements are subjected to the same stress σ, thus the equilibrium equation will be:

$$\sigma_s = \sigma_d = \sigma$$

where σ_s is the stress in the spring and σ_d is the stress in the dashpot.

The equation of motion for the Maxwell fluid will be:

$$\varepsilon(t) = \varepsilon_s + \varepsilon_d = \frac{E}{\sigma(t)} + \frac{\sigma}{\mu} t \tag{3.93}$$

The constitutive equation for the Maxwell fluid can be obtained by derivation of the equation of motion:

$$\frac{d\varepsilon}{dt} = \frac{1}{E} \cdot \frac{d\sigma}{dt} + \frac{\sigma}{\mu}$$
$$\sigma + \frac{\mu}{E} \frac{d\sigma}{dt} = \mu \frac{d\varepsilon}{dt} \tag{3.94}$$

3.4.1.1. Behaviour in creep

For the creep experiment, the stress is kept constant, meaning the variation in stress equals 0. Thus, the equation of motion of the Maxwell fluid will be:

$$\frac{d\varepsilon}{dt} = \frac{\sigma_0}{\mu}, \qquad \frac{d\sigma}{dt} = 0 \tag{3.95a}$$
$$\varepsilon = \varepsilon_0 + \frac{\sigma_0}{\mu} t \tag{3.95b}$$

Expressing Equation (3.95)in terms of the creep compliance $J = \frac{\varepsilon}{\sigma}$:

$$J(t) = J_0 + \frac{t}{\mu} \tag{3.96}$$

The Maxwell element compliance increases without limit as time goes on, resulting in typical viscous liquid behaviour.

3.4.1.2. Behaviour in stress relaxation

For the stress relaxation experiment, the strain is kept constant, meaning the variation in strain equals 0. Thus, the equation of motion of the Maxwell fluid will be:

$$0 = \frac{1}{E} \cdot \frac{d\sigma}{dt} + \frac{\sigma_0}{\mu} \tag{3.97}$$

Introducing the relaxation time $\tau = \frac{\mu}{E}$, Equation (3.97) will become:

$$\frac{d\sigma}{\sigma_0} = -\frac{dt}{\tau} \tag{3.98a}$$

$$\ln\sigma(t) = \ln\sigma_0 - \frac{t}{\tau} \tag{3.98b}$$

$$\sigma(t) = \sigma_0 \cdot e^{-\frac{t}{\tau}} \tag{3.98c}$$

$$E(t) = E_0 \cdot e^{-\frac{t}{\tau}} \tag{3.98d}$$

3.4.2. The Kelvin solid

Another model was developed by W.T. Kelvin and W. Voigt, which had the spring and dashpot connected in parallel (Figure 3.8).

For this model, the strain is equal in both elements during deformation and the kinematic equation will be:

$$\varepsilon_s = \varepsilon_d = \varepsilon \tag{3.99}$$

The equilibrium equation will be:

$$\sigma_K = \sigma_s + \sigma_d \tag{3.100}$$

Thus, the constitutive equation for the Kelvin solid will be:

$$\sigma_K(t) = \varepsilon(t) \cdot E + \mu\frac{d\varepsilon(t)}{dt} \tag{3.101}$$

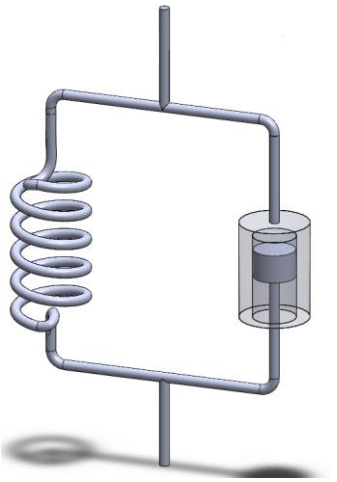

Figure 3.8. Mathematical model of the Kelvin solid

3.4.2.1. Behaviour in creep

For the creep experiment ($\frac{d\sigma(t)}{dt} = 0$), the equation of motion of the Voigt element fluid will be:

$$\frac{\sigma(t)}{\mu} = \frac{\varepsilon(t)}{\tau} + \frac{d\varepsilon(t)}{dt} \tag{3.102}$$

The above equation can be solved with the help of the integrating factor $e^{\frac{t}{\tau}}$:

$$\frac{d}{dt}\left(\varepsilon(t) \cdot e^{\frac{t}{\tau}}\right) = \frac{\sigma(t)}{\eta} \cdot e^{\frac{t}{\tau}} \tag{3.103}$$

$$\varepsilon(t) = \frac{\sigma}{E}\frac{\left(e^{\frac{t}{\tau}} - 1\right)}{e^{\frac{t}{\tau}}} \tag{3.104}$$

Equation (3.104) can be written in compliance terms as:

$$J(t) = J_0\left(1 - e^{-\frac{t}{\tau}}\right) \tag{3.105}$$

3.4.2.2. Behaviour in stress relaxation

The Voigt element is unable to describe accurate behaviour in stress relaxation, as considering $\frac{d\varepsilon(t)}{dt} = 0$ will yield:

$$\sigma(t) = \varepsilon \cdot E \tag{3.106}$$

which describes a plateau.

3.4.3. The Voigt-Kelvin solid (standard linear solid)

The three-parameter model was developed by W.T. Kelvin and W. Voigt has a spring attached in series to a Kelvin element. The equilibrium equation for this model is:

$$\sigma_s = \sigma_K = \sigma \tag{3.107}$$

The equation of motion is:

$$\varepsilon = \varepsilon_s + \varepsilon_K \sigma \tag{3.108}$$

The rate of Kelvin strain $\frac{d\varepsilon_K}{dt}$ can be written as:

$$\frac{d\varepsilon_K}{dt} = \frac{\sigma_K(t) - \varepsilon_K(t) \cdot E_K}{\mu} \sigma \tag{3.109}$$

The constitutive equation for the three-parameter solid will become:

$$\begin{gathered} \frac{d\varepsilon(t)}{dt} = \frac{1}{E_s}\frac{d\sigma(t)}{dt} + \frac{\sigma(t) - \varepsilon_K(t) \cdot E_K}{\mu} \\ \frac{d\varepsilon(t)}{dt} = \frac{1}{E_s}\frac{d\sigma(t)}{dt} + \frac{E_s + E_K}{\mu E_s}\sigma(t) - \frac{E_K}{\mu}\varepsilon(t) \\ \sigma(t) + \frac{\mu}{E_s + E_K}\frac{d\sigma(t)}{dt} = \frac{E_s E_K}{E_s + E_K}\varepsilon(t) + \frac{\mu E_s}{E_s + E_K}\frac{d\varepsilon(t)}{dt} \end{gathered} \tag{3.110}$$

3.4.3.1. Behaviour in creep

The constitutive equation in creep ($\frac{d\sigma(t)}{dt} = 0$) of the three-parameter solid is:

$$\frac{d\varepsilon(t)}{dt} + \frac{E_K}{\mu}\varepsilon(t) = \left(1 + \frac{E_K}{E_s}\right)\frac{\sigma(t)}{\mu} \tag{3.111}$$

By solving the above equation, the response of the Voigt-Kelvin model in creep will be:

$$\varepsilon(t) = \sigma_0 \left[\frac{1}{E_s} + \frac{1}{E_K}\left(1 - e^{-t/\tau}\right)\right] \tag{3.112}$$

where $\tau = \frac{\mu}{E}$ represents the retardation time of the Voigt-Kelvin solid.

The creep compliance will be:

$$J(t) = \frac{1}{E_s} + \frac{1}{E_K}\left(1 - e^{-t/\tau}\right) \tag{3.113}$$

3.4.3.2. Behaviour in stress relaxation

The constitutive equation in stress relaxation ($\frac{d\varepsilon(t)}{dt} = 0$) of the three-parameter solid is:

$$\frac{1}{E_s}\frac{d\sigma(t)}{dt} + \frac{E_s + E_K}{\mu E_s}\sigma(t) = \frac{E_K}{\mu}\varepsilon(t)$$

$$\sigma(t) + \frac{\mu}{E_K + E_s}\frac{d\sigma(t)}{dt} = \frac{E_K E_s}{E_K + E_s}\varepsilon_0 \tag{3.114}$$

Solving the equation yields:

$$\sigma(t) = \varepsilon_0\left[\frac{E_K E_s}{E_K + E_s} + \frac{E_s^2}{E_K + E_s}\left(1 - e^{-\frac{(E_K + E_s)}{\mu}t}\right)\right] \tag{3.115}$$

The stress relaxation function will be:

$$E(t) = \frac{E_K E_s}{E_K + E_s} + \frac{E_s^2}{E_K + E_s}\left(1 - e^{-\frac{(E_K + E_s)}{\mu}t}\right) \tag{3.116}$$

4. NUMERICAL SIMULATIONS

4.1. Simulations overview

All simulations discussed in this chapter were performed in the commercial software Abaqus version 6.10. The aim of the study was to elaborate material models that can capture non-linear characteristics of PA-12 for various types of loading scenarios. In consequence, starting from the gathered experimental data, a series of material models were developed: hyperelastic formulation, elasto-plastic formulation and viscoelastic formulation. Hyperelastic models use experimental stress-strain curves in order to fit the strain-energy density function's parameters using least square algorithms [**62**]. Elasto-plastic models consider isotropic linear elasticity (Young's modulus E and Poisson ratio μ) and von Mises plasticity with various forms of hardening to shape the stress-strain curve accordingly [**62**]. Viscoelastic models take a linear elastic or hyperelastic model and apply a time-dependent softening parameter (the normalized relaxation modulus), calibrated either by long-term test data (creep or stress relaxation tests) or by short-term test data (DMA tests) [**62**].

In order to check the validity of the models experimental procedures were replicated. All material models were calibrated in static tension and the models were evaluated in cyclic tension, static three-point bending and dynamic three-point bending.

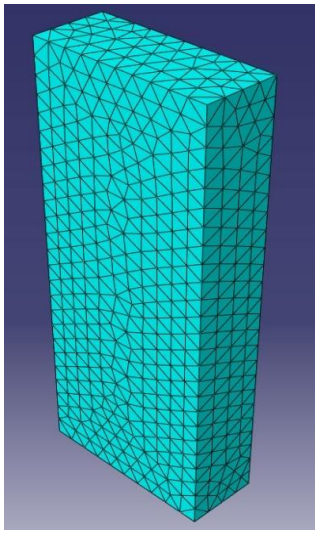

Figure 4.1. Prismatic model for tensile simulations

The static and cyclic tension model consisted of a 4 mm x 10 mm x 25 mm prism (representing half the volume whose strain was recorded with the extensometer, Figure 4.1). It consisted of 1755 nodes and 7894 C3D4H elements, average element size of 1mm. A mesh convergence study was performed determining identical results for finer meshes. Boundary conditions were a Y-symmetry on the bottom surface and a displacement on the top surface.

Static and dynamic three-point bending simulations consisted of consisted of an ISO 527 dogbone shaped specimen [**43**] of 13595 nodes and 7830 C3D10H elements (10 node modified quadratic elements, average element size of 2mm). Mesh convergence studies were performed and determined identical results for two or more quadratic elements per thickness. The supports and indentor were modelled as analytical rigids (cylindrical surfaces of 5 mm radius) (Figure 4.2). The interactions between the specimen and the support were modelled individually as

surface to node region. Interaction properties consisted of tangential penalty with a frictional coefficient of 0.25 and normal "hard contact" behaviour [**62**]. The reaction force and deflection were recorded through the rigid indentor's reference point. In case of dynamic simulations, the density of the material was considered $1.01 \cdot 10^{-9}$ t/mm^3.

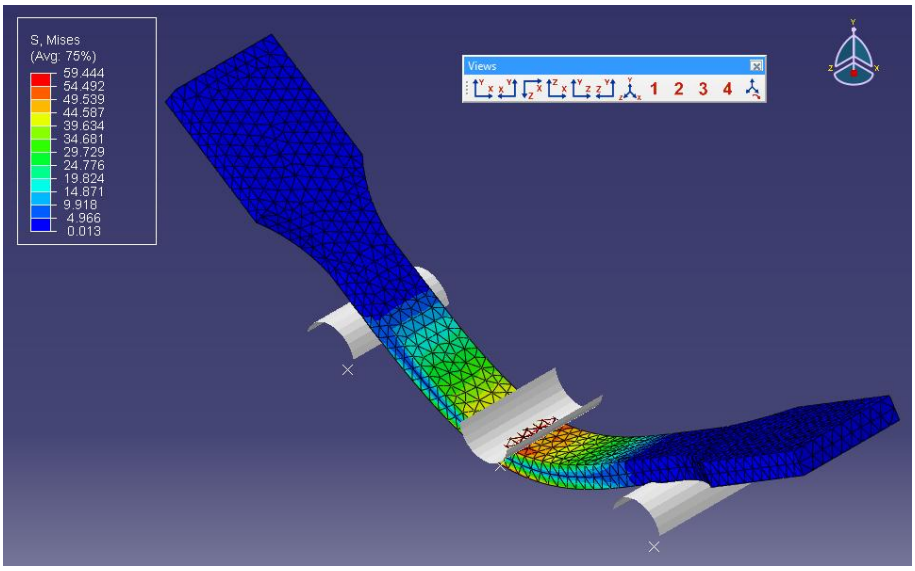

Figure 4.2. Dogbone model for three-point bending simulations

4.2. Hyperelastic material model

4.2.1. Material definition

For hyperlastic model evaluation, several strain-energy density functions were tested in tension on single elements: the Mooney-Rivlin model, the polynomial model, the Ogden model, the Neo-Hookean model, the Yeoh modeol, the van der Waals model and the Marlow.

4.2.1.1. Polynomial model, n=1 (Mooney-Rivlin material)

$$\Psi = \sum_{i+j=0}^{1} C_{ij}(I_1 - 3)^i (I_2 - 3)^j + \frac{1}{D_1}(J_{el} - 1)^2 \tag{3.47}$$

$C_{10} = -1291.36394$	$C_{01} = 1493.82898$
$D_1 = 1.646374813 \cdot 10^{-3}$	

Evaluation results regarding material model stability:

– Uniaxial tension: unstable at a nominal strain larger than 0.08 mm/mm;

- Uniaxial compression: unstable at a nominal strain less than -0.0754 mm/mm;
- Biaxial tension: unstable at a nominal strain larger than 0.04 mm/mm;
- Biaxial compression: unstable at a nominal strain less than -0.0377 mm/mm;
- Planar tension: unstable at a nominal strain larger than 0.07 mm/mm;
- Planar compression: unstable at a nominal strain less than -0.0654 mm/mm;
- Volumetric tension: stable for all volume ratios;
- Volumetric compression: stable for all volume ratios.

4.2.1.2. Polynomial model, n=2

$$\Psi = \sum_{i+j=1}^{2} C_{ij}(I_1 - 3)^i (I_2 - 3)^j + \sum_{i=0}^{2} \frac{1}{D_i}(J_{el} - 1)^{2i} \tag{3.46}$$

$D_1 = 1.87294 \cdot 10^{-3}$	$D_1 = 0$
$C_{10} = 1219.30358$	$C_{01} = -1041.33048$
$C_{20} = -384672.124$	$C_{11} = 886669.648$
$C_{02} = -513341.238$	

Evaluation results regarding material model stability:

- Uniaxial tension: unstable at a nominal strain larger than 0.06 mm/mm;
- Uniaxial compression: unstable at a nominal strain less than -0.0388 mm/mm;
- Biaxial tension: unstable at a nominal strain larger than 0.02 mm/mm;
- Biaxial compression: unstable at a nominal strain less than -0.0287 mm/mm;
- Planar tension: unstable at a nominal strain larger than 0.04 mm/mm;
- Planar compression: unstable at a nominal strain less than -0.0385 mm/mm;
- Volumetric tension: stable for all volume ratios;
- Volumetric compression: stable for all volume ratios.

4.2.1.3. Ogden model, n=3

$$\Psi = \sum_{n=1}^{\infty} \frac{\mu_n}{\alpha_n}\left\{\lambda_1^{\alpha_n} + \lambda_2^{\alpha_n} + (\lambda_1\lambda_2)^{-\alpha_n} - 3\right\} + \sum_{i=0}^{2} \frac{1}{D_i}(J_{el} - 1)^{2i} \tag{3.70}$$

$\mu_1 = -2798.08550$	$\alpha_1 = 2.00139914$	$D_1 = 1.66386 \cdot 10^{-3}$
$\mu_2 = 166.885473$	$\alpha_2 = 4.00005721$	$D_2 = 0$
$\mu_3 = 3031.87331$	$\alpha_3 = -1.99790056$	$D_3 = 0$

Evaluation results regarding material model stability:
- Uniaxial tension: unstable at a nominal strain larger than 0.08 mm/mm;
- Uniaxial compression: unstable at a nominal strain less than -0.0754 mm/mm;
- Biaxial tension: unstable at a nominal strain larger than 0.04 mm/mm;
- Biaxial compression: unstable at a nominal strain less than -0.0377 mm/mm;
- Planar tension: unstable at a nominal strain larger than 0.07 mm/mm;
- Planar compression: unstable at a nominal strain less than -0.0654 mm/mm;
- Volumetric tension: stable for all volume ratios;
- Volumetric compression: stable for all volume ratios.

4.2.1.4. Reduced polynomial model, n=1 (Neo-Hooke material)

$$\Psi = C_{10}(I_1 - 3) + \sum_{i=0}^{2} \frac{1}{D_i}(J_{el} - 1)^{2i} \tag{3.50}$$

$D_1 = 3.070543111 \cdot 10^{-3}$	$C_{10} = 108.558428$

Evaluation results regarding material model stability:
- Uniaxial tension: stable for all strains;
- Uniaxial compression: stable for all strains;
- Biaxial tension: stable for all strains;
- Biaxial compression: stable for all strains;
- Planar tension: stable for all strains;
- Planar compression: stable for all strains;
- Volumetric tension: stable for all volume ratios;
- Volumetric compression: stable for all volume ratios.

4.2.1.5. Reduced polynomial model, n=3 (Yeoh model)

$$\Psi = C_{10}(I_1 - 3) + C_{20}(I_1 - 3)^2 + C_{30}(I_1 - 3)^3 + \sum_{i=0}^{2} \frac{1}{D_i}(J_{el} - 1)^{2i} \tag{3.69}$$

$C_1 = 183.668611$	$D_1 = 1.814862819 \cdot 10^{-3}$
$C_2 = -3931.93617$	$D_2 = 0$
$C_3 = 47561.3645$	$D_3 = 0$

Evaluation results regarding material model stability:
- Uniaxial tension: unstable at a nominal strain larger than 0.07 mm/mm;
- Uniaxial compression: unstable at a nominal strain less than -0.0754 mm/mm;

- Biaxial tension: unstable at a nominal strain larger than 0.04 mm/mm;
- Biaxial compression: unstable at a nominal strain less than -0.0333 mm/mm;
- Planar tension: unstable at a nominal strain larger than 0.06 mm/mm;
- Planar compression: unstable at a nominal strain less than -0.0566 mm/mm;
- Volumetric tension: stable for all volume ratios;
- Volumetric compression: stable for all volume ratios.

4.2.1.6. Arruda-Boyce model

$$\Psi = \mu \sum_{n=1}^{5} \frac{C_i}{\lambda_m^{2i-2}} \left(I_1^i - 3^i\right) + \frac{1}{D}\left(\frac{J_{el}-1}{2} - \ln J_{el}\right)^{2i} \tag{3.71}$$

$\mu = 217.116281$	$\mu_0 = 217.117245$
$\lambda_m = 367.620052$	$D = 3.0705431113 \cdot 10^{-3}$

- Uniaxial tension: stable for all strains;
- Uniaxial compression: stable for all strains;
- Biaxial tension: stable for all strains;
- Biaxial compression: stable for all strains;
- Planar tension: stable for all strains;
- Planar compression: stable for all strains;
- Volumetric tension: stable for all volume ratios;
- Volumetric compression: stable for all volume ratios.

4.2.1.7. Van der Waals material

$$\Psi = \mu \left\{ -(\lambda_m^2 - 3)[\ln(1-\eta) + \eta] - \frac{2}{3}\alpha \left(\frac{\tilde{I}-3}{2}\right)^{\frac{2}{3}} \right\} + \frac{1}{D}\left(\frac{J_{el}-1}{2} - \ln J_{el}\right)^{2i} \tag{3.72}$$

$\eta = 395.91788$	$\alpha = 5.76361489$
$\lambda_m = 8.60962972$	$\beta = 0$
$D = 7.743267578 \cdot 10^{-2}$	

- Uniaxial tension: unstable at a nominal strain larger than 7.6 mm/mm;
- Uniaxial compression: unstable at a nominal strain less than -0.973 mm/mm;
- Biaxial tension: unstable at a nominal strain larger than 5.09 mm/mm;
- Biaxial compression: unstable at a nominal strain less than -0.659 mm/mm;
- Planar tension: unstable at a nominal strain larger than 7.56 mm/mm;

- Planar compression: unstable at a nominal strain less than -0.8832 mm/mm;
- Volumetric tension: stable for all volume ratios;
- Volumetric compression: stable for all volume ratios.

4.2.2. Material evaluation

The hyperelastic material model of Marlow strain-energy density function defined in the previous paragraph was evaluated in several loading scenarios.

4.2.2.1. Uniaxial tests in tension

Since the implemented hyperelastic models cannot account for strain rate dependency, simulations were performed for each set of experimental data in tension (different strain rates). The results for the polynomial-based models (Mooney-Rivlin material, 2nd order polynomial material, Neo-Hooke material and Yeoh material) are presented in Figure 4.3 and simulation results for the other material models (Ogden material, van der Waals material and Marlow material) are presented in Figure 4.4.

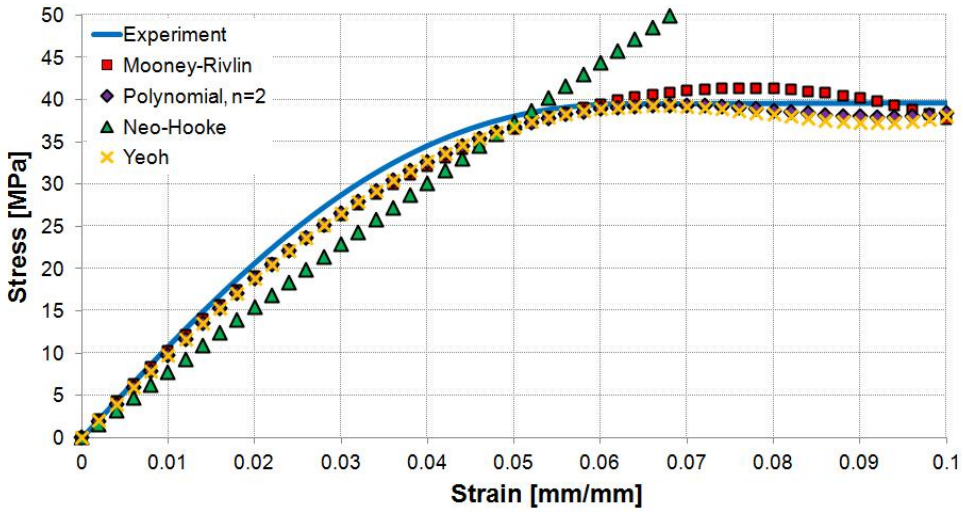

Figure 4.3. Hyperelastic material evaluation for static test in tension at 333 mm/s, 23°C, polynomial-based functions

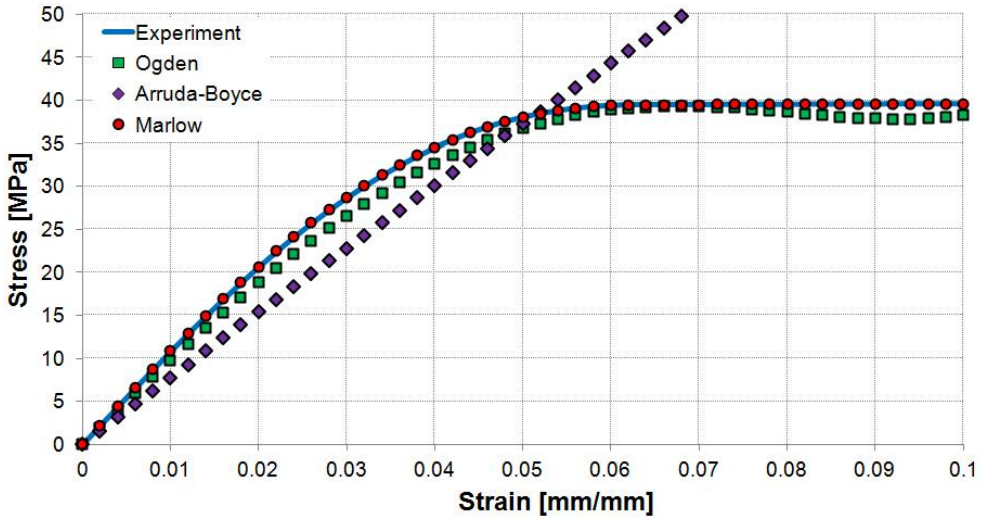

Figure 4.4. Hyperelastic material evaluation for static test in tension at 333 mm/s, 23°C, miscellaneous functions

The only material model that determined accurate simulation results regardless of the test conditions was the Marlow model (due to its specific formulation, see Chapter 3, Paragraph 2.4.7). The material models defined through explicit functions were unable to capture several aspects of PA-12's behaviour, such as the plateau recorded after yielding for high deformation speeds and low temperatures (Chapter 2, Paragraph 1.1).

4.2.2.2. Cyclic tests in tension

The cyclic tests in tension were performed on the same model as the uniaxial tests. The *Mullins Effect* sub-option was added to the hyperelastic Marlow model in order to shape the unloading path from cyclic tests, requiring cyclic stress-strain data for calibration [**62**]. The results for simulations performed for three cycles of different amplitudes are show in Figure 4.5 and for simulations performed on 8 cycles with different amplitudes are presented in Figure 4.7. Experimental results are recalled for comparison purposes, since overlapping the experimental and simulation results would determine unreadable figures.

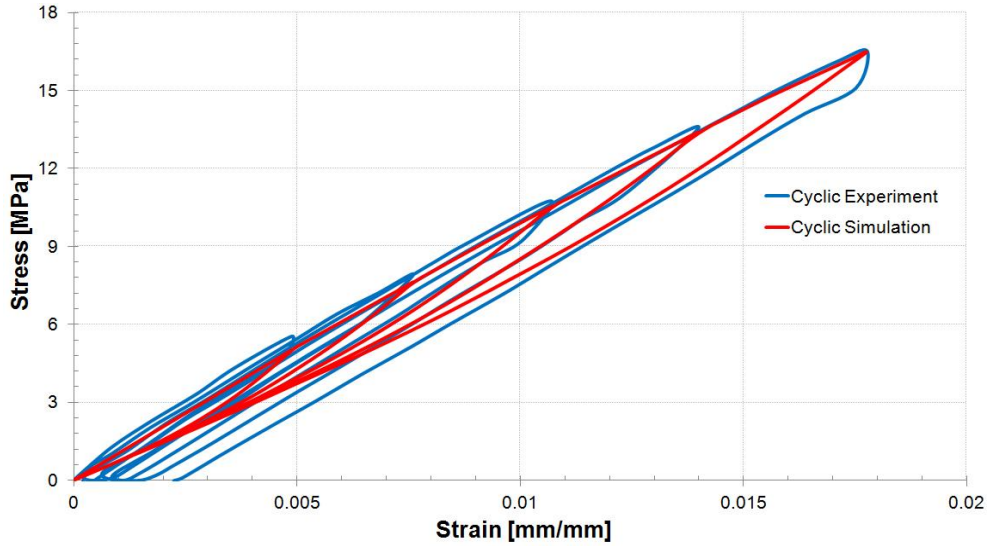

Figure 4.5. Experimental and simulated results for cyclic loadings with the hyperelastic model

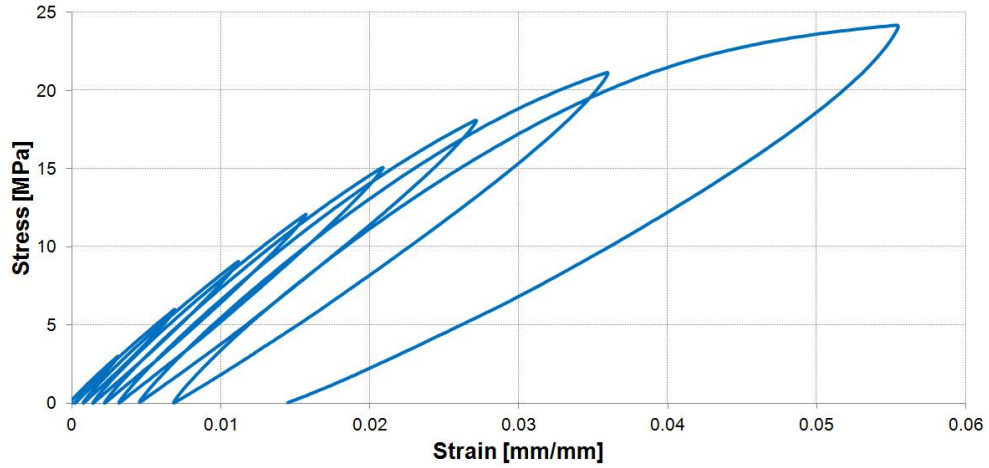

Figure 4.6. Experimental results for cyclic loadings with 8 cycles

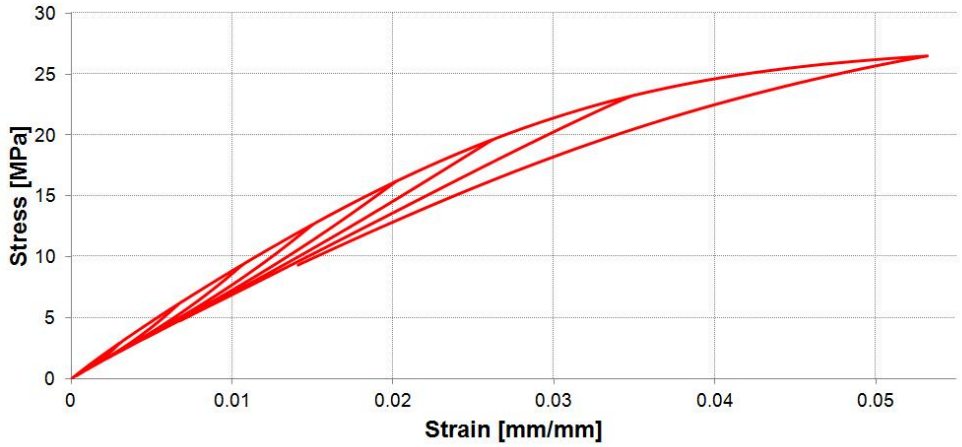

Figure 4.7. Simulation results for cyclic loadings with 8 cycles for hyperelastic material model

Having specified no additional information about plasticity or viscosity, the hyperelastic model could not determine accurate results in cyclic loadings regarding the remnant strain accumulated after each cycle, as seen in Figure 4.5. Another limitation of this model is its incapability of modelling strain softening induced by several cycles of the same amplitude.

4.2.2.3. Static three-point bending tests

The results for static three-point bending tests are presented in Figure 4.24.

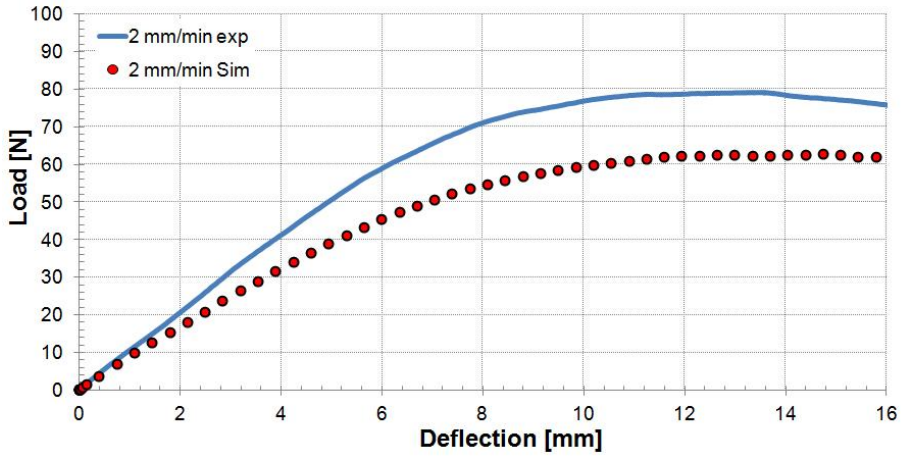

a)

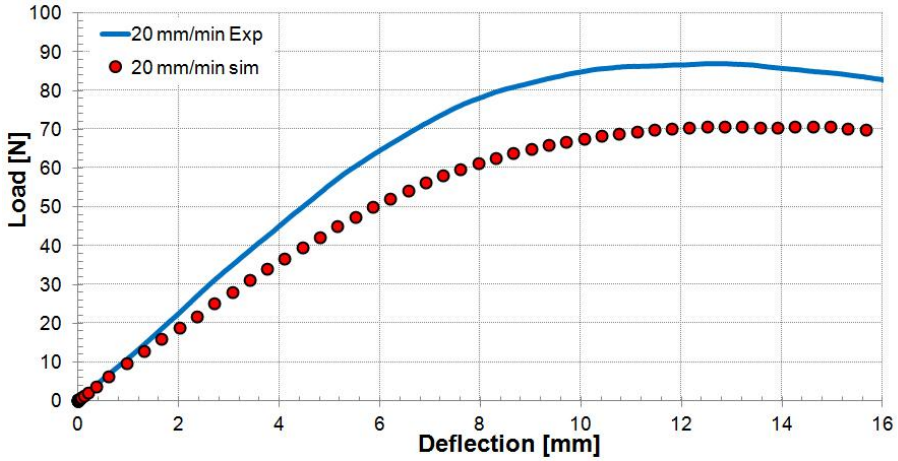

b)

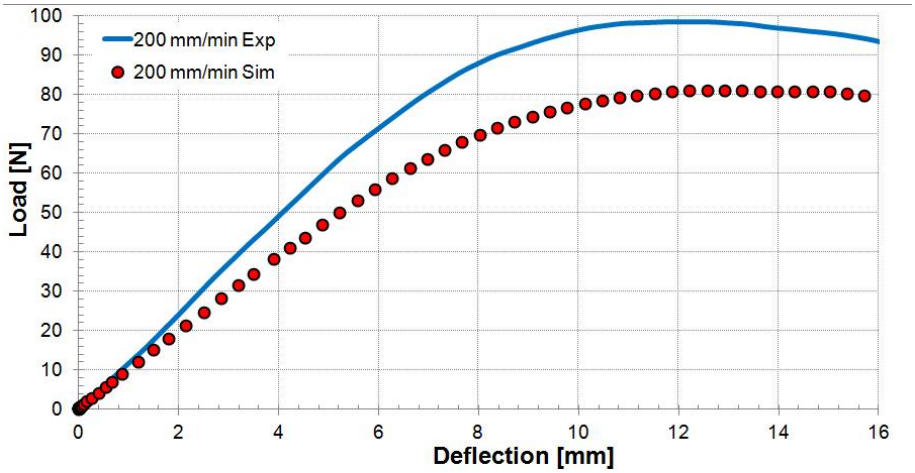

c)

Figure 4.8. Results in static tree-point bending for the hyperelastic material at a) 2 mm/min, b) 20 mm/min and c) 200 mm/min

The hyperelastic model underestimates material behaviour, regardless of the chosen rate dependent calibration data. In terms of flexural strength, the predicted material behaviour is 19% softer for 2 mm/min simulations (64N instead of 79N), 20% softer for 20 mm/min simulations (70N instead of 87N) and 18% softer for 200 mm/min simulations (81N instead of 98N).

Stress analysis for three-point bending simulations determined an equivalent von Mises [**67**] peak stress on the middle YZ plane (the plane with the highest degree of bending), on the edge of the specimen (Figure 4.9). Decomposing the von Mises equivalent stress into its components, it was observed that the highest amount of stress is generated by the compression along the X axis, the maximal value being located on the centre point of the upper surface of the specimen (under the bending indentor, Figure 4.10)

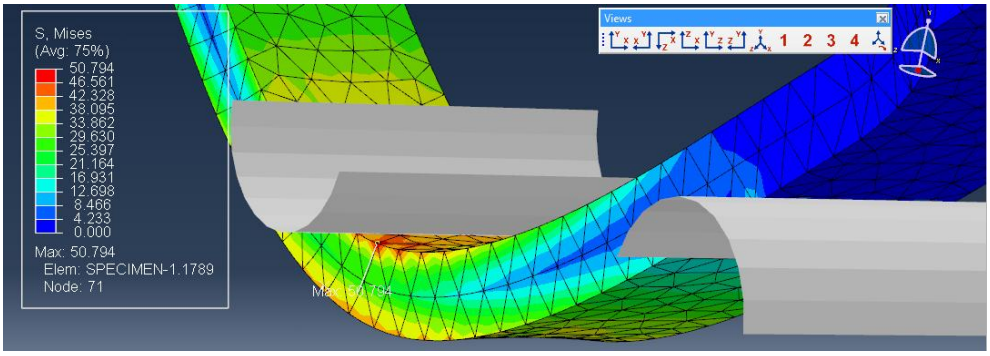

Figure 4.9. Von Mises stress distribution and peak value location

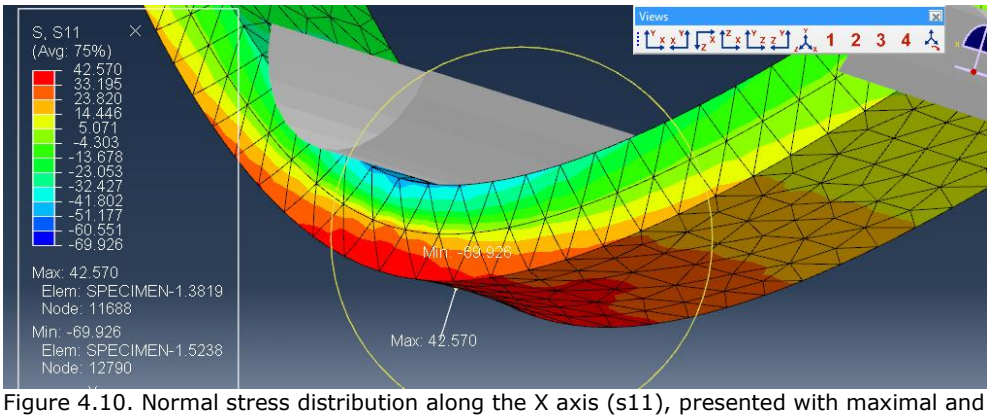

Figure 4.10. Normal stress distribution along the X axis (s11), presented with maximal and minimal value locations

Logarithmic strain analysis determined peak values in the same direction as the normal stress (along the X axis), with the position of the maximum straining in tension and compression being presented in Figure 4.11.

The results for the true stresses and logarithmical strains for all test speeds are presented in Table 4.1 – Table 4.3.

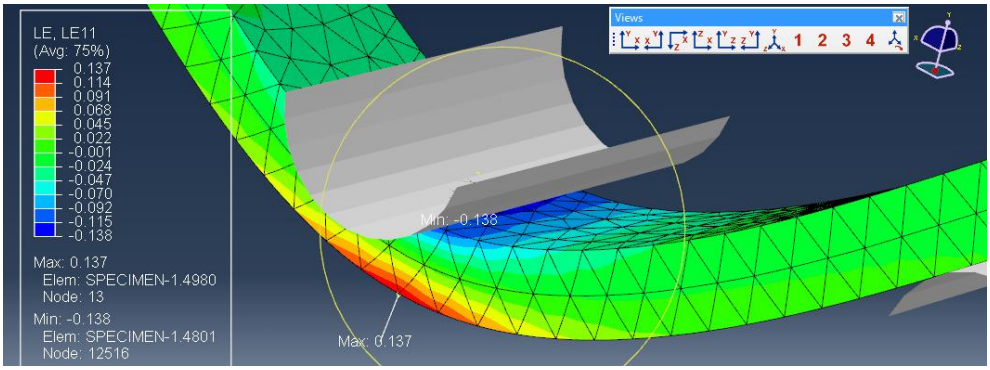

Figure 4.11. Normal logarithmic stain distribution along the X axis (EL11), presented with maximal and minimal value locations

Table 4.1. Stress and strain values recorded for 2 mm/min simulation

Stress	**[MPa]**	**Log strain**	**[mm/mm]**
S_{11}	-39.29	LE_{11}	-0.173
S_{22}	-9.17	LE_{22}	0.063
S_{33}	-13.82	LE_{33}	-0.06
S_{12}	11.61	LE_{12}	0.074
S_{13}	-5.12	LE_{13}	0.053
S_{23}	1.82	LE_{23}	-0.033
von Mises	37.58	Max Principal	0.168

Table 4.2. Stress and strain values recorded for 20 mm/min simulation

Stress	**[MPa]**	**Log strain**	**[mm/mm]**
S_{11}	-43.39	LE_{11}	-0.183
S_{22}	-10.06	LE_{22}	-0.067
S_{33}	-17.87	LE_{33}	-0.064
S_{12}	13.03	LE_{12}	0.073
S_{13}	-5.75	LE_{13}	0.053
S_{23}	2.08	LE_{23}	0.034
von Mises	42.36	Max Principal	0.176

Table 4.3. Stress and strain values recorded for 200 mm/min simulation

Stress	**[MPa]**	**Log strain**	**[mm/mm]**
S_{11}	-48.43	LE_{11}	-0.199
S_{22}	-11.59	LE_{22}	-0.072
S_{33}	-23.97	LE_{33}	-0.068
S_{12}	14.86	LE_{12}	0.069
S_{13}	-6.35	LE_{13}	0.051
S_{23}	-2.45	LE_{23}	0.033
von Mises	48.74	Max Principal	0.187

4.2.2.4. Dynamic three-point bending tests

As with the static scenario, the dynamic simulations determined lower values in reaction force, regardless of the strain-rate dependent calibration test data used. The force-deflection curves for three-point bending at 333 mm/s and 1500 mm/s are presented in Figure 4.12 and in Figure 4.13 respectively and the values for the stress and strain components are presented in Table 4.4 and Table 4.5.

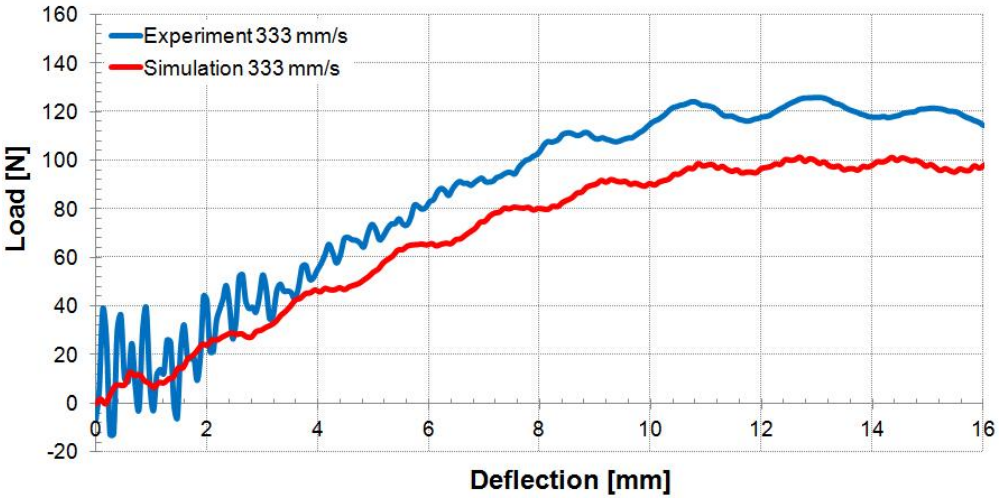

Figure 4.12. Results in dynamic tree-point bending for the hyperelastic material at 333 mm/s

Table 4.4. Stress and strain values recorded for 333 mm/s simulation

Stress	**[MPa]**	**Log strain**	**[mm/mm]**
S_{11}	-57.6	LE_{11}	-0.207
S_{22}	-23.61	LE_{22}	-0.091
S_{33}	-31.25	LE_{33}	-0.067
S_{12}	18.2	LE_{12}	0.112
S_{13}	-7.55	LE_{13}	0.042
S_{23}	-18.02	LE_{23}	-0.082
von Mises	63.88	Max Principal	0.074

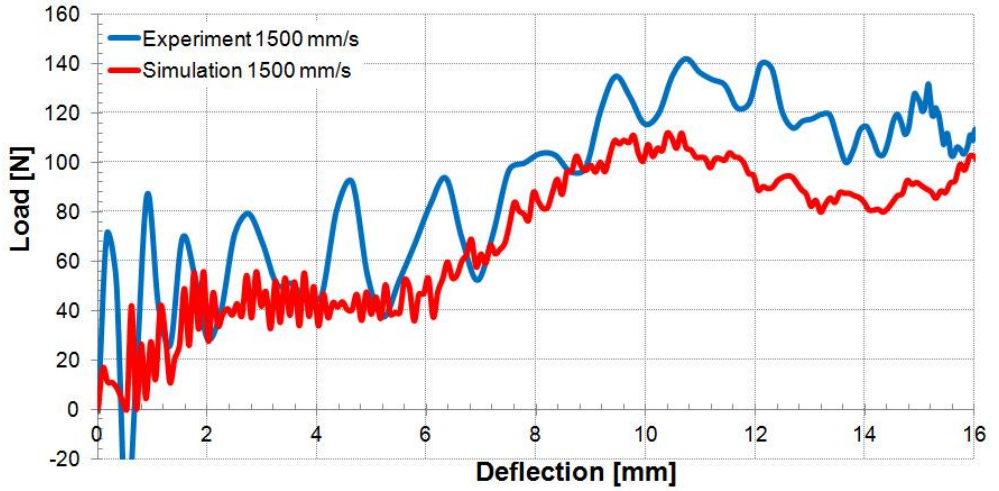

Figure 4.13. Results in dynamic tree-point bending for the hyperelastic material at 1500 mm/s

Table 4.5. Stress and strain values recorded for 1500 mm/s simulation

Stress	**[MPa]**	**Log strain**	**[mm/mm]**
S_{11}	-57.61	LE_{11}	-0.215
S_{22}	-15.81	LE_{22}	-0.074
S_{33}	-30.78	LE_{33}	-0.069
S_{12}	17.93	LE_{12}	0.065
S_{13}	-6.87	LE_{13}	0.047
S_{23}	-8.93	LE_{23}	0.056
von Mises	60.77	Max Principal	0.193

For higher rates of deformation, the oscillations of the simulated stress-strain curves have shapes similar to the experimental curves regarding the type and frequency of the "large" oscillations. Despite the similar shapes of the stress-strain curves, the simulation results show lower reactions regardless of the test speeds. Another difference in the behaviour is the difference in "small" oscillations (noise) for the experiments/simulations. A cause for the difference in results is the conditions of the tests and simulations. As mentioned in Chapter 2, for high deformation speeds, the stiffness of the vices has a noticeable role, altering the results (determining negative values for the reaction force for example). In the simulations, the fixtures were considered analytical rigids, and the reaction forces are only dependent on the tested material.

4.3. Elasto-plastic material model

4.3.1. Material definition

The elasto-plastic material model accounts for Hookean elasticity, the Poisson effect and plasticity with isotropic hardening. In the case of linear elasticity, temperature dependency can be modelled by direct specification of pairs of values of the Young's modulus and corresponding temperature values while strain-rate dependency can only be modelled with the help of the plastic formulation, which allows rate- and temperature-dependent models.

Plastic deformation is deduced from the principle of strain decomposition [**6**,**49**,**67**]:

$$\varepsilon = \varepsilon^e + \varepsilon^p \tag{4.1}$$

where $\mathcal{E}$ is the total strain, ε^e is the elastic strain and ε^p is the plastic strain.

Plastic strain values can be determined from cyclic tests as follows: when loading a specimen up to a given amplitude σ_1 a resulting nominal strain ε_1 is obtained. When unloaded to 0, a remnant deformation is observed (Figure 4.14). This represents the plastic component of the total strain. The elastic component can be obtained by subtracting the plastic strain from the nominal strain. Thus, for a given amplitude σ_1 the corresponding plastic deformation ε_{p1} is obtained. This procedure is repeated for the rest of the amplitudes.

$$\sigma_n \rightarrow \varepsilon_n = \varepsilon_{pn} + \varepsilon_{en} \tag{4.2}$$

The graphic representation of the variation in plastic and elastic strain with total strain is presented in Figure 4.15.

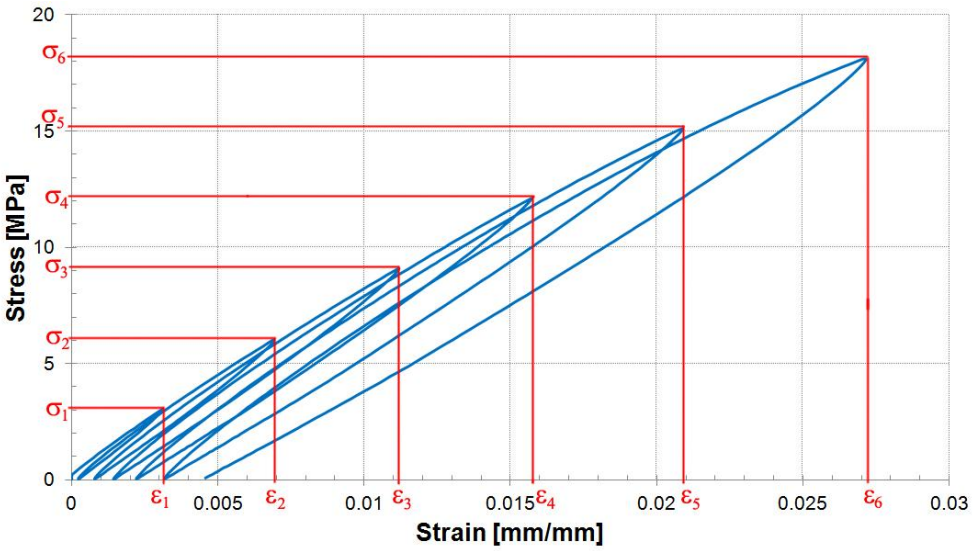

Figure 4.14. Determination of plastic strain and corresponding yield stress

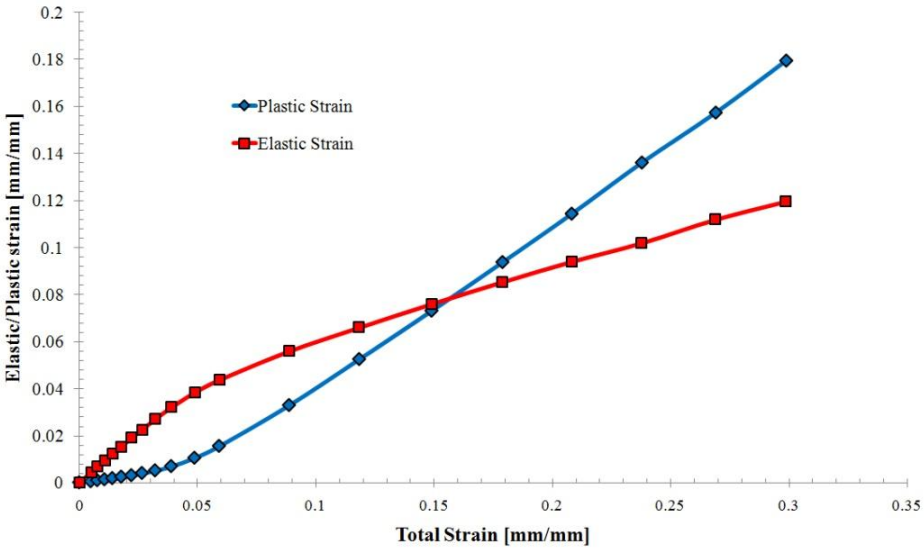

Figure 4.15. Nominal strain decomposition into its plastic and elastic components, for 200mm/min test

If cyclic tests are unavailable, plastic deformation can be obtained from the tensile stress-strain curves by means of a method used for metal plasticity: for a certain amount of plastic deformation ε^p a line, parallel to the elastic portion is generated. Its intersection with the tensile stress-strain curve determines the total

strain ε and the yield stress σ for the chosen value of plastic deformation [**27**,**49**,**67**].

$$y = Ex + a \tag{4.3}$$

where E is the modulus of elasticity and a is a given offset, which represents the plastic strain.

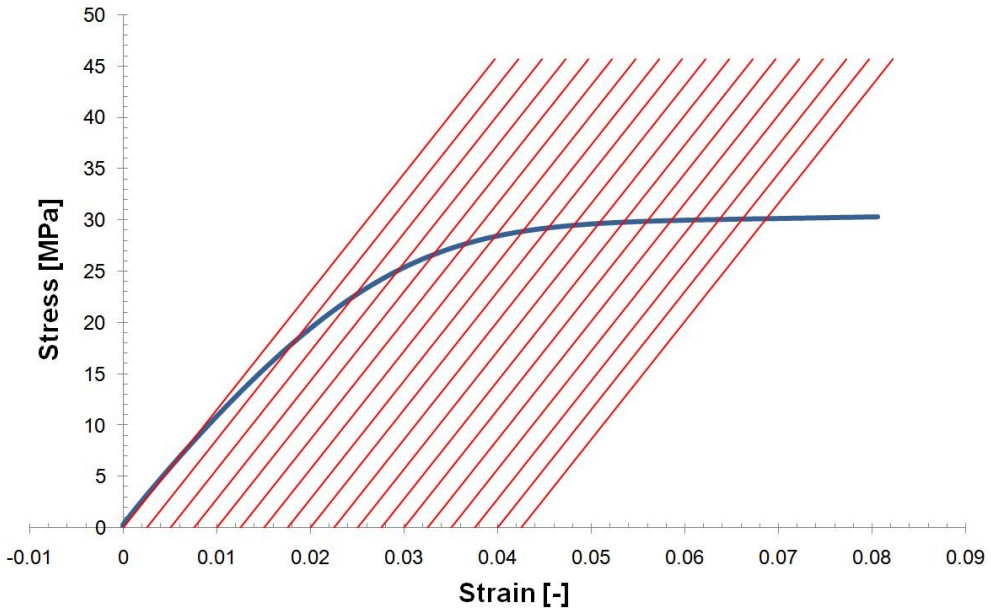

Figure 4.16. Determination of plasticity values beyond cyclic tests

In modelling elasto-plastic materials with isotropic hardening Abaqus requires pairs of Kirchhoff yield stress and corresponding logarithmic plastic strain as input data [**62**]. As volumetric variation during tensile testing could not be recorded, the deformation was considered isochoric and thus the Kirchhoff stress was considered equal to the true (Cauchy) stress [**11**]. Based on the isochoric transformation, the true stress and logarithmic strain were determined from nominal stress and strain with the help of the following relations:

$$\sigma = s \cdot (1 + e) \tag{4.4}$$
$$\varepsilon = \ln(1 + e), \tag{4.5}$$

where σ is the true (Cauchy) stress, s is the nominal (engineering) stress, e is the nominal (engineering) strain and ε is the logarithmic strain.

4.3.2. Material evaluation

4.3.2.1. Uniaxial tests in tension

Following the procedure mentioned above, the Kirchhoff yield stress-logarithmic plastic strain curves were obtained for each deformation speed and temperature (results for ambinent temperature presented in Figure 4.17). The curves were used as input in a single material model using temperature- and rate-dependent options (the average strain-rate for each test was chosen).

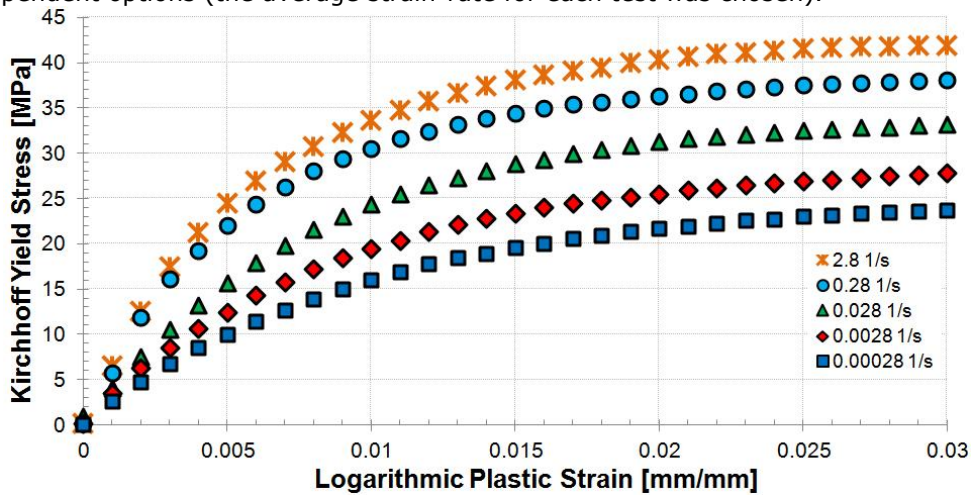

Figure 4.17. Logarithmic plastic strain variation with Kirchhoff yield stress for five strain-rates at ambient temperature

Simulations were performed for all experimental data in tension: strain rate variation on logarithmical scale from 0.00028 s^{-1} to 2.8 s^{-1} and the four temperatures used in experiments: -25°C, 0°c, 23°C and 50°C. All simulations determined accurate results. The stress-strain curves are presented in Figure 4.20 (-25 °C), Figure 4.19 (0°C), Figure 4.20 (23 °C) and Figure 4.21 (50 °C).

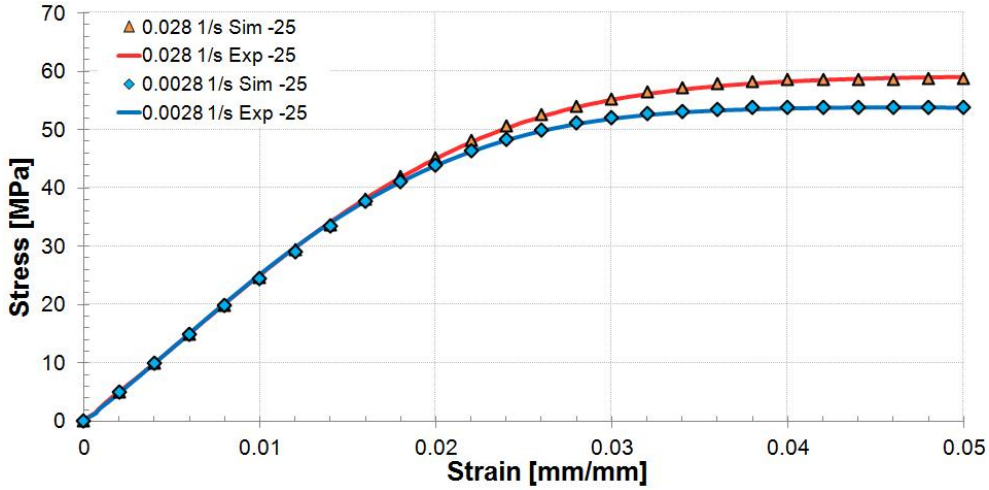

Figure 4.18. Elasto-plastic material evaluation for static test in tension at -25 °C

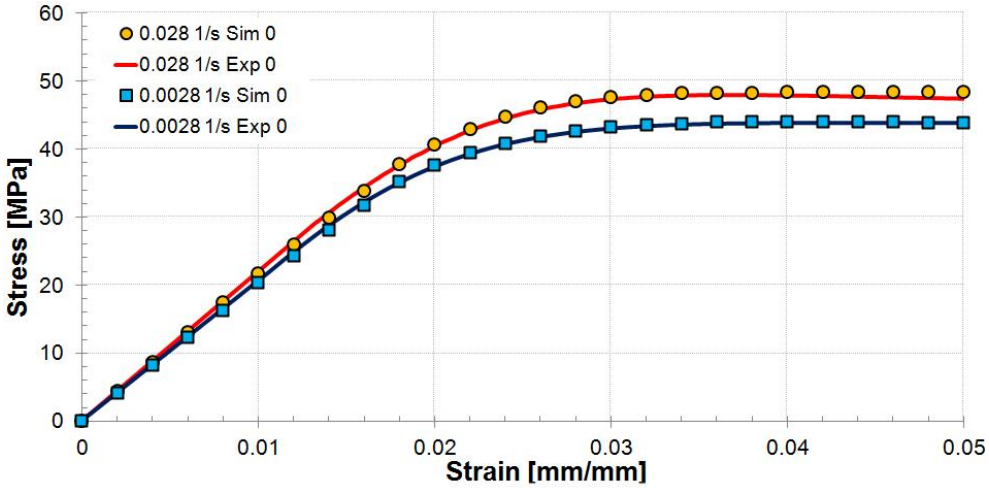

Figure 4.19. Elasto-plastic material evaluation for static test in tension at 0 °C

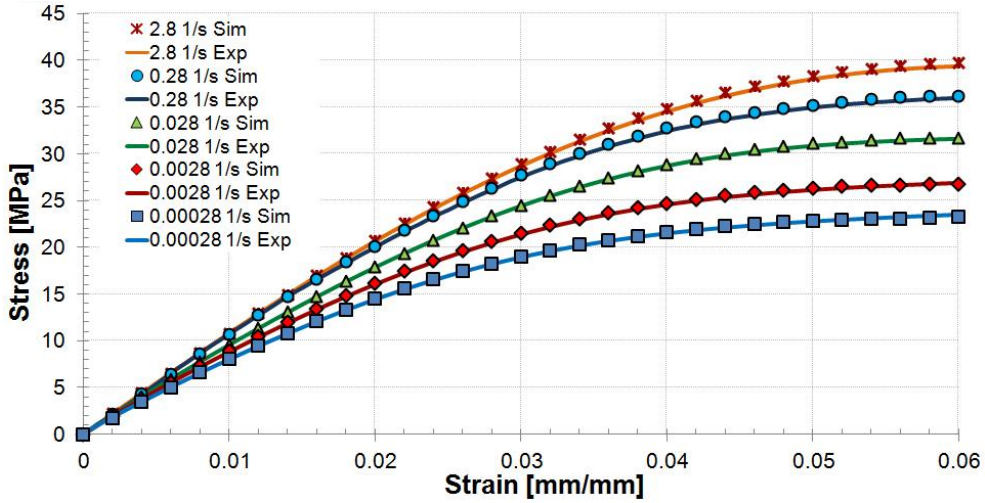

Figure 4.20. Elasto-plastic material evaluation for static test in tension at 23 °C

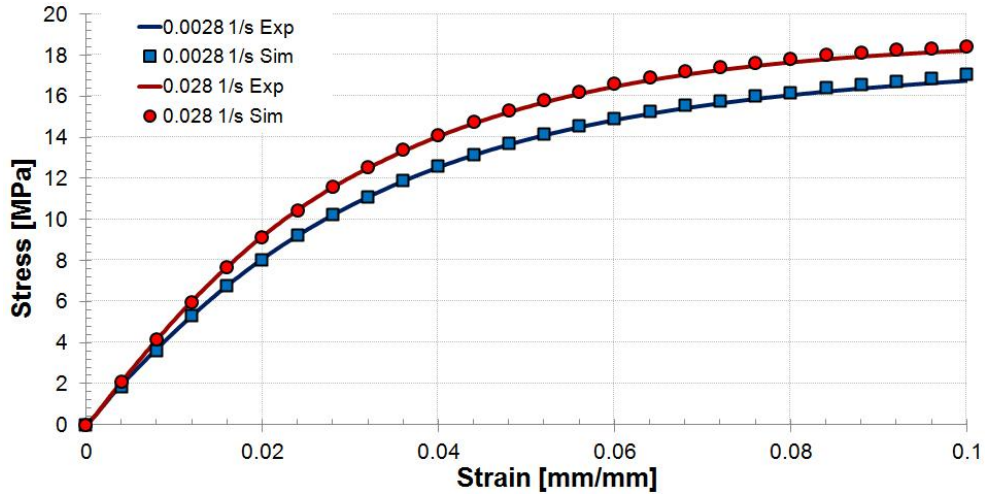

Figure 4.21. Elasto-plastic material evaluation for static test in tension at 50 °C

4.3.2.2. Cyclic tests in tension

Cyclic tests in tension were performed for two programs: 3 amplitudes of 10 cycles per block and 5 amplitudes, one cycle per amplitude. Results for the simulations are presented in Figure 4.22. As with hyperelastic simulations, experimental results are recalled for comparison purposes.

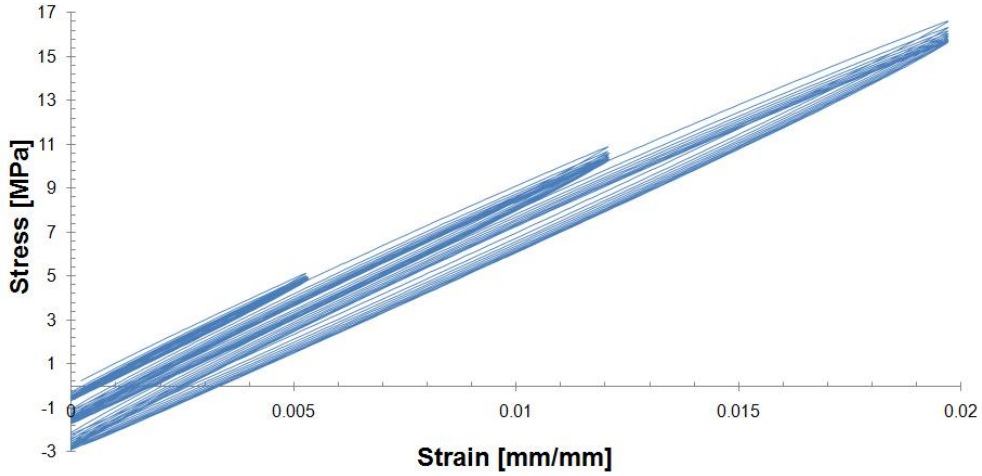

Figure 2.1.12. Experimental results for cyclic loadings with 3 blocks of 10 cycles each

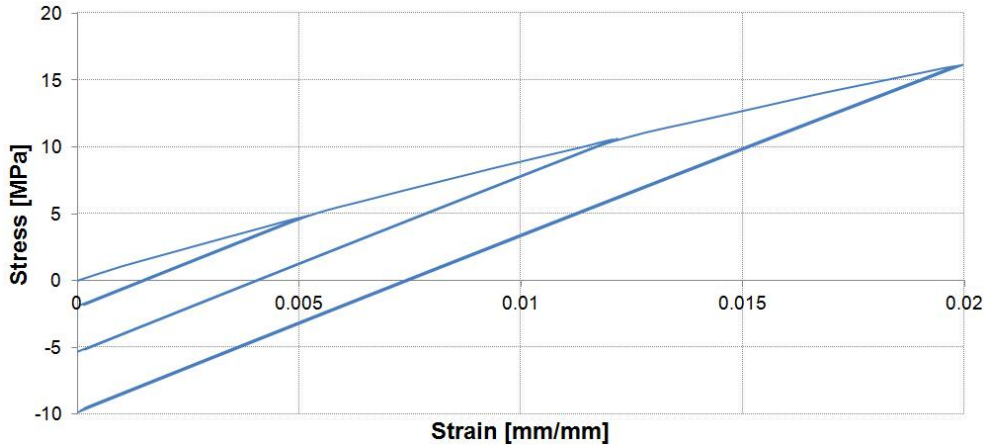

Figure 4.22. Simulated results for cyclic loadings with the elasto-plastic model, first programme

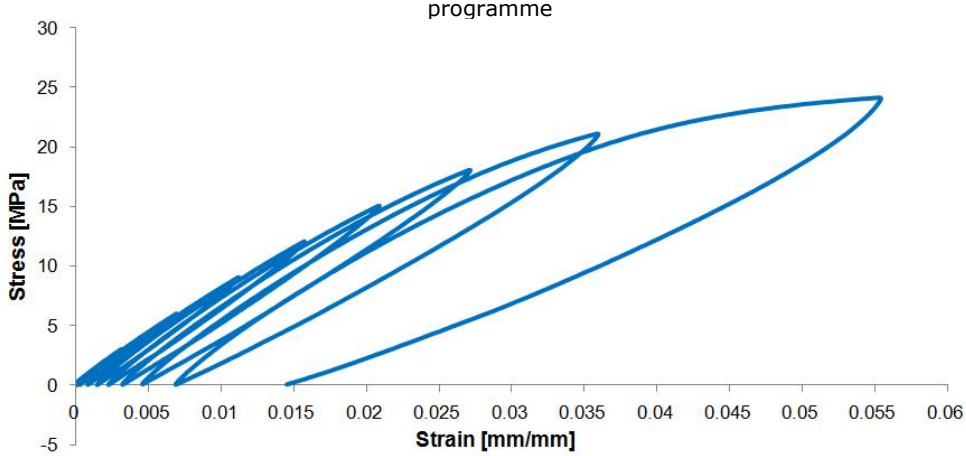

Figure 2.1.14. Experimental results for cyclic loadings with 8 cycles

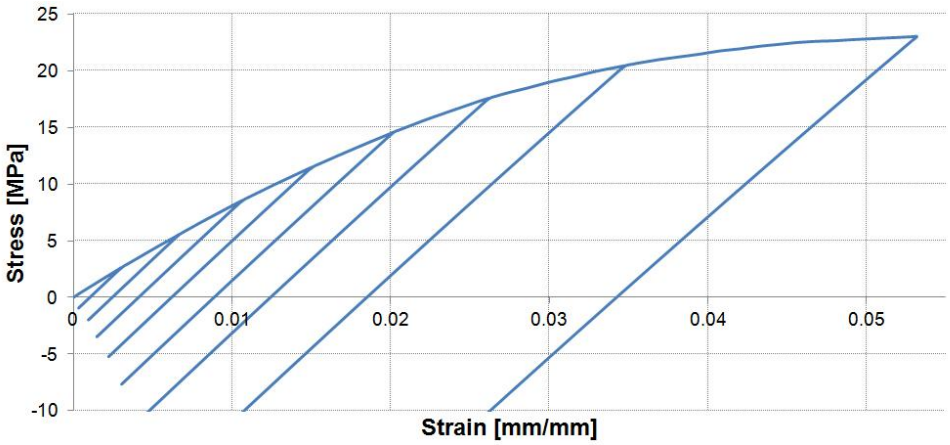

Figure 4.23. Simulated results for cyclic loadings with the elasto-plastic model, secomd programme

4.3.2.3. Static three-point bending tests

The results for static three-point bending tests are presented in Figure 4.24.

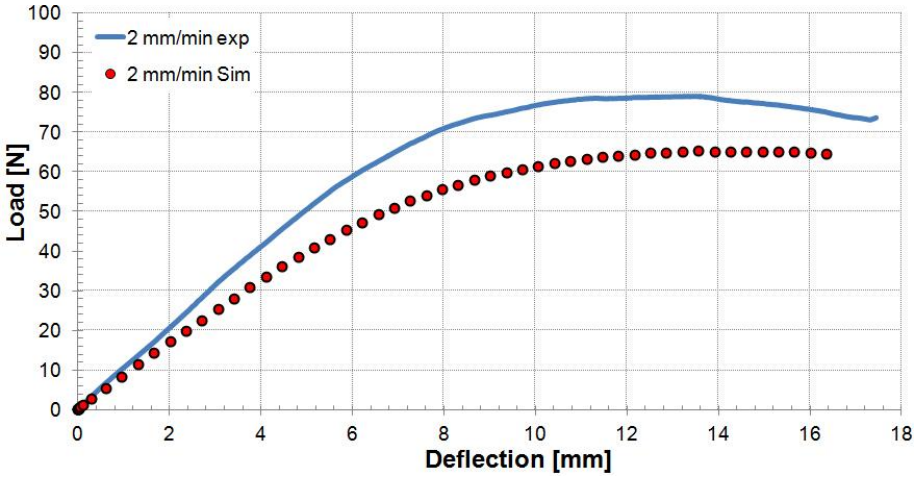

a)

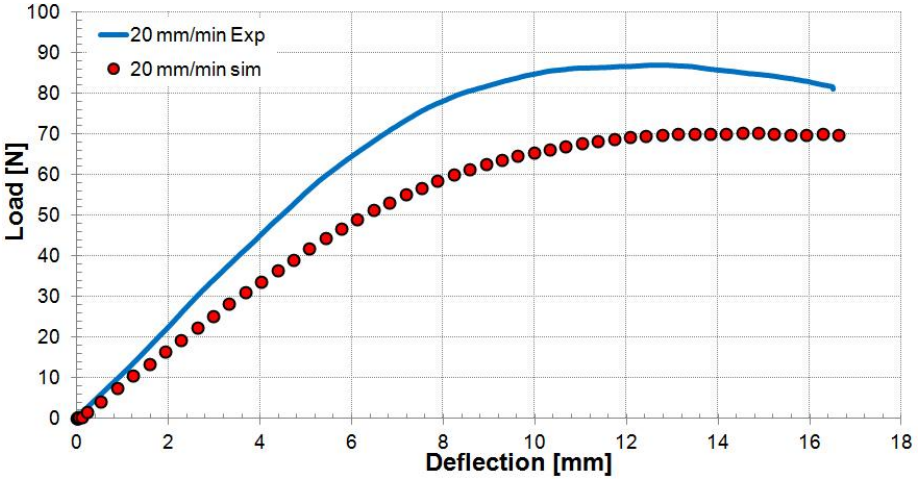

b)

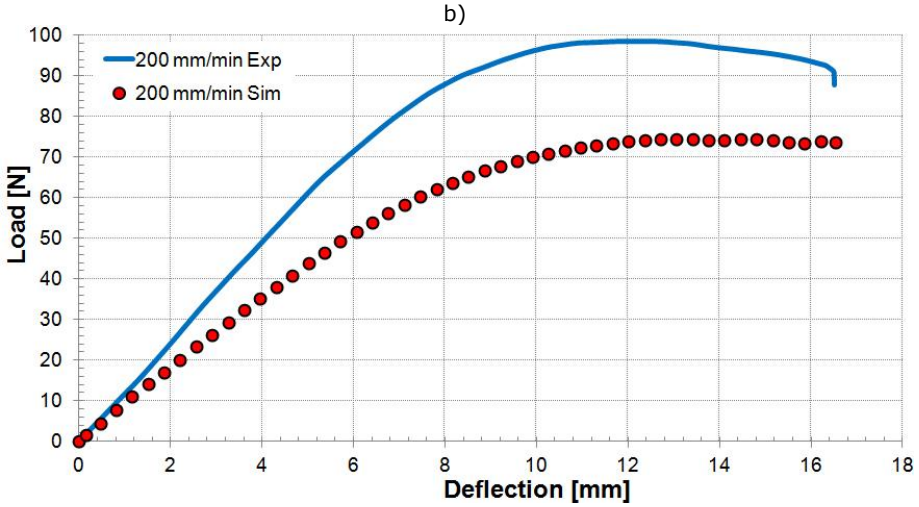

c)

Figure 4.24. Results in static tree-point bending for the elasto-plastic material at a) 2 mm/min, b) 20 mm/min and c) 200 mm/min

Similar to the hyperelastic material, the elasto-plastic model underestimates material behaviour, regardless of the chosen test speed. In terms of flexural strength, the predicted material behaviour is 17% softer for 2 mm/min simulations (65N instead of 79N), 20% softer for 20 mm/min simulations (70N instead of 87N) and 24% softer for 200 mm/min simulations (74N instead of 98N).

Simulations with temperature correction also determined lower reactions and elastic moduli. Simulations performed on a predefined temperature (input in Abaqus with the help of *Predefined fields* option [**62**]) of 18 °C determined an increase of only 7% in flexural strength

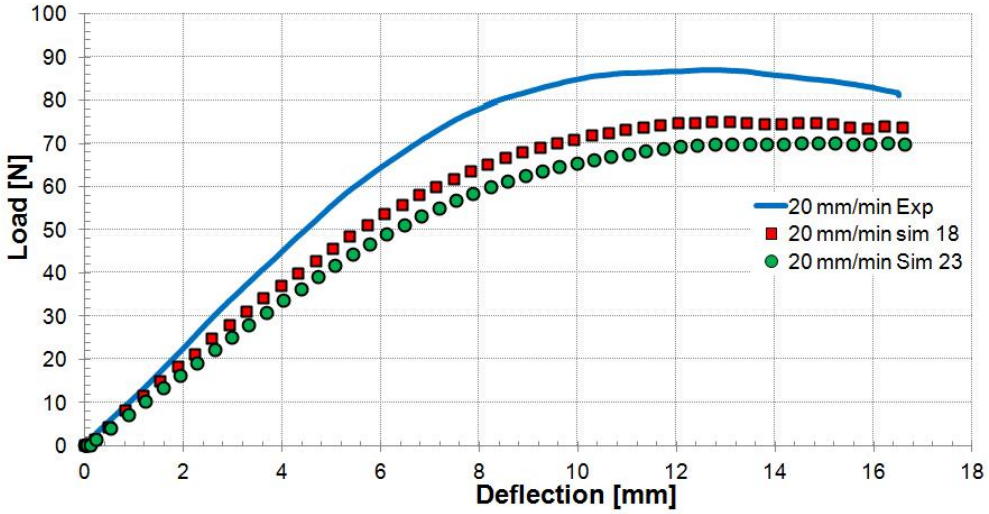

Figure 4.25. Results in static tree-point bending for the elasto-plastic material at different temperatures

Since the simulation conditions are identical with the ones presented for the hyperelastic material the peak values for stresses and strains remain identical, their values being different due to the different constitutive formulations. Due to the plasticity sub-option, additional information is available regarding plastic deformation. Similar to logarithmical strain variation throughout the specimen, the location of the maximal and minimal values of plastic strain are the same, as seen in Figure 4.26.

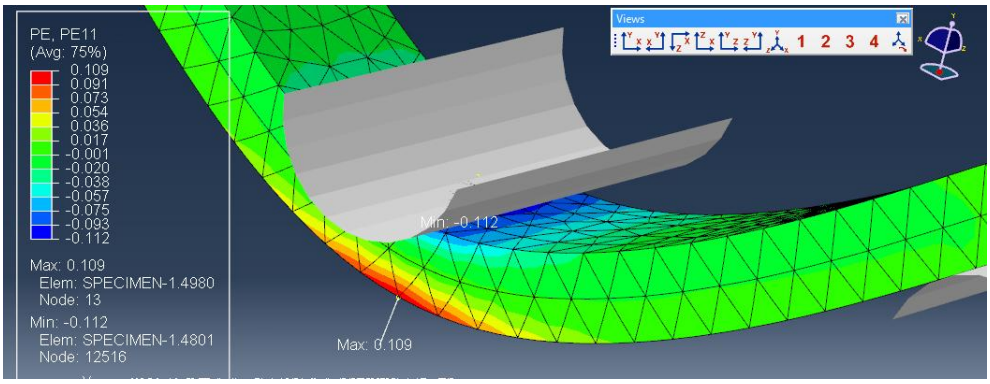

Figure 4.26. Distribution of normal plastic strain along the X axis (PE11)

The results for the true stresses, logarithmical strains and plastic strains for all test speeds are presented in Table 4.6 – Table 4.8. Total logarithmical strain decomposition into its elastic and plastic components is presented in Figure 4.27 – Figure 4.28.

Table 4.6. Stress and strain values recorded for 2 mm/min simulation

Stress	[MPa]	Log strain	[mm/mm]	Plastic strain	[mm/mm]
S_{11}	-53.29	LE_{11}	0.147	PE_{11}	0.123
S_{22}	-42.13	LE_{22}	0.085	PE_{22}	0.075
S_{33}	-22.28	LE_{33}	-0.068	PE_{33}	-0.060
S_{12}	-11.97	LE_{12}	0.087	PE_{12}	-0.067
S_{13}	-3.42	LE_{13}	0.018	PE_{13}	0.013
S_{23}	-8.35	LE_{23}	-0.063	PE_{23}	-0.052
von Mises	39.7	Max Principal	0.147	Max Principal	0.123

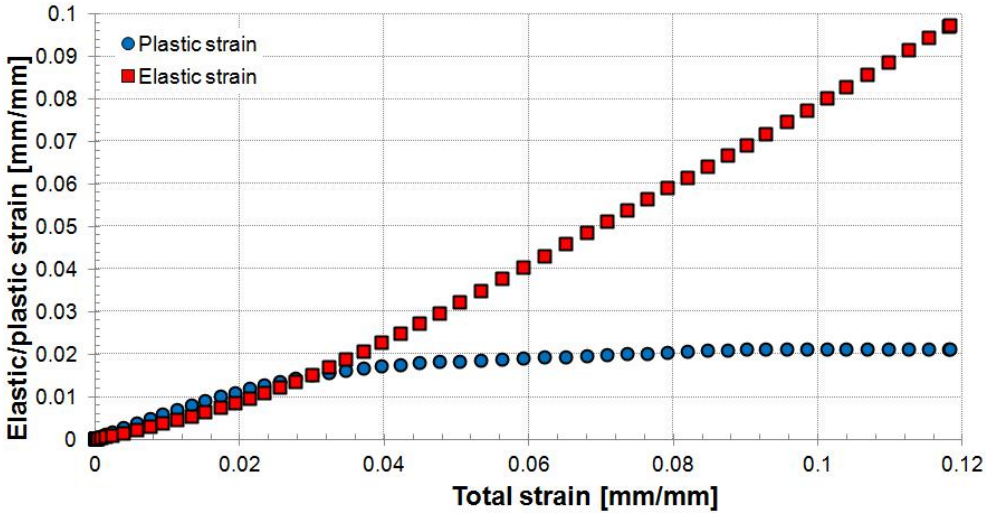

Figure 4.27. Total logarithmical strain (LE) decomposed into its elastic (EE) and plastic (PE) components 2 mm/min simulation

Table 4.7. Stress and strain values recorded for 20 mm/min simulation

Stress	[MPa]	Log strain	[mm/mm]	Plastic strain	[mm/mm]
S_{11}	-55.72	LE_{11}	0.137	PE_{11}	0.111
S_{22}	-41.47	LE_{22}	0.078	PE_{22}	0.067
S_{33}	-22.97	LE_{33}	-0.063	PE_{33}	-0.054
S_{12}	12.84	LE_{12}	0.085	PE_{12}	0.064
S_{13}	-3.26	LE_{13}	0.016	PE_{13}	0.01
S_{23}	8.36	LE_{23}	-0.062	PE_{23}	-0.047
von Mises	40.83	Max Principal	0.137	Max Principal	0.111

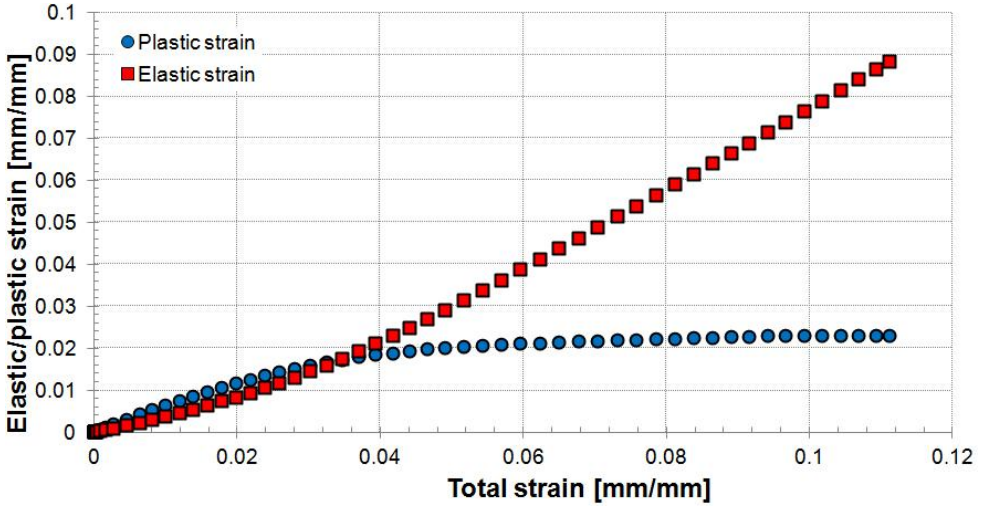

Figure 4.28. Total logarithmical strain (LE) decomposed into its elastic (EE) and plastic (PE) components 20 mm/min simulation

Table 4.8. Stress and strain values recorded for 200 mm/min simulation

Stress	**[MPa]**	**Log strain**	**[mm/mm]**	**Plastic strain**	**[mm/mm]**
S_{11}	-62.19	LE_{11}	0.134	PE_{11}	0.105
S_{22}	-44.15	LE_{22}	0.076	PE_{22}	0.064
S_{33}	-25.29	LE_{33}	-0.061	PE_{33}	-0.051
S_{12}	14.36	LE_{12}	0.081	PE_{12}	0.057
S_{13}	-3.42	LE_{13}	0.015	PE_{13}	0.009
S_{23}	8.83	LE_{23}	-0.056	PE_{23}	-0.039
von Mises	45.93	Max Principal	0.134	Max Principal	0.105

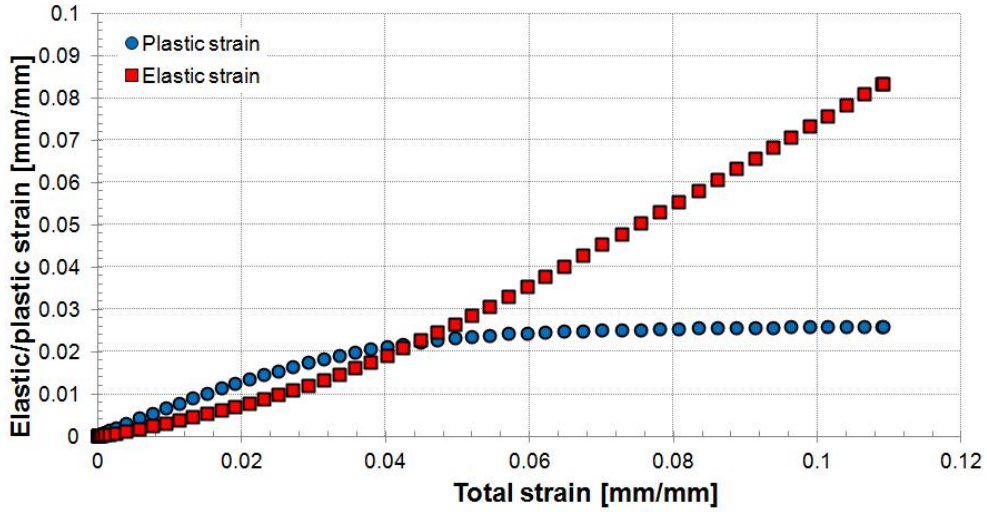

Figure 4.29. Total logarithmical strain (LE) decomposed into its elastic (EE) and plastic (PE) components 200 mm/min simulation

4.3.2.4. Dynamic three-point bending tests

As with the static scenario, the dynamic simulations determined lower values in reaction force, regardless of the strain-rate dependent calibration test data used. The results for three-point bending at 333 mm/s and 1500 mm/s are presented in Figure 4.30 and in Figure 4.31 respectively.

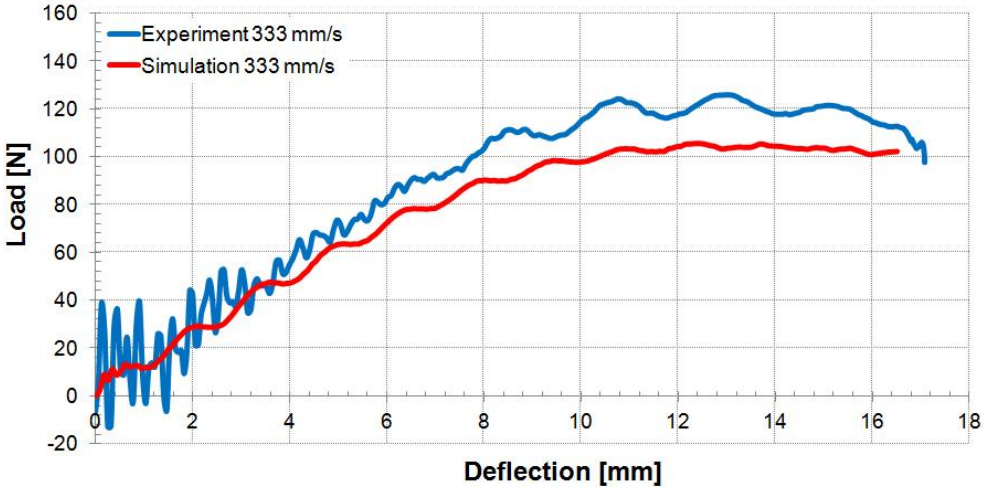

Figure 4.30. Results in dynamic tree-point bending for the elasto-plastic material

Table 4.9. Stress and strain values recorded for 333 mm/s simulation

Stress	[MPa]	Log strain	[mm/mm]	Plastic strain	[mm/mm]
S_{11}	-82.9	LE_{11}	0.15	PE_{11}	0.118
S_{22}	-74.78	LE_{22}	0.094	PE_{22}	0.075
S_{33}	-34.87	LE_{33}	-0.068	PE_{33}	-0.057
S_{12}	-18.68	LE_{12}	0.082	PE_{12}	0.059
S_{13}	-5.12	LE_{13}	0.018	PE_{13}	0.012
S_{23}	17.4	LE_{23}	-0.079	PE_{23}	-0.063
von Mises	62.49	Max Principal	0.15	Max Principal	0.118

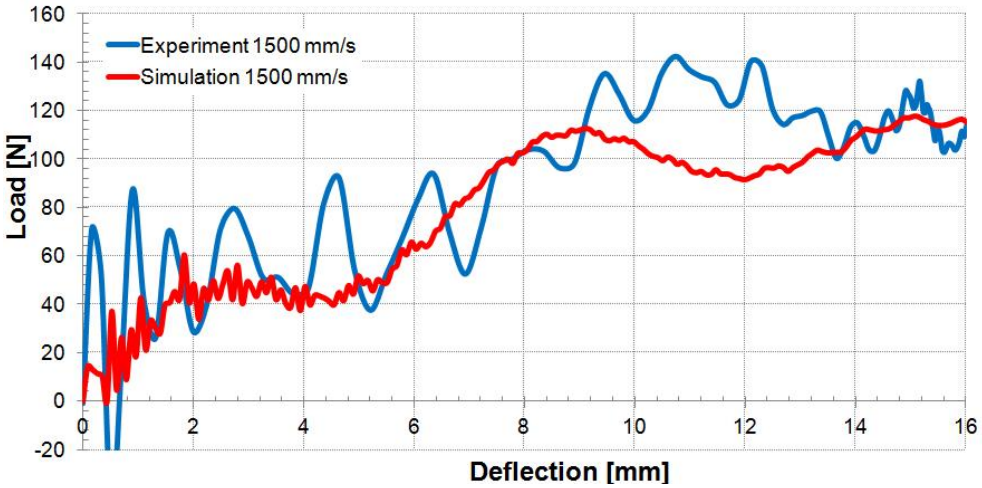

Figure 4.31. Results in dynamic tree-point bending for the elasto-plastic material at 1500 mm/s

Table 4.10. Stress and strain values recorded for 1500 mm/s simulation

Stress	**[MPa]**	**Log strain**	**[mm/mm]**	**Plastic strain**	**[mm/mm]**
S_{11}	-87	LE_{11}	0.211	PE_{11}	0.191
S_{22}	-33.65	LE_{22}	0.122	PE_{22}	0.114
S_{33}	-42.06	LE_{33}	-0.101	PE_{33}	-0.093
S_{12}	24.15	LE_{12}	-0.117	PE_{12}	-0.101
S_{13}	-8.63	LE_{13}	0.036	PE_{13}	0.028
S_{23}	6.24	LE_{23}	0.064	PE_{23}	-0.059
von Mises	66.21	Max Principal	0.211	Max Principal	0.191

The simulation results in dynamic three-point bending determined similar results to the hyperelastic material models, with little difference in the shape of the stress-strain curve.

4.4. Viscoelastic material model

4.4.1. Material definition

The viscoelastic material is implemented in Abaqus with the help of a generalized Voigt-Kelvin solid. The equation of motion for the solid in creep $d\sigma/dt = 0$ is [12]:

$$\varepsilon(t) = \sigma(0)\left[\frac{1}{E(0)} - \sum_{i=1}^{N}\frac{1}{E_i}\left(1 - e^{-t/\tau_i}\right)\right] \tag{4.49}$$

where $\varepsilon(t)$ is the time dependent strain, $\sigma(0)$ is the constant stress, $E(0)$ is the instantaneous Young's modulus, E_i is the relaxation modulus and τ_i is the relaxation time for the element i.

The adimensional normalized relaxation modulus is defined by [13]:

$$e(t) = E(t) \cdot D(0) = E(t) \cdot \frac{1}{E(0)} = \frac{\sigma(t)}{\varepsilon(0)} \cdot \frac{1}{E(0)} \tag{4.50}$$

In consequence, the normalized relaxation modulus of the generalized Voigt-Kelvin solid will be:

$$e(t) = \frac{E(t)}{E(0)} = 1 - \sum_{i=1}^{N} e_i\left(1 - e^{-t/\tau_i}\right) \tag{4.51}$$

Equation (4.51) is also known as a Prony series. Regardless of the chosen type of input test data, Abaqus will use curve fitting procedures to obtain the relaxation time τ_i and the normalized relaxation modulus $e_i = E_i/E_0$.

The Prony series characterize the **Viscoelastic* suboption and are inputted without any reference to a mechanical model (as it uses normalized terms). The mechanical models can either be elastic, hyperelastic or hyperfoam, and their laws will govern the instantaneous Young's modulus ($E(0)$) (in case of a hyperelastic material, the elastic response will be derived from a strain-energy density function Ψ [**11**]).

For loadings with very high strain rates ($t \to 0$) all the dashpots from the model will behave as solids and equation (4.49) will become:

$$\varepsilon(t) = \frac{\sigma(t)}{E(0)} \tag{4.52}$$

This implies that the elastic/hyperelastic characteristics of the mechanical model should be the ones resulting from tests performed at speeds much higher than the relaxation times τ. The strain-rate dependency is modelled in accordance with equation (4.51): after a given time t, the effective Young's modulus $E(t)$ will be obtained by multiplying the instantaneous modulus with the adimensional relaxation function, according to the relation:

$$E(t) = E(0)\left[1 - \sum_{i=1}^{N} e_i\left(1 - e^{-t/\tau_i}\right)\right] \tag{4.53}$$

A similar procedure is performed for hyperelastic materials as the relaxation function diminishes the stress response resulting from the integration of the elastic potential function.

4.4.2. Viscoelastic models from test data

The experimental results presented in Chapter 2 show that the stress response saturates after a certain deformation speed: there is little difference between the 33.33 mm/s, 333.33 mm/s and 1500 mm/s curves.

Mechanically, this phenomenon can be explained by the behaviour of the macromolecules [**44**]: for strain-rates higher than approx 0.6 s^{-1}, viscous flow inside the material no longer occurs and the material behaves like an elasto-plastic solid.

Abaqus allows two different methods of defining the viscoelastic materials: time-domain and frequency-domain [**62**]. Time-domain viscoelasticity requires the instantaneous elastic modulus for calibrating the material model, which represents the saturated stress-strain curve. Frequency-domain viscoelasticity requires the long term modulus for calibrating the material model. Such input data is unavailable, as no tensile tests were performed on previously relaxed specimens. The long-term relaxation modulus recorded in relaxation experiments would only be able to describe a linear elastic material. In consequence, all inputted data was set in the time-domain viscoelasticity. The viscoelastic material model requires the input of (i) creep/stress relaxation curves, (ii) frequency data or (iii) direct specification of Prony series parameters.

The mathematical model used for the simulations used a *Hyperelastic* material model, a Marlow strain-energy density function [**18**,**62**]. Uniaxial test data for the saturated stress-strain curve was used to calibrate the function and the Poisson coefficient was chosen 0.35.

In order to calibrate the material model, DMA data at low strains, DMA data at high strains as well as creep test data were used in order to calibrate the material model.

– **Viscoelastic material based on DMA data**

The DMA data was used to calibrate the material with the *Time-domain: Frequency* option. The required input coefficients are the real ($\omega\Re(e^*)$) and the imaginary ($\omega\Im(e^*)$) parts of the Fourier transform of the relaxation function $e(t) = [E(t)/E(\infty)\,] - 1$:

$$\omega\Re(e^*) = \frac{E''}{E(\infty)} = \frac{1}{E(\infty)} \cdot E(0) \sum_{i=1}^{N} \frac{e_i \tau_i \omega}{1 + \tau_i^2 \omega^2} \tag{4.54a}$$

$$\omega\Im(e^*) = 1 - \frac{E'}{E(\infty)} = 1 - \frac{1}{E(\infty)} \cdot E(0) \left(1 - \sum_{i=1}^{N} e_i - \sum_{i=1}^{N} \frac{e_i \tau_i^2 \omega^2}{1 + \tau_i^2 \omega^2} \right) \tag{4.54b}$$

where E'' is the loss modulus, E' is the storage modulus (obtained from DMA tests), $E(\infty)$ is the long term modulus, N is the number of Prony series terms (number of elements in the generalized Voigt-Kelvin solid) and ω is the frequency.

The Prony series parameters e_i and τ_i were determined by the software from equations (54.52) using the least square algorithm [**62**].

– **Viscoelastic material based on Creep data**

The creep data was used to calibrate the material with the *Time-domain: Creep* option. The input data is the time dependent generalized creep compliance $d(t)$:

$$d(t) = D(t) \cdot E(0) = \frac{\varepsilon(t)}{\sigma(0)} \cdot \frac{\sigma(0)}{\varepsilon(0)} = \frac{\varepsilon(t)}{\varepsilon(0)} \tag{4.54}$$

The software uses relation (4.51) to fit the Prony series parameters to the experimental data.

The resulting Prony series for the normalized relaxation curves for one set of DMA data and one set of creep data are presented in Figure 4.32, along with the experimental relaxation curve (the inverse of the compliance curve). Due to the reduced number of available experimental data points (only three or four frequencies were tested, depending on the test method) from the DMA tests, there is a rather significant difference between the values of the experimental relaxation curve and the calculated Prony series.

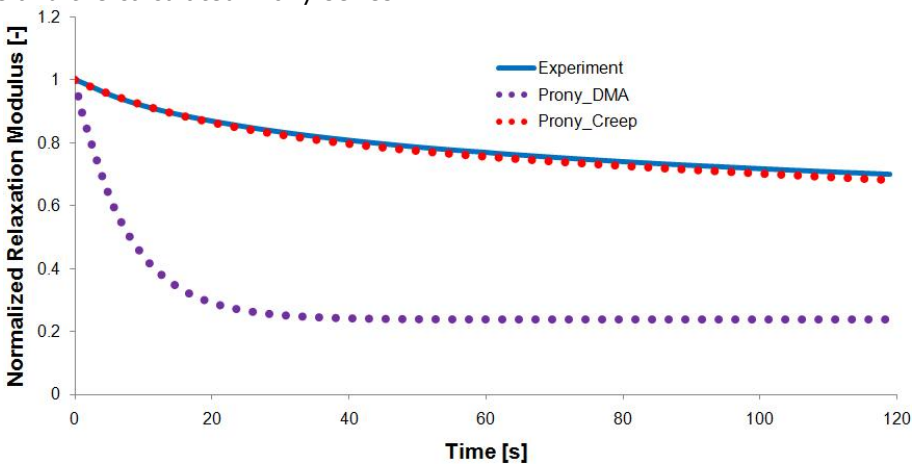

Figure 4.32. Calculated and experimental normalized relaxation curves

– **Viscoelastic material based on experimental data**

The simulations were performed at test speeds identical with the experimental values (logarithmical scale from 0.033 mm/s to 33.33 mm/s, when saturation occurs).

For the DMA data based viscoelastic material, the results are showed in Figure 4.33. The stress response for the DMA based material is much higher than the experimental values, regardless of the test speed.

For the creep based viscoelastic material, the results are presented in Figure 4.34. The material behaviour is similar at high strain rates, but the simulated stresses become significantly higher than the experimental ones as the strain rate decreases.

The conclusion that can be drawn from these simulations is that the Prony series obtained from experimental data are unable to depict an accurate material behaviour regarding strain-rate sensitivity. In order to obtain accurate stress-strain curves for various test speeds, a custom relaxation curve was developed.

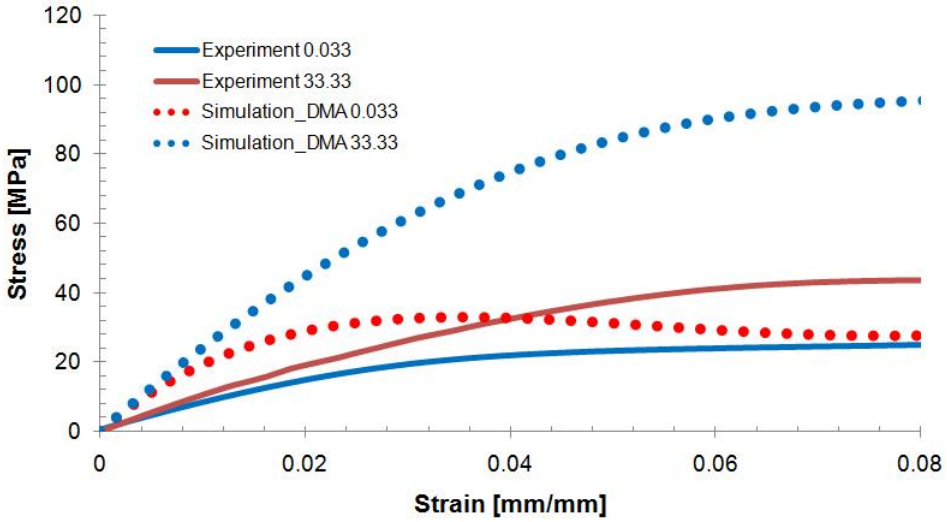

Figure 4.33. Simulation results for the DMA data based viscoelastic material

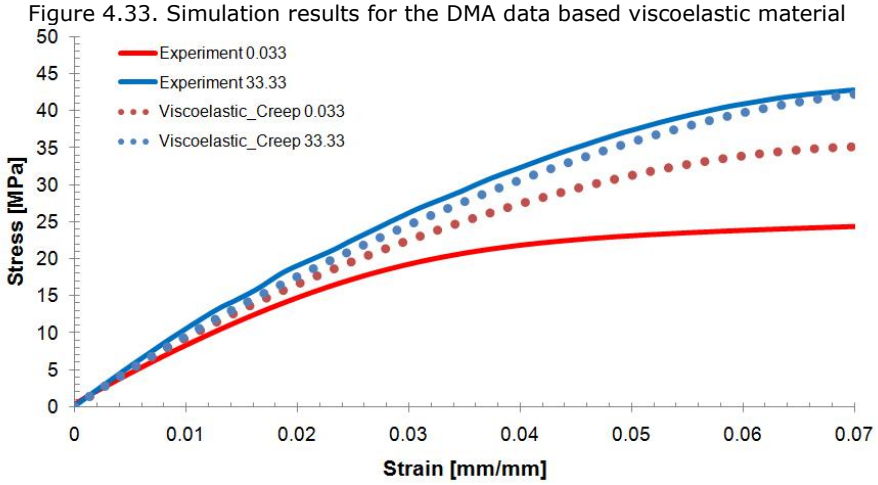

Figure 4.34. Simulation results for the creep data based viscoelastic material

4.4.3. Custom relaxation curve

A reverse engineering approach was used in order to obtain a more accurate response with respect to strain-rate dependency. Instead of determining the relaxation time τ and relaxation function e (Equation 4.53) based on experimental tests, different values for the relative normalized relaxation modulus $e_i(t)$ were determined from experimental stress-strain curves at different deformation speeds.

The first step in determining the custom relaxation curve was to obtain normalized relaxation moduli with respect to the saturation stress-strain response (results obtained for the tests performed at 33.33 mm/s), as a function of strain.

$$\begin{cases} e_{0.03}(\varepsilon) = \dfrac{E_{0.03}(\varepsilon)}{E_{33.3}(\varepsilon)} = \dfrac{\sigma_{0.03}(\varepsilon)}{\sigma_{33.3}(\varepsilon)} \\ e_{0.33}(\varepsilon) = \dfrac{E_{0.33}(\varepsilon)}{E_{33.3}(\varepsilon)} = \dfrac{\sigma_{0.33}(\varepsilon)}{\sigma_{33.3}(\varepsilon)} \\ e_{3.33}(\varepsilon) = \dfrac{E_{3.33}(\varepsilon)}{E_{33.3}(\varepsilon)} = \dfrac{\sigma_{3.33}(\varepsilon)}{\sigma_{33.3}(\varepsilon)} \end{cases} \tag{4.55}$$

Considering the available experimental data, discrete functions were considered (pairs of stress-strain values $\varepsilon(t) \rightarrow \sigma(t)$, Figure 4.35).

Knowing the total time of each test, the strain dependency of each function will be converted into time dependency.

$$t_x(i) = \frac{T_x \cdot \varepsilon(i)}{\varepsilon(T)} \tag{4.56}$$

where t represents the current time, T the total time, $\varepsilon(i)$ the current strain and $\varepsilon(T)$ the total strain, for each crosshead travel speed x.

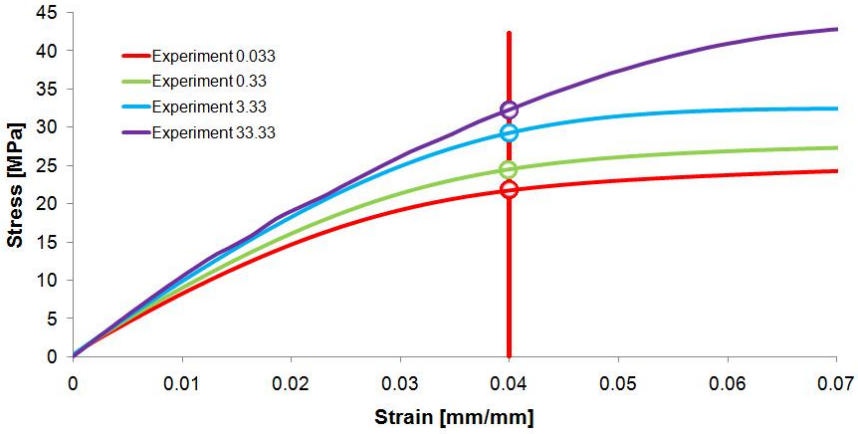

Figure 4.35. Determining stress levels for a reference strain for different test speeds

The time dependency of the normalized relaxation modulus for each crosshead travel speed is presented in Figure 4.36 and Figure 4.37.

The different relaxation behaviour at different strain rates is a consequence of non-linear viscoelasticity. The dashpots characteristics of the mathematical model are not linear (a shear-thickening model would be required instead of a Newtonian fluid [**76**]), as the generalized Kelvin-Voigt solid presumes. In consequence, a new curve must be developed in order to obtain results as accurate as possible for each strain rate. Trial and error iterations were used in order to determine the final version of the relaxation curve, depicted in Figure 4.38 [**46**].

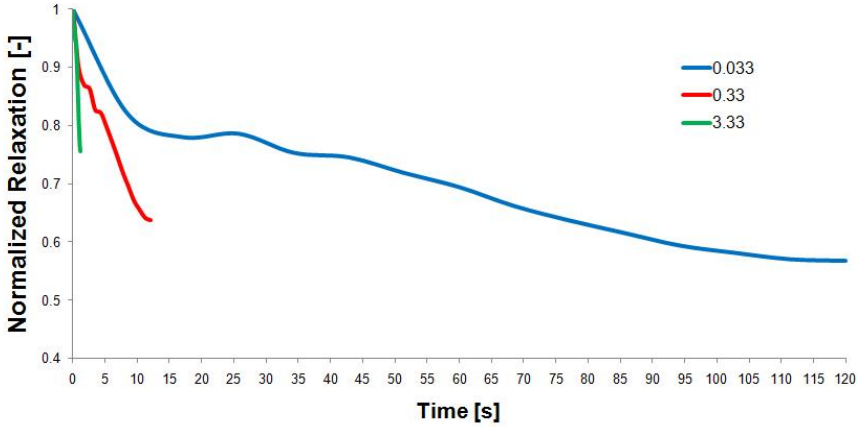

Figure 4.36. Custom normalized relaxation curves for three test speeds

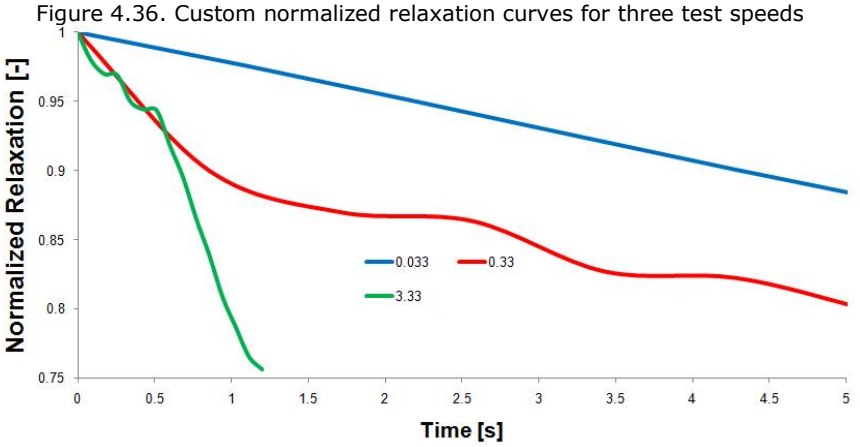

Figure 4.37. Detail of custom normalized relaxation curves for three test speeds

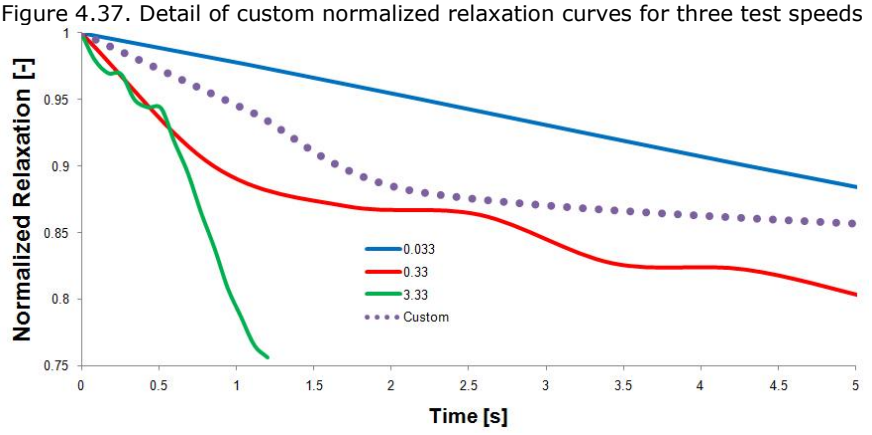

Figure 4.38. Detail of final normalized relaxation curve

4.4.4. Material evaluation

The viscoelastic material model defined in the previous paragraph was evaluated in several loading scenarios.

4.4.4.1. Uniaxial tests in tension

For the uniaxial test in tension, four deformation speeds were tested for the same material model: $2mm/min$; $20mm/min$; $200mm/min$; $2000mm/min$ (Figures 6.11-6.14).

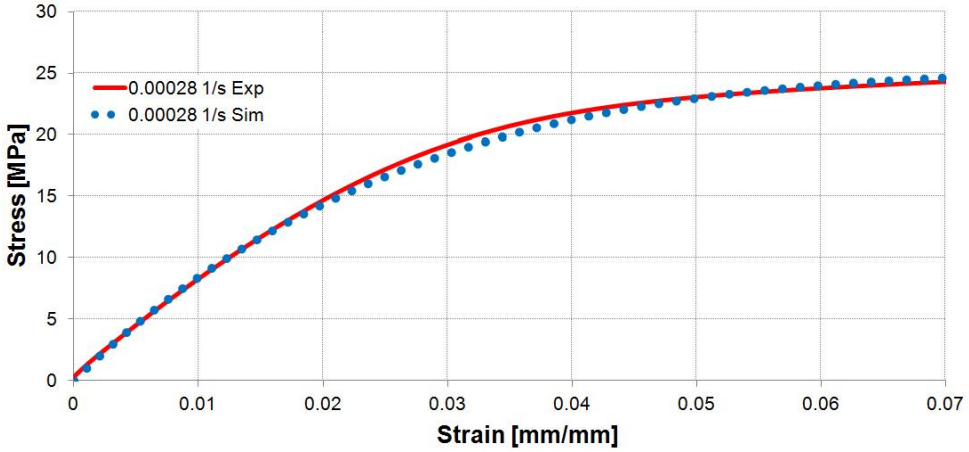

Figure 4.39. Viscoelastic material simulations for a test speed of 0.00028 s^{-1}

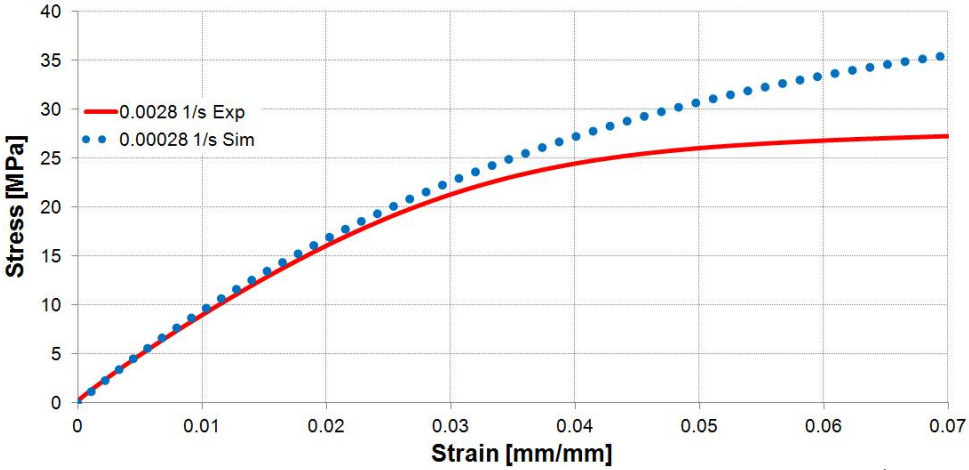

Figure 4.40. Viscoelastic material simulations for a test speed of 0.0028 s^{-1}

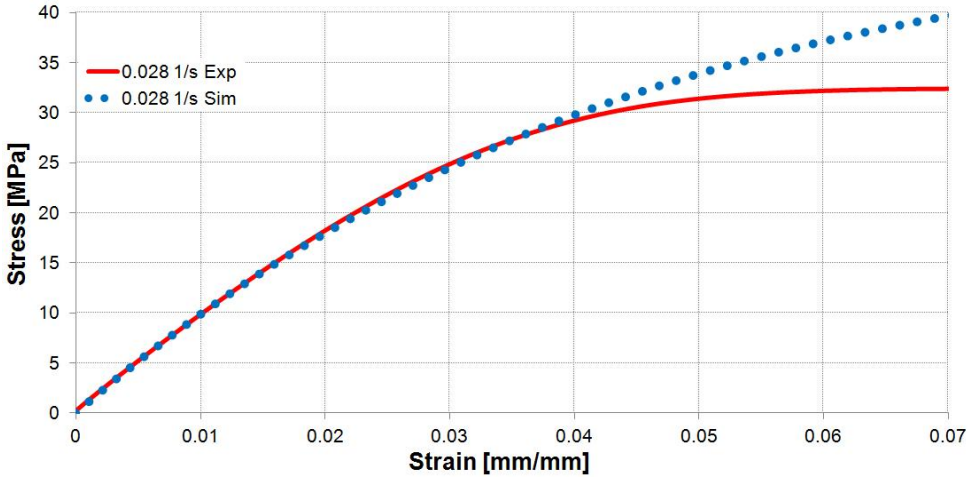

Figure 4.41. Viscoelastic material simulations for a test speed of 0.028 s^{-1}

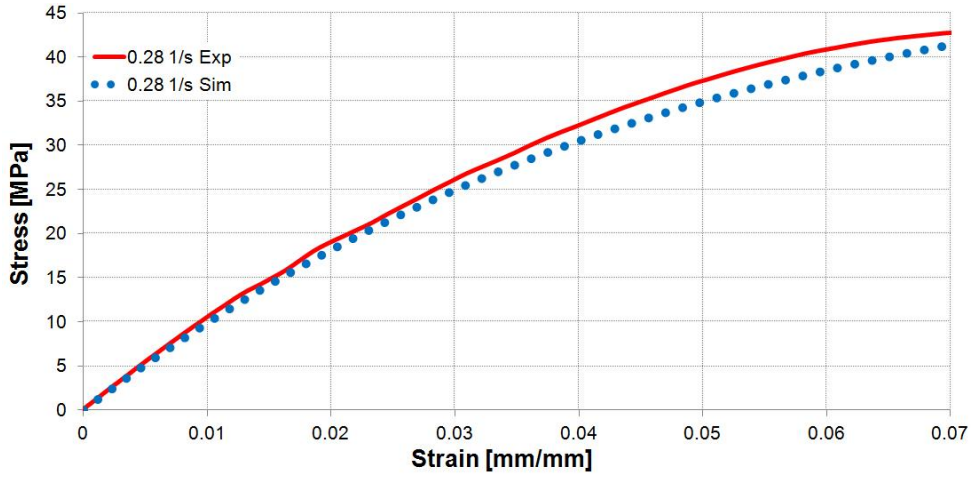

Figure 4.42. Viscoelastic material simulations for a test speed of 0.28 s^{-1}

For static tests, the material model determines accurate results only for very fast or for very low tests speeds. This is due to the fact for these test conditions, material parameters can be input without any interference.

For tests performed at speeds greater than 2000 mm/min, the instantaneous stress-strain response (which is directly input as calibration test data for the Marlow model) characterises the material behaviour (Figure 4.42).

For tests performed at speeds lower than 2 mm/min, the values for the normalized relaxation modulus $d(t)$ for times t longer than 12 seconds (which accounts for 0.01 strain) can be specified directly from the processed experimental data (Figure 4.39).

This procedure cannot be repeated for times shorter than 12 seconds because of viscoelastic nonlinearity. An easier way to explain this aspect is by considering an actual value of relaxation time. After one second for example, the values of the normalized relaxation moduli for each test speed are presented in Table 4.11.

Table 4.11. Normalized relaxation moduli for each test speed after 1 second, and equivalent strain

Test speed [s]	Normalized relaxation modulus [-]	Strain [mm/mm]
0.033	0.97	0.00075
0.33	0.89	0.0075
3.33	0.79	0.075

So, after one second of straining at different rates, the values of the normalized relaxation moduli are higher for low speeds and lower for higher speeds, because of the different level of deformation reached in that amount of time:

- For tests performed at 2 mm/min, a variation of the normalized relaxation modulus for 1 second would hardly make any difference because of the low strain (0.075%) at which it occurs (Figure 4.39).
- For tests performed at 20 mm/min, after one second of deformation the material is strained at 0.75%, which is situated in the elastic domain (before the yield point) (Figure 4.40).
- For tests performed at 200 mm/min, one second of deformation coincides with 7.5% strain which is clearly situated in the plastic domain (after the yield point) (Figure 4.41).

Considering these facts, when designing the custom relaxation curve, it was sensible to choose the normalized stress relaxation value for one second relaxation time corresponding to the tests performed at 20 mm/min. In consequence, the values of the normalized relaxation moduli $d(t)$ were chosen in correspondence with the values from the tests performed at speeds representative for the given relaxation times t.

Another impediment in applying this methodology is that one cannot input the relaxation function as a broken line. The chosen normalized relaxation values had to be tweaked in order to obtain a Prony series that would determine values as accurate as possible for each relaxation time. This aspect determined further inaccuracy of the relaxation function.

4.4.4.2. Cyclic tests in tension

For the cyclic loading simulations, two programs were chosen, in order to observe the non-linear characteristics of the material (strain-softening, hysteresis of energy):

The first test program consisted of 3 blocks, each of a different amplitude, with 10 cycles for each block; The simulations and experimental results are presented in Figure 2.1.12. and Figure 4.43.

The second test program consisted of 8 cycles, each with an equal increment in stress. The simulations and experimental results are presented in Figure 4.44 and Figure 4.45.

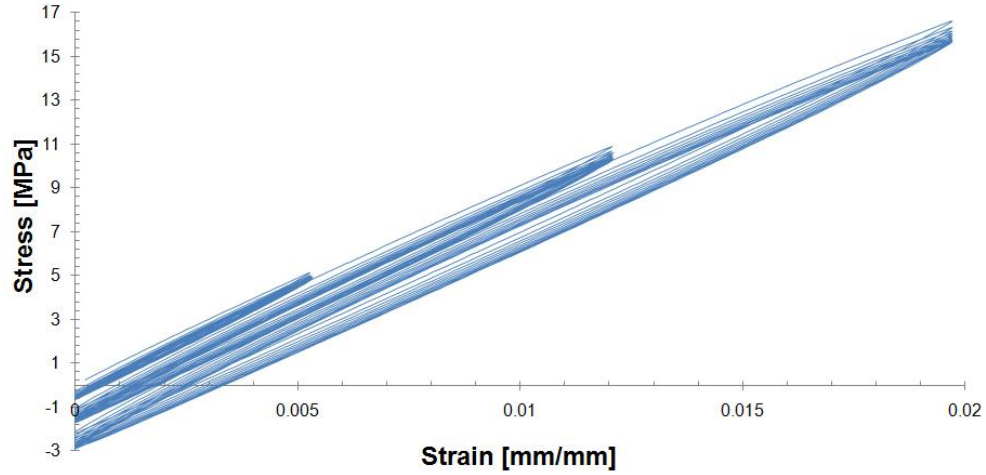

Figure 2.1.12.. Experimental results for cyclic loadings with 3 blocks of 10 cycles each

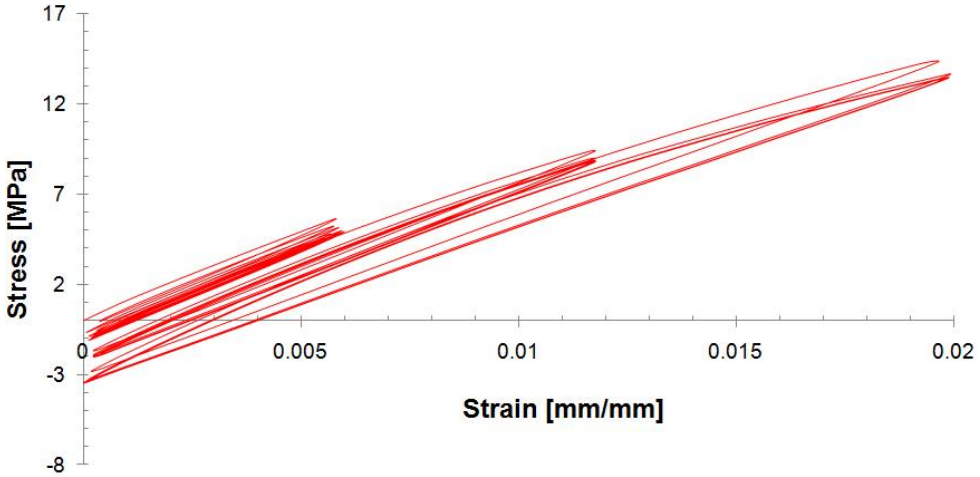

Figure 4.43. Simulation results for cyclic loadings with 3 blocks of 10 cycles each

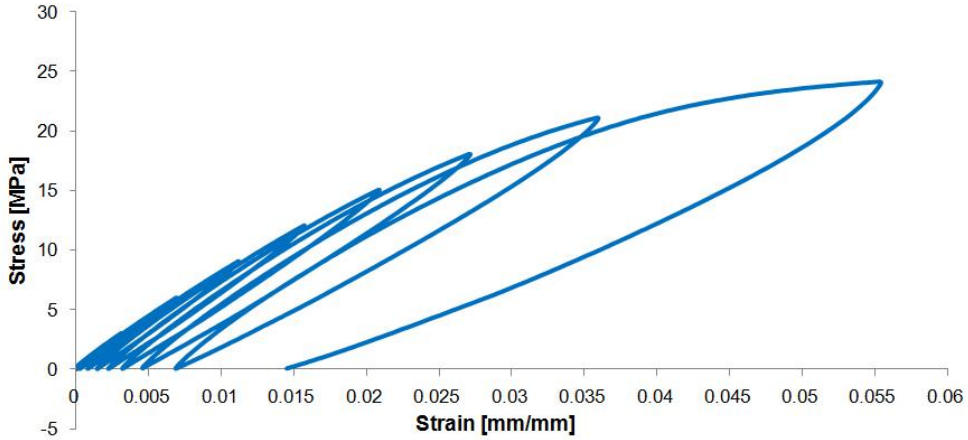

Figure 4.44. Experimental results for cyclic loadings with 8 cycles

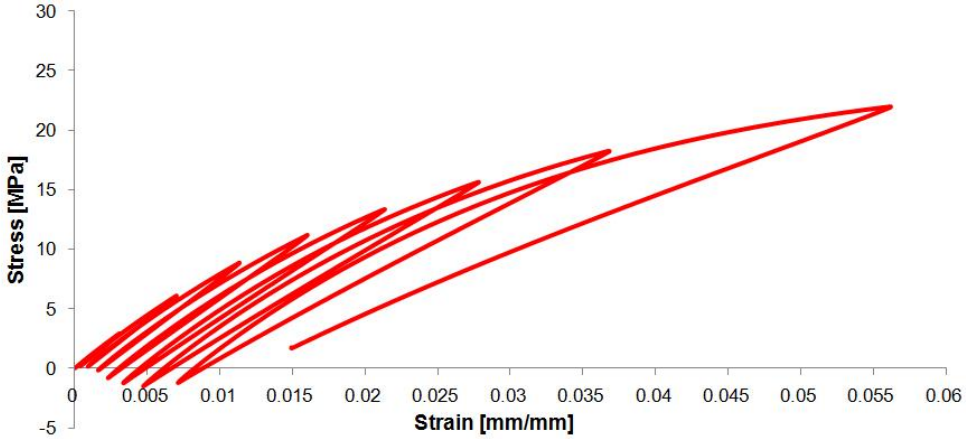

Figure 4.45. Simulation results for cyclic loadings with 8 cycles

Cyclic loadings simulations replicated the softening of the material and the hysteresis in a similar manner to the behaviour observed in experimental tests. The only significant difference is the shape of the unloading curves (which affects the value of the dissipated energy): experiments show a concave shape (Figure 9b) while simulations determine a convex profile (Figure 9a). This feature could be also modelled with the help of a more complex material model, one that would incorporate viscosity as a function of strain and time (the current relaxation function is only time dependent). In Figure 9b) one can observe that the material has a higher relaxation rate at high strains while the simulated curves (Figure 9a) show constant relaxation rate with time.

4.4.4.3. Static three-point bending tests

The results for static three-point bending tests are presented in Figure 4.46.

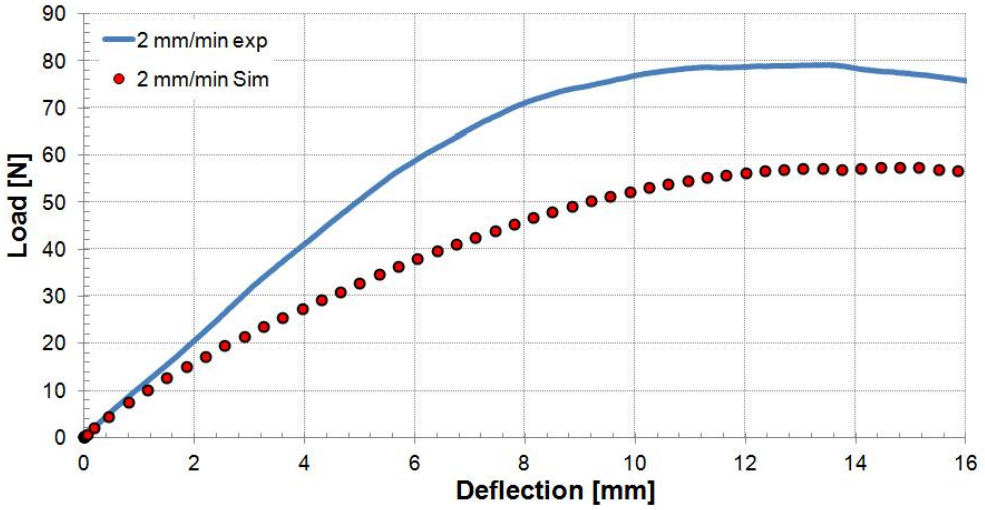
2 mm/min exp
2 mm/min Sim
Load [N]
Deflection [mm]
0
10
20
30
40
50
60
70
80
90
0
2
4
6
8
10
12
14
16

a)

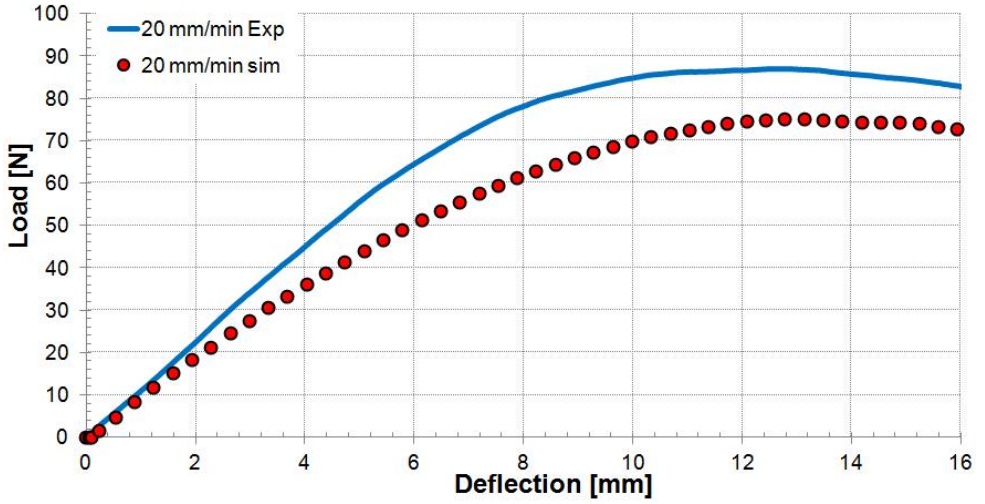
20 mm/min Exp
20 mm/min sim
Load [N]
Deflection [mm]
0
10
20
30
40
50
60
70
80
90
100
0
2
4
6
8
10
12
14
16

b)

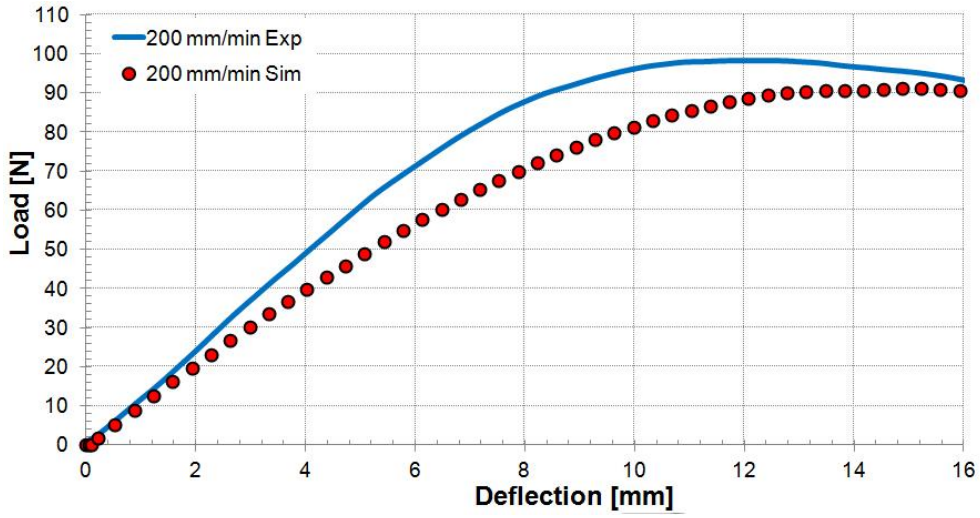

c)

Figure 4.46. Results in static tree-point bending for the viscoelastic material at a) 2 mm/min, b) 20 mm/min and c) 200 mm/min

Similar to the hyperelastic material and the elasto-plastic material model, the viscoelastic model underestimates material behaviour, regardless of the chosen test speed. In terms of flexural strength, the predicted material behaviour is 28% softer for 2 mm/min simulations (57N instead of 79N), 17% softer for 20 mm/min simulations (75N instead of 87N) and 11% softer for 200 mm/min simulations (87N instead of 98N). The errors for the viscoelastic model are lower because, as seen in the paragraph discussing evaluation in tension, this model overestimates material stiffness after around 5% strain.

The results for the true stresses and logarithmical strains for all test speeds are presented in Table 4.12 – Table 4.14.

Table 4.12. Stress and strain values recorded for 2 mm/min simulation

Stress	**[MPa]**	**Log strain**	**[mm/mm]**
S_{11}	-41.52	LE_{11}	0.138
S_{22}	-12.17	LE_{22}	0.07
S_{33}	-10.11	LE_{33}	-0.061
S_{12}	-10.44	LE_{12}	0.073
S_{13}	-3.707	LE_{13}	0.042
S_{23}	2.4	LE_{23}	-0.061
von Mises	35.46	Max Principal	0.138

Table 4.13. Stress and strain values recorded for 20 mm/min simulation

Stress	**[MPa]**	**Log strain**	**[mm/mm]**
S_{11}	-49.15	LE_{11}	0.138
S_{22}	-11.76	LE_{22}	-0.068
S_{33}	-7.41	LE_{33}	-0.059
S_{12}	13.26	LE_{12}	0.071
S_{13}	-5.28	LE_{13}	0.047
S_{23}	10.81	LE_{23}	0.054
von Mises	45.53	Max Principal	0.138

Table 4.14. Stress and strain values recorded for 200 mm/min simulation

Stress	[MPa]	Log strain	[mm/mm]
S_{11}	-59.73	LE_{11}	-0.148
S_{22}	-13.42	LE_{22}	-0.061
S_{33}	-10.99	LE_{33}	-0.056
S_{12}	16.59	LE_{12}	-0.069
S_{13}	7.18	LE_{13}	0.052
S_{23}	9.86	LE_{23}	0.039
von Mises	57.88	Max Principal	0.14

4.4.4.4. Dynamic three-point bending tests

As with the static simulations, the dynamic simulations determined lower values in reaction force, regardless of the tested strain-rate. The force-deflection curves for three-point bending at 333 mm/s and 1500 mm/s are presented in Figure 4.47 and in Figure 4.48 respectively and the values for the stress and strain components are presented in Table 4.4 and Table 4.5.

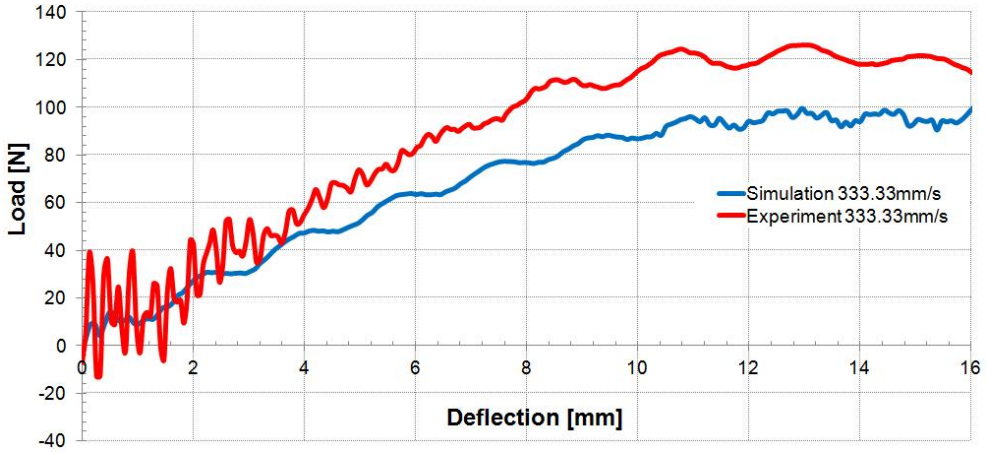

Figure 4.47. Three-point bending experiment and simulation at 333 mm/s

Table 4.15. Stress and strain values recorded for 2 mm/min simulation

Stress	[MPa]	Log strain	[mm/mm]
S_{11}	-64.76	LE_{11}	0.15
S_{22}	-22.13	LE_{22}	-0.054
S_{33}	7.52	LE_{33}	-0.053
S_{12}	25.26	LE_{12}	-0.073
S_{13}	-6.89	LE_{13}	-0.036
S_{23}	-23.23	LE_{23}	-0.101
von Mises	65.65	Max Principal	0.15

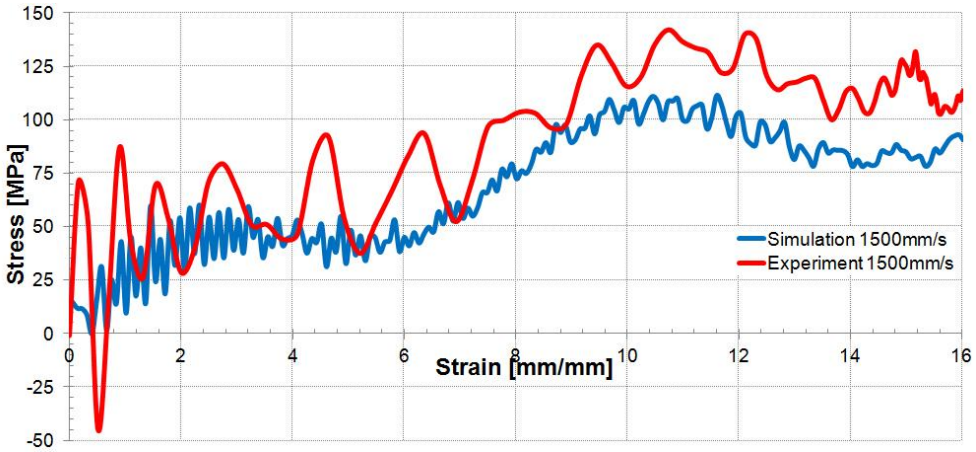

Figure 4.48. Three-point bending experiment and simulation at 1500 mm/s

Table 4.16. Stress and strain values recorded for 2 mm/min simulation

Stress	**[MPa]**	**Log strain**	**[mm/mm]**
S_{11}	-66.48	LE_{11}	-0.16
S_{22}	-20.54	LE_{22}	-0.056
S_{33}	-7.68	LE_{33}	-0.053
S_{12}	-18.4	LE_{12}	0.068
S_{13}	9.15	LE_{13}	0.38
S_{23}	-15.14	LE_{23}	0.66
von Mises	66.29	Max Principal	0.15

The simulation results in dynamic three-point bending determined similar results to the rest of the evaluated material models, with little difference in the shape of the stress-strain curve.

4.5. Top plate simulations

This set of simulations was performed of meshed CAD model of a top plate which is part of the adidas Titan™ running shoe. The mesh consisted of 1,193,392 nodes and 1,920,255 C3D10M elements (Figure 4.49).

The top plate simulations are meant to replicate the experimental procedures presented in Chapter 2, Paragraph 4. In consequence, the boundary conditions consisted of an encastre of the top surface of the model and the compression of the rear cushioning element only. This was achieved by generating a disk-shaped analytical rigid whose only degree of freedom was along the Z axis (the direction that determines the compression of the rear cushioning element, Figure 4.50). The interaction between the rigid and the mesh was set as surface to node region with a penalty type tangential behaviour (0.25 friction coefficient) and "hard" tangential contact, for the interaction properties.

Due to the long experimental test time (around 0.4 s), the simulations were performed in Abaqus Standard (static simulations). The travel and the reaction force were recorded for the reference point of the analytical rigid.

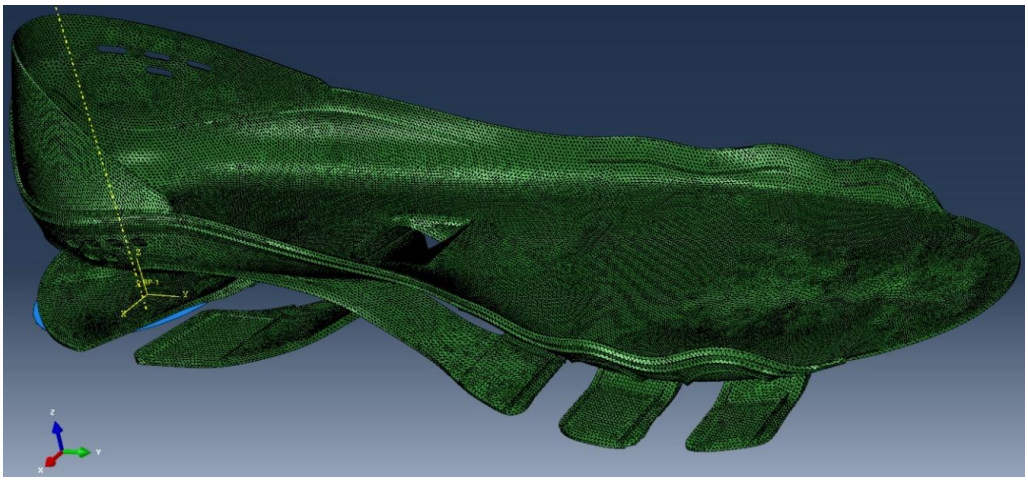

Figure 4.49. Meshed top plate

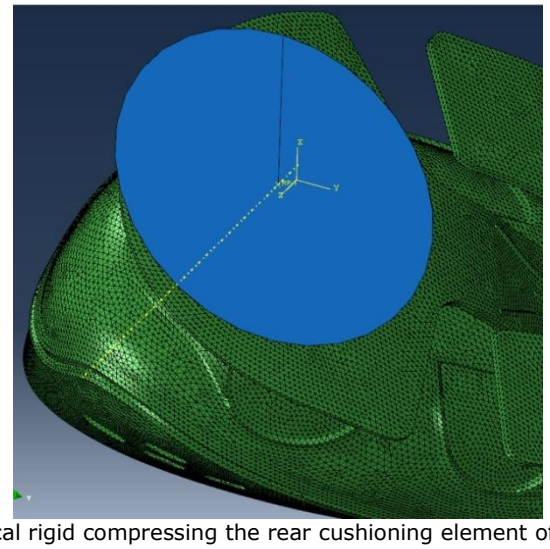

Figure 4.50. Analytical rigid compressing the rear cushioning element of the top plate model

4.5.1. Simulations with the hyperelastic material model

The hyperelastic material model used for top plate simulations consisted of the Marlow energy potential, calibration data for the 2000 mm/min tension test and a Poisson ratio of 0.35. Simulation results graph determined a 5% stiffer response (109 N instead of 104 N at 9 mm deflection) and the force-deflection graph is presented in Figure 4.51.

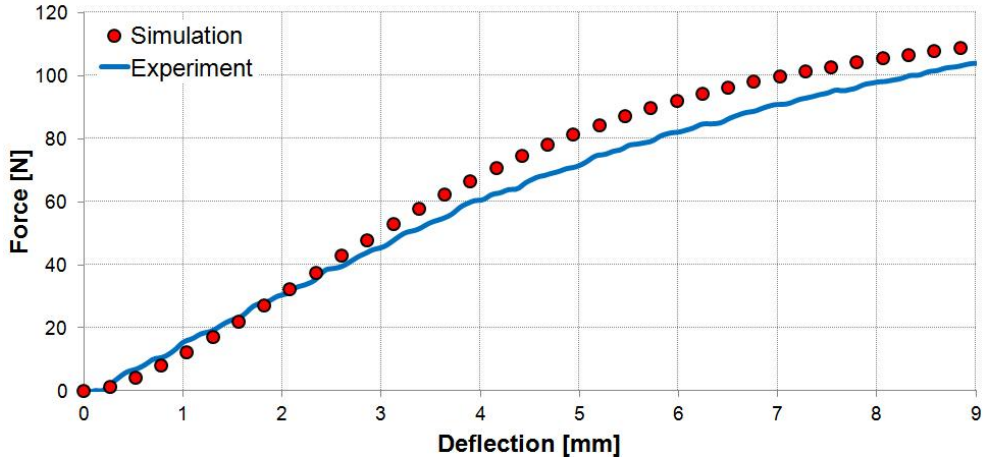

Figure 4.51. Experimental and simulated force-deflection graphs for hyperelastic material model

The maximal values of the equivalent von Mises stress are located near the base of the cushioning element, around the fillet area. The stress distribution is presented in Figure 4.52.

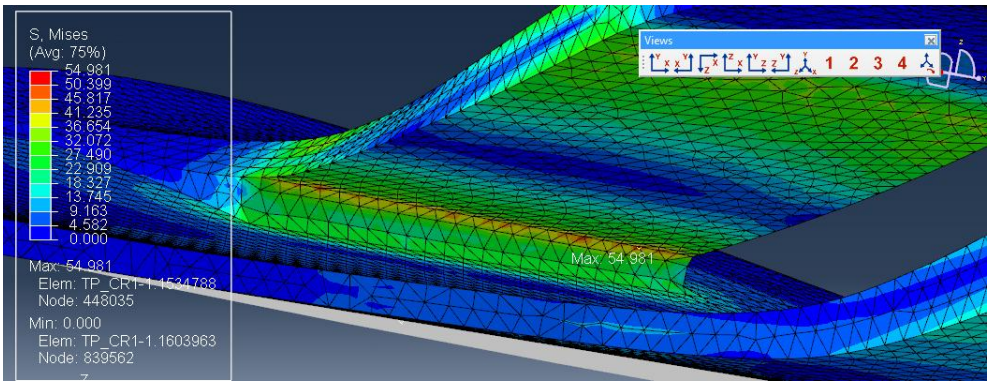

Figure 4.52. Von Mises stress distribution for top plate simulations with hyperelastic model

The largest component of the stress tensor is the one that determines tension and compression in a direction along the surface of the cushioning element base (the Y direction after the orientation of the model). Its distribution is presented in Figure 4.53.

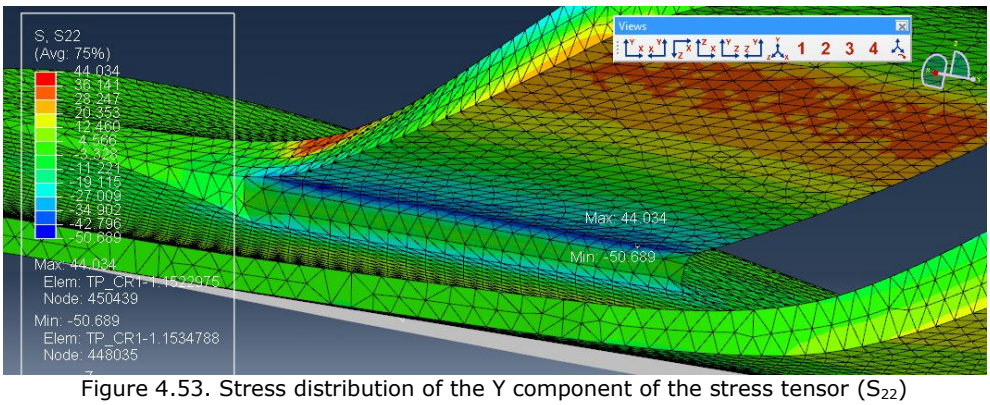

Figure 4.53. Stress distribution of the Y component of the stress tensor (S_{22})

The largest recorded deformation was determined by the shear component acting in the XY plane (the plane of the base of the cushioning element). Its distribution is presented in Figure 4.54.

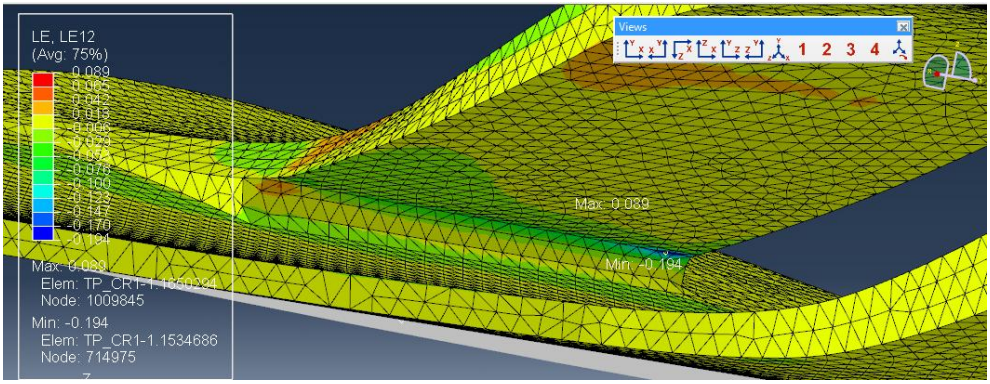

Figure 4.54. Strain distribution of the XY component of the strain tensor (LE_{12})

The peak values recorded for the stress and strain components are shown in Table 4.17

Table 4.17. Stress and strain values recorded for hyperelastic top plate simulation

Stress	**[MPa]**	**Log strain**	**[mm/mm]**
S_{11}	-19.83	LE_{11}	0.04
S_{22}	-50.68	LE_{22}	-0.191
S_{33}	-25.74	LE_{33}	-0.052
S_{12}	-19.13	LE_{12}	-0.194
S_{13}	-12.62	LE_{13}	-0.068
S_{23}	-18.07	LE_{23}	-0.126
von Mises	54.98	Max Principal	0.149

4.5.2. Simulations with the elasto-plastic material model

The hyperelastic material model used for top plate simulations consisted of the Marlow energy potential, calibration data for the 2000 mm/min tension test and a Poisson ratio of 0.35. Simulation results graph determined a 13% stiffer response (117 N instead of 104 N at 9 mm deflection) and the force-deflection graph is presented in Figure 4.55.

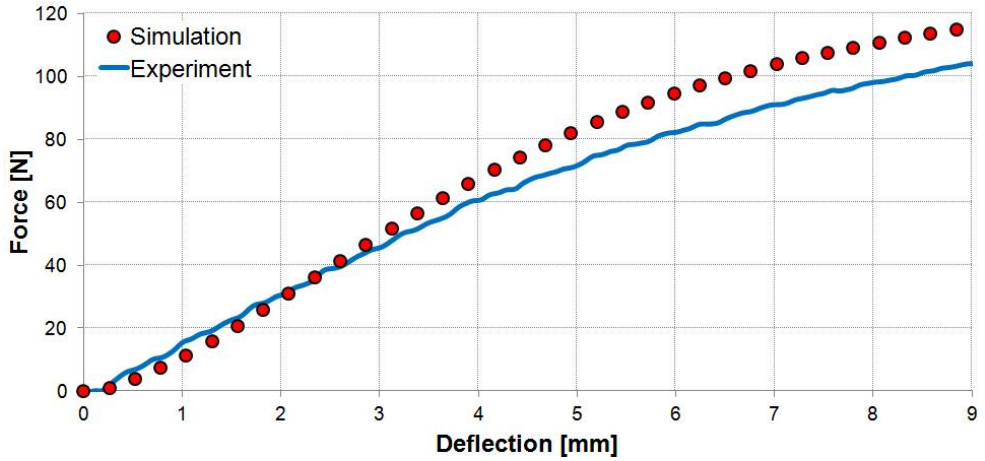

Figure 4.55. Experimental and simulated force-deflection graphs for hyperelastic material model

The maximal values of the equivalent von Mises stress are located near the base of the cushioning element, around the fillet area. The stress distribution is presented in Figure 4.56.

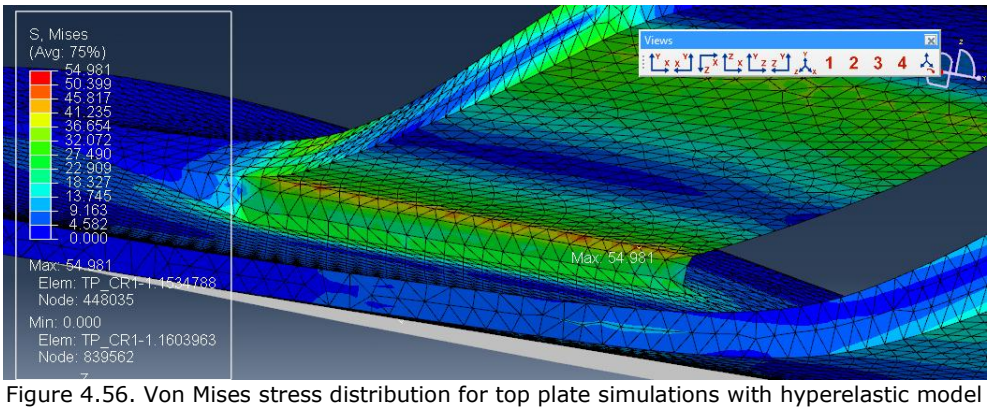

Figure 4.56. Von Mises stress distribution for top plate simulations with hyperelastic model

The largest component of the stress tensor is the one that determines tension and compression in a direction along the surface of the base of the cushioning element (the Y direction after the orientation of the model). Its distribution is presented in Figure 4.57.

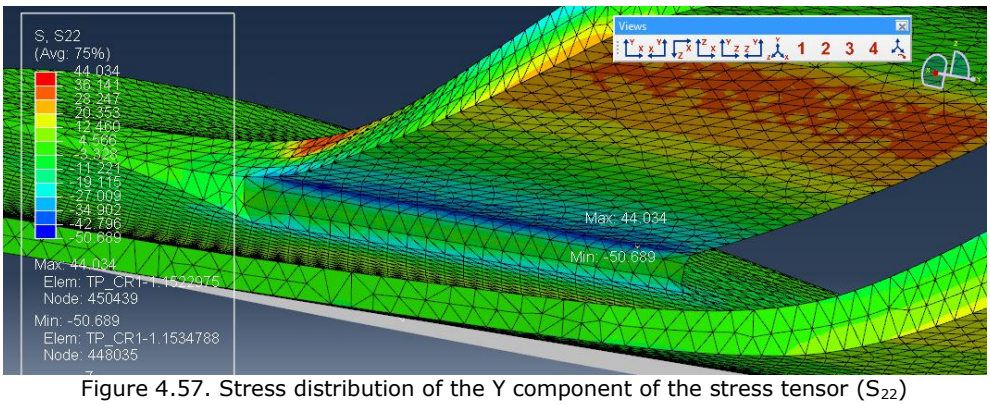

Figure 4.57. Stress distribution of the Y component of the stress tensor (S_{22})

The largest recorded deformation was determined by the shear component acting in the YZ plane. Its distribution is presented in Figure 4.58.

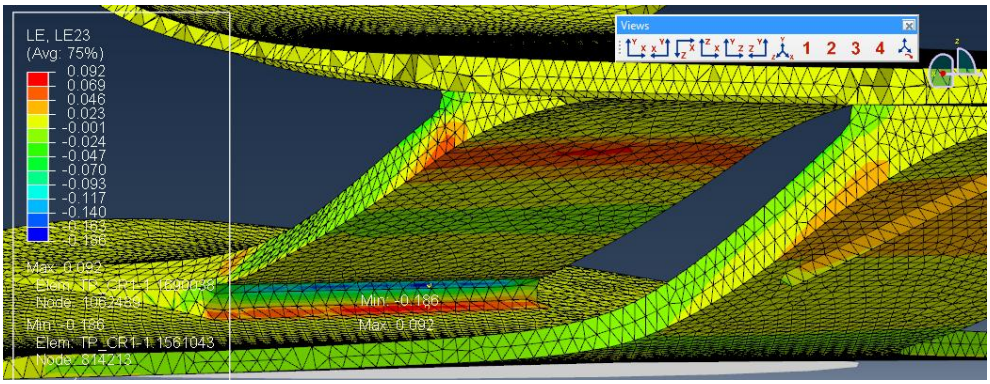

Figure 4.58. Strain distribution of the XY component of the streain tensor (LE_{12})

The peak values recorded for the stress and strain components are shown in Table 4.18.

Table 4.18. Stress and strain values recorded for elasto-plastic top plate simulation

Stress	**[MPa]**	**Log strain**	**[mm/mm]**	**Plastic strain**	**[mm/mm]**
S_{11}	-39.56	LE_{11}	0.033	PE_{11}	0.03
S_{22}	-60.75	LE_{22}	-0.114	PE_{22}	-0.09
S_{33}	-46.95	LE_{33}	0.101	PE_{33}	0.085
S_{12}	-17.57	LE_{12}	-0.13	PE_{12}	0.098
S_{13}	13.31	LE_{13}	0.075	PE_{13}	0.058
S_{23}	-21.04	LE_{23}	0.186	PE_{23}	0.153
von Mises	49.13	Max Principal	0.115	Max Principal	0.153

4.5.3. Simulations with the viscoelastic material model

Simulations presented in this paragraph were performed with the viscoelastic material model described in Paragraph 4. Simulation results graph determined a 10% stiffer response (114 N instead of 104 N at 9 mm deflection) and the force-deflection graph is presented in Figure 4.59.

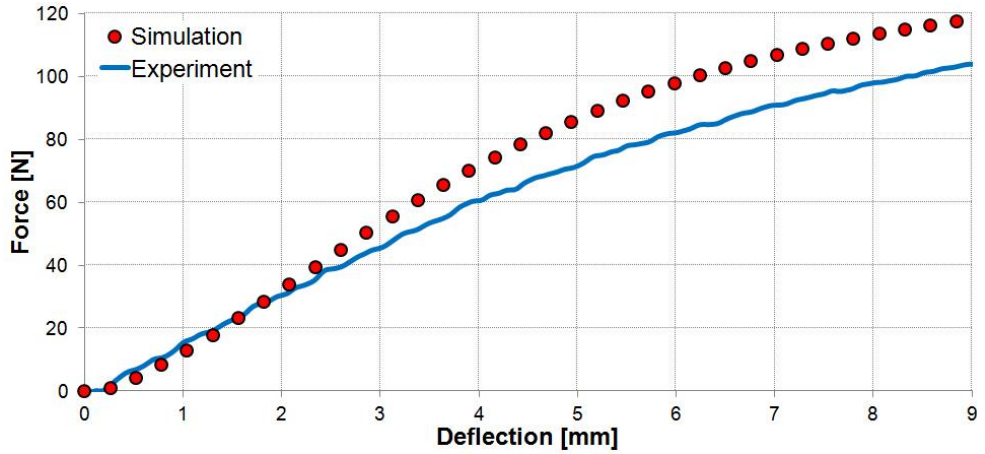

Figure 4.59. Experimental and simulated force-deflection graphs for viscoelastic material model

As with the previous simulations, the maximal values of the equivalent von Mises stress are located near the base of the cushioning element, around the fillet area. The stress distribution is presented in Figure 4.60.

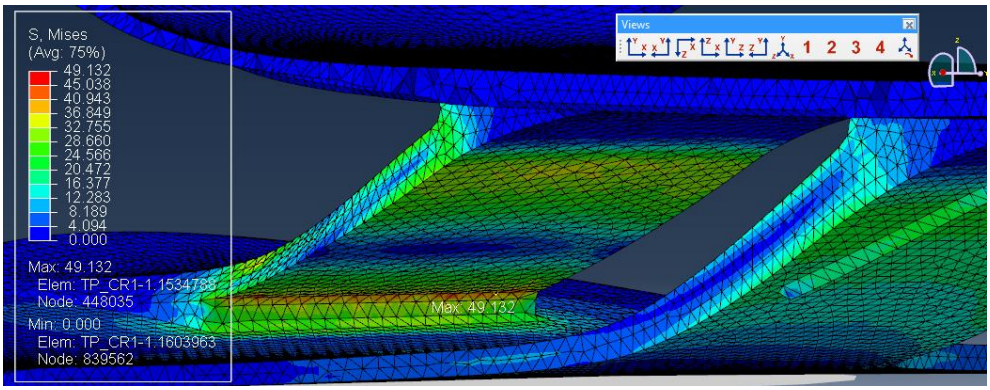

Figure 4.60. Von Mises stress distribution for top plate simulations with viscoelastic model

The largest component of the stress tensor is the one that determines tension and compression in a direction along the surface of the cushioning element base (the Y direction after the orientation of the model). Its distribution is presented in Figure 4.61.

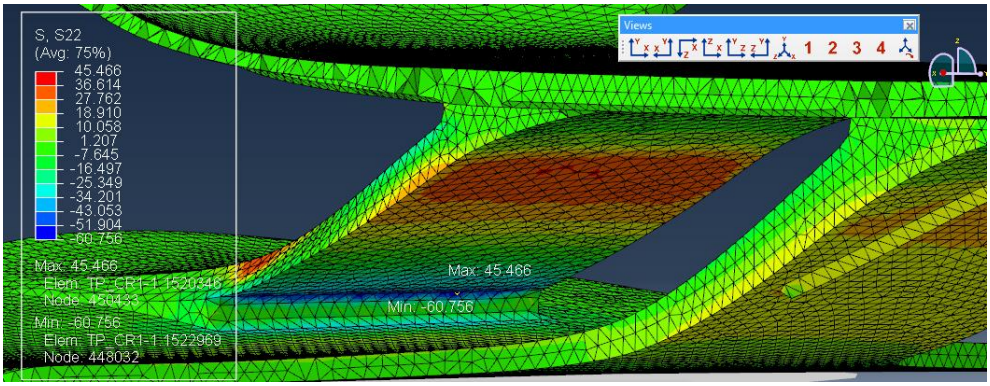

Figure 4.61. Stress distribution of the Y component of the stress tensor (S_{22})

In case of the viscoelastic model, the largest recorded deformation was determined by the normal component acting along the Y direction. Its distribution is presented in Figure 4.62.

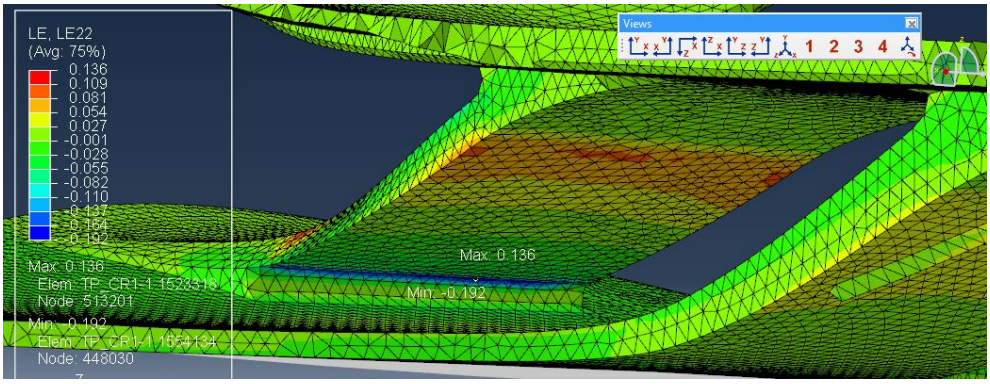

Figure 4.62. Strain distribution of the XY component of the streain tensor (LE_{12})

The peak values recorded for the stress and strain components are shown in Table 4.19.

Table 4.19. Stress and strain values recorded for viscoelastic top plate simulation

Stress	**[MPa]**	**Log strain**	**[mm/mm]**
S_{11}	-28.47	LE_{11}	0.049
S_{22}	-62.95	LE_{22}	-0.192
S_{33}	-36.54	LE_{33}	-0.084
S_{12}	-22.9	LE_{12}	-0.192
S_{13}	-14.78	LE_{13}	-0.071
S_{23}	-24.07	LE_{23}	-0.164
von Mises	59.91	Max Principal	0.112

4.6. Discussions

4.6.1. Simulations in tension

All material models are calibrated after tensile data because this type of experiment is the closest one could get to pure uniaxial loading. Accurate simulations in tension are, consequently, the first step in obtaining accurate material models.

From the results presented in this chapter we can conclude that the best formulation for monotone tensile simulations is the elasto-plastic model. With the input of the correct yield stress-plastic strain parameters accurate rate dependent material models can be developed. The drawback of this formulation is its incapability of simulating cyclic loadings.

Hyperelastic models also determine accurate results, especially the Marlow energy potential. Their major drawback is that strain rate dependency can be modelled only with additional sub-routines (which require programming skills as well as additional compiling software [**62**]). Also, it can generate rather accurate simulations in cyclic loadings but only in the interval defined through the damage model calibration (Mullins effect suboption).

Due to the limitation of the implemented models, the viscoelastic formulation is only capable of determining accurate results until around 5% strain. It can, however produce accurate simulations of the viscoelastic behaviour, namely strain softening, strain hardening and hysteresis (the three characteristics of Mullins effect).

All three material models present an incomplete description of PA-12's behaviour. The material is neither hyperelastic, nor elasto-plastic, nor viscoelastic: large strain deformations are not perfectly reversible (as hyperelastic constitutive relations describe material behaviour); elasto-plastic models overestimate the amount of plastic deformation recorded during straining and viscoelastic formulations do not account for permanent damage induced during deformation. A more accurate material model should consider both plastic deformation as well as viscous flow.

4.6.2. Simulations in bending

Even though simulations in tension were accurate, regardless of the material model used, simulations in three-point bending underestimate material's response with about 15-25% in terms of flexural strength. The viscoelastic formulation determined the smallest errors but this is due to its incapability of anticipating the behaviour in tension. As a consequence, the shape of the force-deflection curve differs after around 5% deformation. A comparison between the results in bending for all material models is presented in Figure 4.63.

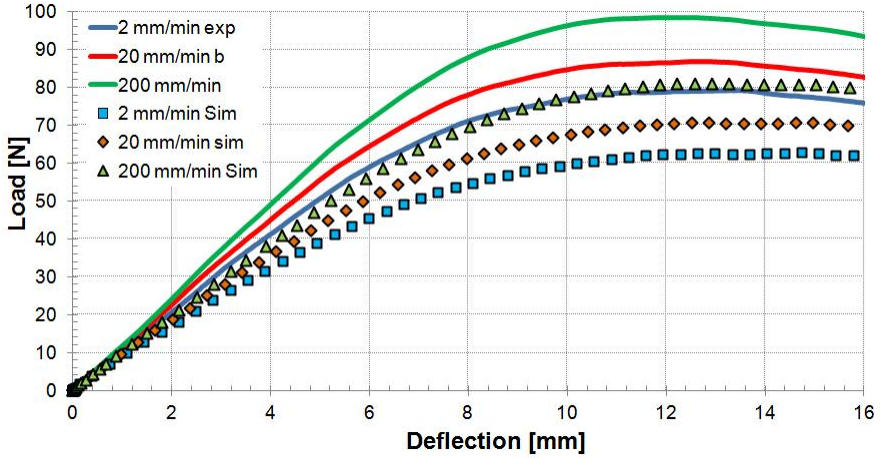

a)

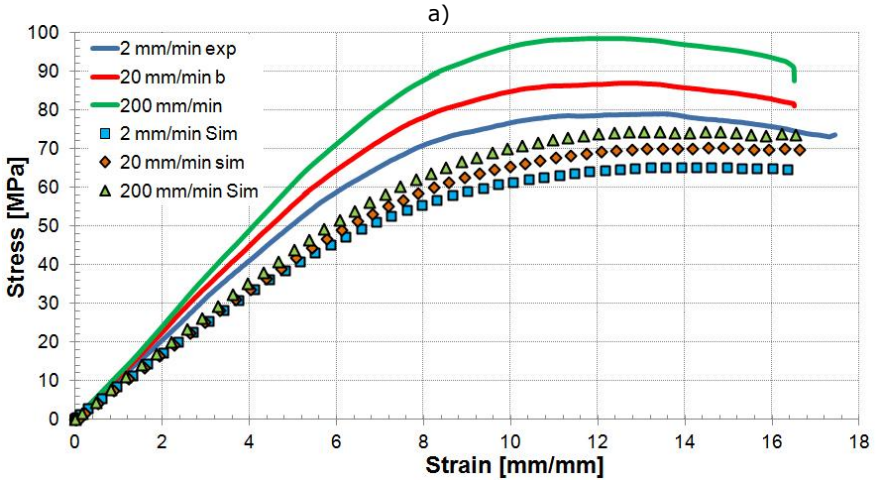

b)

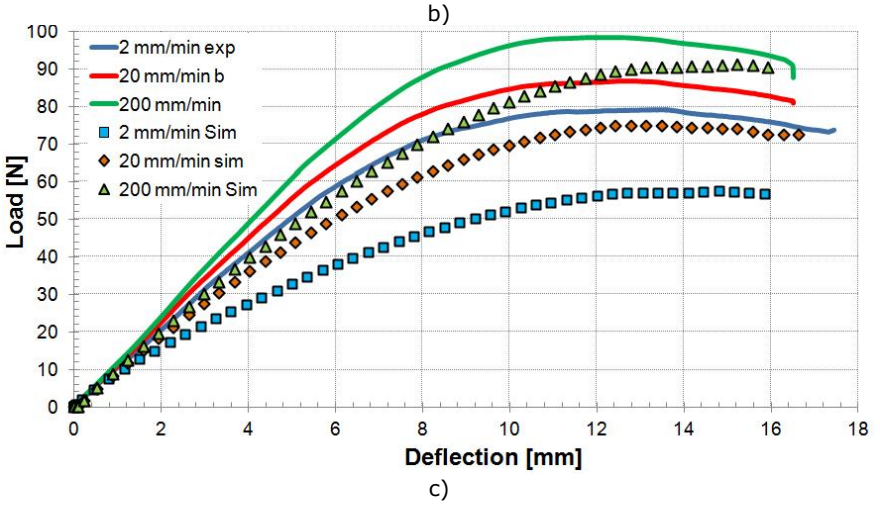

c)

Figure 4.63. Comparison between the experimental and simulation results for a) hyperelastic model, b) elasto-plastic model and c) viscoelastic model

Dynamic bending simulations produced similar results regardless of the material model used. Even though the recorded reaction forces are lower, the shapes of the force-deflection curves are similar to experimental results in terms of stress wave propagation.

The main cause of this response is the anisotropy and inelasticity on PA-12. From the analysis of the components of the Cauchy stress tensor and the Green-Lagrange strain tensor, compression has a significant effect in bending, surpassing tensile deformation. Unfortunately, compression tests which might have given insight about the material's inelasticity could not be performed. As for anisotropy, DMA tests have determined that the Poisson effect cannot account for the relation between shear and normal moduli of elasticity.

4.6.3. Top plate simulations

As with the bending simulations, top plate simulations determined inaccurate results, this time overestimating the reaction forces with a margin of around 10%. A cause for this difference may be the small fillet radius from the cushioning element which determined a number of only three elements to account for the region. This area of the model determined the highest stresses and strain due to its awkward deformation mode (Figure 4.64).

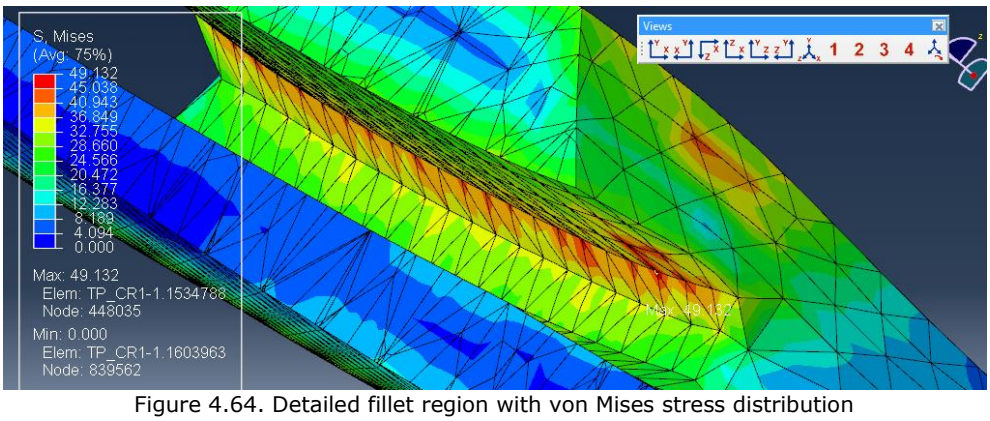

Figure 4.64. Detailed fillet region with von Mises stress distribution

As with three-point bending simulations, shear and compression components of the Cauchy stress tensor determined high degrees of deformation for load directions that have little or no experimental data to calibrate. The shearing of the fillet region along the XY and YZ planes (relative to the model orientation) determined somehow unrealistic strain values of around 20% for the given state of deformation.

Another cause of the difference in simulation and experimental results is anisotropy determined by the remnant stress inside the specimens. Having small thickness, the variation of the temperature gradient during the cooling of the injected top plate might determine remnant stresses that can determine further anisotropy or non-homogenous regions.

5. CONCLUSIONS

5.1. Conclusions

The experimental programme presented in this thesis covers the investigation of the non-linear behaviour associated with the viscoelastic properties of a polyamide-based semi-crystalline thermoplastic polymer. The procedures covered monotone tensile tests (both static and dynamic), cyclic tests in tension, low-cycle fatigue tests in tension, creep tests in tension, static and dynamic three-point bending tests, DMA tests, puncture impact tests and tests on components

Monotone tensile tests studied the influence of test parameters on the tensile properties of PA-12, namely temperature, strain rate and humidity. Temperature influence tests were performed on a range of -25 °C to 50 °C determining a 410 % increase in Young's modulus (from E=500 MPa to E=2550 MPa) and a 185 % increase in tensile strength (from σ_{max}=20 MPa to σ_{max}=57 MPa). Though not as considerable as the influence of temperature, strain rate affects the material's properties in tension: for a variation of strain rate from 0.00028 s^{-1} to 2.8 s^{-1} recorded values show an increase in the Young's modulus of 64 % (from 850 MPa at 0.00028 s^{-1} to 1400 MPa at 9.4 s^{-1}) and an increase in tensile strength of 33 % (from 30 MPa at 0.00028 s^{-1} to 40 MPa at 9.4 s^{-1}). An important material characteristic was determined following the dynamic tensile tests: the material reaches a saturation in stress-strain response after around 2.8 s^{-1} (the strain rate at which viscous effects no longer take place and the material behaves as an elaso-plastic solid. Humidity also has a noticeable effect on mechanical properties, tensile tests on conditioned specimens determined a softening in stress-strain response of around 20%.

Cyclic tests in tension were performed with three experimental programmes: the first programme consisted of 3 blocks of different strain amplitudes with 10 cycles per bloc; the second programme consisted of 10 cycles with a linear increase in the stress increment; the third programme consisted of 10 cycles with a linear increase in the strain increment. The purposes of the cyclic tests were to identify the three main characteristics of the Mullins effect: strain softening, strain hardening and hysteresis. Strain softening can be observed in in the case of multiple cycles with the same amplitude as the material gradually softens. Strain hardening is observed in loadings with different amplitudes as the stress-strain response follows the path described by a previously undefformed specimen. The hysteresis phenomenon is associated with the energy dissipated during deformation (through heat, viscous flow, plastic flow or other damage mechanisms) and it can be observed for any cyclic loading program. Another goal of cyclic tests was to provide a tool for extracting the plastic component of the total deformation.

Following the observations from Mullins effect tests regarding strain softening, an experimental programme was designed in order to determine the maximal damage induced by cyclic loadings and the consequent determination of the stabilized material properties (steady-state material behaviour). The influence of several test parameters was investigated: the number of cycles, frequency and strain level. Regardless of the test conditions, the same behaviour was observed:

the most significant softening was recorded after 1000 cycles (around 30%). After another 49,000 cycles, the material only softens with around 16%.

Creep tests were performed on three stress levels accounting for 30%, 60% and 90% of the yield stress. Tensile loading was maintained for 24h and the strain was recorded in equal intervals. The normalized compliance curve shows an accelerated softening of the material in the first few hours subsequently determining a plateau. The maximum recorded value of the normalized creep compliance was 4.5.

The flexural properties of PA-12 were studied with the help of three-point bending tests. Non-linear behaviour was studied in terms of strain rate influence and anisotropy resulted from the manufacturing process. Two types of specimens were tested: prismatic specimens cut from injected sheets and ISO 527 standard dogbones. The first set of tests determined a dispersion of results due to sheet anisotropy (around 20% variation in flexural properties) and up to 40% variation in flexural strength due to the variation in deformation speed (an increase in crosshead travel speed from 3.14 mm/min up to 314 mm/min determined an increase in flexural strength from 20 MPa to 20.3 MPa). Another inconvenience regarding the tests performed on sheet specimens is the low reaction forces, which produces wobbles in the recorded values (the recorded forces are near the error tolerance of the load cell). Tests on dogbone specimens determined a more stable response and a negligible dispersion of results. For these tests, an increase in crosshead travel speed from 2 mm/min to 2000 mm/min (the last value for which dynamic effects are unnoticeable) determined a 31% increase in flexural strength (from 42MPa to 55MPa). Tests at higher deformation speeds (333 mm/s and 1500 mm/s) show the effect of stress wave propagation and system ringing in dynamic tests.

DMA tests presented in this thesis can be grouped in two major categories: DMA tests at small strain (around 0.00001 mm/mm) and DMA tests at large strains (0.01 to 0.04 mm/mm). The DMA tests at small strains were performed on specialized machines in two deformation modes: single cantilever and shear. The aim of these tests was to determine the influence of temperature and frequency on the viscoelastic properties of the material (storage moduli, loss moduli and damping coefficients). As with the tensile tests, the influence of temperature was considerable in comparison with the influence of frequency: a 75% decrease in the storage modulus (from 1200 MPa to 300 MPa combined modulus of tension and shear) was recorded over a temperature variation from -30 °C to 90 °C while for a decrease in frequency from 100 Hz to 0.1 Hz, only an 11% decrease in the storage modulus (from 350 MPa to 310 MPa, shear modulus) was recorded. Due to PA-12's non-linear stress-strain response it was considered worthwhile to investigate DMA properties at larger strains (in the usability envelope of the components manufactured from this material). DMA tests at large strains were performed in tension. Several pre-deformation levels, amplitudes and frequencies were tested. Along with the increase in mechanical properties with frequency (also determined in the tests at low strains), a 10% decrease in properties with strain variation from 0.015 mm/mm to 0.043 mm/mm was recorded.

Instrumented puncture impact tests were performed in order to determine the energy required to fracture the material. In this scope, several experiments were designed constituting of two different impact speeds (4.4 m/s and 1 m/s), two temperatures (ambient temperature, 23 °C and low temperatures, around -5 °C). For an impact speed of 4.4 m/s the recorded puncture energy was 37 J regardless of the test temperature (the shape of the force-deflection graph is different, showing larger reactions but smaller puncture travel for tests at negative values). Tests performed at 1 m/s did not puncture the specimen.

As a validation tool for the upcoming material models, tests on components that undergo complex deformations are required. In this scope, top plates were tested in different loading scenarios. Tests in compression acting on the rear cushioning element represent a simple approximation of the type of loading these components undergo in service. Four crosshead travel speeds were tests, determining a 36% variation in compression strength (just before the cushioning element becomes fully compressed). Compression tests were also performed on conditioned top plates (same conditions as the dogbones tested in tension), determining a 20% softening in the force-deflection response. Top plates were also tested in low-cycle fatigue, determining the same behaviour seen in tensile tests: a 23% softening is observed after 1000 cycles with an additional 7% softening after another 4000 cycles. Similar results were obtained for low-cycle fatigue tests performed on conditioned top plates.

The second part of the thesis deals with developing material models for finite element analysis of PA-12. Three types of materials were investigated: hyperelastic materials, elasto-plastic materials and viscoelastic materials.

Hyperelastic material definition is based on a strain-energy density function. Several models implemented in Abaqus were tested for the tensile stress-strain response: Arruda-Boyce, 2^{nd} order polynomial, Neo-Hooke, Yeoh, Mooney-Rivlin, Ogden, van der Waals and Marlow. Function parameter calibration was performed by Abaqus using the least square algorithm. The function that was able to determine most accurate results regardless of the input data was the Marlow model. A shortcoming of this material formulation is its incapability of generating strain-rate dependency. For each strain rate test, a different set of input data must be implemented.

Besides monotone tension, the Marlow model was evaluated in cyclic loadings. To aid behaviour prediction in cyclic deformation, the Mullins effect sub-option was employed, which shapes the unloading curve. Despite determining accurate results for small strain simulation, the shape of the unloading curve cannot be accurately predicted beyond data definition and no permanent deformation can be modelled.

The elasto-plastic material model is based on Hookean elasticity and von Mises plasticity with isotropic hardening. The input data consisted of temperature dependent Young's modulus and the Poisson ratio. Dependency on the rate of deformation is modelled with the help of strain rate dependent plasticity. Plasticity values were extracted from Cauchy stress-logarithmical strain data. Lines parallel with Young's modulus were generated for different values of plastic strain, their intersection with the stress-strain curve generating the correspondent yield stress.

The model was tested in tension for different strain rate experiments determining accurate results in all cases. The shortcoming of this model is its incapability of simulating cyclic loadings as the model overestimates plasticity and cannot generate the recovery determined by the viscous component of the total deformation.

The developed Viscoplastic material model represents a time-dependent viscous softening coefficient (the normalized relaxation modulus) applied to a hyperelastic strain-energy density function (the Marlow function employed in the Hyperelastic model). The calibration of the viscoelastic coefficient was performed with experimental data in creep (which determined inaccurate results) and through a reverse engineering approach, starting from tensile stress-strain curves and developing a custom relaxation curve. This material model still determined inaccurate results when strained over 5%.

Simulations in three-point bending determined an average of 20% lower reaction forces regardless of the material model used. This effect might be due to PA-12's anisotropy and inelasticity. Analyzing strain data calculated in bending simulations, a considerable effect of negative strains is observed. It is probable that the material has a different behaviour in compression, determining a stiffer response. Also, the Poisson effect might not be characteristic for this material, regarding the relation between tensile and shear properties.

A difference in experimental and numerical results was also observed in the case of top plate simulations. In this case, the analysis overestimated the component's response in compression with around 10%. Apart from the anisotropy and inelasticity, the mesh might be another reason for the erroneous results. The highest values for stress and strain were recorded in the fillet region, which, due to the small radius, is only composed of three elements per radius. This aspect might determine unrealistic deformations, as some strain components reach values up to 20%.

5.2. Personal contributions

For monotone tensile tests, the main contributions refer to the determination of the influence several test parameters have on mechanical properties. For PA-12, temperature has the most significant influence on tensile properties, followed by strain rate and condition. Another important characteristic of this material is that the stress-strain response reaches saturation before the tensile test data becomes unusable due to stress wave propagation and system ringing.

In case of cyclic loadings, the main contribution was the determination of Mullins effect characteristics (strain softening, strain hardening and hysteresis) for polyamides.

As far as the consulted literature reveals, no low-cycle fatigue tests with emphasis on determining quantitative cycle induced softening were performed on polymers. The most significant amount of softening was recorded after 1000 cycles, regardless of the variation of other test parameters such as frequency and reference strain level.

Regarding DMA tests at high strain (1%-4%), literature reviews could not point out to any reference of similar procedures. Determination of the variation of viscoelastic properties at deformations close to values expected in service represents a significant aspect regarding material characterisation.

Experiments performed on components with procedures similar to in service load patterns represent an important tool for validating material models. The determination of the influence of deformation speed and condition on component behaviour in compression also represents an important aspect of this work.

For the second part of the thesis, the main contributions refer to the calibration of material parameters. For the elasto-plastic material, it is the case of the procedure used for accurately extracting plasticity data. For the viscoelastic material, it is the case of the reverse engineering procedure used for designing a relaxation curve that can accurately account for strain rate sensitivity.

The most important contribution of this thesis is the deliverable steady-state elasto-plastic material model that will be used by *Adidas Innovation Team* in modelling athletic footwear.

6. BIBLIOGRAPHY

[1] L. H. Sperling, An introduction to Physical Polymer Science, Fourth Edition. Wiley-Interscience, 2006.

[2] D. I. Bower, An Introduction to Polymer Physics. Cambridge University Press, 2002.

[3] H. F. Brinson and L. C. Brinson, Polymer Engineering Science and Viscoelasticity: An Introduction. Springer Science, 2008.

[4] J. E. Mark, Physical Properties of Polymers Handbook. Springer, 2007.

[5] M. T. Shaw and W. J. MacKnight, Introduction to Polymer Viscoelasticity. Wiley-Interscience, 2005.

[6] G. Strobl, The Physics of Polymers. Springer, 2007.

[7] Presidential Commision on the Space Shuttle Challenger Accident, "Report to the President of the Presidential Commision on the Space Shuttle Challenger Accident," 1986.

[8] J. S. Bergstrom, Large strain time-dependent behaviour of elastomeric materials. Massachusetts Institute of Technology, 1999.

[9] T. G. Mase and G. E. Mase, Continuum Mechanics for Engineers, 2nd ed. CRC Press, 1999.

[10] A. A. Shabana, Computational continuum mechanics. Cambridge University Press, 2008.

[11] J. Bonet and W. R.D., Nonlinear Continuum Mechanics for Finite Element Analysis. Cambridge University Press, 1997.

[12] R. S. Rivlin, "Large elastic deformations of isotropic materials," vol. Experiments on deformable rubber, Philosophical Transactions of the Royal Society A240 , pp. 459-490, 1948.

[13] R. S. Rivlin and D. W. Saunders, "Large elastic deformations of isotropic materials. Experiments on deformable rubber," vol. Experiments on deformable rubber, Philosophical Transactions of the Royal Society, pp. 459-490, 1951.

[14] O. H. Yeoh, "Some Forms of the Strain Energy Function for Rubber," Rubber Chemistry and Technology, no. 66, p. 754–771, 1993.

[15] R. W. Ogden, "Large deformation isotropic elasticity - on the correlation of theory and experimental for incompressible rubber like solids," Proc. Royal Society, vol. Proc. Royal Society, 326, no. 565-584, 1972.

[16] H. G. Kilian, H. F. Enderle, and K. Unseld, "The use of the Van der Waals model to elucidate universal aspects of structure-propery relationships in simply extended dry and swollen rubbers," Collid & Polymer Sciense, vol. Colloid & Polymer Science 264, pp. 866-876, 1986.

[17] E. M. Arruda and M. C. Boyce, "A three-dimensional constitutive model for the large stretch behvaiour of rubber elastic materials," Jurnal of Mwxhanics & Physics of Solids, vol. J. Mechanics & Physics of Solids 41, pp. 389-411, 1993.

[18] R. S. Marlow, "A general first invariant hyperelastic constitutive model," Constitutive models for rubber, vol. III, 2003.

[19] L. Mullins, "Effect of stretching on the properties of rubber," Journal of Rubber Research, no. 16, p. 275–289, 1947.

[20] J. A. C. Harwood, L. Mullins, and A. R. Payne, "Stress softening in natural rubber vulcanizates. Part II. Stress softening effects in pure gum and filler loaded rubber," Rubber Chemistry and Technology, no. 39, p. 814–22, 1966.

[21] L. Mullins, "Softening of rubber by deformation," Rubber Chemistry and Technology, no. 42, pp. 339-362, 1969.

[22] J. Diani, B. Fayolle, and P. Gilormini, "A review on the Mullins effect," European Polymer Journal, no. 45, p. 601–612, 2009.

[23] H. J. Qi and M. C. Boyce, "Stress–strain behavior of thermoplastic polyurethanes," Mechanics of Materials, no. 37, p. 817–839, 2005.

[24] S. Merabia, P. Sotta, and D. R. Long, "A microscopic model for the reinforcement and the nonlinear behavior of filled elastomers and thermoplastic elastomers (Payne and Mullins effects)," Macromolecules, no. 41, p. 8252–8266, 2008.

[25] S. Cantournet, D. Desmorat, and J. Besson, "Mullins effect and cyclic stress softening of filled elastomers by internal sliding and friction thermodynamics model," no. 46, 2009.

[26] D. A. Şerban, L. Marşavina, L. Culea, and V. V. Silberschmidt, "Experimental determination of Mullins effect in semi-crystalline thermoplastic polymers," Acta Technica Napocensis, 2010.

[27] D. A. Şerban, L. Marşavina, and V. V. Silberschmidt, "Behaviour of semi-crystalline thermoplastic polymers: Experimental studies and simulations," Computational Material Science, vol. 52, p. 139–146, 2012.

[28] A. D. Drozdov, "Mullins' effect in semicrystalline polymers," International Journal of Solids and Structures, no. 46, p. 3336–3345, 2009.

[29] P. Ciarletta, P. Dario, and S. Micera, "Pseudo-hyperelastic model of tendon hysteresis from adaptive recruitment of collagen type I fibrils," Biomaterials, no. 29, p. 764–770, 2008.

[30] E. Pena and M. Doblare, "An anisotropic pseudo-elastic approach for modelling Mullins effect in fibrous biological material," Mechanics Research Communications, no. 36, p. 784–790, 2009.

[31] A. Dorfmann and R. W. Ogden, "A constitutive model for the Mullins effect with permanent set in particle-reinforced rubber," International Journal of Solids and Structures, no. 41, p. 1855–1878, 2004.

[32] A. Dorfmann and R. W. Ogden, "A constitutive model for the Mullins effect with permanent set in particle-reinforced rubber," no. 41, 2004.

[33] A. D. Drozdov, "Mullins' effect in thermoplastic elastomers: Experiments and modeling," no. 36 pg. 437-443, 2009.

[34] J. Diani, M. Brieu, and J. M. Vacherand, "A damage directional constitutive model for Mullins effect with permanent set and induced anisotropy," European Journal of Mechanics A/Solids, no. 25, p. 483–496, 2006.

[35] J. S. Bergstrom and M. C. Boyce, "Constitutive modelling of large strain time dependend behaviour of elastomers," J. Mech. Phys. Solids, no. 46, p. 931–954, 1998.

[36] P. M. Nagdi and S. A. Murch, "On the mechanical behaviour of viscoelastic-plastic solids," Journal of Applied Mechanics, no. 30, 1963.

[37] M. J. Crochet, "Symmetric deformations of viscoelastic-plastic cylinders," Journal of Applied Mechanics, no. 33, 1966.

[38] M. Reiner, Advanced Rheology. H.K. Lewis, 1971.

[39] E. C. Bingham, Fluidity and Plasticity. Mc Graw Hill, 1922.

[40] A. D. Drozdov and J. Christiansen, "Finite viscoplasticity of semicrystalline polymers," Archive of Applied Mechanics, no. 72, p. 779–803, 2003.

[41] A. D. Drozdov and J. Christiansen, "Cyclic viscoplasticity of carbon black-filled thermoplastic elastomers: Experiments and modelling," Computational Materials Science, no. 45, p. 398–406, 2009.

[42] A. D. Drozdov and N. Dusunceli, "Mullins-type phenomena in polypropilene," International Journal of Appllied Mathematics and Mechanics, no. 8 (11), pp. 82-98.

[43] British Standard, Plastics – Determination of Tensile Properties. 1996.

[44] A. Kumar and R. K. Gupta, Fundamentals of Polymer Engineering, Second Edition. 2003: Marcel Dekker Inc.

[45] A. Meunier, G. Chagnon, D. Favier, L. Orgéas, and P. Vacher, "Mechanical experimental characterisation and numerical modelling of an unfilled silicone rubber," no. 27 pg 765–777, 2008.

[46] D. A. Şerban, L. Marşavina, and V. Silberschmidt, "Response of semi-crystalline thermoplastic polymers to dynamic loading:," Computational Material Science, vol. 64, p. 116–121, 2012.

[47] D. A. Şerban, H. Hanson, L. Marşavina, and V. Silberschmidt, "Viscoelastic properties of semi-crystalline thermoplastic polymers: dynamic analysis and creep," Solid State Phenomena, vol. 188, no. Advanced Materials and Structures IV, pp. 211-218, 2011.

[48] D. A. Şerban, G. Weber, L. Marşavina, V. V. Silberschmidt, and W. Hufenbach, "Tensile properties of semi-crystalline thermoplastic polymers: Effects of temperature and strain rates," Polymer Testing, no. 32, p. 413–425, 2013.

[49] D. W. A. Rees, Basic Engineering Plasticity. Elsevier, 2006.

[50] European Standard, Polyamides - Accelerated conditioning of test specimens. 1995.

[51] European Standard, Plastics - Determination of water absorption. 1999.

[52] ASTM Standards, Standard Test Methods for Flexural Properties of Unreinforced and Reinforced Plastics and Electrical Insulating Materials. 2003.

[53] S. Timoshenko, Strength of Materials - Part I: Elementary Theories and Problems. D. Van Nostrand Company, 1948.

[54] E. Kausel, Fundamental Solutions in Elastodynamics. Cambridge University Press, 2006.

[55] A. Cemal Heringen and E. H. Şuhubi, Elastodynamics. Academic Press, 1974.

[56] E. Parsons, M. C. Boyce, and D. M. Parks, "An experimental investigation of the large-strain tensile behavior of neat and rubber-toughened polycarbonate," vol. Polymer 45, p. 2665–2684, 2004.

[57] Q. Z. Fang, T. J. Wang, and H. M. Li, "Large tensile deformation behavior of PC/ABS alloy," vol. Polymer 47, p. 5174–5181, 2006.

[58] E. M. Parsons, M. C. Boyce, D. M. Parks, and M. Weinberg, "Three-dimensional large-strain tensile deformation of neat and calcium carbonate-filled high-density polyethylene," vol. Polymer 46, p. 2257–2265, 2005.

[59] M. Jerabek, Z. Major, and R. W. Lang, "Strain determination of polymeric materials using digital image correlation," vol. Polymer Testing 29, p. 407–416, 2010.

[60] X. Xiao, "Dynamic tensile testing of plastic materials," vol. Polymer Testing 27, pp. 164-178, 2008.

[61] International Standard, Plastics — Determination of puncture impact behaviour of rigid plastics — Part 2: Instrumented impact testing. 2000, ISO 6630 2.

[62] Abaqus, "User's Manual," vol. Analysis, 2008.

[63] N. Faur, Elemente Finite. Fundamente. Editura Politehnica Timisoara, 2007.

[64] O. Rand and V. Rovenski, Analytical Methods in Anisotropic Elasticity. Birkhauser, 2005.

[65] O. H. Yeoh, "Characterization of the elastic properties of carbon-black filled black rubber vulcanisates," Rubber Chemistry & Technology, no. 63 792-805, 1990.

[66] F. Dunne and N. Petrinic, Introduction to Computational Plasticity. Oxford University Press, 2006.

[67] S. Abrate, "Criteria for Yielding or Failure of Cellular Materials," Journal of Sandwhich Structures and Materials, vol. 10, 2008.

[68] D. C. Drucker and W. Prager, "Soil Mechanics and Plastic Analysis of Limit Design," Quarterly of Applied Mathematics, vol. 10, pp. 157-165, 1952.

[69] L. J. Gibson, M. F. Ashby, J. Zhang, and T. C. Triantafilliou, "Failure Surfaces for Cellular Materials Under Multi-Axial Loads. (I) Modeling,," International Journal of, vol. 31, p. 635–665, 1989.

[70] V. S. Deshpande and N. A. Fleck, "Multi-axial Yield Behaviour of Polymer Foams," Acta Materialia, no. 49, p. 1859–1866, 2001.

[71] R. S. Raghava, R. M. Caddell, and G. S. Yeh, "The Macroscopic Yield Behavior of Polymers," Journal of Materials Science, no. 8, p. 225–232, 1973.

[72] C. Liu, Y. Huang, and M. G. Stout, "On the Asymmetric Yield Surface of Plastically," Acta Materiallia, no. 45, p. 2397–2406, 1997.

[73] R. Hill, "A Theory of the Yielding and Plastic Flow of Anisotropic Metals," Proceedings of the Royal Society of London, Series A, no. 193, p. 281–297, 1948.

[74] R. Hill, The Mathematical Theory of Plasticity. Oxford University Press, 1950.

[75] O. Cazacu and F. Barlat, "Generalization of Drucker's Yield Criterion to Orthotropy," Mathematics and Mechanics of Solids, no. 6, pp. 613-630, 2001.

[76] D. S. Viswanath, Viscosity of Liquids. Springer, 2007.

[77] J. Blackwell. (2002) case.edu.

ANNEXES

I. MATERIAL SPECIFICATIONS SHEET

Heat stabilized and light resistant polyamide 12 compound

This compound has especially been developed for the extrusion and co-extrusion of ski upper and decorative films. Decoration on the bottom side of injection moulded sports shoe soles is a further application field.

Films made of this material feature high transparency, good screen and sublimation printing, outstanding scratch resistance, and excellent impact strength at low temperatures.

The semi-crystalline compounds based on PA 12 absorb only low quantities of water. Therefore, moulded parts show excellent dimensional stability, constantly high impact strength, low coefficient of friction and good chemical resistance at changing ambient humidity.

This compound is supplied as cylindrical granules, ready for processing in moisture-proof packaging.

Table I.1. PA12 properties

Property	Test method		Unit	PA12
	international	national		
Density 23°C	ISO 1183	DIN EN ISO 1183	g/cm3	1.01
Tensile test Stress at yield Strain at yield Strain at break	ISO 527-1 ISO 527-2	DIN EN ISO 527-1 DIN EN ISO 527-2	MPa % %	37 5 > 200
Tensile modulus	ISO 527-1 ISO 527-2	DIN EN ISO 527-1 DIN EN ISO 527-2	MPa	1100
CHARPY impact strength	ISO 179/1eU	DIN EN ISO 179/1eU	kJ/m^2	No break
CHARPY notched impact strength	ISO 179/1eA	DIN EN ISO 179/1eA	kJ/m^2	15, complete break
Temperature of deflection under load Method A 1.8 MPa Method B 0.45 MPa	ISO 75-1 ISO 75-2	DIN EN ISO 75-1 DIN EN ISO 75-2	°C °C	45 105
Vicat softening temperature Method A 10 N Method B 50 N	ISO 306	DIN EN ISO 306	°C °C	170 130

II. MATHEMATICAL PRELIMINARIES

II.1. Notions of calculus

II.1.1. Sequences, series and their limits

II.1.1.1. Sequences

A sequence is defined as an ordinary list of numbers. Usually, a sequence of numbers is considered to be infinite, unless otherwise specified (the so called *finite sequence*). The sequence notation can be expressed in indicial form (with the help of a subscript letter). The index is always considered to be a positive integer number in succession from the first term:

$$a_n = a_1 + a_2 + a_3 + \cdots a_i + \cdots \tag{II. 1.1}$$

In the above equation, the sequence's terms are defined in closed form. Other sequences can have terms defined through a recursive formula:

$$a_i = f(x) \cdot x_{i-1}, \qquad i = 1,2,3, \ldots. \tag{II. 1.2}$$

where f can be a constant value or a function.

In such cases, the closed form can be obtained by specifying an initial value a_0 of the sequence.

A sequence a_n has the limit L (and it is called *convergent*) if for every $\varepsilon > 0$ there is a corresponding integer N such that if $n > N$ then $|a_n - L| < \varepsilon$. The notation will be:

$$\lim_{n\to\infty} a_n = L \qquad \text{or} \qquad a_n \to L \text{ as } n \to \infty \tag{II. 1.3}$$

Otherwise, the sequence is called *divergent*.

II.1.1.2. Series

Consider a sequence expressed as:

$$S_i = S_{i-1} + f_i(x) \tag{II. 1.4}$$

Notice that

$$\begin{gathered} S_1 = f_1(i) = a_1 \\ S_2 = S_1 + f_2(i) = a_2 \\ S_3 = S_2 + f_3(i) = a_3 \\ \ldots\ldots\ldots\ldots\ldots\ldots\ldots \\ S_n = S_{n-1} + f_n(i) = a_n \\ \ldots\ldots\ldots\ldots\ldots\ldots\ldots \end{gathered} \tag{II. 1.5}$$

The above sequence is called an *infinite series* and can be written as:

$$S = \sum_{i=1}^{\infty} a_i \tag{II.1.6}$$

In order to determine whether or not a certain infinite series has a sum, partial sums are considered.

Consider a series

$$\sum_{i=1}^{\infty} a_n = a_1 + a_1 + a_1 + \cdots \tag{II.1.7}$$

Let S_n denote its partial sum

$$S_n = \sum_{i=1}^{n} a_i = a_1 + a_1 + a_1 + \cdots a_n \tag{II.1.8}$$

If the sequence $\{S_n\}$ is convergent and if $\lim_{n\to\infty} S_n = s$ exists as a real number, then the series $\sum a_n$ is convergent, and we write

$$\sum_{i=1}^{\infty} a_n = s \tag{II.1.9}$$

The number s is called the sum of the series.

Otherwise, the series are divergent.

II.1.2. Representations of functions as power series

A *power series* is a series that takes the form:

$$\sum_{i=1}^{\infty} c_n x^n = c_0 x^0 + c_1 x^1 + c_2 x^2 + c_3 x^3 + \cdots \tag{II.1.10}$$

In the above expression c_n are constants called coefficients. For each fixed value of x equation (II.1.10) becomes a series of constants and can be tested for convergence or divergence.

A series of the form

$$\sum_{n=0}^{\infty} c_n (x-a)^n = c_0 + c_1 (x-a) + c_2 (x-a)^2 + \cdots \tag{II.1.11}$$

is called *power series in* $(x-a)$ or *power series centred at* a. Notice that when $x = a$ all the terms are equal to 0 and thus the power series centred at a are always convergent for $x = a$.

In general there are three possibilities for a power series centred at a:

a) the series is convergent only when $x = a$

b) the series is convergent for all x

c) there is a positive number R for which the series converges for $|x-a|<R$ and the series diverges for $|x-a|>R$, where R is called the radius of convergence.

For a) the radius of convergence is $R=0$ and for b) $R=\infty$.

The interval of convergence of a power series consists of all the values of x for which the series converge. For a), the interval of convergence is a single number a, for b) it is $(-\infty,\infty)$ and for c) $(a-R)<x<(a+R)$.

The representation of a function as a power series is required for integrating functions that do not have elementary primitives, for solving differential equations and for approximating functions with polynomials.

The *term-by-term differentiation and integration theorem* states that we can differentiate or integrate a function by doing so to each individual term, similar to a polynomial:

If the power series

$$\sum_{n=0}^{\infty} c_n(x-a)^n$$

has a radius of convergence $R>0$, then the function $f(x)$ defined by:

$$f(x)=c_0+c_1(x-a)+c_2(x-a)^2+\cdots=\sum_{n=0}^{\infty} c_n(x-a)^n \qquad \text{(II. 1.12)}$$

is differentiable and therefore continuous on the interval $(a-R,a+R)$ and

a)

$$\frac{df}{dx}=c_1+2c_2(x-a)+3c_3(x-a)^2+\cdots=\sum_{n=0}^{\infty} nc_n(x-a)^{n-1} \qquad \text{(II. 1.13}a\text{)}$$

$$\frac{df}{dx}\left[\sum_{n=0}^{\infty} c_n(x-a)^n\right]=\sum_{n=0}^{\infty}\frac{d}{dx}[c_n(x-a)^n] \qquad \text{(II. 1.13}b\text{)}$$

b)

$$\int f(x)dx=C+c_0(x-a)+c_1\frac{(x-a)^2}{2}+c_2\frac{(x-a)^3}{3}+\cdots=C+\sum_{n=0}^{\infty} c_n\frac{(x-a)^{n+1}}{n+1} \qquad \text{(II. 1.14}a\text{)}$$

$$\int\left[\sum_{n=0}^{\infty} c_n(x-a)^n\right]dx=\sum_{n=0}^{\infty}\int c_n(x-a)^n dx \qquad \text{(II. 1.14}b\text{)}$$

II.1.3. Taylor and MacLaurin series

Consider f a function that can be expressed as a power series:

$$f(x)=c_0+c_1(x-a)+c_2(x-a)^2+c_3(x-a)^3+\cdots \qquad |x-a|<R \qquad \text{(II. 1.15)}$$

For $x = a$ we have:

$$f(a) = c_0 \tag{II. 1.16}$$

According to (II. 1.13a):

$$\frac{df}{dx} = c_1 + 2c_2(x-a) + 3c_3(x-a)^2 + \cdots \tag{II. 1.17}$$

Substituting $x = a$:

$$\frac{df}{dx}(a) = c_1 \tag{II. 1.18}$$

If we derive equation (II. 1.17) in respect with x we obtain:

$$\frac{d^2f}{dx^2} = 2c_2 + 6c_3(x-a) + 12c_3(x-a)^2 + \cdots \tag{II. 1.19}$$

Substituting $x = a$:

$$\frac{d^2f}{dx^2}(a) = 2c_2 \tag{II. 1.20}$$

It can be demonstrated with the help of mathematical induction that:

$$\frac{d^nf}{dx^n}(a) = n! \cdot c_n$$
$$c_n = \frac{1}{n}\frac{d^nf}{dx^n}(a) \tag{II. 1.21}$$

Substituting (II. 1.23) in (II. 1.17) we obtain the Taylor series expansion of a function f at a:

$$f(x) = \frac{1}{0!}f(a) + \frac{1}{1!}\frac{df}{dx}(a)\cdot(x-a) + \frac{1}{2!}\frac{d^2f}{dx^2}(a)\cdot(x-a)^2 + \cdots + \frac{1}{n!}\frac{d^nf}{dx^n}(a)\cdot(x-a)^n + \cdots \tag{II. 1.22}$$

A special case for the Taylor series expansion is for $a = 0$, in which case it is called the MacLaurin series expansion:

$$f(x) = \frac{1}{0!}f(0) + \frac{1}{1!}\frac{df}{dx}(0)\cdot x + \frac{1}{2!}\frac{d^2f}{dx^2}(0)\cdot x^2 + \cdots + \frac{1}{n!}\frac{d^nf}{dx^n}(0)\cdot(x)^n + \cdots \tag{II. 1.23}$$

II.1.4. Limits and derivatives of functions

II.1.4.1. Definitions of limits

Consider f a function defined on an interval that contains the number a. The limit of $f(x)$ as x approaches a is L and we write

$$\lim_{x \to a} f(x) = L$$

if for every number $\varepsilon > 0$ there is a number $\delta > 0$ such that

if $\quad 0 < |x - a| < \delta \quad$ then $\quad |f(x) - L| < \varepsilon \qquad$ (II. 1.24)

The left-hand limit of a function $f(x)$ as x approaches a is L, and we write

$$\lim_{x \to a^-} f(x) = L \qquad \text{(II. 1.25)}$$

if for every $\varepsilon > 0$ there is a number $\delta > 0$ such that

if $\quad (a - \delta) < x < a \quad$ then $\quad |f(x) - L| < \varepsilon \qquad$ (II. 1.26)

The right-hand limit of a function $f(x)$ as x approaches a is L, and we write

$$\lim_{x \to a^+} f(x) = L \qquad \text{(II. 1.27)}$$

if for every $\varepsilon > 0$ there is a number $\delta > 0$ such that

if $\quad a < x < (a + \delta) \quad$ then $\quad |f(x) - L| < \varepsilon \qquad$ (II. 1.28)

II.1.4.2. Continuity

Consider f a function defined on an interval that contains the number a. If the limit $\lim_{x \to a} f(x)$ exists, then it is continuous if:

$$\lim_{x \to a} f(x) = f(a) \qquad \text{(II. 1.29)}$$

A function is continuous from the left of a number a if

$$\lim_{x \to a^-} f(x) = f(a) \qquad \text{(II. 1.30)}$$

A function is continuous from the right of a number a if

$$\lim_{x \to a^+} f(x) = f(a) \qquad \text{(II. 1.31)}$$

The following functions are continuous on the domain they are defined on: polynomial functions, rational functions, root functions, trigonometric functions, inverse trigonometric functions, exponential functions, logarithmic functions.

II.1.4.3. Tangents and derivatives

The tangent line of a function $y = f(x)$ at a point $P\big(a, f(a)\big)$ is a line through P with a slope

$$m = \lim_{x \to a} \frac{f(x) - f(a)}{x - a} \tag{II.1.32}$$

The rate of change of a function or *the derivative of a function* f *at a number* a is defined by the relation:

$$\left.\frac{df}{dx}\right|_{x=a} = f'(a) = \dot{f}(a) = Df(a) = \lim_{x \to a} \frac{f(x) - f(a)}{x - a} \tag{II.1.33}$$

where df/dx is the Leibniz notation, $f'(x)$ is the Lagrangian notation, $\dot{f}(x)$ is the Newtonian notation and $Df(x)$ is the Eulerian notation.

From (II.1.32) and (II.1.33) we can say that the tangent line to $y = f(x)$ at a point $P\big(a, f(a)\big)$ is a line through $\big(a, f(a)\big)$ whose slope is equal to the derivative of $f(x)$ at a.

The derivative can be described as a function, by replacing the constant a with a variable x:

$$\frac{df}{dx} = f'(x) = \dot{f}(x) = Df(x) = \lim_{h \to 0} \frac{f(x + h) - f(x)}{h} \tag{II.1.34}$$

A function is differentiable in a if $f'(a)$ exists. It is differentiable on an interval if it is differentiable on each point of the interval.

If $f(x)$ is differentiable, it is continuous. However, if $f(x)$ is continuous does not imply that it is differentiable.

II.1.4.4. Higher order derivatives

If $f(x)$ is a differentiable function, then its derivative df/dx is also a function. If df/dx is differentiable, then the new function called the *second derivative* will be

$$\frac{d^2 f}{dx^2} = f''(x) = \ddot{f}(x) = D^2 f(x) = \frac{d}{dx}\left(\frac{df}{dx}\right) \tag{II.1.35}$$

In a similar fashion, the third derivative of the function will be

$$\frac{d^3 f}{dx^3} = f'''(x) = D^3 f(x) = \frac{d}{dx}\left(\frac{d^2 f}{dx^2}\right) \tag{II.1.36}$$

Note that for orders higher than two, the Newtonian notation is rarely used, as it is predominantly used in mechanics to describe the rates of change (speed or acceleration).

The n^{th} order derivative of a function will be:

$$\frac{d^n f}{dx^n} = f^{(n)}(x) = D^n f(x) = \frac{d}{dx}\left(\frac{d^{n-1} f}{dx^{n-1}}\right) \tag{II.1.37}$$

II.2. Notions of algebra

II.2.1. Vector algebra

A vector is a coordinate independent geometrical entity characterized by 3 values: direction, sense and magnitude. In linear algebra, a *unit vector* in a vector space has a magnitude of 1 and represents a reference direction (other vectors are defined in report with unit vectors). So a vector v in an n-dimensional vector space is defined as:

$$\overline{v} = \sum_{i=1}^{n} v_i \cdot \overline{e_i} \tag{II.2.1}$$

where v_i represent the vector's projections on the axes defined by the unit vectors e_i.

Other notations may include

$$\overline{v} = \{v_1, v_2, \dots, v_n\} \tag{III.2}$$

$$\overline{v} = \begin{bmatrix} v_1 \\ v_2 \\ \vdots \\ v_n \end{bmatrix} \tag{II.2.3}$$

The *sum of two vectors* is another vector that is defined as:

$$\overline{u} = \overline{v} + \overline{w} = \sum_{i=1}^{n} (v_i + w_i) \cdot \overline{e_i} \tag{II.2.4}$$

The *multiplication of a vector with a scalar* is another vector that is defined as:

$$\lambda\overline{v} = \sum_{i=1}^{n} (\lambda v_i) \cdot \overline{e_i} \tag{II.2.5}$$

The *scalar* or *dot product* of two vectors is a scalar number defined as:

$$\overline{v} \cdot \overline{w} = \sum_{i=1}^{n} v_i \cdot w_i \tag{II.2.6}$$

$$\overline{v} \cdot \overline{w} = v \cdot w^T = \begin{bmatrix} v_1 \\ v_2 \\ \vdots \\ v_n \end{bmatrix} \cdot [w_1 \quad w_2 \quad \cdots \quad w_n] \tag{II.2.7}$$

The *vector* or *cross product* of two vectors is a third vector whose direction is perpendicular to the plane containing the vectors. In a three dimensional vector space, it is defined as:

$$\overline{v} \times \overline{w} = \begin{vmatrix} e_1 & e_2 & e_3 \\ v_2 & v_2 & v_3 \\ w_1 & w_2 & w_3 \end{vmatrix} \tag{II. 2.8}$$

In Newtonian mechanics, each vector is defined in relationship with the three Cartesian axes. In Lagrangian and Hamiltonian mechanics, vectors are expressed in relation with the generalized coordinates.

The Cartesian axes system (also known as the orthogonal axes system) is composed of 3 unit vectors that respect the relations:

$$e_1 = \begin{bmatrix} 1 \\ 0 \\ 0 \end{bmatrix}; \quad e_2 = \begin{bmatrix} 0 \\ 1 \\ 0 \end{bmatrix}; \quad e_3 = \begin{bmatrix} 0 \\ 0 \\ 1 \end{bmatrix} \Rightarrow \begin{cases} e_1 = e_2 \times e_3 \\ e_2 = e_3 \times e_1 \\ e_3 = e_1 \times e_2 \end{cases} \tag{II. 2.9}$$

A vector's components according to the Cartesian axes system are pictured in figure 2.

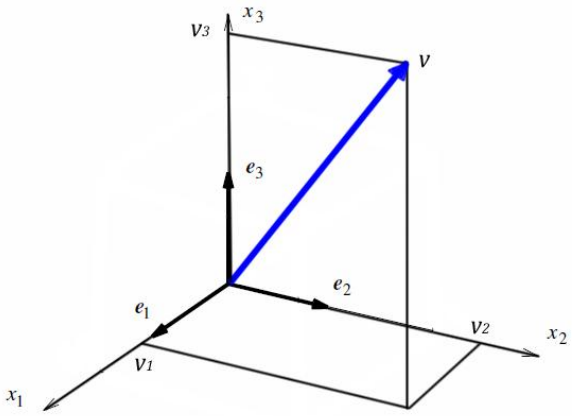

Figure II.1. Vector's components in the Cartesian axes system

The same vector can be expressed in different Cartesian axes systems, if the problem requires it (for example, in dynamics, a body has its own axes system and its movement is described in report to a fixed axes system).

$$\overline{v} = \sum_{i=1}^{n} v_i \cdot \overline{e_i} = \sum_{i=1}^{n} v'_i \cdot \overline{e'_i} \tag{II. 2.10}$$

The Cartesian axes transformation is performed with the help of the direction cosines matrix $[Q]$.

$$[e] = [Q][e'] \Rightarrow \begin{bmatrix} e_1 \\ e_2 \\ e_3 \end{bmatrix} = \begin{bmatrix} a_{11} & a_{12} & a_{13} \\ a_{21} & a_{22} & a_{23} \\ a_{31} & a_{32} & a_{33} \end{bmatrix} \cdot \begin{bmatrix} e'_1 \\ e'_2 \\ e'_3 \end{bmatrix} \tag{II. 2.11}$$

where

$$a_{ij} = e_j \cdot e'_i = \cos\left(\widehat{e_j, e'_i}\right) \tag{II. 2.12}$$

thus

$$[Q] = \begin{bmatrix} e_1 \cdot e'_1 & e_1 \cdot e'_2 & e_1 \cdot e'_3 \\ e_2 \cdot e'_1 & e_2 \cdot e'_2 & e_2 \cdot e'_3 \\ e_3 \cdot e'_1 & e_3 \cdot e'_2 & e_3 \cdot e'_3 \end{bmatrix} \tag{II. 2.13}$$

A more explicit formulation of equation (II. 2.9) is:

$$\begin{bmatrix} e_1 \\ e_2 \\ e_3 \end{bmatrix} = \begin{bmatrix} e_1 \cdot e'_1 & e_1 \cdot e'_2 & e_1 \cdot e'_3 \\ e_2 \cdot e'_1 & e_2 \cdot e'_2 & e_2 \cdot e'_3 \\ e_3 \cdot e'_1 & e_3 \cdot e'_2 & e_3 \cdot e'_3 \end{bmatrix} \cdot \begin{bmatrix} e'_1 \\ e'_2 \\ e'_3 \end{bmatrix} \tag{II. 2.14}$$

The inverse transformation is performed according to the formula:

$$[e'_i] = [Q]^T [e_i] \Rightarrow \begin{bmatrix} e'_1 \\ e'_2 \\ e'_3 \end{bmatrix} = \begin{bmatrix} a_{11} & a_{21} & a_{31} \\ a_{12} & a_{22} & a_{32} \\ a_{13} & a_{23} & a_{33} \end{bmatrix} \cdot \begin{bmatrix} e_1 \\ e_2 \\ e_3 \end{bmatrix} \tag{II. 2.15}$$

II.2.2. Tensor algebra

A tensor represents a geometric entity that performs linear mappings and it is expressed in the form of an array. The number of indices of the array represents the tensor's order and run from zero to the dimension of the related vector space. So, a zero order tensor represents a scalar value; a first order tensor T_i represents a vector; a second order tensor T_{ij} represents a two dimensional array, used for example in continuum mechanics to express the state of stress or deformation at a given point. Higher order tensors are also used in continuum mechanics, but are not as common as second order tensors.

As examples of second order tensors, the identity tensor $\boldsymbol{I}$ that maps a vector to itself and the direction cosines matrix $[\boldsymbol{Q}]$, expressed in equation (II. 2.13), which, in a given vector space, rotates the coordinate system so that the unit vectors e_i become e'_i.

Basic matrix operations and properties like sum, product, inversion and transposition are also valid for second order tensors. A tensor that satisfies the relation $\boldsymbol{S} = \boldsymbol{S}^T$ is called *symmetric tensor*, a tensor for which $\boldsymbol{S} = -\boldsymbol{S}^T$ is called *skew tensor* and a tensor for which $\boldsymbol{S}^{-1} = \boldsymbol{S}^T$ is called *orthogonal tensor*.

A *tensor product* is a bilinear operation that can be applied to various geometric entities such as vectors, matrices, tensors, vector spaces, algebras, etc. In the case of vectors of the same dimension, it is called a *dyadic product,* and it determines a tensor. For a dyadic product of two vectors $\overline{v} = \sum_{i=1}^{n} v_i \cdot \overline{e_i}$ and $\overline{w} = \sum_{i=1}^{n} w_i \cdot \overline{e_i}$, the tensor product can be defined by the relation:

$$\boldsymbol{S} = v \otimes w = \sum_{i,j=1}^{n} S_{ij} e_i \otimes e_j \tag{II. 2.16}$$

where

$$S_{ij} = \sum_{i,j=1}^{n} v_i \cdot w_j = e_i \cdot \boldsymbol{S} e_j \tag{II.2.17}$$

From (II.2.16) and (II.2.17) we have:

$$\begin{aligned} \boldsymbol{S} = v \otimes w &= \sum_{i,j=1}^{n} v_i \cdot w_j \cdot e_i \otimes e_j \\ &= \sum_{i,j=1}^{n} (e_i \cdot v_i)\left(w_j \cdot e_j\right) \end{aligned} \tag{II.2.18}$$

If written in matrix form, the dyadic product is a special case of the Kronecker product and it can be expressed as:

$$\boldsymbol{S} = v \otimes w = \begin{bmatrix} v_1 \\ v_2 \\ \vdots \\ v_n \end{bmatrix} \otimes \begin{bmatrix} w_1 & w_2 & \cdots & w_n \end{bmatrix} = \begin{bmatrix} v_1 w_1 & v_1 w_2 & \cdots & v_1 w_n \\ v_2 w_1 & v_2 w_2 & \cdots & v_2 w_n \\ \vdots & \vdots & \ddots & \vdots \\ v_n w_1 & v_n w_2 & \cdots & v_n w_n \end{bmatrix} \tag{II.2.19}$$

In consequence, a square matrix can be assigned to a second order tensor in similar way column matrices can be assigned to vectors.

II.2.3. Vector and tensor invariants

Similar to vectors, the same tensor has different components in different bases.

$$\boldsymbol{S} = \sum_{i,j=1}^{n} \boldsymbol{S}_{ij} e_i \otimes e_j = \sum_{i,j=1}^{n} \boldsymbol{S'}_{ij} e'_i \otimes e'_j \tag{II.2.20}$$

An exception to this rule is given by the identity tensor $\boldsymbol{I}$ or its multiples $\alpha \boldsymbol{I}$. According to (II.2.16)

$$\boldsymbol{S'}_{ij} = \sum_{i,j=1}^{n} v'_i \cdot w'_j \tag{II.2.21}$$

Relation (II.2.15) gives us a vector's coordinates in a different base:

$$v'_i = [\boldsymbol{Q}]^T v_i \tag{II.2.22}$$

Introducing (II.2.22) in (II.2.21) we have

$$\boldsymbol{S'}_{ij} = [\boldsymbol{Q}]^T \sum_{i,j=1}^{n} v_i \cdot w_j = [\boldsymbol{Q}]^T \boldsymbol{S}_{ij} \tag{II.2.23}$$

According to (II.2.13), $Q_{ij} = e_i \cdot e'_j$, thus

$$e_i = \sum_{j=1}^{n} Q_{ij} \cdot e'_j \quad and \quad e'_j = \sum_{i=1}^{n} Q_{ij} \cdot e_i \tag{II. 2.24}$$

Analogous,

$$e'_i = \sum_{j=1}^{n} Q_{ij} \cdot e_j \tag{II. 2.25}$$

Introducing (II. 2.23), (II. 2.24) and (II. 2.25) in (II. 2.20) we obtain:

$$\begin{aligned} \boldsymbol{S}' &= [\boldsymbol{Q}]^T \sum_{i,j=1}^{n} \boldsymbol{S}_{ij} \left[\left(\sum_{j=1}^{n} Q_{ij} \cdot e_j \right) \otimes \left(\sum_{i=1}^{n} Q_{ij} \cdot e_i \right) \right] \\ &= [\boldsymbol{Q}]^T \left(\sum_{i,j=1}^{n} \boldsymbol{S}_{ij} \sum_{i,j=1}^{n} \boldsymbol{Q}_{ij} \right) (e_i \otimes e_j) \end{aligned} \tag{II. 2.26}$$

The direction cosines matrix $[\boldsymbol{Q}]$ can be defined as

$$\sum_{i,j=1}^{n} \boldsymbol{Q}_{ij} (e_i \otimes e_j) = [\boldsymbol{Q}] \tag{II. 2.27}$$

Introducing (II. 2.16) and (II. 2.27) in (II. 2.26) we obtain

$$[\boldsymbol{S}'] = [\boldsymbol{Q}]^T [\boldsymbol{S}] [\boldsymbol{Q}] \tag{II. 2.28}$$

For the multiplied identity matrix $\alpha \boldsymbol{I}$ we have:

$$\begin{aligned} [\alpha \boldsymbol{I}'] &= [\boldsymbol{Q}]^T [\alpha \boldsymbol{I}] [\boldsymbol{Q}] \\ &= \alpha [\boldsymbol{Q}^T \boldsymbol{Q}] \\ [\alpha \boldsymbol{I}'] &= [\alpha \boldsymbol{I}] \end{aligned} \tag{II. 2.29}$$

Tensors that satisfy the condition described in relation (II. 2.29) are called *isotropic tensors*. Such tensors are used in continuum mechanics to describe material whose properties are identical in all directions.

In general, the second order tensor's components will change when the base transformation is performed, but certain intrinsic magnitudes associated with it will remain unchanged, such as a vector's magnitude, the scalar product, the trace, the double contraction or its determinant.

The firs invariant of the second order tensor represents the *tensor's contraction to a scalar*, or *the trace of the tensor* and it is defined as the sum of the diagonal components:

$$I_{\boldsymbol{S}} = \mathrm{tr}(\boldsymbol{S}) = \sum_{i=1}^{3} S_{ii} = S_{11} + S_{22} + S_{33} \tag{II. 2.30}$$

A trace has the following properties:

$$\mathrm{tr}(v \otimes w) = v \cdot w \tag{II.2.31a}$$
$$\mathrm{tr}(\boldsymbol{S})^T = \mathrm{tr}(\boldsymbol{S}) \tag{II.2.31b}$$
$$\mathrm{tr}(\boldsymbol{S}_1\boldsymbol{S}_2) = \mathrm{tr}(\boldsymbol{S}_2\boldsymbol{S}_1) \tag{II.2.31c}$$

The *double product* or the *double contraction* and is defined in terms of a trace as:

$$\boldsymbol{A}\!:\!\boldsymbol{B} = \mathrm{tr}(\mathbf{A}^{\mathrm{T}}\mathbf{B}) \tag{II.2.32}$$

A double contraction of two second order tensors can be also written as:

$$\boldsymbol{A}\!:\!\boldsymbol{B} = \sum_{i,j=1}^{n} \boldsymbol{A}_{ij} \cdot \boldsymbol{B}_{ji} \tag{II.2.33}$$

Introducing (II.2.30) and (II.2.31) in (II.2.32) we obtain:

$$\boldsymbol{A}\!:\!\boldsymbol{B} = \mathrm{tr}(\mathbf{A}^{\mathrm{T}}\mathbf{B}) = \mathrm{tr}(\mathbf{B}\mathbf{A}^{\mathrm{T}}) = \mathrm{tr}(\mathbf{B}^{\mathrm{T}}\mathbf{A}) = \mathrm{tr}(\mathbf{A}\mathbf{B}^{\mathrm{T}}) = \sum_{i,j=1}^{n} A_{ij}B_{ij} \tag{II.2.34}$$

The double contraction has the following properties:

$$\mathrm{tr}\boldsymbol{S} = \boldsymbol{I}\!:\!\boldsymbol{S} \tag{II.2.35a}$$
$$\boldsymbol{S}\!:\!(v \otimes w) = u \cdot \boldsymbol{S}v \tag{II.2.35b}$$
$$(v \otimes w)\!:\!(x \otimes y) = (v \cdot w)(x \cdot y) \tag{II.2.35c}$$
$$\boldsymbol{S}\!:\!\boldsymbol{W} = 0 \quad if \quad \boldsymbol{S}^T = \boldsymbol{S} \quad and \quad \boldsymbol{W} = -\boldsymbol{W}^T \tag{II.2.35d}$$

The second invariant of the second order tensor is defined as:

$$II_{\boldsymbol{S}} = \boldsymbol{S}\!:\!\boldsymbol{S} \tag{II.2.36a}$$
$$or \quad II_{\boldsymbol{S}} = \frac{1}{2}\left(\left(\mathrm{tr}(\boldsymbol{S})\right)^2 - \mathrm{tr}(\boldsymbol{S}^2)\right) \tag{II.2.36b}$$

The third invariant of the second order tensor represents its determinant:

$$III_{\boldsymbol{S}} = det[\boldsymbol{S}] = |\boldsymbol{S}| \tag{II.2.37}$$

Another way to express the second order tensor's invariants is through its eigenvectors and eigenvalues.

For a tensor $\boldsymbol{S}$ a vector n is considered an eigenvector with an associated eigenvalue λ if:

$$\boldsymbol{S}n = \lambda n \tag{II.2.38}$$

A way to express the relation (II.2.41) in polynomial form is:

$$\det(\boldsymbol{S} - \lambda\boldsymbol{I}) = 0 \tag{II.2.39}$$

In most cases, the roots of the polynomial (II.2.43) are imaginary and thus they are of little practical use. A particular case of interest is the symmetric tensor, for which its real eigenvalues' $\lambda_1, \lambda_2, \lambda_3$ corresponding vectors n_1, n_2, n_3 are orthogonal:

$$\boldsymbol{S}n_i = \lambda n_i \tag{II. 2.40a}$$
$$n_i \cdot n_j = \delta_{ij} \tag{II. 2.40b}$$

where δ_{ij} is called the Kronecker delta.

Consequently, the tensor $\boldsymbol{S}$ can be expressed in a new base determined by the eigenvectors, with the off-diagonal components equalling 0:

$$\boldsymbol{S} = \sum_{i=1}^{3} \lambda_i n_i \otimes n_i \tag{II. 2.41}$$

The eigenvalues of the symmetric tensor are coordinate independent, and therefore the three second order tensor invariants can be expressed in relationship with them:

$$I_{\boldsymbol{S}} = \lambda_1 + \lambda_2 + \lambda_3 \tag{II. 2.42a}$$
$$II_{\boldsymbol{S}} = \lambda_1^2 + \lambda_2^2 + \lambda_3^2 \tag{II. 2.42b}$$
$$III_{\boldsymbol{S}} = \lambda_1 \lambda_2 \lambda_3 \tag{II. 2.42c}$$

II.2.4. Higher order tensors

A third order tensor can be defined analogous to relation (II. 2.16):

$$\boldsymbol{\mathcal{A}} = u \otimes v \otimes w = \sum_{i,j,k=1}^{n} \mathcal{A}_{ijk} e_i \otimes e_j \otimes e_k \tag{II. 2.43}$$

where

$$\mathcal{A}_{ijk} = \sum_{i,j,k=1}^{n} u_i v_j w_k = (e_i \otimes e_j) : \boldsymbol{\mathcal{A}} e_k \tag{II. 2.44}$$

In continuum mechanics, such a third order tensor is used to describe the *alternating tensor* $\boldsymbol{\mathcal{E}}$ which is defined as:

$$\boldsymbol{\mathcal{E}} v = -\boldsymbol{W}_v \tag{II. 2.45}$$

where $\boldsymbol{W}_v$ is a skew tensor.

According to equation (II. 2.43),

$$\begin{aligned} \varepsilon_{ijk} &= (e_i \otimes e_j)\boldsymbol{\varepsilon} e_k \\ &= -(e_i \otimes e_j)\boldsymbol{W}_{e_k} \\ &= -e_i(\boldsymbol{W}_{e_k} e_j) \\ \varepsilon_{ijk} &= e_i \cdot (e_j \times e_k)\boldsymbol{W}_v \end{aligned} \tag{II. 2.46}$$

Note that the alternating tensor's components are the same for any Cartesian base. This means that $\boldsymbol{\mathcal{E}}$ is an isotropic third order tensor.

When describing hyperelastic materials, the relation between the second order stress and strain tensors is given by a fourth order constitutive tensor. A fourth order tensor is a geometric entity that performs a linear map between a vector v and a third order tensor $\boldsymbol{\mathcal{A}}$:

$$\boldsymbol{\mathcal{C}}v = \boldsymbol{\mathcal{A}} \tag{II.2.47}$$

Another way to define a fourth order tensor is through an equation analogous to (II.2.43), as a linear combination of the 81 tensor products of the Cartesian base vectors:

$$\boldsymbol{\mathcal{C}} = v_1 \otimes v_2 \otimes v_3 \otimes v_4 = \sum_{i,j,k,l=1}^{n} \mathcal{C}_{ijkl} e_i \otimes e_j \otimes e_k \otimes e_l \tag{II.2.48}$$

The tensor's components $\mathcal{C}_{ijkl}$ are defined as:

$$\mathcal{C}_{ijkl} = \sum_{i,j,k,l=1}^{n} v_{1_i} v_{2_j} v_{3_k} v_{4_l} = \left(e_i \otimes e_j\right) : \boldsymbol{\mathcal{C}} : (e_k \otimes e_l) \tag{II.2.49}$$

Fourth order tensors can also be expressed in terms of linear mapping between two second order tensors. In this case, a way to define the fourth order tensor is in matrix form, through the Kronecker product:

$$\boldsymbol{S} \otimes \boldsymbol{T} = \begin{bmatrix} s_{11}\boldsymbol{T} & s_{12}\boldsymbol{T} & \cdots & s_{1n}\boldsymbol{T} \\ s_{21}\boldsymbol{T} & s_{22}\boldsymbol{T} & \cdots & s_{2n}\boldsymbol{T} \\ \vdots & \vdots & \ddots & \vdots \\ s_{n1}\boldsymbol{T} & s_{n2}\boldsymbol{T} & \cdots & s_{nn}\boldsymbol{T} \end{bmatrix} \tag{II.2.50}$$

In a more explicit form, equation (II.2.49) can be written:

$$\boldsymbol{S} \otimes \boldsymbol{T} = \begin{bmatrix} \begin{pmatrix} s_{11}t_{11} & \cdots & s_{11}t_{1n} \\ \vdots & \ddots & \vdots \\ s_{11}t_{n1} & \cdots & s_{11}t_{nn} \end{pmatrix} & \cdots & \begin{pmatrix} s_{1n}t_{11} & \cdots & s_{1n}t_{1n} \\ \vdots & \ddots & \vdots \\ s_{1n}t_{n1} & \cdots & s_{1n}t_{nn} \end{pmatrix} \\ \vdots & \ddots & \vdots \\ \begin{pmatrix} s_{n1}t_{11} & \cdots & s_{n1}t_{1n} \\ \vdots & \ddots & \vdots \\ s_{n1}t_{n1} & \cdots & s_{n1}t_{nn} \end{pmatrix} & \cdots & \begin{pmatrix} s_{nn}t_{11} & \cdots & s_{nn}t_{1n} \\ \vdots & \ddots & \vdots \\ s_{nn}t_{n1} & \cdots & s_{nn}t_{nn} \end{pmatrix} \end{bmatrix} \tag{II.2.51}$$

If we consider:

$$\boldsymbol{S} = v_1 \otimes v_2 = \begin{bmatrix} v_{1_1}v_{2_1} & \cdots & v_{1_1}v_{2_n} \\ \vdots & \ddots & \vdots \\ v_{1_n}v_{2_1} & \cdots & v_{1_n}v_{2_n} \end{bmatrix} \; and \; \boldsymbol{T} = v_3 \otimes v_4 = \begin{bmatrix} v_{3_1}v_{4_1} & \cdots & v_{3_1}v_{4_n} \\ \vdots & \ddots & \vdots \\ v_{3_n}v_{4_1} & \cdots & v_{3_n}v_{4_n} \end{bmatrix} \tag{II.2.52}$$

then relations (II.2.47) and (II.2.50) are equivalent.

Thus, a double contraction of the fourth order tensor with a second order tensor results in another second order tensor. In consequence, the fourth order identity tensor $\boldsymbol{\mathcal{I}}$ and the fourth order transposition tensor $\tilde{\boldsymbol{\mathcal{I}}}$ are defined as:

$$\boldsymbol{\mathcal{I}} : \boldsymbol{S} = \boldsymbol{S} \tag{II.2.53a}$$

$$\tilde{\mathcal{J}}:\boldsymbol{S}=\boldsymbol{S}^{T} \qquad (\text{II. } 2.53b)$$

From (II. 2.49) and (II. 2.53a) we obtain:

$$\begin{aligned}\mathcal{J}_{ijkl} &= \left(e_i \otimes e_j\right):\boldsymbol{\mathcal{J}}:\left(e_k \otimes e_l\right)\\ &= \left(e_i \otimes e_j\right):\left(e_k \otimes e_l\right)\\ &= \left(e_i \cdot e_j\right)\left(e_k \cdot e_l\right)\end{aligned} \qquad (\text{II. } 2.54)$$

And from (II. 2.49) and (II. 2.53b) we obtain:

$$\begin{aligned}\tilde{\mathcal{J}}_{ijkl} &= \left(e_i \otimes e_j\right):\tilde{\boldsymbol{\mathcal{J}}}:\left(e_k \otimes e_l\right)\\ &= \left(e_i \otimes e_j\right):\left(e_l \otimes e_k\right)\\ &= \left(e_i \cdot e_j\right)\left(e_l \cdot e_k\right)\end{aligned} \qquad (\text{II. } 2.55)$$

Both $\boldsymbol{\mathcal{J}}$ and $\tilde{\boldsymbol{\mathcal{J}}}$ are isotropic fourth order tensors (they have the same components in every Cartesian base), and are of particular interest because they help describe the elasticity tensor for materials which have identical properties in all directions.

All fourth order isotropic tensors can be expressed as combinations of the identity and transposition fourth order tensors and the additional isotropic tensor $I \otimes I$:

$$\boldsymbol{\mathcal{C}} = \alpha I \otimes I + \beta\boldsymbol{\mathcal{J}} + \gamma\tilde{\boldsymbol{\mathcal{J}}} \qquad (\text{II. } 2.56)$$

A fourth order tenor $\boldsymbol{\mathcal{C}}$ is considered symmetric if it respects the relation:

$$\boldsymbol{\mathcal{C}}:\boldsymbol{T}:\boldsymbol{S} = \boldsymbol{T}:\boldsymbol{\mathcal{C}}:\boldsymbol{S} \qquad (\text{II. } 2.57)$$

where $\boldsymbol{T}$ and $\boldsymbol{S}$ are two arbitrary second order tensors.

II.3. Differential calculus

II.3.1. Linearization and the directional derivative

The non-linear problems that occur in continuum mechanics are solved through linearization, and iteratively solving the linear equations until a solution of the non-linear problem is found. The most common method of linearization is the Newton-Raphson method.

II.3.1.1. One degree of freedom

Consider the non linear one degree of freedom equation $f(x)$. From an initial solution x_0, according to (II. 1.22) the function can be written as:

$$f(x) = f(x_0) + \frac{1}{1!}\frac{df}{dx}\Big|_{x_0}(x - x_0)^1 + \frac{1}{2!}\frac{d^2f}{dx^2}\Big|_{x_0}(x - x_0)^2 + \cdots \quad \text{(II. 1.22)}$$

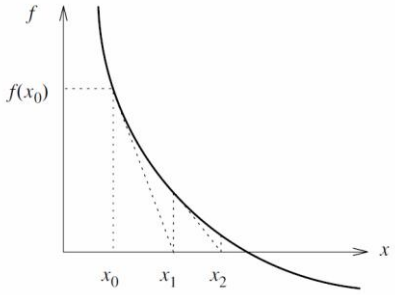

Figure II.2. One degree of freedom problem
[reprint from **[11]**]

The increment in x can be expressed as:

$$u = (x - x_0) \quad \text{(II. 3.1)}$$

Introducing (II. 3.1) in (II. 1.22) we obtain:

$$f(x_0 + u) = f(x_0) + \frac{1}{1!}\frac{df}{dx}\Big|_{x_0}u + \frac{1}{2!}\frac{d^2f}{dx^2}\Big|_{x_0}u^2 + \cdots \quad \text{(II. 3.2)}$$

The linearization of the one degree of freedom equation using the Newton-Rapshon method is obtained by truncating the Taylor series after the second term:

$$f(x_0 + u) \approx f(x_0) + \frac{df}{dx}\Big|_{x_0}u \quad \text{(II. 3.3)}$$

Equation (II. 3.3) represents a linear function in u and the term $u(df/dx)|_{x_0}$ is called the linearized increment of $f(x)$ at x_0 with respect to u.

$$\frac{df}{dx}\Big|_{x_0}u = Df(x_0)[u] \approx f(x_0 + u) - f(x_0) \quad \text{(II. 3.4)}$$

The Newton-Raphson iterative procedure is set up using the equation (II. 3.3) and requesting the function $f(x_k + u)$ to disappear, leaving a linear equation in u:

$$f(x_k) + Df(x_k)[u] = 0 \quad \text{(II. 3.5)}$$

for which the iterative value x_{k+1} (Figure II.3) is obtained as:

$$u = \left[-\frac{df}{dx}\Big|_{x_k} \right]^{-1} f(x_k); \qquad x_{k+1} = x_k + u \tag{II.3.6}$$

II.3.1.2. Generalized solution

A generalized solution will be proposed, starting from the one degree of freedom case.

Consider a set of general nonlinear equations:

$$\boldsymbol{\mathcal{F}}(\mathbf{x}) = 0 \tag{II.3.7}$$

where $\mathbf{x}$ represents a set of unknown variables or functions.

Consider an initial set of variables $\mathbf{x}$ and a general increment $\mathbf{u}$ so that:

$$\mathbf{x} = \mathbf{x}_0 + \mathbf{u} \tag{II.3.8}$$

In order to simplify the determination of the directional derivative of a function $\boldsymbol{\mathcal{F}}$ of multiple variables $\mathbf{x}$, a single parameter ϵ is introduced so that:

$$\mathbf{F}(\epsilon) = \boldsymbol{\mathcal{F}}(\mathbf{x}_0 + \epsilon\mathbf{u}) \tag{II.3.9}$$

In the case of a function of two variables x_1 and x_2, the parameter ϵ changes the function $\boldsymbol{\mathcal{F}}$ in the direction $\mathbf{u}$ as shown in Figure 4.

In order to develop the Newton-Raphson linearization, a Taylor's series expansion of the nonlinear function $\mathbf{F}(\epsilon)$ about $\epsilon = 0$, corresponding to $\mathbf{x} = \mathbf{x}_0$ gives:

$$\mathbf{F}(\epsilon) = \mathbf{F}(0) + \frac{1}{1!}\frac{d\mathbf{F}}{d\epsilon}\Big|_{\epsilon=0} \epsilon^1 + \frac{1}{2!}\frac{d^2\mathbf{F}}{d\epsilon^2}\Big|_{\epsilon=0} \epsilon^2 + \cdots \tag{II.3.10}$$

Introducing (II.3.9) in (II.3.10) we obtain:

$$\boldsymbol{\mathcal{F}}(\mathbf{x}_0 + \epsilon\mathbf{u}) = \boldsymbol{\mathcal{F}}(\mathbf{x}_0) + \frac{1\epsilon^1}{1!}\frac{d}{d\epsilon}\Big|_{\epsilon=0} \boldsymbol{\mathcal{F}}(\mathbf{x}_0 + \epsilon\mathbf{u}) + \frac{1\epsilon^2}{2!}\frac{d^2}{d\epsilon^2}\Big|_{\epsilon=0} \boldsymbol{\mathcal{F}}(\mathbf{x}_0 + \epsilon\mathbf{u}) + \cdots \tag{II.3.11}$$

By truncating the Taylor's series, the function $\boldsymbol{\mathcal{F}}(\mathbf{x})$ increment will result:

$$\boldsymbol{\mathcal{F}}(\mathbf{x}_0 + \epsilon\mathbf{u}) - \boldsymbol{\mathcal{F}}(\mathbf{x}_0) \approx \epsilon\frac{d}{d\epsilon}\Big|_{\epsilon=0} \boldsymbol{\mathcal{F}}(\mathbf{x}_0 + \epsilon\mathbf{u}) \tag{II.3.12}$$

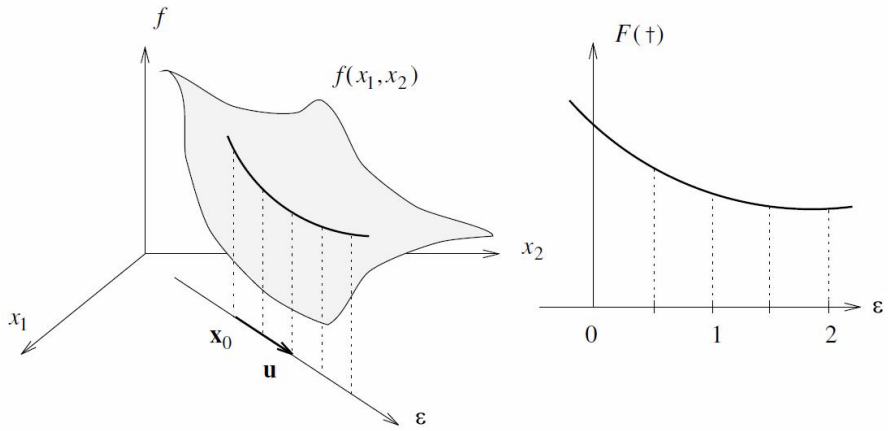

Figure II.3. Two degree of freedom linear problem
[reprint from **[11]**]

In the above equations, ϵ is an artificial parameter used as a vehicle to perform the derivative. For $\epsilon = 1$, a linear approximation of the increment of $\boldsymbol{\mathcal{F}}(\mathbf{x})$ is given by the equation:

$$\boldsymbol{\mathcal{F}}(\mathbf{x}_0 + \mathbf{u}) - \boldsymbol{\mathcal{F}}(\mathbf{x}_0) \approx 1 \frac{d}{d\epsilon}\bigg|_{\epsilon=0} \boldsymbol{\mathcal{F}}(\mathbf{x}_0 + \epsilon\mathbf{u}) \qquad \text{(II. 3.13)}$$

The term on the right hand side is called the directional derivative of $\boldsymbol{\mathcal{F}}(\mathbf{x})$ at $\mathbf{x}_0$ in the direction of $\mathbf{u}$:

$$\frac{d}{d\epsilon}\bigg|_{\epsilon=0} \boldsymbol{\mathcal{F}}(\mathbf{x}_0 + \epsilon\mathbf{u}) = D\boldsymbol{\mathcal{F}}(\mathbf{x}_0)[\mathbf{u}] \qquad \text{(II. 3.14)}$$

With the help of the directional derivative, the value of $\boldsymbol{\mathcal{F}}(\mathbf{x}_0 + \mathbf{u})$ can now be linearly approximated as:

$$\boldsymbol{\mathcal{F}}(\mathbf{x}_0 + \mathbf{u}) \approx \boldsymbol{\mathcal{F}}(\mathbf{x}_0) + D\boldsymbol{\mathcal{F}}(\mathbf{x}_0)[\mathbf{u}] \qquad \text{(II. 3.15)}$$

Introducing (II. 3.7) in (II. 3.15) and setting $\boldsymbol{\mathcal{F}}(\mathbf{x}_0 + \mathbf{u}) = 0$, we obtain:

$$\boldsymbol{\mathcal{F}}(\mathbf{x}_0) + D\boldsymbol{\mathcal{F}}(\mathbf{x}_0)[\mathbf{u}] = 0 \qquad \text{(II. 3.16)}$$

So, the general Newton-Raphson procedure can be written as:

$$D\boldsymbol{\mathcal{F}}(\mathbf{x}_k)[\mathbf{u}] = -\boldsymbol{\mathcal{F}}(\mathbf{x}_k); \qquad \mathbf{x}_{k+1} = \mathbf{x}_k + \mathbf{u} \qquad \text{(II. 3.17)}$$

II.3.1.3. Properties of the directional derivative

a) If $\boldsymbol{\mathcal{F}}(\mathbf{x}) = \boldsymbol{\mathcal{F}}_1(\mathbf{x}) + \boldsymbol{\mathcal{F}}_1(\mathbf{x})$, then

$$D\boldsymbol{\mathcal{F}}(\mathbf{x}_0)[\mathbf{u}] = D\boldsymbol{\mathcal{F}}_1(\mathbf{x}_0)[\mathbf{u}] + D\boldsymbol{\mathcal{F}}_2(\mathbf{x}_0)[\mathbf{u}] \tag{II. 3.18a}$$

b) If $\boldsymbol{\mathcal{F}}(\mathbf{x}) = \boldsymbol{\mathcal{F}}_1(\mathbf{x}) \cdot \boldsymbol{\mathcal{F}}_1(\mathbf{x})$ (for any type of product), then

$$D\boldsymbol{\mathcal{F}}(\mathbf{x}_0)[\mathbf{u}] = D\boldsymbol{\mathcal{F}}_1(\mathbf{x}_0)[\mathbf{u}] \cdot \boldsymbol{\mathcal{F}}_2(\mathbf{x}_0) + \boldsymbol{\mathcal{F}}_1(\mathbf{x}_0) \cdot D\boldsymbol{\mathcal{F}}_2(\mathbf{x}_0)[\mathbf{u}] \tag{II. 3.18b}$$

c) If $\boldsymbol{\mathcal{F}}(\mathbf{x}) = \boldsymbol{\mathcal{F}}_1\big(\boldsymbol{\mathcal{F}}_2(\mathbf{x})\big)$, then

$$D\boldsymbol{\mathcal{F}}(\mathbf{x}_0)[\mathbf{u}] = D\boldsymbol{\mathcal{F}}_1\big(\boldsymbol{\mathcal{F}}_2(\mathbf{x}_0)\big)\big[D\boldsymbol{\mathcal{F}}_2(\mathbf{x}_0)[\mathbf{u}]\big] \tag{II. 3.18c}$$

II.3.2. Tensor analysis

In continuum mechanics the tensors change their components from point to point throughout the domain. The resulting fields will have the order of the tensor that generated them: zero order tensor fields (scalar fields, such as temperature or density fields), first order tensor fields (vector fields, such as velocity or acceleration fields) or second order tensor fields (such as stress fields).

II.3.2.1. Gradient and divergence operators

Consider a three dimensional vector space and a function $f(x)$ (scalar field) that varies throughout the domain. The function's gradient $\boldsymbol{\nabla} f$ at a given point x_0 represents a vector that accounts for the change in the function f in the direction of an arbitrary incremental vector u:

$$\boldsymbol{\nabla} f(x_0) \cdot u = Df(x_0)[u] \tag{II. 3.19}$$

Introducing (II. 3.14) in (II. 3.19) we obtain:

$$\boldsymbol{\nabla} f(x_0) \cdot u = \frac{d}{d\epsilon}\bigg|_{\epsilon=0} f(\mathbf{x}_0 + \epsilon\mathbf{u}) \;= \sum_{i=1}^{n} u_i \frac{\partial f}{\partial x_i}\bigg|_{x_i = x_{0,i}} \tag{II. 3.20}$$

Thus, the components of the gradient are partial derivatives of the function f in respect to each of the three spatial directions:

$$\boldsymbol{\nabla} f = \sum_{i=1}^{3} \frac{\partial f}{\partial x_i} e_i \tag{II. 3.21}$$

In the case of a vector field v, its gradient at a point x_0 is a *second order tensor* $\nabla v(x_0)$ that maps an arbitrary vector u into the directional derivative of v at x_0 in the direction of u:

$$\boldsymbol{\nabla} v(x_0) \cdot u = Dv(x_0)[u] \tag{II. 3.22}$$

Analogous to (II. 3.21), it can be demonstrated that the gradient of a vector field represents the vector components' partial derivatives:

$$\nabla v = \sum_{i,j=1}^{3} \frac{\partial v_i}{\partial x_j} e_i \otimes e_j \tag{II. 3.23}$$

The trace of the gradient of a vector field represents the *divergence* of the field. The divergence is a scalar value ($\div v$) and it can be expressed as:

$$\div v = \mathrm{tr}\nabla v = \nabla v : \boldsymbol{I} = \sum_{i=1}^{3} \frac{\partial v}{\partial x_i} \tag{II. 3.24}$$

Analogous to the vector field v, the gradient of a second order tensor $\boldsymbol{S}$ at a point x_0 is a *third order tensor* $\nabla \boldsymbol{S}(x_0)$ that maps an arbitrary vector u into the directional derivative of $\boldsymbol{S}$ at x_0 in the direction of u:

$$\nabla \boldsymbol{S}(x_0) \cdot u = D\boldsymbol{S}(x_0)[u] \tag{II. 3.25}$$

The components of $\nabla \boldsymbol{S}$ are, in similar fashion, the partial derivatives of the components of $\boldsymbol{S}$:

$$\nabla \boldsymbol{S} = \sum_{i,j,k=1}^{3} \frac{\partial S_{ij}}{\partial x_k} e_i \otimes e_j \otimes e_k \tag{II. 3.26}$$

The divergence of a second order tensor $\boldsymbol{S}$ represents the vector $\div \boldsymbol{S}$ that can be defined as:

$$\div \boldsymbol{S} = \mathrm{tr}\nabla \boldsymbol{S} = \nabla \boldsymbol{S} : \boldsymbol{I} = \sum_{i,j=1}^{3} \frac{\partial S_{i,j}}{\partial x_i} e_i \tag{II. 3.27}$$

II.3.2.2. Properties of the gradient and divergence operators

$$\nabla(fv) = f\nabla v + v \otimes \nabla f \tag{II. 3.28a}$$
$$\div(fv) = f \div v + v \cdot \nabla f \tag{II. 3.28b}$$
$$\nabla(v \cdot w) = (\nabla v)^T w + (\nabla w)^T v \tag{II. 3.28c}$$
$$\div(v \otimes w) = v \div w + (\nabla v) w \tag{II. 3.28d}$$
$$\div(\boldsymbol{S}^T v) = \boldsymbol{S} : \nabla v + v \cdot \div \boldsymbol{S} \tag{II. 3.28e}$$
$$\div(f\boldsymbol{S}) = f \div \boldsymbol{S} + \boldsymbol{S} \cdot \nabla f \tag{II. 3.28f}$$
$$\nabla(f\boldsymbol{S}) = f\nabla \boldsymbol{S} + \boldsymbol{S} \otimes \nabla f \tag{II. 3.28g}$$

II.3.2.3. Integration theorems

Consider a volume V with the boundary surface ∂V and n the unit normal to this surface at a given point (Figure 5). For the gradient of the scalar field f, the basic equation giving the integral is:

$$\int_V \nabla f dV = \int_{\partial V} f n dA \qquad (\text{II}.3.29)$$

Similar to (II.3.29), for a vector field v or a second order tensor field $\boldsymbol{S}$, the integral can be expressed as:

$$\int_V \nabla v dV = \int_{\partial V} v \otimes n dA \qquad (\text{II}.3.30)$$

For the trace of the above expression, the *Gauss theorem* (or the divergence theorem) is obtained:

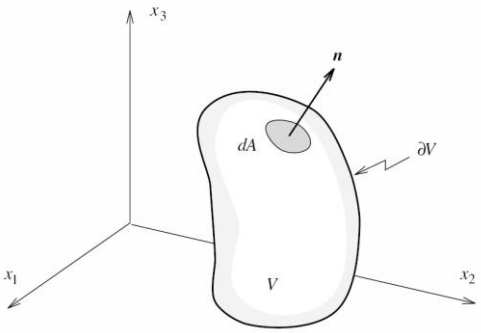

Figure 2.4. General volume and area element
[reprint from **[11]**]

$$\int_V \div v dV = \int_{\partial V} v \cdot n dA \qquad (\text{II}.3.31)$$

The Gauss theorem for the second order tensor can be expressed as:

$$\int_V \div \boldsymbol{S} dV = \int_{\partial V} \boldsymbol{S} n dA \qquad (\text{II}.3.32)$$

III. MECHANICS OF MATERIALS

III.1. Notions of Kinematics

III.1.1. Introduction

Kinematics is a branch of mechanics that deals with the movement/deformation of bodies or systems of bodies without considering the forces that caused the motion/deformation.

This chapter will deal with finite deformations and the best way to characterize the motion is this case is through different coordinate systems such as the Lagrangian and Eulerian systems.

The nonlinear kinematic quantities that may occur are linearized in order to be included in the linear equilibrium equations that form the basis of the Newton-Raphson solution to finite element equilibrium equations.

III.1.2. Motion

In Lagrangian mechanics, a body is considered to be composed of particles, each being characterized by a coordinate $\boldsymbol{X}(X_1, X_2, X_3)$ in the Cartesian base $\boldsymbol{E}(E_1, E_2, E_3)$ at the initial time $t_0 = 0$. At a given time t, the position of the particles will be characterized by the coordinate $x(x_1, x_2, x_3)$ in the Cartesian base $e(e_1, e_2, e_3)$ (figure 6). The motion of a given particle can be mathematically expressed through a function ϕ [1]:

$$x = \phi(\boldsymbol{X}, t) \qquad \text{(III. 1.1)}$$

In case of constant time (a fixed value of t), the function ϕ describes the mapping between the undeformed and the deformed bodies. In the case of a fixed particle (a fixed value of $\boldsymbol{X}$), the function ϕ describes the trajectory of the given particle as a function of time.

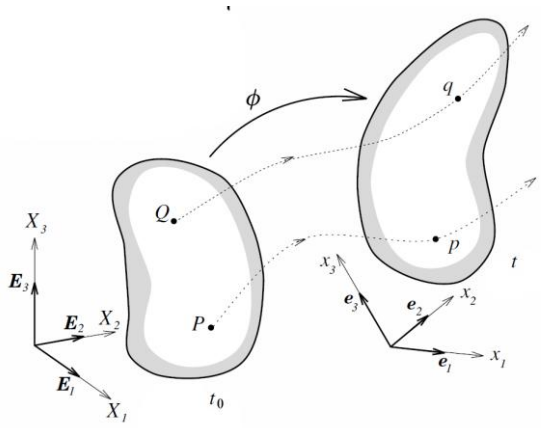

Figure III.1. General motion of a deformable body
[reprint from **[11]**]

III.1.3. Material and spatial descriptions

In deformation analysis, the distinction between the chosen coordinate systems that describe the motion must be made. The variation of relevant quantities can be described in terms of where the particle was before the deformation (the material or Lagrangian description) and in terms of where the particle is during the deformation (the spatial or Eulerian description). The former approach deals with the behaviour of the material particle, while the latter deals with the behaviour at a spatial position [1][2].

In fluid mechanics, in almost all cases the equations are written after the spatial description, because a Newtonian fluid's behaviour is independent on its previous states, and thus it is unnecessary and sometimes impossible to describe the material after its initial states. In solid mechanics however, a formulation after the material description will be required at some point, due to the constitutive behaviour of the particle [1].

Regardless of the chosen approach, the governing equation must refer to the whole body, so they must be formulated after the spatial description.

Consider a variable function ψ that describes the particle, which can be in form of a scalar, (density), vector (velocity), second order tensor (stress field) etc. In mathematical terms, the two approaches can be expressed as:

a) *Material description*: the variation of ψ over the body is described with respect of the initial coordinate $\boldsymbol{X}$, used to characterise the material particle at time $t_0 = 0$:

$$\psi = \psi(\boldsymbol{X}, t) \qquad \text{(III. 1.2}a\text{)}$$

In this case, a change in time implies that the same material particle characterized by $\boldsymbol{X}$ has a different value of the variable quantity ψ (different density, velocity, stress field, etc).

b) *Spatial description*: ψ is described with the respect of the position in space of the given particle x at the time t:

$$\psi = \psi(x,t) \qquad (\text{III. } 1.2b)$$

In this case, a change in time implies that a variation of the variable quantity ψ is observed at the same spatial position characterized by x (occupied by a different particle) [1].

III.1.4. Deformation gradient

The deformation gradient tensor $\boldsymbol{F}$ is a key quantity in finite deformation analysis, linking the initial state of the body to the corresponding quantities during deformation. Thus the deformation gradient tensor describes the relative spatial positions of two particles during deformation in terms of their relative positions before deformation.

Consider two material particles Q_1 and Q_2 described by the coordinates $\boldsymbol{X}_{Q_1}$ and $\boldsymbol{X}_{Q_2}$ respectively at $t_0 = 0$, in the neighbourhood of a particle P of coordinates $\boldsymbol{X}_P$ (Figure 7). The positions of the particles Q_1 and Q_2 in respect with P are given by the vectors $d\boldsymbol{X}_1$ and $d\boldsymbol{X}_2$:

$$d\boldsymbol{X}_1 = \boldsymbol{X}_{Q_1} - \boldsymbol{X}_P \qquad (\text{III. } 1.3a)$$
$$d\boldsymbol{X}_2 = \boldsymbol{X}_{Q_2} - \boldsymbol{X}_P \qquad (\text{III. } 1.3b)$$

According to $(\text{I. } 108a)$, after the deformation, the particles P, Q_1 and Q_2 have acquired new coordinates described by the mapping:

$$x_p = \phi(\boldsymbol{X}_P, t) \qquad (\text{III. } 1.4a)$$
$$x_{Q_1} = \phi\left(\boldsymbol{X}_{Q_1}, t\right) \qquad (\text{III. } 1.4b)$$
$$x_{Q_2} = \phi\left(\boldsymbol{X}_{Q_2}, t\right) \qquad (\text{III. } 1.4c)$$

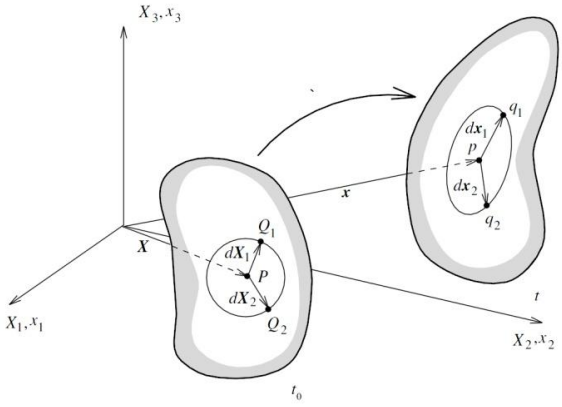

Figure III.2. General motion of particles during deformation
[reprint from **[11]**]

The corresponding position vectors become:

$$dx_1 = x_{Q_1} - x_P = \phi\left(\boldsymbol{X}_{Q_1}, t\right) - \phi(\boldsymbol{X}_P, t) = \phi(\boldsymbol{X}_P + d\boldsymbol{X}_1, t) - \phi(\boldsymbol{X}_P, t) \qquad (\text{III. } 1.5a)$$
$$dx_2 = x_{Q_2} - x_P = \phi\left(\boldsymbol{X}_{Q_2}, t\right) - \phi(\boldsymbol{X}_P, t) = \phi(\boldsymbol{X}_P + d\boldsymbol{X}_2, t) - \phi(\boldsymbol{X}_P, t) \qquad (\text{III. } 1.5b)$$

The deformation gradient tensor is defined as [1]:

$$\boldsymbol{F} = \nabla\phi = \frac{\partial \phi}{\partial \boldsymbol{X}} \tag{III. 1.6a}$$

Another way to write equation (III. 1.6a) is for the notation $x = x(\boldsymbol{X}, t)$ [1]:

$$\boldsymbol{F} = \nabla\phi = \frac{\partial x}{\partial \boldsymbol{X}} \tag{III. 1.6b}$$

From (III. 1.5a) and (III. 1.6) it results that:

$$dx_1 = \boldsymbol{F} d\boldsymbol{X}_1 \tag{III. 1.7a}$$
$$dx_2 = \boldsymbol{F} d\boldsymbol{X}_2 \tag{III. 1.7b}$$

A generalized formula for constructing the deformation gradient tensor is [1]:

$$\boldsymbol{F} = \sum_{i,I=1}^{3} F_{iI} e_i \otimes E_I \tag{III. 1.8}$$

where $F_{iI} = \partial x_i / \partial \boldsymbol{X_I}$

The explicit form of equation (III. 1.8) is:

$$\boldsymbol{F} = \begin{pmatrix} \frac{\partial x_1}{\partial \boldsymbol{X}_1} & \frac{\partial x_1}{\partial \boldsymbol{X}_2} & \frac{\partial x_1}{\partial \boldsymbol{X}_3} \\ \frac{\partial x_2}{\partial \boldsymbol{X}_1} & \frac{\partial x_2}{\partial \boldsymbol{X}_2} & \frac{\partial x_2}{\partial \boldsymbol{X}_3} \\ \frac{\partial x_3}{\partial \boldsymbol{X}_1} & \frac{\partial x_3}{\partial \boldsymbol{X}_3} & \frac{\partial x_3}{\partial \boldsymbol{X}_3} \end{pmatrix} \tag{III. 1.9}$$

The inverse of $\boldsymbol{F}$ is:

$$\boldsymbol{F}^{-1} = \sum_{i,I=1}^{3} F_{iI}^{-1} E_I \otimes e_i \tag{III. 1.10}$$

where

$$F_{iI}^{-1} = \frac{\partial \boldsymbol{X}_I}{\partial x_i} = \nabla\phi^{-1} \tag{III. 1.11}$$

In literature, the relationship between the initial position vectors and the current position vectors is referred to as *push forward* and *pull back* relations: the spatial vector dx is considered the push forward of the material vector $d\boldsymbol{X}$ and the material vector $d\boldsymbol{X}$ is considered the pull back of the spatial vector dx [1].

$$dx = \phi_*[d\boldsymbol{X}] = \boldsymbol{F} d\boldsymbol{X} \tag{III. 1.12a}$$
$$d\boldsymbol{X} = \phi_*^{-1}[dx] = \boldsymbol{F}^{-1} dx \tag{III. 1.12b}$$

III.1.5. Strain

The strain components can be introduced by taking into account the elongation of a linear element. In the material description, the square of the length of the line element is expressed as:

$$L^2 = d\boldsymbol{X}^T \cdot d\boldsymbol{X} \tag{III.1.13}$$

In the spatial description, recalling equation (III.1.12a), the square of the length of the line element is expressed as:

$$\begin{aligned} l^2 &= dx^T \cdot dx \\ l^2 &= d\boldsymbol{X}^T \boldsymbol{F}^T \cdot \boldsymbol{F} d\boldsymbol{X} \end{aligned} \tag{III.1.14}$$

The product $\boldsymbol{F}^T \cdot \boldsymbol{F}$ is called the *left Cauchy-Green* tensor $\boldsymbol{C}$:

$$\boldsymbol{C} = \boldsymbol{F}^T \boldsymbol{F} \tag{III.1.15}$$

Considering that:

$$\frac{\partial x_i}{\partial \boldsymbol{X}_1} = \begin{pmatrix} \frac{\partial x_1}{\partial \boldsymbol{X}_1} \\ \frac{\partial x_2}{\partial \boldsymbol{X}_1} \\ \frac{\partial x_3}{\partial \boldsymbol{X}_1} \end{pmatrix}; \qquad \frac{\partial x_i}{\partial \boldsymbol{X}_2} = \begin{pmatrix} \frac{\partial x_1}{\partial \boldsymbol{X}_2} \\ \frac{\partial x_2}{\partial \boldsymbol{X}_2} \\ \frac{\partial x_3}{\partial \boldsymbol{X}_2} \end{pmatrix}; \qquad \frac{\partial x_i}{\partial \boldsymbol{X}_3} = \begin{pmatrix} \frac{\partial x_1}{\partial \boldsymbol{X}_3} \\ \frac{\partial x_2}{\partial \boldsymbol{X}_3} \\ \frac{\partial x_3}{\partial \boldsymbol{X}_3} \end{pmatrix} \tag{III.1.16}$$

an explicit form of equation (III.1.15) will be:

$$\boldsymbol{C} = \begin{pmatrix} \left(\frac{\partial x_i}{\partial \boldsymbol{X}_1}\right)^T \frac{\partial x_i}{\partial \boldsymbol{X}_1} & \left(\frac{\partial x_i}{\partial \boldsymbol{X}_1}\right)^T \frac{\partial x_i}{\partial \boldsymbol{X}_2} & \left(\frac{\partial x_i}{\partial \boldsymbol{X}_1}\right)^T \frac{\partial x_i}{\partial \boldsymbol{X}_3} \\ \left(\frac{\partial x_i}{\partial \boldsymbol{X}_2}\right)^T \frac{\partial x_i}{\partial \boldsymbol{X}_1} & \left(\frac{\partial x_i}{\partial \boldsymbol{X}_2}\right)^T \frac{\partial x_i}{\partial \boldsymbol{X}_2} & \left(\frac{\partial x_i}{\partial \boldsymbol{X}_2}\right)^T \frac{\partial x_i}{\partial \boldsymbol{X}_3} \\ \left(\frac{\partial x_i}{\partial \boldsymbol{X}_3}\right)^T \frac{\partial x_i}{\partial \boldsymbol{X}_1} & \left(\frac{\partial x_i}{\partial \boldsymbol{X}_3}\right)^T \frac{\partial x_i}{\partial \boldsymbol{X}_2} & \left(\frac{\partial x_i}{\partial \boldsymbol{X}_3}\right)^T \frac{\partial x_i}{\partial \boldsymbol{X}_3} \end{pmatrix} \tag{III.1.17}$$

For a spatial description approach, the *right Cauchy-Green deformation tensor* $\boldsymbol{B}$ is used, which operates with the spatial position vector dx:

$$\begin{aligned} L^2 &= d\boldsymbol{X}^T \cdot d\boldsymbol{X} \\ &= (\boldsymbol{F}^{-1} dx)^T \cdot \boldsymbol{F}^{-1} dx \\ L^2 &= dx^T \cdot \boldsymbol{B}^{-1} dx \end{aligned} \tag{III.1.18}$$

where

$$\boldsymbol{B}^{-1} = (\boldsymbol{F}^{-1})^T \cdot \boldsymbol{F}^{-1} \tag{III.1.19a}$$

$$\boldsymbol{B} = \boldsymbol{F}\boldsymbol{F}^T \tag{III.1.19b}$$

Recalling equation (III.1.16), the explicit form of the right Cauchy-Green tensor will be:

$$\boldsymbol{B}=\begin{pmatrix}\frac{\partial x_i}{\partial \boldsymbol{X}_1}\left(\frac{\partial x_i}{\partial \boldsymbol{X}_1}\right)^T & \frac{\partial x_i}{\partial \boldsymbol{X}_2}\left(\frac{\partial x_i}{\partial \boldsymbol{X}_1}\right)^T & \frac{\partial x_i}{\partial \boldsymbol{X}_3}\left(\frac{\partial x_i}{\partial \boldsymbol{X}_1}\right)^T\\ \frac{\partial x_i}{\partial \boldsymbol{X}_1}\left(\frac{\partial x_i}{\partial \boldsymbol{X}_2}\right)^T & \frac{\partial x_i}{\partial \boldsymbol{X}_2}\left(\frac{\partial x_i}{\partial \boldsymbol{X}_2}\right)^T & \frac{\partial x_i}{\partial \boldsymbol{X}_3}\left(\frac{\partial x_i}{\partial \boldsymbol{X}_2}\right)^T\\ \frac{\partial x_i}{\partial \boldsymbol{X}_1}\left(\frac{\partial x_i}{\partial \boldsymbol{X}_3}\right)^T & \frac{\partial x_i}{\partial \boldsymbol{X}_2}\left(\frac{\partial x_i}{\partial \boldsymbol{X}_3}\right)^T & \frac{\partial x_i}{\partial \boldsymbol{X}_3}\left(\frac{\partial x_i}{\partial \boldsymbol{X}_3}\right)^T\end{pmatrix} \tag{III. 1.20}$$

A measure of the stretch can be written as the difference in the position vectors:

$$\begin{aligned} l^2-L^2 &= dx^T dx - dx^T\cdot \boldsymbol{B}^{-1}dx\\ l^2-L^2 &= dx^T(\boldsymbol{I}-\boldsymbol{B}^{-1})dx \end{aligned} \tag{III. 1.21}$$

In case of a rigid body motion, the magnitudes of the position vectors of the material and spatial descriptions must remain equal:

$$d\boldsymbol{X}^T\cdot d\boldsymbol{X} = dx^T\cdot dx \tag{III. 1.22}$$

Introducing again equation $(\text{III. } 1.12a)$, the above equation becomes:

$$\begin{aligned} d\boldsymbol{X}^T\cdot d\boldsymbol{X} &= \boldsymbol{F}^T d\boldsymbol{X}^T\cdot \boldsymbol{F}d\boldsymbol{X}\\ \Rightarrow \boldsymbol{F}^T\cdot\boldsymbol{F} &= \boldsymbol{F}\cdot\boldsymbol{F}^T = \boldsymbol{I} \end{aligned} \tag{III. 1.23}$$

So, in the case of a rigid body motion, the deformation gradient $\boldsymbol{F}$ is an orthogonal tensor. Introducing $(\text{III. } 1.23)$ in $(\text{III. } 1.21)$ we obtain:

$$l^2-L^2 = dx^T(\boldsymbol{I}-\boldsymbol{I})dx = 0 \tag{III. 1.24}$$

The above equation shows that the Cauchy-Green strain tensor can be used as a measure of deformation, while the deformation gradient cannot, because it changes values under an arbitrary rigid body movement.

A more appropriate description of the Cauchy-Green tensor derived from equation $(\text{III. } 1.21)$ shows that it is a measure of stretch. Even though the Cauchy-Green deformation tensor is independent on rigid body rotations, it has a drawback in the sense that if the stretch is 0, it has non-zero components:

$$\begin{aligned} l^2-L^2=0 &\Rightarrow dx^T(\boldsymbol{I}-\boldsymbol{B}^{-1})dx = 0\\ &\Rightarrow \boldsymbol{B}=\boldsymbol{I} \end{aligned} \tag{III. 1.25}$$

A method for measuring large strains is by summing up all the small increments (elongations) that take place when the linear element is stretched from L to l. Consider a small linear increment dl. By definition, the elongation will be expressed as:

$$\lambda = \frac{dl}{L} \tag{III. 1.26}$$

Consequently, the strain will be:

$$\varepsilon = \int_L^l \frac{dl}{L} = \ln\frac{l}{L} \tag{III. 1.27}$$

Recalling the definition of the length of the elements the above equation becomes:

$$\varepsilon^2 = \ln\frac{dx^T dx}{d\boldsymbol{X}^T d\boldsymbol{X}} \tag{III. 1.28}$$

Introducing equation (III. 1.18) in (III. 1.28):

$$\varepsilon = \frac{1}{2}\ln \boldsymbol{B}^{-1} \tag{III. 1.29}$$

Relation (III. 1.29) represents the *true* or *logarithmical strain.* In engineering applications, equation (III. 1.27) is used to express the uniaxial true or logarithmical stress. Due to its rather complex form, this type of strain is rarely used in computational applications.

In order to obtain a more appropriate strain measure, the *Eulerian* or *Almansi strain tensor* $\boldsymbol{E_A}$ is introduced:

$$l^2 - L^2 = dx^T(\boldsymbol{I} - \boldsymbol{B}^{-1})dx = 2dx^T \cdot \boldsymbol{E_A} \cdot dx \tag{III. 1.30}$$

where

$$\boldsymbol{E_A} = \frac{1}{2}(\boldsymbol{I} - \boldsymbol{B}^{-1}) \tag{III. 1.31}$$

If we are to express the Almansi tensor in terms of the stretch, equation (III. 1.30) becomes:

$$\begin{aligned} l^2 - L^2 &= 2dx^T \cdot \boldsymbol{E_A} \cdot dx \\ \boldsymbol{E_A} &= \frac{1}{2}\frac{dx^T \cdot dx - d\boldsymbol{X}^T \cdot d\boldsymbol{X}}{dx^T \cdot dx} \\ \boldsymbol{E_A} &= \frac{1}{2}\frac{l^2 - L^2}{l^2} \end{aligned} \tag{III. 1.32}$$

Equation (III. 1.32) is also used in engineering applications for small strains ($l \cong L$). In unixaial loadings, it relates the change in length to the current length of the specimen:

$$E_{\boldsymbol{A}}^{(l\cong L)} = \frac{l - L}{l} \tag{III. 1.33a}$$

If the material description is chosen, the stretch can be expressed as:

$$\begin{aligned} l^2 - L^2 &= \boldsymbol{F}^T d\boldsymbol{X}^T \cdot \boldsymbol{F} d\boldsymbol{X} - d\boldsymbol{X}^T \cdot d\boldsymbol{X} \\ l^2 - L^2 &= d\boldsymbol{X}^T(\boldsymbol{F}^T \cdot \boldsymbol{F} - \boldsymbol{I})d\boldsymbol{X} \end{aligned} \tag{III. 1.34}$$

Equation (III. 1.34) can be written in terms of the *Green-Lagrange strain tensor* $\boldsymbol{E_G}$ as:

$$l^2 - L^2 = 2d\boldsymbol{X}^T \boldsymbol{E_G} d\boldsymbol{X} \tag{III. 1.35}$$

where

$$\boldsymbol{E_G} = \frac{1}{2}(\boldsymbol{F}^T \cdot \boldsymbol{F} - \boldsymbol{I}) \tag{III. 1.36}$$

Recalling equations (III. 1.16), an explicit form of equation (III. 1.36) will be:

$$\boldsymbol{E_G} = \frac{1}{2}\begin{pmatrix} \left[\left(\frac{\partial x_i}{\partial \boldsymbol{X}_1}\right)^T \frac{\partial x_i}{\partial \boldsymbol{X}_1} - 1\right] & \left(\frac{\partial x_i}{\partial \boldsymbol{X}_1}\right)^T \frac{\partial x_i}{\partial \boldsymbol{X}_2} & \left(\frac{\partial x_i}{\partial \boldsymbol{X}_1}\right)^T \frac{\partial x_i}{\partial \boldsymbol{X}_3} \\ \left(\frac{\partial x_i}{\partial \boldsymbol{X}_2}\right)^T \frac{\partial x_i}{\partial \boldsymbol{X}_1} & \left[\left(\frac{\partial x_i}{\partial \boldsymbol{X}_2}\right)^T \frac{\partial x_i}{\partial \boldsymbol{X}_2} - 1\right] & \left(\frac{\partial x_i}{\partial \boldsymbol{X}_2}\right)^T \frac{\partial x_i}{\partial \boldsymbol{X}_3} \\ \left(\frac{\partial x_i}{\partial \boldsymbol{X}_3}\right)^T \frac{\partial x_i}{\partial \boldsymbol{X}_1} & \left(\frac{\partial x_i}{\partial \boldsymbol{X}_3}\right)^T \frac{\partial x_i}{\partial \boldsymbol{X}_2} & \left[\left(\frac{\partial x_i}{\partial \boldsymbol{X}_3}\right)^T \frac{\partial x_i}{\partial \boldsymbol{X}_3} - 1\right] \end{pmatrix} \tag{III. 1.37}$$

Equation (III. 1.37) shows that the Green-Lagrange strain tensor is also a symmetric tensor. Its $E_{\boldsymbol{G}}^{ij}$ components for $i = j$ represent the *normal strains* that measure the change in length of the position vectors, while its $E_{\boldsymbol{G}}^{ij}$ components for $i \neq j$ represent the *shear strains* that measure the change of the relative orientation of the position vectors.

If we are to express the Green-Lagrange strain tensor in terms of stretches, equation (III. 1.35) becomes:

$$\begin{aligned} l^2 - L^2 &= 2d\boldsymbol{X}^T \boldsymbol{\varepsilon} d\boldsymbol{X} \\ \boldsymbol{E_G} &= \frac{1}{2}\frac{l^2 - L^2}{d\boldsymbol{X}^T d\boldsymbol{X}} \\ \boldsymbol{E_G} &= \frac{1}{2}\frac{l^2 - L^2}{2L^2} \end{aligned} \tag{III. 1.38}$$

Again, for small strains, it can be demonstrated through Taylor series expansion that

$$E_G^{(l \cong L)} = \frac{l - L}{L} \tag{III. 1.39a}$$

$$\boldsymbol{E_G}^{(l \cong L)} = \sum_{\mathrm{i,j=1}}^{3} \left(\frac{l_{ij} - L_{ij}}{L_{ij}}\right) e_i \otimes e_j \tag{III. 1.39b}$$

which represents the *nominal* or *engineering strain* used in the majority of the engineering applications.

III.1.6. Polar decomposition

The deformation gradient tensor $\boldsymbol{F}$ can be decomposed into its stretch and rotation components: it can be expressed as a product of a rotation tensor $\boldsymbol{R}$ and a stretch tensor $\boldsymbol{U}$:

$$\boldsymbol{F} = \boldsymbol{R}\boldsymbol{U} \tag{III. 1.40}$$

In order to obtain these tensor, equation (III. 1.15) will be introduced in (III. 1.21):

$$\boldsymbol{C} = \boldsymbol{F}^T\boldsymbol{F} = \boldsymbol{U}^T\boldsymbol{R}^T\boldsymbol{R}\boldsymbol{U} \tag{III. 1.41}$$

As discussed in Chapter **II.2.2**, a rotation tensor is a orthogonal tensor, and thus $\boldsymbol{R}^T\boldsymbol{R} = \boldsymbol{I}$. If $\boldsymbol{U}$ is chosen as a symmetric tensor, equation (III. 1.41) becomes:

$$\boldsymbol{C} = \boldsymbol{U}^T \cdot \boldsymbol{I} \cdot \boldsymbol{U} = \boldsymbol{U} \cdot \boldsymbol{U} \tag{III. 1.42}$$

The principal directions of the right Cauchy-Green deformation tensor are given by the triad $\{\boldsymbol{N}_1, \boldsymbol{N}_2, \boldsymbol{N}_2\}$ and their corresponding eigenvalues λ_1^2, λ_2^2 and λ_3^2. According to (II. 2.46), $\boldsymbol{C}$ can be expressed as:

$$\boldsymbol{C} = \sum_{i=1}^{3} \lambda_i^2 N_i \otimes N_i \tag{III. 1.43}$$

Introducing (III. 1.42) in (III. 1.43) we obtain:

$$\boldsymbol{U} = \sum_{i=1}^{3} \lambda_i N_i \otimes N_i \tag{III. 1.44}$$

Once the stretch tensor is known, the rotation tensor can be obtained from equation (III. 1.40):

$$\boldsymbol{R} = \boldsymbol{F}\boldsymbol{U}^{-1} \tag{III. 1.45}$$

In terms of polar decomposition, the relation between the spatial and the material vectors is obtained by introducing equation (III. 1.7) in (III. 1.40):

$$dx = \boldsymbol{F}d\boldsymbol{X} = \boldsymbol{R}(\boldsymbol{U}d\boldsymbol{X}) \tag{III. 1.46}$$

In equation (III. 1.46) $d\boldsymbol{X}$ is first stretched by $\boldsymbol{U}$, resulting in the vector is $\boldsymbol{U}d\boldsymbol{X}$, which is then rotated to the new coordinates dx by the tensor $\boldsymbol{R}$.

III.1.7. Volume change

Consider an infinitesimal volume element defined by the dimension vectors $d\boldsymbol{X}_1 = dX_1\boldsymbol{E}_1$, $d\boldsymbol{X}_2 = dX_2\boldsymbol{E}_2$ and $d\boldsymbol{X}_3 = dX_3\boldsymbol{E}_3$, where $\boldsymbol{E}_1$, $\boldsymbol{E}_2$ and $\boldsymbol{E}_3$ are the orthogonal unit vectors (Figure 8). Thus the volume element is defines as:

$$dV = dX_1 dX_2 dX_3 \tag{III. 1.47}$$

According to (III. 1.6) and (III. 1.7)

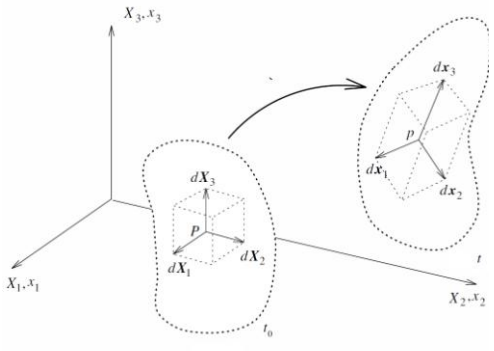

Figure III.3. Volume change
[reprint from **[11]**]

$$dx_1 = \boldsymbol{F} d\boldsymbol{X}_1 = \frac{\partial \phi}{\partial \boldsymbol{X}} dX_1 \quad (\text{III. } 1.48a)$$
$$dx_2 = \boldsymbol{F} d\boldsymbol{X}_2 = \frac{\partial \phi}{\partial \boldsymbol{X}} dX_2 \quad (\text{III. } 1.48b)$$
$$dx_3 = \boldsymbol{F} d\boldsymbol{X}_3 = \frac{\partial \phi}{\partial \boldsymbol{X}} dX_3 \quad (\text{III. } 1.48c)$$

The deformed volume dv is given by the triple product of these position vectors:

$$dv = dx_1 \cdot (dx_2 \times dx_3) = \frac{\partial \phi}{\partial X_1} \cdot \left(\frac{\partial \phi}{\partial X_2} \times \frac{\partial \phi}{\partial X_3} \right) dX_1 dX_2 dX_3 \quad (\text{III. } 1.49)$$

The relation $(\text{III. } 1.49)$ can also be expressed in terms of the Jacobian J as:

$$dv = JdV; \qquad J = det\boldsymbol{F} \quad (\text{III. } 1.50)$$

The mass element dm can be related to the volume element in terms of the initial and current densities:

$$dm = \rho_0 dV = \rho dV \quad (\text{III. } 1.51)$$

Thus the conservation of mass can expressed as:

$$\rho_0 = \rho J \quad (\text{III. } 1.52)$$

III.1.8. Distortional component of the deformation gradient

During deformation, incompressible materials suffer no change in volume $(J = 1)$. Thus it is necessary to separate the volumetric components from the distortional (isochoric) components $\widehat{\boldsymbol{F}}$ (that have no change in volume) of the deformation.

$$\det\widehat{\boldsymbol{F}} = 1 \quad (\text{III. } 1.53)$$

The distortional component can be expressed in terms of the Jacobian and the deformation gradient as:

$$\begin{aligned} &\det\widehat{\boldsymbol{F}} = 1 \\ &\det\widehat{\boldsymbol{F}} = J^{-1} J \\ &\det\widehat{\boldsymbol{F}} = \left(J^{-\frac{1}{3}}\right)^3 \det\boldsymbol{F} \\ &\det\widehat{\boldsymbol{F}} = \det\left(J^{-\frac{1}{3}}\boldsymbol{F}\right) \\ &\widehat{\boldsymbol{F}} = J^{-\frac{1}{3}}\boldsymbol{F} \end{aligned} \quad (\text{III. } 1.54)$$

A similar decomposition can be obtained for the right Cauchy-Green deformation tensor:

$$\widehat{\boldsymbol{C}} = \widehat{\boldsymbol{F}}^T \widehat{\boldsymbol{F}} \quad (\text{III. } 1.55)$$

Introducing (III. 1.54) in (IIII. 1.55) we obtain:

$$\widehat{\boldsymbol{C}} = (\det\boldsymbol{C})^{-\frac{1}{3}}\boldsymbol{C} \tag{III. 1.56}$$

III.1.9. Area change

Consider an area element of initial configuration $d\boldsymbol{A} = dA \cdot \boldsymbol{N}$ which becomes $d\boldsymbol{a} = da \cdot \boldsymbol{n}$ after deformation (Figure 9).

In order to express the relationship between the two states, consider an arbitrary vector $d\mathcal{L}$ which becomes $d\ell$ after deformation. The corresponding initial and current element volumes can be expressed as:

$$dV = d\mathcal{L} \cdot d\boldsymbol{A} \tag{III. 1.57a}$$
$$dv = d\ell \cdot d\boldsymbol{a} \tag{III. 1.57b}$$

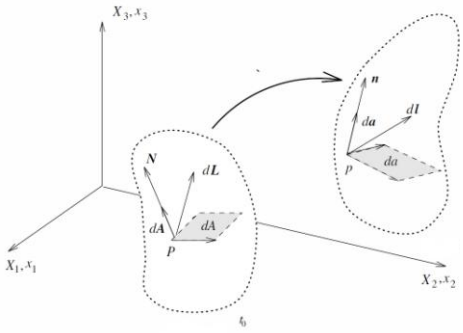

Figure III.4. Area change
[reprint from **[11]**]

Introducing (III. 1.50) and (III. 1.7) in (III. 1.57) we obtain:

$$Jd\mathcal{L} \cdot d\boldsymbol{A} = (\boldsymbol{F}d\mathcal{L}) \cdot d\boldsymbol{a} \tag{III. 1.58}$$

Expression (III. 1.58) is valid for any arbitrary vector $d\mathcal{L}$, which enables the elements of area to be related as:

$$d\boldsymbol{a} = J\boldsymbol{F}^{-T}d\boldsymbol{A} \tag{III. 1.59}$$

III.1.10. Velocity and acceleration

III.1.10.1. Material time derivative

Consider a given scalar or tensor quantity ψ expressed in terms of material coordinates $\psi(\boldsymbol{X}, t)$, the time derivative of ψ can be expressed as:

$$\dot{\psi} = \psi' = \frac{d\psi}{dt} = \frac{\partial\psi(\boldsymbol{X}, t)}{\partial t} \tag{III. 1.60}$$

In the above equation, $\dot{\psi}$ is the Newton notation, ψ' is the Lagrange notation and $d\psi/dt$ is the Leibnitz notation.

Relation (III. 1.60) represents the *material time* derivative and it measures the change in ψ associated with a specific particle initially located at $\boldsymbol{X}$. Expressing the derivative of ψ after spatial description $(\psi(x,t) = \psi(\phi(\boldsymbol{X}, t), t))$ represents a challenging aspect, because the given particle changes position as time progresses. So the material-time derivative can be obtained by considering the motion of the given particle:

$$\frac{d\psi(x,t)}{dt} = \lim_{\Delta t \to 0} \frac{\psi(\phi(\boldsymbol{X}, t+\Delta t), t+\Delta t) - \psi(\phi(\boldsymbol{X}, t), t)}{\Delta t} \tag{III. 1.61}$$

Using the chain rule, equation (III. 1.61) becomes:

$$\chi = \frac{d\psi(x,t)}{dt} = \frac{\partial\psi(x,t)}{\partial t} + \frac{\partial\psi(x,t)}{\partial x}\frac{\partial\phi(\boldsymbol{X},t)}{\partial t} = \frac{\partial\psi(x,t)}{\partial t} + (\boldsymbol{\nabla}\psi)\chi \qquad \text{(III. 1.62)}$$

where the term $(\boldsymbol{\nabla}\psi)\chi$ is called the connective or transport derivative.

III.1.10.2. Velocity

Consider the equation of motion of a given particle:

$$x = \phi(\boldsymbol{X},t) \qquad \text{(III. 1.63)}$$

The absolute velocity of the given body is defined by deriving the equation of motion with respect to time:

$$v(\boldsymbol{X},t) = \frac{d\phi(\boldsymbol{X},t)}{dt} \qquad \text{(III. 1.64)}$$

In these equations, the vector $\boldsymbol{X}$ is considered to be time independent as it describes the position of the particle in the reference configuration.

In fluid mechanics, the curl of the velocity (called *vorticity*) is given by the vector product $\boldsymbol{\nabla} \times v$, where $\boldsymbol{\nabla} = \left[\frac{\partial}{\partial x_1} \quad \frac{\partial}{\partial x_2} \quad \frac{\partial}{\partial x_3}\right]^T$:

$$\boldsymbol{\nabla} \times v = \left[\left(\frac{\partial v_3}{\partial x_2} - \frac{\partial v_2}{\partial x_3}\right) \quad \left(\frac{\partial v_3}{\partial x_1} - \frac{\partial v_1}{\partial x_3}\right) \quad \left(\frac{\partial v_2}{\partial x_1} - \frac{\partial v_1}{\partial x_2}\right)\right] \qquad \text{(III. 1.65)}$$

In case of irrotational flow, all the vortocity's elements are zero

The spatial description of the velocity can be obtained by recalling equation (III. 1.62):

$$\begin{aligned} v(x,t) &= \frac{d\varphi(x,t)}{dt} \\ &= \frac{\partial\varphi(x,t)}{\partial t} + \frac{\partial\varphi(x,t)}{\partial x}\frac{\partial\phi(\boldsymbol{X},t)}{\partial t} \\ v(x,t) &= \frac{\partial\varphi(x,t)}{\partial t} + (\boldsymbol{\nabla}\psi)v \end{aligned} \qquad \text{(III. 1.65)}$$

III.1.10.3. Acceleration

The absolute acceleration of a particle is defined as the rate of change of the velocity with respect to time:

$$a(\boldsymbol{X},t) = \frac{dv(\boldsymbol{X},t)}{\partial t} = \frac{d^2\phi(\boldsymbol{X},t)}{\partial t^2} \qquad \text{(III. 1.66)}$$

As with the velocity, the position vector $\boldsymbol{X}$ in the above equation is considered to be time independent.

In order to express the acceleration in the Eulerian reference, we recall equation (III. 1.62):

$$a(x,t) = \frac{dv(x,t)}{dt} = \frac{dv(\phi(\boldsymbol{X},t),t)}{dt}$$
$$a(x,t) = \frac{\partial v(x,t)}{\partial t} + (\boldsymbol{\nabla}\psi)a \qquad \text{(III. 1.67)}$$

III.1.11. Velocity gradient

In section **III.1.10** velocity was expressed as a function of the spatial coordinates and time ($v(x,t)$). The given expression's derivative with respect to the spatial coordinates gives the velocity gradient tensor $\boldsymbol{l}$:

$$\boldsymbol{l} = \frac{\partial v(x,t)}{\partial x} = \boldsymbol{\nabla} v \qquad \text{(III. 1.68)}$$

This tensor gives the relative velocity of particle currently at point p with respect to a particle currently at point q as $dv = \boldsymbol{l}dx$. A more useful formulation for the velocity gradient can be obtained by introducing the time derivative of the deformation gradient $\boldsymbol{F}$:

$$\frac{d\boldsymbol{F}}{dt} = \frac{d}{dt}\left(\frac{\partial \phi}{\partial \boldsymbol{X}}\right)$$
$$= \frac{d}{\partial \boldsymbol{X}}\left(\frac{\partial \phi}{dt}\right)$$
$$\frac{d\boldsymbol{F}}{dt} = \frac{dv}{\partial \boldsymbol{X}} \qquad \text{(III. 1.69)}$$

Recalling relation (III. 1.12b) the above equation becomes:

$$\frac{d\boldsymbol{F}}{dt} = \frac{dv}{dx \cdot \boldsymbol{F}^{-1}}$$
$$\frac{d\boldsymbol{F}}{dt} = \frac{dv}{dx}\boldsymbol{F}$$
$$\frac{d\boldsymbol{F}}{dt} = \boldsymbol{l}\boldsymbol{F} \qquad \text{(III. 1.70)}$$

From this relation, a new expression for the velocity gradient can be obtained:

$$\boldsymbol{l} = \frac{d\boldsymbol{F}}{dt}\boldsymbol{F}^{-1} \qquad \text{(III. 1.71)}$$

III.1.12. Rate of deformation

Consider the initial elemental vectors $d\boldsymbol{X}_1$ and $d\boldsymbol{X}_2$ and their corresponding post-deformation counterparts dx_1 and dx_2 given by the relations (III. 1.7a) and (III. 1.7b):

$$dx_1 = \boldsymbol{F} d\boldsymbol{X}_1 \tag{III. 1.7a}$$
$$dx_2 = \boldsymbol{F} d\boldsymbol{X}_2 \tag{III. 1.7b}$$

Analogous to the strain definition, the rate of volume change is defined as the rate of change of the scalar product of the two vectors.

According to (III. 1.13), the scalar product can be expressed in terms of time independent material vectors $d\boldsymbol{X}_1$ and $d\boldsymbol{X}_2$ and time dependent right Cauchy-Green tensor $\boldsymbol{C}$:

$$dx_1 \cdot dx_2 = d\boldsymbol{X}_1 \cdot \boldsymbol{C} d\boldsymbol{X}_2 \tag{III. 1.13}$$
$$\frac{d}{dt}(dx_1 \cdot dx_2) = d\boldsymbol{X}_1 \cdot \frac{d\boldsymbol{C}}{dt} d\boldsymbol{X}_2 \tag{III. 1.72}$$

According to (III. 1.17), the derivative of the Green-Lagrange strain tensor $\boldsymbol{E_G}$ can be written as:

$$\boldsymbol{E} = \frac{1}{2}(\boldsymbol{C} - \boldsymbol{I})$$
$$\frac{d\boldsymbol{E_G}}{dt} = \frac{1}{2}\frac{d\boldsymbol{C}}{dt} = \frac{1}{2}\left(\frac{d\boldsymbol{F}^T}{dt}\boldsymbol{F} + \boldsymbol{F}^T\frac{d\boldsymbol{F}}{dt}\right) \tag{III. 1.73}$$

$d\boldsymbol{E_G}/dt$ is called the material strain rate tensor, and gives the rate of deformation in report to the initial elemental vectors.

Introducing (III. 1.73) in (III. 1.72) we obtain:

$$\frac{d}{dt}(dx_1 \cdot dx_2) = 2d\boldsymbol{X}_1 \cdot \frac{d\boldsymbol{E_G}}{dt} d\boldsymbol{X}_2 \tag{III. 1.74}$$

The rate of deformation can be expressed in terms of the current vectors dx_1 and dx_2 by introducing equation (III. 1.12b) in (III. 1.74):

$$\frac{1}{2}\frac{d}{dt}(dx_1 \cdot dx_2) = dx_1 \cdot \left(\boldsymbol{F}^{-T} \cdot \frac{d d\boldsymbol{E_G}}{dt} \cdot \boldsymbol{F}^{-1}\right) dx_2 \tag{III. 1.75}$$

The tensor on the right-hand side of equation (I. 163) represents the rate of deformation tensor $\boldsymbol{d}$ and it is the push forward spatial counterpart of the material strain rate tensor:

$$\boldsymbol{d} = \phi_*\left[\frac{d\boldsymbol{E_G}}{dt}\right] = \boldsymbol{F}^{-T} \cdot \frac{d\boldsymbol{E_G}}{dt} \cdot \boldsymbol{F}^{-1} \tag{III. 1.76a}$$
$$\frac{d\boldsymbol{E}}{dt} = \phi_*^{-1}[\boldsymbol{d}] = \boldsymbol{F}^T \cdot \boldsymbol{d}\boldsymbol{F} \tag{III. 1.76b}$$

III.1.13. Spin tensor

The velocity gradient $\boldsymbol{l}$ can also be expressed as the sum of the symmetric rate of deformation tensor $\boldsymbol{d}$ and a antisymmetric component $\boldsymbol{w}$, called the *spin tensor*:

$$\boldsymbol{l} = \boldsymbol{d} + \boldsymbol{w}; \qquad \boldsymbol{d}^T = \boldsymbol{d}; \qquad \boldsymbol{w}^T = -\boldsymbol{w} \tag{III.1.77}$$

The spin tensor $\boldsymbol{w}$ can be determined with the relation:

$$\boldsymbol{w} = \frac{1}{2}(\boldsymbol{l} + \boldsymbol{l}^T) \tag{III.1.78}$$

Introducing equation (III.1.71) in (III.1.78) we obtain:

$$\boldsymbol{w} = \frac{1}{2}\left(\frac{d\boldsymbol{F}}{dt}\boldsymbol{F}^{-1} + \boldsymbol{F}^{-T}\left(\frac{d\boldsymbol{F}}{dt}\right)^T\right) \tag{III.1.79}$$

Recalling equation for the polar decomposition (III.1.40) and its time derivative

$$\frac{d\boldsymbol{F}}{dt} = \frac{d\boldsymbol{R}}{dt}\boldsymbol{U} + \boldsymbol{R}\frac{d\boldsymbol{U}}{dt} \tag{III.1.80}$$

it can be demonstrated after some algebra that:

$$\boldsymbol{w} = \frac{1}{2}\left(\frac{d\boldsymbol{R}}{dt}\boldsymbol{R}^T - \boldsymbol{R}\left(\frac{d\boldsymbol{R}}{dt}\right)^T\right) + \frac{1}{2}\boldsymbol{R}\left(\frac{d\boldsymbol{U}}{dt}\boldsymbol{U}^{-1} - \boldsymbol{U}^{-1}\frac{d\boldsymbol{U}}{dt}\right)\boldsymbol{R}^T \tag{III.1.81}$$

It can be shown that

$$\frac{d}{dt}(\boldsymbol{R}\boldsymbol{R}^T) = \boldsymbol{I} = \frac{d\boldsymbol{R}}{dt}\boldsymbol{R}^T + \boldsymbol{R}\left(\frac{d\boldsymbol{R}}{dt}\right)^T \tag{III.1.82}$$

which implies that

$$\boldsymbol{R}\left(\frac{d\boldsymbol{R}}{dt}\right)^T = -\frac{d\boldsymbol{R}}{dt}\boldsymbol{R}^T \tag{III.1.83}$$

Consequently, equation (III.1.81) can be rewritten as:

$$\boldsymbol{w} = \boldsymbol{R}\left(\frac{d\boldsymbol{R}}{dt}\right)^T + \frac{1}{2}\boldsymbol{R}\left(\frac{d\boldsymbol{U}}{dt}\boldsymbol{U}^{-1} - \boldsymbol{U}^{-1}\frac{d\boldsymbol{U}}{dt}\right)\boldsymbol{R}^T \tag{III.1.84}$$

In some particular cases such as rigid body rotation the second term equals 0, thus

$$\boldsymbol{w} = \boldsymbol{R}\left(\frac{d\boldsymbol{R}}{dt}\right)^T \tag{III.1.85}$$

The physical interpretation of the spin tensor is through its associated angular velocity terms:

$$\begin{cases} \omega_1 = w_{32} = -w_{23} \\ \omega_2 = w_{13} = -w_{31} \\ \omega_3 = w_{21} = -w_{12} \end{cases} \tag{III.1.86}$$

III.1.14. Rate of volume change

The volume change between the initial and the current state was expressed in section **III.1.7** in terms of the Jacobian (III. 1.31):

$$dv = JdV; \tag{III. 1.31}$$

Deriving this expression in respect to time, the material rate of volume change is obtained:

$$\frac{d}{dt}dv = \frac{dJ}{dt}dV \tag{III. 1.87}$$

The material rate of the Jacobian can be evaluated with the help of the directional derivative:

$$\frac{dJ}{dt} = DJ[\boldsymbol{v}] \tag{III. 1.88}$$

The directional derivative of J with respect to $\boldsymbol{v}$ can be expressed as:

$$DJ[\boldsymbol{v}] = D\det(\boldsymbol{F})\big[D\boldsymbol{F}[\boldsymbol{v}]\big] \tag{III. 1.89}$$

After some algebra, considering the directional derivative of the determinant form and the linearization of the deformation gradient and the rate of deformation tensor $\boldsymbol{d}$, the directional derivative of the Jacobian J will be:

$$DJ[\boldsymbol{v}] = J\mathrm{tr} \div \boldsymbol{v} \tag{III. 1.90a}$$

$$\frac{dJ}{dt} = J\mathrm{tr}\boldsymbol{d} \tag{III. 1.90b}$$

An alternate formulation for the time derivative of the Jacobian dJ/dt can be expressed in terms of the material rate tensors $d\boldsymbol{C}/dt$ and $d\boldsymbol{E_G}/dt$ from equations (III. 1.73) and (III. 1.76):

$$\frac{dJ}{dt} = J\mathrm{tr}\boldsymbol{d} = \frac{1}{2}J\boldsymbol{C}^{-1} : \frac{d\boldsymbol{C}}{dt} \tag{III. 1.91}$$

III.1.15. Objectivity

Objectivity is an important solid mechanics concept that deals with the variation of mechanical quantities with the frame of reference. Thus, under rigid body motion, some quantities characterizing the body will remain unchanged such as the distance between two points or the stress state. These quantities are said to be objective.

Let $d\boldsymbol{X}$ be a element vector in the initial configuration, $d\boldsymbol{x}$ the element vector after the body deforms and $d\tilde{\boldsymbol{x}}$ the element vector after the deformed body rotates. The relationship between the three can be written as:

$$d\tilde{\boldsymbol{x}} = \boldsymbol{Q}d\boldsymbol{x} = \boldsymbol{Q}\boldsymbol{F}d\boldsymbol{X} \tag{III. 1.92}$$

where $\boldsymbol{Q}$ is an orthogonal tensor describing the superimposed rigid body rotation and $\boldsymbol{F}$ is the deformation gradient.

Although the element vectors $d\tilde{\boldsymbol{x}}$ and $d\boldsymbol{x}$ are different, their magnitudes are equal, thus one can state that $d\boldsymbol{x}$ is objective to rigid body motion. The definition of objectivity can be extended to any quantity ψ that satisfies the relation:

$$\tilde{\psi} = \boldsymbol{Q}\psi \tag{III. 1.93}$$

An example of an objective second order tensor is the deformation gradient $\boldsymbol{F}$:

$$\tilde{\boldsymbol{F}} = \boldsymbol{Q}\boldsymbol{F} \tag{III. 1.94}$$

Considering the equations (III. 1.15) and (III. 1.36) it can be stated that the left Cauchy-Green strain tensor and the Green-Lagrange strain tensor are also objective.

Introducing equation (III. 1.92) in equations (III. 1.19b) and (III. I. 31) for the right Cauchy-Green strain tensor and the Almansi strain tensor we will obtain:

$$\tilde{\boldsymbol{B}} = \boldsymbol{Q}\boldsymbol{B}\boldsymbol{Q}^T \tag{III. 1.95a}$$
$$\tilde{\boldsymbol{E}}_{\boldsymbol{A}} = \boldsymbol{Q}\boldsymbol{E}_{\boldsymbol{A}}\boldsymbol{Q}^T \tag{III. 1.95b}$$

Note that although $\tilde{\boldsymbol{E}}_{\boldsymbol{A}}$ is not equal to $\boldsymbol{E}_{\boldsymbol{A}}$, their magnitudes are equal:

$$\frac{1}{2}(ds^2 - dS^2) = d\boldsymbol{x} \cdot \boldsymbol{E}_{\boldsymbol{A}}d\boldsymbol{x} = d\tilde{\boldsymbol{x}} \cdot \tilde{\boldsymbol{E}}_{\boldsymbol{A}}d\tilde{\boldsymbol{x}} \tag{III. 1.96}$$

Consequently, any tensor that transform in the above manner is said to be objective. All measures of material behaviour such as second-order stress and strain need to be objective.

III.2. Stress and equilibrium

III.2.1. Cauchy stress tensor

Consider a deformable body at its current position (Figure 1.10). In order to define the stress tensor, it is necessary to study the action of the forces applied by one part of the rigid body R_1 on the remaining part of the body R_2 with which it is in contact. Consider the element of area Δa to normal $\boldsymbol{n}$ in the neighbourhood of the spatial point p (Figure 1.10). Consider $\Delta\boldsymbol{p}$ the resultant force on this area; the traction vector $\boldsymbol{t}$ corresponding to the normal $\boldsymbol{n}$ at p is defined as:

$$\boldsymbol{t}(\boldsymbol{n}) = \lim_{\Delta a \to 0} \frac{\Delta \boldsymbol{p}}{\Delta a} \tag{III. 2.1}$$

The relationship between $\boldsymbol{t}$ and $\boldsymbol{n}$ must satisfy Newton's third law:

$$-\boldsymbol{t}(\boldsymbol{n}) = \boldsymbol{t}(-\boldsymbol{n}) \qquad (\text{III. } 2.2)$$

In order to define the stress tensor, consider three traction vectors associated with the three Cartesian directions e_1, $e_2$and e_3, being expressed in component form (Figure I.11):

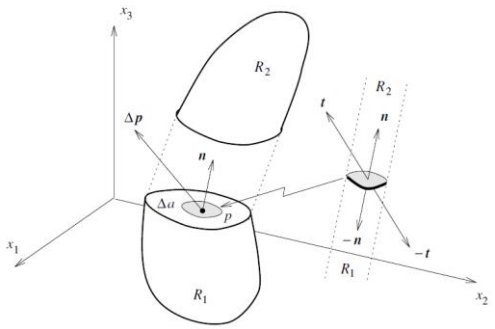

Figure III.5. Traction vector
[reprint from **[11]**]

$$\boldsymbol{t}(e_1) = \sigma_{11}e_1 + \sigma_{21}e_2 + \sigma_{31}e_3 \qquad (\text{III. } 2.3a)$$
$$\boldsymbol{t}(e_2) = \sigma_{12}e_1 + \sigma_{22}e_2 + \sigma_{32}e_3 \qquad (\text{III. } 2.3b)$$
$$\boldsymbol{t}(e_3) = \sigma_{13}e_1 + \sigma_{23}e_2 + \sigma_{33}e_3 \qquad (\text{III. } 2.3c)$$

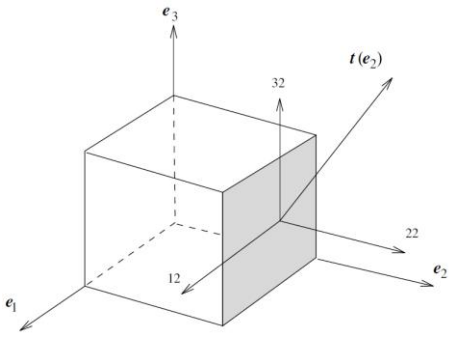

Figure III.6. Stress components
[reprint from [11]]

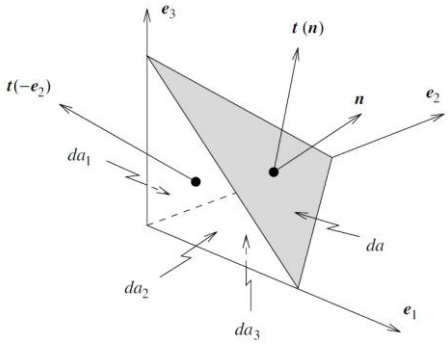

Figure III.7. Elemental tetrahedron
[reprint from **[11]**]

The relationship between the traction vector $\boldsymbol{t}$ corresponding to a general direction $\boldsymbol{n}$ and the components σ_{ij} can be obtained by studying the translational equilibrium of the elemental tetrahedron shown in Figure 12. Consider $\boldsymbol{f}$ the force per unit volume acting on the body at the point p, the equilibrium of the tetrahedron is given by the relation:

$$\boldsymbol{t}(\boldsymbol{n})d\boldsymbol{a} + \sum_{i=1}^{3} \boldsymbol{t}(-e_i)da_i + \boldsymbol{f}dv = 0 \qquad (\text{III. } 2.4)$$

where $da_i = (\boldsymbol{n} \cdot e_i)da$ is the projection of the area da onto the plane orthogonal to the Cartesian direction i (Figure I.12).

Dividing equation $(\text{III. } 2.4)$ by da, recalling Newton's third law, noting that $dv/da \to 0$ and introducing equation $(\text{III. } 2.3)$ we obtain:

$$\boldsymbol{t}(\boldsymbol{n}) = -\sum_{j=1}^{3} \boldsymbol{t}(-e_i)\frac{da_i}{d\boldsymbol{a}} - \boldsymbol{f}\frac{dv}{da}$$

$$= \sum_{j=1}^{3} \boldsymbol{t}(e_i)\left(\boldsymbol{n} \cdot e_j\right)$$

$$\boldsymbol{t}(\boldsymbol{n}) = \sum_{i,j=1}^{3} \sigma_{ij}\left(e_j \cdot \boldsymbol{n}\right)(e_i) \tag{III. 2.5}$$

The tern $\left(e_j \cdot \boldsymbol{n}\right)(e_i)$ can be rewritten in terms of the tensor product as $\left(e_i \otimes e_j\right)\boldsymbol{n}$ so that equation (III. 2.5) becomes:

$$\boldsymbol{t}(\boldsymbol{n}) = \left[\sum_{i,j=1}^{3} \sigma_{ij}\left(e_i \otimes e_j\right)\right]\boldsymbol{n} \tag{III. 2.6}$$

where

$$\boldsymbol{\sigma} = \sum_{i,j=1}^{3} \sigma_{ij}\left(e_i \otimes e_j\right) \tag{III. 2.7}$$

is called the *Cauchy stress tensor*, which relates the normal vector $\boldsymbol{n}$ to the traction vector $\boldsymbol{t}$:

$$\boldsymbol{t}(\boldsymbol{n}) = \boldsymbol{\sigma}\boldsymbol{n} \tag{III. 2.8}$$

Because the Cauchy stress is an important quantity in describing material equilibrium, it is important to determine if $\boldsymbol{\sigma}$ is objective to rigid body motion. For a superimposed rigid body motion $\boldsymbol{Q}$, the traction vector $\boldsymbol{t}(\boldsymbol{n})$ and the normal $\boldsymbol{n}$ will become:

$$\tilde{\boldsymbol{t}}(\boldsymbol{n}) = \boldsymbol{Q}\boldsymbol{t}(\boldsymbol{n}) \tag{III. 2.9a}$$

$$\tilde{\boldsymbol{n}} = \boldsymbol{Q}\boldsymbol{n} \tag{III. 2.9b}$$

Introducing equations (III. 2.9) in equation (III. 2.8) yields:

$$\tilde{\boldsymbol{\sigma}} = \boldsymbol{Q}\boldsymbol{\sigma}\boldsymbol{Q}^T \tag{III. 2.10}$$

III.2.2. Transitional equilibrium

Consider the configuration of a general deformable body of volume v with boundary area dv. Consider also that the body is under the action of body forces per unit volume $\boldsymbol{f}$ and traction force per unit area $\boldsymbol{t}$ acting on the boundary. For simplicity, inertia forces will be ignored and the transitional equilibrium will result in the sum of all forces acting on the body being equal to 0:

$$\int_{v} \boldsymbol{f} dv + \int_{\partial v} \boldsymbol{t} da = 0 \tag{III. 2.11}$$

Introducing (III. 2.7) in (III. 2.8) we obtain:

$$\int_v \boldsymbol{f} dv + \int_{\partial v} \boldsymbol{\sigma n} da = 0 \tag{III. 2.12}$$

Introducing the Gauss integration theorem (II. 3.31) in (III. 2.12), the second term is transformed into a volume integral:

$$\int_v \boldsymbol{f} dv + \int_v \div \boldsymbol{\sigma} dv = 0 \tag{II. 3.31}$$

$$\int_v (\div \boldsymbol{\sigma} + \boldsymbol{f})\, dv = 0 \tag{III. 2.13}$$

Equation (III. 2.13) can be applied for any region of the enclosed body, so the local spatial equilibrium equation for a deformed body can be expressed as:

$$\div \boldsymbol{\sigma} + \boldsymbol{f} = 0 \tag{III. 2.14}$$

In the situation in which the equilibrium relation is not satisfied, the above equation determines the local out-of-balance or residual force $\boldsymbol{r}$:

$$\div \boldsymbol{\sigma} + \boldsymbol{f} = \boldsymbol{r} \tag{III. 2.15}$$

III.2.3. Rotational equilibrium

In order to define the symmetry of the Cauchy stress tensor, the study of the rotational equilibrium of a deformable body must be studied, under the action of traction and body forces. That is, the moment of those forces in relation to any of the body's points must be zero:

$$\int_v x \times \boldsymbol{f} dv + \int_{\partial v} x \times \boldsymbol{t} da = 0 \tag{III. 2.16}$$

Introducing (III. 2.8) in (III. 2.16) we obtain:

$$\int_v x \times \boldsymbol{f} dv + \int_{\partial v} x \times \boldsymbol{\sigma n} da = 0 \tag{III. 2.17}$$

Switching to indicial notation:

$$\int_{\partial v} x \times \boldsymbol{\sigma n} da = \int_{\partial v} \left(\sum_{i,j,k,l=1}^{3} \boldsymbol{\varepsilon}_{ijk} x_j \boldsymbol{\sigma}_{kl} \boldsymbol{n}_l \right) da \tag{III. 2.18}$$

where $\boldsymbol{\varepsilon}_{ijk}$ is the third order alternating tensor (II. 2.46), which equals 0 if one of the indices is repeated, 1 if the permutation $\{i, j, k\}$ is even and -1 if it is odd:

$$\boldsymbol{\varepsilon}_{ijk} = e_i \cdot (e_j \times e_k) \boldsymbol{W}_v \tag{II. 2.46}$$

and recalling equation (II. 3.29):

$$\int_V \nabla f dV = \int_{\partial V} f \boldsymbol{n} dA \tag{II.3.29}$$

$$\Rightarrow \int_{\partial v} \left(\sum_{i,j,k,l=1}^{3} \boldsymbol{\varepsilon}_{ijk} x_j \boldsymbol{\sigma}_{kl} \boldsymbol{n}_l \right) da = \int_v \left[\sum_{i,j,k,l=1}^{3} \frac{\partial}{\partial x_l} \left(\boldsymbol{\varepsilon}_{ijk} x_j \boldsymbol{\sigma}_{kl} \right) \right] dv \tag{III.2.19}$$

equation (III.2.17) becomes:

$$\int_v x \times \boldsymbol{f} dv + \int_v x \times (\div \boldsymbol{\sigma})\, dv + \int_v \boldsymbol{\varepsilon} : \boldsymbol{\sigma}^T = 0 \tag{III.2.20}$$

The vector determined by the double contraction $\boldsymbol{\varepsilon} : \boldsymbol{\sigma}^T$ is:

$$\boldsymbol{\varepsilon} : \boldsymbol{\sigma}^T = \begin{bmatrix} \sigma_{32} - \sigma_{23} \\ \sigma_{13} - \sigma_{31} \\ \sigma_{21} - \sigma_{12} \end{bmatrix} \tag{III.2.21}$$

Noting that $\div \boldsymbol{\sigma} = -\boldsymbol{f}$ (III.2.14) and that the equation (III.2.20) is valid in any point of the enclosed volume of the body, relation (III.2.21) becomes:

$$\boldsymbol{\varepsilon} : \boldsymbol{\sigma}^T = 0 \Rightarrow \begin{bmatrix} \sigma_{32} - \sigma_{23} \\ \sigma_{13} - \sigma_{31} \\ \sigma_{21} - \sigma_{12} \end{bmatrix} = 0 \Rightarrow \begin{cases} \sigma_{32} = \sigma_{23} \\ \sigma_{13} = \sigma_{31} \\ \sigma_{21} = \sigma_{12} \end{cases} \tag{III.2.22}$$

Equation (II.2.22) denotes the symmetric character of the Cauchy stress tensor $\boldsymbol{\sigma}$.

III.2.4. Principle of virtual work

Consider $\delta \boldsymbol{v}$ an arbitrary virtual velocity from the current position of a deformable body. The virtual work δw per unit volume and time done by the residual force $\boldsymbol{r}$ during the virtual motion is:

$$\delta w = \boldsymbol{r} \cdot \delta \boldsymbol{v} \tag{III.2.23}$$

Equilibrium conditions imply that

$$\delta w = 0 \tag{III.2.24}$$

Recalling equation (II.2.15) and integrating over the volume of the body will give a weak statement of the equilibrium of the body:

$$\delta W = \int_v (\div \boldsymbol{\sigma} + \boldsymbol{f}) \cdot \delta \boldsymbol{v} dv \tag{III.2.25}$$

Recalling property (II.3.28e)

$$\div (\boldsymbol{S}^T v) = \boldsymbol{S} : \nabla v + v \cdot \div \boldsymbol{S} \tag{II.3.28e}$$

the divergence of the vector $\boldsymbol{\sigma} \delta \boldsymbol{v}$ will be:

$$\div(\boldsymbol{\sigma}\delta\boldsymbol{v}) = \boldsymbol{\sigma}:\nabla\delta\boldsymbol{v} + (\div\boldsymbol{\sigma})\cdot\delta\boldsymbol{v} \tag{III. 2.26}$$

Introducing the Gauss integration theorem (II. 3.31) and (III. 2.26) in (III. 2.25) we obtain:

$$\int_{\partial v}\boldsymbol{n}\cdot\boldsymbol{\sigma}\delta\boldsymbol{v}da - \int_{v}\boldsymbol{\sigma}:\nabla\delta\boldsymbol{v}dv + \int_{v}\boldsymbol{f}\cdot\delta\boldsymbol{v}dv = 0 \tag{III. 2.27}$$

Analogous to Section **III.1.13**, the gradient of the virtual velocity is, by definition $\delta\boldsymbol{l}$:

$$\nabla\delta\boldsymbol{v} = \delta\boldsymbol{l} \tag{III. 2.28}$$

Introducing equation (III. 2.8) in (III. 2.24) and remembering the symmetry of the stress tensor (III. 2.22) we obtain:

$$\int_{v}\boldsymbol{\sigma}:\delta\boldsymbol{l}dv = \int_{v}\boldsymbol{f}\cdot\delta\boldsymbol{v}dv + \int_{\partial v}\boldsymbol{t}\cdot\delta\boldsymbol{v}da \tag{III. 2.29}$$

In order to express the virtual work in report with the rate of deformation, we recall the relations for the velocity gradient (III. 1.71), for the material strain rate tensor (III. 1.72) and for the rate of deformation tensor (III. 1.76a):

$$\boldsymbol{l} = \frac{d\boldsymbol{F}}{dt}\boldsymbol{F}^{-1} \quad \text{(III. 1.53)}; \qquad \frac{d\boldsymbol{E}}{dt} = \frac{1}{2}\left(\frac{d\boldsymbol{F}^{T}}{dt}\boldsymbol{F} + \boldsymbol{F}^{T}\frac{d\boldsymbol{F}}{dt}\right) \quad \text{(III. 1.72)}; \qquad \boldsymbol{d} = \boldsymbol{F}^{-T}\cdot\frac{d\boldsymbol{E}}{dt}\cdot\boldsymbol{F}^{-1} \quad \text{(II. 1.76}a\text{)}$$

$$\boldsymbol{d} = \boldsymbol{F}^{-T}\cdot\frac{d\boldsymbol{E}}{dt}\cdot\boldsymbol{F}^{-1} = \frac{1}{2}(\boldsymbol{l}^{T} + \boldsymbol{l}) \tag{III. 2.31}$$

Equation (III. 2.31) states that the rate of deformation tensor $\boldsymbol{d}$ is the symmetric part of the velocity gradient $\boldsymbol{l}$.

Expressing the virtual velocity gradient in terms of the symmetric virtual rate of deformation and the antisymmetric virtual spin tensor and taking into account the symmetry of the stress tensor, the spatial virtual work equation is expresses as:

$$\delta W = \int_{v}\boldsymbol{\sigma}:\delta\boldsymbol{d}dv - \int_{v}\boldsymbol{f}\cdot\delta\boldsymbol{v}dv - \int_{\partial v}\boldsymbol{t}\cdot\delta\boldsymbol{v}da \tag{III. 2.32}$$

III.2.5. The Kirchhoff stress tensor

In equation (III. 2.29) the internal virtual work done by the stresses is

$$\delta W_{\epsilon} = \int_{v}\boldsymbol{\sigma}:\delta\boldsymbol{d}dv \tag{III. 2.33}$$

In the above equations, pairs such as $\boldsymbol{\sigma}$ and $\boldsymbol{d}$ are said to be work conjugate with respect to the current deformed volume; their product gives the work per unit of current volume.

If the relation for the virtual work is expressed in the material coordinate system, alternative work conjugate pairs will emerge. Recalling relation (III. 1.50) and

rewriting relation (III. 2.29) for the initial forces per unit volume $\boldsymbol{f}_0 = \boldsymbol{f} \cdot J$ and initial traction forces $\boldsymbol{t}_0 = \boldsymbol{t}(da/dA)$, we obtain:

$$dv = JdV; \tag{III. 1.50}$$

$$\delta W = \int_V J \cdot \boldsymbol{\sigma}: \delta \boldsymbol{d} dV - \int_V \boldsymbol{f}_0 \cdot \delta \boldsymbol{v} dV - \int_{\partial V} \boldsymbol{t}_0 \cdot \delta \boldsymbol{v} dA \tag{III. 2.34}$$

The internal work form equation (III. 2.34) can be expressed in terms of the *Kirchhoff stress tensor* as:

$$\delta W_\epsilon = \int_V \boldsymbol{\tau}: \delta \boldsymbol{d} dV \; ; \qquad \boldsymbol{\tau} = J \cdot \boldsymbol{\sigma} \tag{III. 2.35}$$

The above relations states that the Kirchhoff stress tensor is work conjugate with the virtual rate of deformation tensor with respect to the initial volume. Note that the work per current volume is not equal with the work per initial volume. However, the work per unit mass is invariant, because of the relation (III. 1.52) ($\rho_0 = \rho J$):

$$\frac{1}{\rho} \boldsymbol{\sigma}: \boldsymbol{d} = \frac{1}{\rho_0} \boldsymbol{\tau}: \boldsymbol{d} \tag{III. 2.36}$$

III.2.6. The first Piola-Kirchhoff stress tensor

Even though the above transformation expressed the stress in relationship with the initial volume, relation (III. 2.35) is still dependent on spatial quantities, namely $\boldsymbol{\sigma}$ and $\boldsymbol{\tau}$. In order to correct this issue, the symmetric character of $\boldsymbol{\sigma}$ along with relations (II. 2.32), (III. 1.53) and (II. 2.31) are introduced in equation (III. 2.32) so that:

$$\mathrm{tr}(v \otimes w) = v \cdot w \tag{II. 2.31a}$$

$$\boldsymbol{A}: \boldsymbol{B} = \mathrm{tr}(\mathbf{A}^{\mathrm{T}}\mathbf{B}) = \mathrm{tr}(\mathbf{B}\mathbf{A}^{\mathrm{T}}) = \mathrm{tr}(\mathbf{B}^{\mathrm{T}}\mathbf{A}) = \mathrm{tr}(\mathbf{A}\mathbf{B}^{\mathrm{T}}) = \sum_{i,j=1}^{n} A_{ij} B_{ij} \tag{II. 2.32}$$

$$\delta W_\epsilon = \int_V J \cdot \boldsymbol{\sigma}: \delta \boldsymbol{l} dV = \int_V (J \boldsymbol{\sigma} \boldsymbol{F}^{-T}): \delta \frac{d\boldsymbol{F}}{dt} dV \tag{III. 2.37}$$

In this equation, the work conjugate of the virtual rate of deformation gradient $d\boldsymbol{F}/dt$ is called *the first Piola-Kirchhoff stress tensor*:

$$\boldsymbol{P} = J \boldsymbol{\sigma} \boldsymbol{F}^{-T} \tag{III. 2.38}$$

The first Piola-Kirchhoff stress tensor can also be expressed as:

$$\boldsymbol{P} = \sum_{i,I=1}^{3} P_{i,I} e_i \otimes E_I \tag{III. 2.39}$$

where

$$P_{i,I} = \sum_{j=1}^{3} J\sigma_{ij}(F^{-1})_{I,j} \tag{III. 2.40}$$

Rewriting the equation for the principle of virtual work in terms of the first Piola-Kirchoff stress tensor we obtain:

$$\int_V \boldsymbol{P}: \delta\frac{d\boldsymbol{F}}{dt}dV - \int_V \boldsymbol{f}_0 \cdot \delta\boldsymbol{v}dV - \int_{\partial V} \boldsymbol{t}_0 \cdot \delta\boldsymbol{v}dA \tag{III. 2.41}$$

The differential equilibrium equation can now be obtain in terms of the first Piola-Kirchhoff stress tensor form a reverse algorithm than the one used in obtaining the virtual work equation (III. 2.32) from the spatial differential equilibrium equation (III. 2.15):

$$r_0 = J \cdot r = \mathbf{DIV}\boldsymbol{P} + \boldsymbol{f}_0 = 0 \tag{III. 2.42}$$

where $\mathbf{DIV}\boldsymbol{P}$ is the divergence of the first Piola-Kirchhoff stress tensor with respect to the initial coordinate system:

$$\mathbf{DIV}\boldsymbol{P} = \boldsymbol{\nabla}_0\boldsymbol{P}: \boldsymbol{I}; \qquad \boldsymbol{\nabla}_0\boldsymbol{P} = \frac{\partial \boldsymbol{P}}{\partial \boldsymbol{X}} \tag{III. 2.43}$$

The physical meaning of the Cauchy and second Piola-Kirchhoff stress tensors is as follows:

Consider an element of force $d\boldsymbol{p}$ acting on an element of area $da = \boldsymbol{n} \cdot d\boldsymbol{a}$. In the spatial configuration, the expression can be written as follows:

$$\begin{aligned} d\boldsymbol{p} = \boldsymbol{t} \cdot d\boldsymbol{a} = \boldsymbol{t} \cdot \boldsymbol{n} \cdot da = \boldsymbol{\sigma}da \\ \Rightarrow \boldsymbol{\sigma} = \frac{d\boldsymbol{p}}{da} \end{aligned} \tag{III. 2.44}$$

The Cauchy stress gives the current force per unit of deformed area. In engineering, it is also known as the *true stress*.

Recalling equation (III. 1.59):

$$d\boldsymbol{a} = J\boldsymbol{F}^{-T}d\boldsymbol{A} \tag{III. 1.59}$$

And replacing $d\boldsymbol{a}$ in equation (III. 2.44) we obtain:

$$\begin{aligned} \boldsymbol{\sigma} = \frac{d\boldsymbol{p}}{J\boldsymbol{F}^{-T}d\boldsymbol{A}} \Rightarrow \boldsymbol{\sigma} \cdot J\boldsymbol{F}^{-T} = \frac{d\boldsymbol{p}}{d\boldsymbol{A}} \\ \boldsymbol{P} = \frac{d\boldsymbol{p}}{d\boldsymbol{A}} \end{aligned} \tag{III. 2.45}$$

Equation (III. 2.45) shows that, similar to the deformation gradient $\boldsymbol{F}$, the first Piola-Kirchhoff stress tensor relates an area vector in the initial configuration to the corresponding vector in the current configuration. Thus the first Piola-Kirchhoff stress tensor can be interpreted as the current force per initial surface. These stresses are also known as *nominal or engineering stresses*.

III.2.7. The second Piola-Kirchhoff stress tensor

The first Piola-Kirchhoff stress tensor is not completely configured after the material description. However, *the second Piola-Kirchhoff stress tensor* $\boldsymbol{S}$ is a symmetric tensor obtained by pulling back the spatial element of force $d\boldsymbol{p}$ form equation (III. 2.45) and so replacing it with a material force vector $d\boldsymbol{\mathcal{P}}$:

$$d\boldsymbol{\mathcal{P}} = \phi_*^{-1}[d\boldsymbol{p}] = \boldsymbol{F}^{-1}d\boldsymbol{p} \tag{III. 2.46}$$

Replacing $d\boldsymbol{p}$ in equation (III. 2.46) we obtained the transformed force in terms of the second Piola-Kirchhoff stress tensor $\boldsymbol{S}$ and the element of initial area $d\boldsymbol{A}$:

$$d\boldsymbol{\mathcal{P}} = \boldsymbol{S}d\boldsymbol{A}; \qquad \boldsymbol{S} = J\boldsymbol{F}^{-1}\boldsymbol{\sigma}\cdot\boldsymbol{F}^{-T} \tag{III. 2.47}$$

Similarly, the strain rate work conjugate for the second Piola-Kirchhoff stress tensor is obtained, with the use of equation (III. 1.58b):

$$\delta\boldsymbol{d} = \boldsymbol{F}^{-T}\cdot\frac{\partial\boldsymbol{E}}{\partial t}\cdot\boldsymbol{F}^{-1} \tag{III. 1.76b}$$

Introducing (III. 1.58b) in (III. 2.33) we obtain:

$$\delta W_\epsilon = \int_v \boldsymbol{\sigma}:\delta\boldsymbol{d}dv = \int_V \boldsymbol{S}:\frac{\partial\boldsymbol{E}}{\partial t}dV \tag{III. 2.48}$$

Equation (III. 2.48) shows that the second Piola-Kirchhoff stress tensor $\boldsymbol{S}$ is work conjugate to the material strain rate tensor $\partial\boldsymbol{E}/\partial t$. Thus, the *material virtual work equation* can be written as:

$$\int_V \boldsymbol{S}:\frac{\partial\boldsymbol{E}}{\partial t}dV = \int_V \boldsymbol{f}_0\cdot\delta\boldsymbol{v}dV + \int_{\partial V}\boldsymbol{t}_0\cdot\delta\boldsymbol{v}dA \tag{III. 2.49}$$

The inverses of equations (III. 2.38) and (III. 2.47) are:

$$\boldsymbol{\sigma} = J^{-1}\boldsymbol{P}\boldsymbol{F}^{-T} \quad \text{(III. 2.50}a\text{)}; \qquad \boldsymbol{\sigma} = J^{-1}\boldsymbol{F}\boldsymbol{S}\boldsymbol{F}^{T} \quad \text{(III. 2.50}b\text{)}$$

Applying the push forward/pull back concepts for the Kirchhoff stress and the second Piola-Kirchhoff stress we obtain:

$$\boldsymbol{S} = \boldsymbol{F}^{-1}\boldsymbol{\tau}\boldsymbol{F}^{-T} = \phi_*^{-1}[\boldsymbol{\tau}] \quad \text{(III. 2.51}a\text{)} \qquad \boldsymbol{\tau} = \boldsymbol{F}\boldsymbol{S}\boldsymbol{F}^{T} = \phi_*[\boldsymbol{\tau}] \quad \text{(III. 2.51}b\text{)}$$

The Cauchy stress and the second Piola-Kirchhoff stress are related as:

$$\boldsymbol{S} = J\phi_*^{-1}[\boldsymbol{\sigma}] \quad \text{(III. 2.52}a\text{)} \qquad \boldsymbol{\sigma} = J^{-1}\phi_*[\boldsymbol{S}] \quad \text{(III. 2.52}a\text{)}$$

In equation (III. 2.52) $\boldsymbol{S}$ and $\boldsymbol{\sigma}$ are related by the so called *Piola transformation*, which involves a push forward/pull back operation combine with the volume scaling Jacobian.

III.2.8. Deviatoric and pressure components

In many applications it is necessary to isolate the deviatoric component $\boldsymbol{\sigma}'$ from the hydrostatic pressure p component of the Cauchy stress tensor $\boldsymbol{\sigma}$.

$$\boldsymbol{\sigma} = \boldsymbol{\sigma}' + p\boldsymbol{I} \qquad \text{(III. 2.53a)} \qquad p = \frac{1}{3} tr\boldsymbol{\sigma} = \frac{1}{3}\boldsymbol{\sigma} : \boldsymbol{I} \qquad \text{(III. 2.53b)}$$

Similar relations can be written for the first Piola-Kirchhoff stress tensor and for the second Piola-Kirchhoff stress tensor introducing relations (III. 2.38) and (III. 2.47) in (III. 2.53):

$$\boldsymbol{P} = \boldsymbol{P}' + pJ\boldsymbol{F}^{-T}; \qquad \boldsymbol{P}' = J\boldsymbol{\sigma}'\boldsymbol{F}^{-T} \qquad \text{(III. 2.54a)}$$
$$\boldsymbol{S} = \boldsymbol{S}' + pJ\boldsymbol{C}^{-1}; \qquad \boldsymbol{S}' = J\boldsymbol{F}^{-1}\boldsymbol{\sigma}'\boldsymbol{F}^{-T} \qquad \text{(III. 2.54b)}$$

The relationship between the true deviatoric components $\boldsymbol{P}'$ and $\boldsymbol{S}'$ of the first and second Piola-Kirchhoff stress tensors $\boldsymbol{P}$ and $\boldsymbol{S}$ can be obtained by taking into account the properties of the trace (II. 2.31) and of the double contraction (II. 2.38):

$$\mathrm{tr}(v \otimes w) = v \cdot w \qquad \text{(II. 2.31}a\text{)}$$
$$\mathrm{tr}(\boldsymbol{S})^T = \mathrm{tr}(\boldsymbol{S}) \qquad \text{(II. 2.31}b\text{)}$$
$$\mathrm{tr}(\boldsymbol{S}_1\boldsymbol{S}_2) = \mathrm{tr}(\boldsymbol{S}_2\boldsymbol{S}_1) \qquad \text{(II. 2.31}c\text{)}$$

$$\mathrm{tr}\boldsymbol{S} = \boldsymbol{I} : \boldsymbol{S} \qquad \text{(II. 2.38}a\text{)}$$
$$\boldsymbol{S} : (v \otimes w) = u \cdot \boldsymbol{S}v \qquad \text{(II. 2.38}b\text{)}$$
$$(v \otimes w) : (x \otimes y) = (v \cdot w)(x \cdot y) \qquad \text{(II. 2.38}c\text{)}$$
$$\boldsymbol{S} : \boldsymbol{W} = 0 \quad if \quad \boldsymbol{S}^T = \boldsymbol{S} \quad and \quad \boldsymbol{W} = -\boldsymbol{W}^T \qquad \text{(II. 2.38}d\text{)}$$

$$\boldsymbol{S}' : \boldsymbol{C} = 0 \qquad \text{(III. 2.55a)}$$
$$\boldsymbol{P}' : \boldsymbol{F} = 0 \qquad \text{(III. 2.55b)}$$

With the help of relations (III. 2.55) the hydrostatic pressure can be evaluated in terms of the first and second Piola-Kirchhoff stress tensors $\boldsymbol{P}$ and $\boldsymbol{S}$:

$$p = \frac{1}{3} J^{-1}\boldsymbol{P} : \boldsymbol{F} \qquad \text{(III. 2.56a)}$$
$$p = \frac{1}{3} J^{-1}\boldsymbol{S} : \boldsymbol{C} \qquad \text{(III. 2.56b)}$$

III.2.9. Stress rates

Equation (III. 2.10) gives the relation for the Cauchy stress after the rigid body motion. Its time derivative will be:

$$\frac{d\tilde{\boldsymbol{\sigma}}}{dt} = \frac{d\boldsymbol{Q}}{dt}\boldsymbol{\sigma}\boldsymbol{Q}^T + \boldsymbol{Q}\frac{d\boldsymbol{\sigma}}{dt}\boldsymbol{Q}^T + \boldsymbol{Q}\boldsymbol{\sigma}\frac{d\boldsymbol{Q}^T}{dt} \qquad \text{(III. 2.57)}$$

The above equation shows that in general, the rate of Cauchy stress is not an objective quantity, unless the rigid body motion is time independent. For

materials that exhibit rate-dependency, it is necessary to determine objective stress-rate measures.

Given the fact that the second Piola-Kirchhoff stress tensor $\boldsymbol{S}$ is independent of any possible rigid body motion, a stress-rate measure was developed based on the properties $\boldsymbol{S}$, namely the *Truesdell strain-rate tensor* $\boldsymbol{\sigma}^{\circ}$, which is defined in terms of the Piola transformation of the derivative of the second Piola-Kirchhoff stress tensor $\boldsymbol{S}$.

$$\boldsymbol{\sigma}^{\circ} = J^{-1}\phi_{*}\left[\frac{d\boldsymbol{S}}{dt}\right] = J^{-1}\boldsymbol{F}\left[\frac{d}{dt}(J\boldsymbol{F}^{-1}\boldsymbol{\sigma}\boldsymbol{F}^{-T})\right]\boldsymbol{F}^{T} \tag{III. 2.58}$$

If we are to express the time derivative of $\boldsymbol{F}^{-1}$ in terms of the time derivative of $\boldsymbol{I}$ as:

$$\begin{aligned} \boldsymbol{I} &= \boldsymbol{F}\boldsymbol{F}^{-1} \\ \frac{d\boldsymbol{I}}{dt} &= \frac{d\boldsymbol{F}}{dt}\boldsymbol{F}^{-1} + \boldsymbol{F}\frac{d\boldsymbol{F}^{-1}}{\boldsymbol{dt}} \\ \boldsymbol{F}\frac{d\boldsymbol{F}^{-1}}{\boldsymbol{dt}} &= -\frac{d\boldsymbol{F}}{dt}\boldsymbol{F}^{-1} \end{aligned} \tag{III. 2.59}$$

Recalling equation (III. 1.53) and replacing it equation (III. 2.59) will give

$$\boldsymbol{l} = \frac{d\boldsymbol{F}}{dt}\boldsymbol{F}^{-1} \tag{III. 1.53}$$

$$\frac{d\boldsymbol{F}^{-1}}{dt} = -\boldsymbol{F}^{-1}\boldsymbol{l} \tag{III. 2.60}$$

Expanding equation (III. 2.58) will give:

$$\boldsymbol{\sigma}^{\circ} = J^{-1}\frac{dJ}{dt}\boldsymbol{\sigma} + \boldsymbol{F}\frac{d\boldsymbol{F}^{-1}}{dt}\boldsymbol{\sigma} + \frac{d\boldsymbol{\sigma}}{dt} + \boldsymbol{\sigma}\frac{d\boldsymbol{F}^{-T}}{dt}\boldsymbol{F}^{T} \tag{III. 2.61}$$

Recalling equations (III. 1.72b) and (III. 2.60) and introducing them in equation (III. 2.61)

$$\frac{dJ}{dt} = J\mathrm{tr}\boldsymbol{d} \tag{III. 1.72b}$$

$$\boldsymbol{\sigma}^{\circ} = \frac{d\boldsymbol{\sigma}}{dt} - \boldsymbol{l}\boldsymbol{\sigma} + (\mathrm{tr}\boldsymbol{d})\boldsymbol{\sigma} - \boldsymbol{\sigma}\boldsymbol{l}^{T} \tag{III. 2.62}$$

The Truesdell rate of the Kirchhoff stress tensor can be described in terms of the Lie derivative:

$$\boldsymbol{\tau}^{\circ} = J\boldsymbol{\sigma}^{\circ} = \mathcal{L}_{\phi}[\boldsymbol{\tau}] \tag{III. 2.63}$$